



University of  
**Nottingham**

UK | CHINA | MALAYSIA

DOCTORAL THESIS

---

**Multi-material hot-melt inkjet 3D printing:  
towards complex and personalised dosage form**

---

*Author:*

Anna Lion

*Supervisors:*

Prof. Clive J. Roberts,  
Prof. Ricky D. Wildman,  
Prof. Morgan R. Alexander.

*A thesis submitted in fulfilment of the requirements  
for the degree of Doctor of Philosophy*

*in the*

School of Pharmacy

University of Nottingham

September 28, 2021



# Declaration of Authorship

I, Anna Lion, declare that this thesis titled, "Multi-material hot-melt inkjet 3D printing:

towards complex and personalised dosage form" and the work presented in it are my own. I confirm that:

- This work was done wholly or mainly while in candidature for a research degree at this University.
- Where any part of this thesis has previously been submitted for a degree or any other qualification at this University or any other institution, this has been clearly stated.
- Where I have consulted the published work of others, this is always clearly attributed.
- Where I have quoted from the work of others, the source is always given. With the exception of such quotations, this thesis is entirely my own work.
- I have acknowledged all main sources of help.
- Where the thesis is based on work done by myself jointly with others, I have made clear exactly what was done by others and what I have contributed myself.

Signed: *Anna Lion*

---

Date: 28-09-2021

---



*“Oh, now what’s this, then? I love this. A big, flashy-lighty thing. That’s what brought me here. Big, flashy-lighty things have got me written all over them. Not actually, but give me time... and a crayon.”*

The Doctor



# *Abstract*

Three-dimensional printing includes a wide variety of manufacturing techniques, which are based on the digitally-controlled deposition of materials (layer-by-layer) to create freeform 3D geometries. 3D printing with single-materials is a well-established technology that has found application across many different fields from engineering to medicine and pharmacy by enabling the production of complex and high quality prototypes and devices that were previously either difficult to manufacture expensive or time consuming.

The focus of this thesis is the design and development of a 3D system capable of fabricating, in a single additive process, multi-material solid dosage forms showing tailored release profiles. Hot-melt piezo-activated inkjet 3D printing was identified as an alternative to the traditional solvent based inkjet printing (IJP). Inks are kept liquid above their melting temperature eliminating the need of additional solvent and its consequent removal post processing step. This becomes of particular interest when considering those material, such as lipids which cannot be processed by traditional additive methods without the need of other excipients. Making thermal jetting for pharmaceutical application a great alternative 3DP method.

A commercially available printer was modified to include a dual reservoir unit capable of dispensing two different materials during the same additive process. A detailed description is presented of all the modifications and implementation introduced, including its main elements such as the choice of printer and printing head, the custom designed printing unit and supports, the temperature control and power supply system. In addition, the development of a complementary software update and slicing strategy is discussed.

To complement the new set-up, a library of suitable material was established. Candidates were selected to comply with the limitations imposed by the printing technique (melting point below 90 °C and viscosity in the 8-20 cP range) and on the base of their suitability for pharmaceutical use.

Specifically our attention focused on lipids, which present thermo-mechanical properties compatible with the range of interest. In addition, they are well known excipients used in traditional tableting techniques as enhancer in the delivery of poorly soluble drugs. Commonly used pharmaceutical lipids (Apifil CG, Candelilla, Compritol 888 ATO, Compritol HD5 ATO and Precirol ATO) and Fenofibrate (model drug) were used to prepare

both drug-free and drug-loaded inks with drug concentrations varying between 5% and 30% (w/w). Each ink formulation was thoroughly tested for printability to ensure compatibility with the method here reported.

Finally, the gathered knowledge was used to design and produce several proof-of-concept tailored release profile solid dosage forms. These included single and multi-material complex 3D patterns with defined localised drug loading where the drug-free ink is used as a release-retarding material to produce a series of tablets structures displaying immediate, extended, delayed and pulsatile drug release. This work adds significantly to the current landscape of 3D printing in that it illustrates the ability to design and build a multi-head hot-melt ink jet printer for the co-deposition of materials to form complex dosage forms with high spatial resolution. The potential of this approach is then illustrated with the manufacture of lipidic based complex geometry dosage forms able to demonstrate 'programmable' drug release patterns in *in vitro* studies.

## *Acknowledgements*

The work presented in this thesis could not have been achieved without the support and assistance of many people and I would like to take this opportunity to express my deepest appreciation. I would like to thank:

- My supervisors Prof. Clive J. Roberts, Prof. Ricky Wildman and Morgan R. Alexander for giving me the opportunity to step out of my comfort zone and discover the amazing field of 3D printing. I would also like to offer a special thank you to Clive for his patience and availability.
- My internal examiner Prof. Cameron Alexander for the interesting discussions and challenging questions during my first and second year reviews, and in particular during my final viva. He always challenged me to look a little bit further and to question my understanding of my work and science in general. I will always cherish these conversations.
- Prof. Sheng Qi for taking the role of external assessor during my final viva and for making it a little bit less scary. It was a blessing to have this opportunity. Despite the nerve-wrecking circumstances it was a pleasure to be able to discuss science and receive all the useful feedback on this work.
- Vincenzo di Bari, postdoc and friend, who taught me so much about lipids and life with his enthusiastic approach to science. I also want to thank him for all the discussion and guidance and laughter and all the time invested in this project. I don't think this work would have reached this high standards if it wasn't for him. I cannot thank him enough.
- The Addictive Manufacturing Lab people, Mark East, Mark Hardy, Chris Strong, Negar Gilani and everyone else in the B19. Thank you guys, for sharing with me the frustration with the lab challenges, the thrill for each new promising result and the happiness for every achievement.
- The department's workshops technicians and administration for their patience, help and valuable suggestions.
- My housemate Giulia and Federico. You made me feel at home.
- Elisa and Marco because after 10 years of friendship, 2 different continents and 3 different states you are still there for me and I couldn't ask

for better friends. Elisa you have been part of my life for so long and I don't even know how. Though our ups and downs we have always been there for each other and I cannot wait to hug you again.

- All my friends, old and new, and in particular Nathan and Sophie (plus Rowan of course), for being there for me despite everything, for always believing in me and for showing me what friendship is. Not to forget for all the board games and the dnd nights, the climbing days the hiking trips and of course for all the laughter and generic happiness.
- Dean, who not only read this entire work, but also had to listen to me repeating it multiple times for meetings, presentations and finally in preparation of my viva. He believed in me when I didn't, and kept me grounded and calm in the darkest times. It is safe to say that if I was able to find the strength to finish this thesis it is because I borrowed some of his. Thank you for being with me through these absurd and hard times. I love you.
- My brother Luca. Does this one really need an explanation? Thank you for always being there for calling out my insanity while also sharing it, for making me laugh even in the darkest of days and for having my back always. *Ti voglio un bene dell'anima!*
- I miei genitori, che mi hanno supportato ed incoraggiato in tutti questi anni, che hanno accettato la distanza, che hanno rispettato le mie scelte, anche quando le ritenevano sbagliate, e sono sempre stati pronti ad aiutarmi anche quando non avevo la forza di chiedere aiuto. Tutto questo non sarebbe stato possibile senza di voi. *Vi voglio bene,*

# Contents

## Declaration of Authorship

<b>Abstract</b>	<b>i</b>
<b>Acknowledgements</b>	<b>iv</b>
<b>1 Introduction</b>	<b>1</b>
1.1 History of oral solid dosage forms manufacturing . . . . .	1
1.2 Pharmaceutical challenges and 3D printing solutions . . . . .	5
1.2.1 Oral solid dosage forms distribution and environmental sustainability . . . . .	5
1.2.2 Personalised medicine . . . . .	6
1.2.3 Production of drug release profiles via SDFs . . . . .	8
1.2.4 Polypharmacy . . . . .	10
1.3 3D printing . . . . .	12
1.3.1 3D printed pharmaceuticals . . . . .	15
1.3.1.1 Extrusion-based methods . . . . .	15
1.3.1.2 Laser based systems . . . . .	21
1.3.1.3 Jetting systems . . . . .	25
1.4 Contribution of the present work . . . . .	31
1.4.0.1 Aims and objectives . . . . .	32
<b>2 Platform development and understanding</b>	<b>36</b>
2.1 Commercially available systems . . . . .	40
2.2 Hardware implementations . . . . .	48
2.3 Software implementations . . . . .	53
2.3.1 LP50 software adaptations . . . . .	53
2.3.2 Temperature control . . . . .	54
2.3.3 Calibration . . . . .	55
2.3.4 3D object design and slicing . . . . .	56
2.3.5 Material deposition conditions . . . . .	57

2.4	Final set-up . . . . .	59
<b>3</b>	<b>Materials and methods</b>	<b>61</b>
3.1	Materials . . . . .	61
3.1.1	Fenofibrate . . . . .	61
3.1.2	Candelilla . . . . .	62
3.1.3	Apifil CG . . . . .	62
3.1.4	Compritol 888 ATO . . . . .	63
3.1.5	Compritol HD5 ATO . . . . .	64
3.1.6	Precirol ATO 5 . . . . .	65
3.1.7	Flexible polyethylene terephthalate film . . . . .	65
3.2	Methods . . . . .	67
3.2.1	Statistical analysis . . . . .	67
3.2.2	Ink preparation . . . . .	68
3.2.3	Density studies . . . . .	69
3.2.4	Differential Scanning Calorimetry . . . . .	70
3.2.5	Thermogravimetric Analysis . . . . .	71
3.2.6	Shear viscosity characterisation . . . . .	72
3.2.7	Scanning electron microscopy and Energy Dispersive X-ray Spectroscopy . . . . .	78
3.2.8	Attenuated Total Reflection-Fourier Transform Infrared Spectroscopy . . . . .	81
3.2.9	Raman Spectroscopy . . . . .	83
3.2.10	X-ray Powder diffraction . . . . .	85
3.2.11	Advanced Drop Analysis . . . . .	86
3.2.12	Hot-melt inkjet 3D printing . . . . .	88
3.2.13	<i>In vitro</i> drug release . . . . .	88
3.2.14	UV-Visible spectrophotometry . . . . .	91
<b>4</b>	<b>Carrier selection and solid dosage forms print.</b>	<b>93</b>
4.1	Results and discussion: Inks characterisation . . . . .	95
4.1.1	Density studies . . . . .	95
4.1.2	Differential Scanning Calorimetry . . . . .	98
4.1.3	Thermogravimetric analysis . . . . .	107
4.1.4	Shear viscosity characterisation . . . . .	113
4.1.5	Fourier Transform Infrared Spectroscopy . . . . .	122
4.1.6	Conclusions . . . . .	125
4.2	Results and discussion: 3D deposition of solid dosage forms .	126
4.2.1	Drop formation and deposition . . . . .	126

4.2.1.1	Drop formation . . . . .	127
4.2.1.2	Drop deposition, 2D and 3D resolution . . . . .	132
4.2.2	3D functional deposition . . . . .	134
4.2.2.1	Optical imaging . . . . .	135
4.2.2.2	Drug loading evaluation . . . . .	136
4.2.2.3	Drug crystallinity: X-ray Powder diffraction (XRPD) . . . . .	139
4.2.2.4	<i>In Vitro</i> release study . . . . .	142
4.2.2.5	Conclusions . . . . .	148
<b>5</b>	<b>Influence of 3D design on model drug release profiles.</b>	<b>150</b>
5.1	Material and Methods . . . . .	150
5.1.1	Material . . . . .	150
5.1.2	Methods . . . . .	152
5.1.2.1	Tablets structure design . . . . .	152
5.1.2.2	3DP Tablet production . . . . .	157
5.2	Results and discussion . . . . .	159
5.2.1	Immediate release tablets . . . . .	159
5.2.1.1	Optical spectroscopy and printed tablets geometrical evaluation. . . . .	159
5.2.1.2	Content uniformity and weight variation . . . . .	162
5.2.1.3	<i>In vitro</i> drug release . . . . .	166
5.2.2	Delayed release tablets . . . . .	169
5.2.2.1	Optical spectroscopy and printed tablets geometrical evaluation . . . . .	169
5.2.2.2	Raman spectroscopy . . . . .	174
5.2.2.3	<i>In vitro</i> drug release . . . . .	175
5.2.3	Pulsatile release tablets . . . . .	177
5.2.3.1	Optical spectroscopy and printed tablets geometrical evaluation . . . . .	177
5.2.3.2	Content uniformity and weight variation . . . . .	180
5.2.3.3	Raman spectroscopy . . . . .	182
5.2.3.4	<i>In vitro</i> drug release . . . . .	183
5.3	Conclusions . . . . .	185
<b>6</b>	<b>Conclusions and future work</b>	<b>187</b>
6.1	Platform design and development . . . . .	188
6.2	Carrier selection and solid dosage forms evaluation . . . . .	190
6.3	Fabrication of 3D multi-material functional structures . . . . .	193

<b>A Appendix</b>	<b>198</b>
A.1 Code . . . . .	198
A.2 Materials review . . . . .	204
A.3 Dimatix cartridge adaptation . . . . .	206
<b>Bibliography</b>	<b>211</b>

# List of Figures

1.1	Schematic diagram of granulation methods and their unit processes by different techniques. . . . .	3
1.2	Additive manufacturing technologies . . . . .	14
1.3	Pressure-assisted microsyringes . . . . .	16
1.4	Schematic structural diagram of captopril osmotic pump and nifedipine and glipizide sustained release tablet [67] . . . . .	18
1.5	Fused deposition modelling . . . . .	19
1.6	Digital and Raman images alongside with their dissolution profiles of the multi material tablets with multilayer and sectioned DuoCaplet design [71] . . . . .	20
1.7	Selective laser sintering schematics(SLS) . . . . .	22
1.8	Image and dissolution study of tablets composed of 5% Paracetamol, 3% of Candurin® Gold Sheen and 92% HPMC (TOP) or kollidon (BOTTOM) [76]. . . . .	23
1.9	Stereolithography schematics (SLA) . . . . .	24
1.10	Digital and optical images of disc and ring printlets produced using multi-material SLA [79] . . . . .	25
1.11	Schematic diagram of a continuous inkjet (CIJ) printer (Left), and a drop on demand (DoD) inkjet printing system, (middle) is the thermal inkjet and (right) is the piezoelectric inkjet . . . . .	26
1.12	Schematic representation of the concentric tablets with material gradients [85]. . . . .	28
1.13	Dissolution profiles for the printed solid tablet and honeycomb like tablets with constant weight and various cell size [95]. . . . .	30
2.1	Schematic of the PiXDRO LP50, Dimatix printers and relative cartridges. . . . .	39
2.2	Schematic representation of the LP50 machine including its major features and a detail picture of the magnetic mounting ring. . . . .	41
2.3	Schematic of the hot-melt inkjet assembly for PiXDRO LP50 printer. . . . .	45

2.4	Spectra head Se 128 (A) and DPI tilt (B) . . . . .	46
2.5	Photo of the assembled prototype and rendered image of the assembled prototype and the single support parts . . . . .	49
2.6	Detail of the print head holder. . . . .	51
2.7	Comparison between the original hot-melt reservoir from Meyer Burger and our redesigned version. . . . .	52
2.8	Microscope images of multi-material depositions including prob- lematic areas. . . . .	56
2.9	Piezoelectric actuator trapezoidal printing pulse. . . . .	59
2.10	Final the dual hot-melt system set-up. . . . .	60
3.1	Chemical structure of Fenofibrate( $C_{20}H_{21}ClO_4$ ). . . . .	61
3.2	Chemical structure of Compritol 888 ATO. . . . .	63
3.3	Chemical structure of Compritol HD5 ATO. . . . .	64
3.4	Chemical structure of Precirol ATO 5. . . . .	65
3.5	Chemical structure of polyethylene terephthalate ( $ C_{10}H_8O_4 _n$ ). . . . .	66
3.6	Differential Scanning Calorimeter schematics. . . . .	70
3.7	Thermogravimetric Analyzer schematics. . . . .	72
3.8	Cone-plate geometry. . . . .	75
3.9	Kinexus Pro Rheometer. . . . .	76
3.10	Thermogravimetric curves of Newtonian and non-Newtonian fluids. . . . .	77
3.11	Scanning electron microscope and sputter coater. . . . .	80
3.12	Fourier Transform Infrared Spectroscopy (FTIR) schematics . . . . .	82
3.13	Perkin Elmer FT-IR Spectrometer Frontier . . . . .	82
3.14	Raman schematics . . . . .	84
3.15	X-ray Powder diffraction (XRPD) schematics . . . . .	86
3.16	Advanced Drop Analysis (ADA) schematics . . . . .	87
3.17	<i>In vitro</i> drug release: dissolution tester. . . . .	89
3.18	Schematics of UV-Visible spectrophotometer . . . . .	91
4.1	Density determination of ink compounds. . . . .	96
4.2	Differential Scanning Calorimetry heating curve of pure Fenofi- brate . . . . .	99
4.3	Differential Scanning Calorimetry curve of pure Fenofibrate, Compritol HD and mixture of the two. . . . .	100
4.4	Differential Scanning Calorimetry heating curve of pure Fenofi- brate, Compritol 888 ATO and mixture of the two. . . . .	102

4.5	Differential Scanning Calorimetry curve of pure Fenofibrate, Apifil CG and mixture of the two. . . . .	103
4.6	Differential Scanning Calorimetry heating curve of pure Fenofibrate, Candelilla wax and mixture of the two. . . . .	104
4.7	Differential Scanning Calorimetry heating curve of pure Fenofibrate, Precirol ATO 5 and mixture of the two. . . . .	106
4.8	Thermogravimetric and derivative curves of pure Fenofibrate. . . . .	108
4.9	Thermogravimetric and derivative curves of pure Apifil CG, Candelilla and Precirol. . . . .	109
4.10	Thermogravimetric and derivative curves of pure Compritol 888 ATO and Compritol HD5 ATO. . . . .	110
4.11	Thermogravimetric curves of pure Fenofibrate, Compritol HD5 ATO and mixture of the two. . . . .	112
4.12	Flow curves of Fenofibrate. . . . .	114
4.13	Flow curves of Candelilla and $\eta = \eta_{\infty}$ behaviour in response to API content. . . . .	116
4.14	Flow curves of Compritol 888 ATO and $\eta = \eta_{\infty}$ behaviour in response to API content. . . . .	117
4.15	Flow curves of Precirol ATO 5 and $\eta = \eta_{\infty}$ behaviour in response to API content. . . . .	118
4.16	Flow curves of Apifil CG and $\eta = \eta_{\infty}$ behaviour in response to API content. . . . .	121
4.17	Flow curves of Compritol HD5 ATO and $\eta = \eta_{\infty}$ behaviour in response to API content. . . . .	122
4.18	Fourier Transform Infrared Spectroscopy analysis of ink and carrier samples. . . . .	123
4.19	Piezoelectric actuator trapezoidal printing pulse. . . . .	128
4.20	Printing parameters optimisation via Advance Drop Analysis of Compritol HD5 ATO . . . . .	129
4.21	Non-breakup condition study . . . . .	133
4.22	Digital honeycomb design of 3D functional tablets. . . . .	135
4.23	Photos of 3D printed tablets showing honeycomb structured alongside with a conventional disc tablet . . . . .	136
4.24	X-ray powder diffraction curves of Compritol HD5 ATO printlets . . . . .	139
4.25	X-ray powder diffraction curves of Compritol 888 ATO printlets . . . . .	140
4.26	X-ray powder diffraction curves of Precirol ATO 5 printlets . . . . .	141

4.27	Dissolution profiles of printed circular tablets as a function of time, drug concentration and carrier material . . . . .	145
5.1	Digital design of immediate release tablets. . . . .	153
5.2	Digital design of delayed release tablets. . . . .	154
5.3	Digital design of pulsatile release tablets. . . . .	155
5.4	Photos of immediate release tablets. . . . .	160
5.5	Optical microscope images of immediate release tablets. . . . .	160
5.6	SEM images of immediate release tablet $\varnothing = 0,60mm$ channels. . . . .	162
5.7	Fourier Transform Infrared Spectroscopy analysis of immediate release tablets. . . . .	166
5.8	<i>In vitro</i> dissolution test of immediate release tablets. . . . .	168
5.9	Photos of delayed release tablets. . . . .	169
5.10	Optical microscope images of delayed release tablets. . . . .	171
5.11	SEM images of delayed release tablets, 1 mm shell thickness. . . . .	172
5.12	Fourier Transform Infrared Spectroscopy analysis of delayed release tablets. . . . .	173
5.13	Fourier Transform Infrared Spectroscopy analysis of delayed release tablets. . . . .	174
5.14	Raman spectra and linear mapping of the core shell interface in delayed release tablet. . . . .	175
5.15	<i>In vitro</i> dissolution test of delayed release tablets. . . . .	177
5.16	Photo of pulsatile release tablets. . . . .	179
5.17	Optical microscope images of pulsatile release tablets. . . . .	179
5.18	SEM images of pulsatile release tablet. . . . .	180
5.19	Fourier Transform Infrared Spectroscopy analysis of pulsatile release tablets. . . . .	181
5.20	Raman spectra and linear mapping of the core-shell and ring-shell interfaces in pulsatile release tablet. . . . .	183
5.21	<i>In vitro</i> dissolution test of Pulsatile release tablets. (a) Shows the discrete release profile while (b) shows the cumulative release profiles obtained by addition of the data in graph (a). . . . .	184
A.1	Dual Dimatix assembly for the LP50 printer . . . . .	206
A.2	Dimatix Material Cartridge . . . . .	207
A.3	Dimatix Material Cartridge plus heating element . . . . .	207
A.4	Thermogravimetric curves of shell and bag materials samples from Dimatix cartridge . . . . .	208
A.5	Damage to Dimatix cartridge after heating experiment . . . . .	209

# List of Tables

1.1	Advantages and disadvantages of 3D printing . . . . .	34
2.1	PiXDRO LP50 technical data [105] . . . . .	44
2.2	Hot-melt unit product data [106] . . . . .	47
3.1	Dissolution test conditions. . . . .	90
4.1	Linear regression parameters for density determination . . . . .	97
4.2	Density determination of drug loaded inks . . . . .	98
4.3	Identification of endothermic peaks for Compritol HD5 ATO based inks . . . . .	101
4.4	Identification of endothermic peaks for Compritol 888 ATO based inks . . . . .	102
4.5	Identification of endothermic peaks for Apifil CG wax based inks . . . . .	104
4.6	Identification of endothermic peaks for Candelilla wax based inks . . . . .	105
4.7	Identification of endothermic peaks for Precirol ATO 5 based inks . . . . .	106
4.8	Main Thermogravimetical parameters . . . . .	107
4.9	Compritol HD5 ATO Thermogravimetical parameters . . . . .	111
4.10	Fenofibrate $\eta_{\dot{\gamma} \rightarrow \infty}$ . . . . .	114
4.11	Fenofibrate, Candelilla, Compritol 888 ATO and Precirol ATO 5 comparative table of $\eta_{\dot{\gamma} \rightarrow \infty}$ values. . . . .	115
4.12	Fenofibrate, Compritol HD5 ATO and Apifil CG comparative table of $\eta_{\dot{\gamma} \rightarrow \infty}$ values [mPa s . . . . .	120
4.13	FTIR characterisation of ink samples . . . . .	124
4.14	Linear regression of FTIR characterisation intensities of ink samples. . . . .	125
4.15	Optimised printing waveform parameters . . . . .	131
4.16	Optimised depositional parameters. . . . .	134
4.17	Printlets Fenofibrate content . . . . .	137

4.18	FTIR characterisation of Immediate release tablets via the intensity of the Fenofibrate characteristic $765\text{ cm}^{-1}$ peak. . . . .	138
4.19	UV-Vis Fenofibrate calibration curve parameters . . . . .	143
4.20	Drug release kinetics study . . . . .	147
5.1	Summary of the immediate, delayed and pulsatile tablets geometrical and compositional properties . . . . .	156
5.2	Summary of printing parameters . . . . .	158
5.3	Channel diameter of immediate release tablets at constant drug loading concentration (10%). . . . .	161
5.4	Summary of the immediate release tablets geometrical and weight properties . . . . .	164
5.5	FTIR characterisation of immediate release tablets via the intensity of the Fenofibrate characteristic $765\text{ cm}^{-1}$ peak. . . . .	165
5.6	UV-Vis Fenofibrate calibration curve parameters . . . . .	167
5.7	Summary of the delayed release tablets geometrical and weight properties . . . . .	170
5.8	FTIR characterisation of immediate release tablets via the intensity of the Fenofibrate characteristic $765\text{ cm}^{-1}$ peak. . . . .	174
5.9	Summary of the pulsatile release tablets geometrical and weight properties . . . . .	181
5.10	FTIR characterisation of pulsatile release tablets via the intensity of the Fenofibrate characteristic $765\text{ cm}^{-1}$ peak. . . . .	182
A.1	Material review . . . . .	205

# List of Abbreviations

<b>2D</b>	2-dimensional
<b>3D</b>	3-dimensional
<b>ADA</b>	Advanced Drop Analysis
<b>AFM</b>	Atomic Force Microscope
<b>AM</b>	Additive Manufacturing
<b>API</b>	Active Pharmaceutical Ingredient
<b>ATR</b>	Attenuated Total Reflection
<b>BMP</b>	Bitmap (file)
<b>C#</b>	C-sharp (programming)
<b>CAD</b>	Computer Assisted Design
<b>CCD</b>	Charged-Coupled Device
<b>CIJ</b>	Continuous Inkjet
<b>CRDDS</b>	controlled release drug delivery systems
<b>DoD</b>	Drop-on-Demand
<b>DPI</b>	Drops Per Inch
<b>DSC</b>	Differential scanning calorimetry
<b>DTG</b>	Derivative Thermogravimetric
<b>FDM</b>	Fused Deposition Modelling
<b>FOV</b>	Field Of View
<b>FPS</b>	Frames Per Second
<b>FTIR</b>	Fourier Transform Infrared Spectroscopy
<b>GUI</b>	Graphics User Interface
<b>HMI</b>	Human Machine Interface
<b>HPLC</b>	High Performance Liquid Chromatography
<b>IJP</b>	InkJet Printing
<b>I/O</b>	Electronic Input / Output
<b>IR</b>	Infrared (Radiation)
<b>LS</b>	Laser Sintering
<b>NGS</b>	Next Generation Sequencing
<b>NIR</b>	Near infrared radiation
<b>OSD</b>	Oral Solid Dosage
<b>PAM</b>	Pressure-assisted microsyringes

<b>PC</b>	Personal computer
<b>PEG</b>	Polyethylene Glycol
<b>PET</b>	Polyethylene Terephthalate
<b>PIJ</b>	Piezoelectric Ink-jet
<b>PLA</b>	Polylactic Acid
<b>PVA</b>	poly(vinyl alcohol)
<b>SDF</b>	Solid Dosage Form
<b>SEM</b>	Scanning Electron Microscope
<b>SLA</b>	Stereolithography
<b>SLS</b>	Laser Sintering
<b>STL</b>	Stereolithography (file)
<b>TGA</b>	Thermogravimetric Analysis
<b>ToF</b>	Time of Flight
<b>UV</b>	Ultraviolet (Radiation)
<b>XML</b>	Extensible Markup Language
<b>.HML</b>	HostMonitor TestList (file)

# Chapter 1

## Introduction

### 1.1 History of oral solid dosage forms manufacturing

Oral solid dosage forms (SDFs) is a term which identifies any pharmaceutical drug product that is orally ingested, dissolved in the digestive system, and delivered to the body through absorption into the bloodstream [1]. Among these, the most common are tablets (or pills in common parlance) and capsules.

The first known references to pills dates back to around 1500 BC and were found on papyrus in ancient Egypt [2, 3], with the recipe calling for bread dough, honey or grease with medicinal ingredients, such as plant powders or spices compressed into a ball and administered to the patient. Similar treatments were described in Greece by the word *katapotia* ("something to be swallowed")[4] and the Roman scholar Pliny talked about it in his "naturalis historia", dating back to 23-79 AD, where he named it "pilula" for the first time, from which we derive the modern name pill [5].

In 1843, William Brockedon was granted a patent for a machine capable of compressing powder into a tablet without use of an adhesive. Its first tablets were made of compressed sodium and potassium carbonate and were used as a calcium supplement and antacid [2, 6]. Just like this, tablets were 'born' as we still know them today, meaning that whilst manufacturing has been refined, it never really evolved in basic principle over the last two centuries. This lack of evolution has roots strongly anchored in the manufacturing process, SDFs are easy to administer, are non-perishable and the manufacturing methods are cheap, well understood and well-developed.

Traditionally, tablets are obtained via compression of the active pharmaceutical ingredient (API) and excipients including lubricants, binders, disintegrants, diluents and fillers. Furthermore, tablets can either be uncoated,

meaning that once formed the tablets are left in their bare state without any additional external layer, or coated, when an extra layer is added to encase the tablet and create a smooth surface. Coating is also the main principle in much of capsule production where the drug substance and dry ingredients are layered around a core. Regardless of type the main goal in the production of any SDFs is to ensure repeatability between batches and consistent distribution of ingredients within each dosage form guaranteeing consistency of dissolution and bioavailability.

Focusing attention on the production of tablets, three main methods are commonly used in preparing powder for compression: wet granulation, dry granulation and direct compression. Each method is catered towards the requirement of the individual solid formulation, such as particle size, bulk density and flowability.

**Wet granulation** is the process of joining powder particles together to form what is known as a granule using a binder solution or a solvent. The granules are then dried and often sieved. Once the desirable particle size and distribution has been reached the granules are compressed to form the final uncoated product [7, 8]. The main benefit of wet granulation lies in the control that it offers over particle size and uniformity, increased bulk density and improvement in solubility and bioavailability by coating the particle surface with hydrophilic polymer improving wettability [9]. However, the long processing time required during the wetting and drying process are more likely to allow for API transformations changing the long term drug delivery capability and efficiency and consequently the overall performance of the solid dosage form [7, 9].

**Dry granulation** is the process of combining powder particles together via a high-intensity force which joins the granules and compacts the powders without the use of an additional binder or solvent. This system is particularly useful when dealing with moist and temperature sensitive ingredients [10, 11]. During dry granulation a combination of counter rotating press rolls and milling are used to compact the particles and generate compact ribbons, which are then milled to produce granules with the desired particle size. Compared to previous cases dry granulation is a fast method to produce high bulk density at the price however of higher particle defects and reduced plasticity [10, 9]. Furthermore due to the high compression energy involved it is not suitable for APIs sensitive to heat and high pressures [10, 11].

Lastly, in **direct compression** the initial granules are blended and compacted together, without directly changing or impacting the starting granules [12, 13]. This process is faster than both types of granulation due to the fewer steps involved. In addition, it causes no physical changes to the starting particles reducing active ingredient stability issues. However, the number of materials suitable for this process are limited due to the specific property requirements of the technique, including: high bulk density, good compression and flowability, additionally the excipients and APIs must have similar particle size distribution to avoid segregation. Specialist powders created for Direct Compression are often more expensive than their granulation equivalents. All granulation techniques are summarised in Figure 1.1.

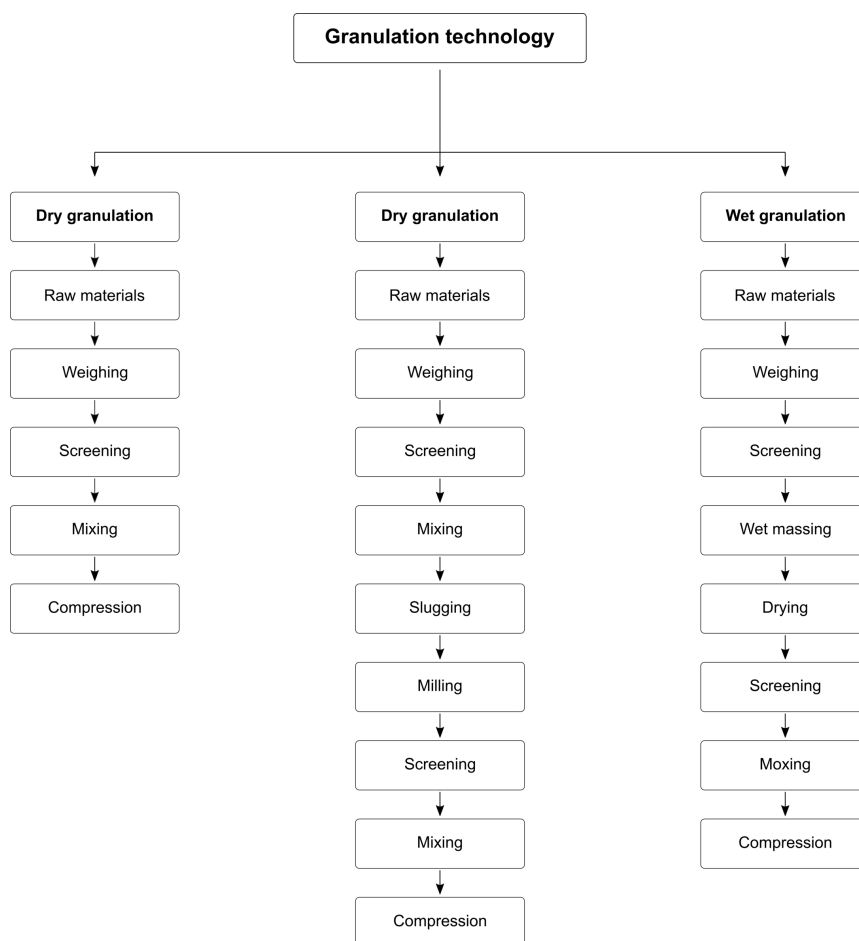


FIGURE 1.1: Schematic diagram of granulation methods and their unit processes by different techniques [10].

As a consequence of this stagnating approach to tablet production, manufacturers are constantly on the lookout for ways to innovate the pharmaceutical field while minimising their expensive research costs and reducing the

risks associated with attempting to develop new technologies.

**3D printing** is an additive manufacturing technique based on the digitally-controlled deposition of materials (layer-by-layer) to create freeform geometries. As such it finds application both as rapid prototyping tool as well as a small scale to a mass-producing technology. In the first case it shows clear advantages in comparison to traditional moulding technologies, by producing customised products with complex geometry at no extra tooling cost with fewer limitations and without the need for purposefully made plug-ins, it enables rapid cost-effective modifications of a product at a computer design level [14, 15]. Furthermore, 3D printing allows the production of multiple different individual parts during the same additive manufacturing process, reducing material waste associated with traditional fabrication methods [16]. 3D printing therefore has an excellent capability to produce personalised product series with complex geometry and tailored high quality of dosage forms which would be difficult to recreate using traditional compacting techniques. As a result, while traditional manufacturing techniques are cheaper and more effective when it comes to mass-production of standardised doses, 3D printing comes through as an economical, sustainable and customisable option for the manufacturing of personalised tablets to meet the individual patient needs [14, 15]. The last decade has witnessed a shift towards patient-centric and individual -specific drug treatment (personalised medicine) and a resulting growing demand for technologies such as 3D printing, capable of satisfying the need for highly personalized medicine through the production of small batches of individually-selected doses and tailor-made release profiles [14].

## 1.2 Pharmaceutical challenges and 3D printing solutions

To better understand the effect of additive manufacturing on the pharmaceutical field, in the next few sections are presented a selection of the most pressing challenges effecting tablets production alongside the potential benefit of a 3D printing approach.

### 1.2.1 Oral solid dosage forms distribution and environmental sustainability

The term supply chain includes planning, sourcing, production and distribution of goods, in the case of pharmaceuticals this last step includes pharmacies, hospitals and the end users that need access to the products. As such efficient supply chains play a key role in ensuring the success of essential pharmaceutical supply through a territory [17]. In the last decade multiple studies have shown the importance of accessibility to distribution centres and how the inadequate access to healthcare is associated with lower levels of health and well-being, especially in older adults [18, 19, 20, 21]. As a result disruption of any step of the supply chain can have a devastating effect on patient healthcare, as is evident in the current issues dealing with providing an even supply of COVID vaccines to populations around the world. While production can generally be managed using forecasts and marketing intelligence strategies unforeseen occurrences can strongly compromise this essential service. Events such as an epidemic outbreak have taught us how quickly the supply chains can be broken, disrupted, and even come to a grinding halt because of the nation-wide lockdowns, closed borders, and halted air travel. But this is not the only scenario, war and politics as well as potential geographical barriers can lead to shortage in the pharmaceutical supply to the manufacturing sites as well as impeding patient access to distribution points [22, 23, 24].

Furthermore, when thinking of supply chains and specifically transportation and logistics it is fundamental to keep in mind the environmental impact on the planet and on the production of anthropogenic emissions. In 2007, 40% of the overall American's emission are accounted for by transportation suggesting that a more efficient and effective approach is required [25]. In addition every year multiple tons of medications are wrongly disposed of by the consumers in the home refuse or the sewage system. For example, in Taiwan in 2013, 3 tons of unused and expired medications were wastefully

discarded [26, 27]. This constitutes an expensive waste in terms of money and resources both as prime materials and energy. In addition improper disposal of expired or unwanted medication has the potential to cause contamination of the fresh waterways resource as well as a biohazard for wildlife [28].

Both supply chains and environmental issue could potentially find a solution in the adoption of 3DP technologies that can provide on-demand immediate manufacturing of medicine at the point of care directly in response to local request, eliminating the need for physical warehouses by instead using a virtual approach by storing products specifications instead of physical ones. By having both drug and carrier materials in their pure form they can be assign as to best fit the needs of a specific situation. Indeed, with a traditional approach all medications are pre-prepared and cannot be altered, meaning that in a crisis scenario there is no possibility to convert the less essential medications into lifesaving ones. However, when using a 3D printing approach all materials are kept in their base form until needed. As a result, if necessity arises, it is possible to reroute all resources towards producing life-saving medication extending the time coverage for such essential treatments. Furthermore, by bringing the production line closer to the patient and producing only the necessary quantity of medicines 3D printing offers to reduce recalls and wastage of materials, minimise cost and optimise production efficiency while increasing the territorial reach.

### 1.2.2 Personalised medicine

Healthcare currently mostly involves a reactive “one-size-fits-all” approach to patient medication where treatments are generally administered on the base of symptoms and patient or patient’s family history [29]. In addition, most commercially available pharmaceutical treatment come in only few discrete dose, while patients are unique and have individual genetic makeup, history and environmental factors. In a 2001 study Spear and co-workers reported that more than 20% of subjects treated for common diseases showed poor or even adverse response to generic non-tailored treatments [30].

In contrast personalized medicine is an approach based on precise prediction of an individual response to therapy, on the basis of patient characteristics, symptoms and responses via the use of sequencing (NGS) and biomarkers [30]. The idea of personalized medicine originated more than 20 years ago and become a tangible possibility in 2003 as a complete sequence

and map of all the genes in the human body became available thanks to the work of the Sanger Centre in Cambridge [31].

Advances in personalized medicine have already led to powerful new discoveries and several new FDA-approved treatments that are tailored to an individual's genetic makeup, or the genetic profile of a patient's tumour [32].

An example of the benefit offered by tailored therapy in contrast to fixed dose is the study of TSH-suppressive therapy [33]. Patients receiving long term TSH-suppressive therapy with fixed doses of L-T4, reported several mild cardiovascular abnormalities including myocardial remodelling reflected by significantly increased IST, LVPWT, and LVMi [34].

In their work Mercurio and co-workers proved that no detectable cardiovascular abnormalities, with the possible exception of a very mild increased ventricular mass, can be found when TSH-suppressive L-T4 therapy is individually tailored to the lowest dose required to keep the serum TSH concentration below the normal range [33]. This clearly shows the benefit of a personalised treatment, so while not always necessary patient specific doses might become beneficial when it comes to potent drugs, drugs with narrow therapeutic window and drugs with extreme side effects.

Traditionally dose adjustments are commonly achieved by breaking a commercially available dose into smaller parts till the desired amount is achieved and then administered to the individual, alternatives such as mini tablets, pellets and granules are also available for a limited amount of formulations. However, most tablets will have shape and coating designed to address specific requirements and compromising such integrity might cause the tablets and capsules to not work properly or to show harmful side effects. As an example, for a drug designed for slow release breaking of the coating in dividing a dosage form might induce an overdose, moreover the acidity of the stomach environment might reduce their efficiency if the coating is compromised. Furthermore, since patients are left with the burden of dose portioning by splitting tablets this is done in an approximate way often with inadequate tools such as kitchen knives which leads to uneven splitting of the tablet and consequent dosing errors [35, 36]. As a result producing patient specific therapy using commercially available SDFs can be extremely complex and at time counterproductive [35, 36].

3D printing technologies have the potential to mass-produce customised components without substantially increasing the time or amount of material required [15, 37]. This technique is also capable of producing tailored 3D geometries to accommodate the needs of individuals in paediatric age or with

swallowing difficulties [38].

Lastly the ease of operation, once the correct routines have been put into place and the personnel correctly trained, and size of 3D printers would allow for easy integration in both a pharmacy or hospital environment.

### 1.2.3 Production of drug release profiles via SDFs

The main goal of any pharmaceutical solid dosage form is the delivery of the active ingredient in an effective, deliberate and controlled manner. The most obvious way is to create solid dosage forms that will allow for a controlled release of the drug content over time. Such systems are commonly identified as: controlled release drug delivery systems (CRDDS) and are divided into three macro-categories, monolithic matrix systems, osmotic pump systems and reservoir systems depending on the release mechanism being exploited [39].

As the name suggest a **monolithic matrix system** is composed of a single solid unit. Specifically, they involve the use of a polymer matrix, hydrophobic or hydrophilic, within which the drug is dissolved or dispersed [40, 41]. This type of preparation is the most common due to its versatility in terms of drug content variation (low to high) as well as the variety of release profiles and the ease of production via compression methods.

An **osmotic pump system** exploits osmotic pressure as the main mechanism to drive drug release [42, 43]. Tablet belonging to this category are usually made of a compressed tablet core coated with a semipermeable membrane containing one or more delivery ports through which a solution or suspension of the drug is released over time. In order to create an osmotic pressure within the tablet the core is produced using an osmotic agent, a water swellable polymer and a drug solution. The resulting drug release is dependent on the choice of constituents of the core and the permeability of the membrane coating. As the core absorbs water, it expands pushing the drug solution out of the tablet through the delivery ports. Osmotic pump produce sustained drug release, are easy to formulate and simple in operation [42, 43].

**Reservoir-based systems**, are similar to monolithic matrix systems where the drug reservoir is enclosed within a functional polymer coatings. However, while for the monolithic the drug is delivered thanks to rate-controlling

polymer matrix, for the reservoir systems the drug release happens through the rate-controlling porous polymeric membrane [44, 45].

By changing the matrix composition and coating layer thickness it is possible to achieve different release profiles targeted to the need of the specific treatment. Specifically pain treatments such as Percocet and Norco need to be readily active shortly after administration and an immediate release represents the best approach. On the other hand for patients suffering from chronic illnesses the use of extended drug release is to be preferred due to the reduction in dosing frequency and the capability to maintain constant drug level within the therapeutic range reducing the sides effects linked to high plasma drug concentration or dose dumping and as a result increasing patients' compliance.

An extremely promising type of drug release achievable using CRDDS is delayed delivery. In this case the drug is released after a pre determined amount of time in a predictable pattern i.e. at appropriate time and/or at appropriate site of action. The simplest delayed formulation is a two layer coated tablet composed of polymers with different dissolution rates. While such systems are promising, a disadvantage is that the lag time to drug release cannot always be predicted correctly as it relies on factors such as the pH of the target site, the enzymes present in the intestinal tract and the transit time/pressure of various parts of the intestine which are highly specific to the single individual [46].

Lastly chrono-pharmaceutical drug delivery systems are currently the most sought after release methods. These type of systems are aimed at matching the human circadian rhythms or the disease development and are generally fabricated using a multi-unit or multilayer systems with various combinations of immediate and sustained-release preparation. As a result, they are complex to fabricate and consequently subject to errors and, are expensive and time consuming both in the design and fabrication stage [37, 46].

3D printing technologies offer an alternative approach for the manufacture of solid dosage forms where the API release can be controlled as above and also potentially via tablet geometry and drug distribution within the tablet itself. The main feature of 3DP is indeed the capability of producing solid dosage forms with multiple varied complex geometries without any additional cost or change in equipment. The same base formulation can, thus be used for multiple patients while the drug content and delivery profile can

be tailored on the individual by simply changing the geometry file at no additional cost [14].

### 1.2.4 Polypharmacy

Polypharmacy is a therapeutic approach that involves the use of multiple medications. This type of therapy is most commonly used to treat chronic or elderly patients, which can be subjected to regularly taking 8 and up to 60 medicines (median of 22.9) [47]. It is easy to understand then how compliance is only 32.6% among the oldest patients. The contributing factors to this staggering statistic can be divided into two categories, patient and physician driven. In the first case the complexity of administration often associated with tight time schedule and complex dosing can lead to misassumption and increased risk of adverse reactions and drug interactions. As a result the complexity of the treatment and the severity of the side effect might lead elderly patients to take only part of the therapy, to stop the therapy completely or to decide to self-medicate. On the physician side factors such as excessive prescribing, multiple providers and lack of a coordination can lead to confusion, duplication and lack of compliance [48, 49].

In a 2018 study Lai and co-workers showed how a better understanding and medical knowledge of the therapy had a positive effect on compliance, while age and medication classes were independently negatively associated with conformity [47].

A solution to this problem is the use of a polypill approach. As the name suggests this is a combination of drugs and excipients carefully distributed within a solid dosage form in order to provide the desired therapeutic delivery of multiple APIs, reducing the number of daily intake and increasing compliance.

Despite the clear potential benefit of a polypill approach only a few are available on the market, Polycap being the exception [50]. It contains five different medications and is aimed at lowering blood pressure and preventing heart attacks. This is due to the complexity of design, number of possible combinations and the ingrained individuality of a multi drug therapy. In addition, regulatory hurdles are higher than developing each individual dosage form and the manufacture of such solid dosage forms is complex and expensive and requires the use of specialised machinery, becoming even more prohibitive from a commercial point of view [51, 52].

3D printing once more holds the potential to address this issue. In recent years 3D printers mounting multiple ink cartridges have reached the market making it possible to utilise multiple different material formulation for the production of a complex multi material solid dosage forms. The use of multiple materials in one print potentially allows tailoring not only the geometrical distribution of the drugs within the tablet geometry but also, by matching different compounds to change the mechanical properties of the part and tailor the solubility of each section [14, 15, 37]. By changing the location of the drug within the tablet it is possible to use drug-free materials as barrier layers, as well as guaranteeing separation between incompatible active ingredients and as a result tailoring the release profile. In addition the use of soluble or erodible layers instead of insoluble matrices can greatly affect the tablet release capabilities.

As a result, 3D printing offers the potential to produce complex dosage forms containing multiple APIs each showing a unique release profile tailored on the specific pharmaceutical treatment and for the individual patient. By reducing the number of tablets to be taken by the patient and by increasing the delivery precision of therapeutics both in terms of administration time and dosage 3D printing hopes to reduce the effect of adverse reactions and drug interactions and thus to increase compliance.

## 1.3 3D printing

Additive manufacturing is an umbrella term that includes any process in which material is joined or solidified under computer control to create a three-dimensional object, with material being added together (such as liquid molecules or powder grains being fused together) typically layer by layer [53]. While 3D printing started gaining its popularity in the late 2000 it is a process that started almost forty years ago. The first mention of a 3D printing machine dates back to 1971 when Johannes F Gottwald patented the Liquid Metal Recorder. In the patent Gottwald explains the process as "printing" of inks which are "not only dye or pigment-containing materials, but any flowable substance or composition " laying for the first time the foundations of what we nowadays call 3D printing [54]. Two years later Pierre Ciraud filed a new patent describing for the first time a laser sintering metal procedure where a predetermined geometry was manufactured by solidifying metal powder via the use of a concentrated energy beam[55].

Despite these initial efforts, 3D printing didn't see any further advancement till 1981 when Hideo Kodama developed two additive methods where a photo-hardening thermoset polymer was selectively cured using UV light and a mask pattern or a scanning fibre transmitter. The project however did not convince Kodama peers and was thus overlooked [56]. What all these systems were lacking was a reliable automated way to control the printing process. It was not until 1984, when Bill Masters revisited these ideas and patented his Computer Automated Manufacturing Process and System [57] and 3D printing as we know it today was born.

Since then, additive manufacturing has kept evolving and branching into new areas thanks to the addition of multiple new techniques including Fused Deposition Modelling (FDM) and Inkjet Printing (IJP). However, it was not until 2009 when FDM process patents expired that 3D printing became more generally available to the public and started the race to the future of manufacturing that is still going on today.

As a result, a large variety of 3D printing techniques exist today (Figure 1.2). These can be categorised into three main classes in accordance with their core curing working principle: powder solidification (including powder fusion and binder jetting), liquid solidification (including photopolymerisation and material jetting) and extrusion.

Despite the differences between the various techniques, they all share the same core stages:

- 
- Part design: the desired part geometry is designed using a computer-aided design software (CAD).
  - Conversion to .STL: during the conversion process the original part is segmented into triangles, the informations about the triangular coordinates are then saved in a .stl text file.
  - Slicing and printing parameters: the .stl file needs to be sliced according to the properties of the printing material and technique. Material and technique properties also play a key role in the determination of the printing conditions such as, layer height, precision, operational temperature etc. Depending on the machine the slicing step can be performed automatically by the printer software once all parameters have been set or has to be done by the operator using a complementary software as part of the preparation stage, printing parameter selection will still be a key component to obtain a solid print and cannot be skipped.
  - Print: during this stage the part is produced following the parameter inputs and accordingly to the file design, no human intervention is necessary.
  - Post processing: this step is highly dependent on the additive manufacturing technology involved and the final application. It can include a variety of processes from letting the part rest, to curing, washing and polishing. The result of the final product is strongly linked to this stage and the selection of treatment applied to the part.
  - Final result: the part is now finished and can be used as required.

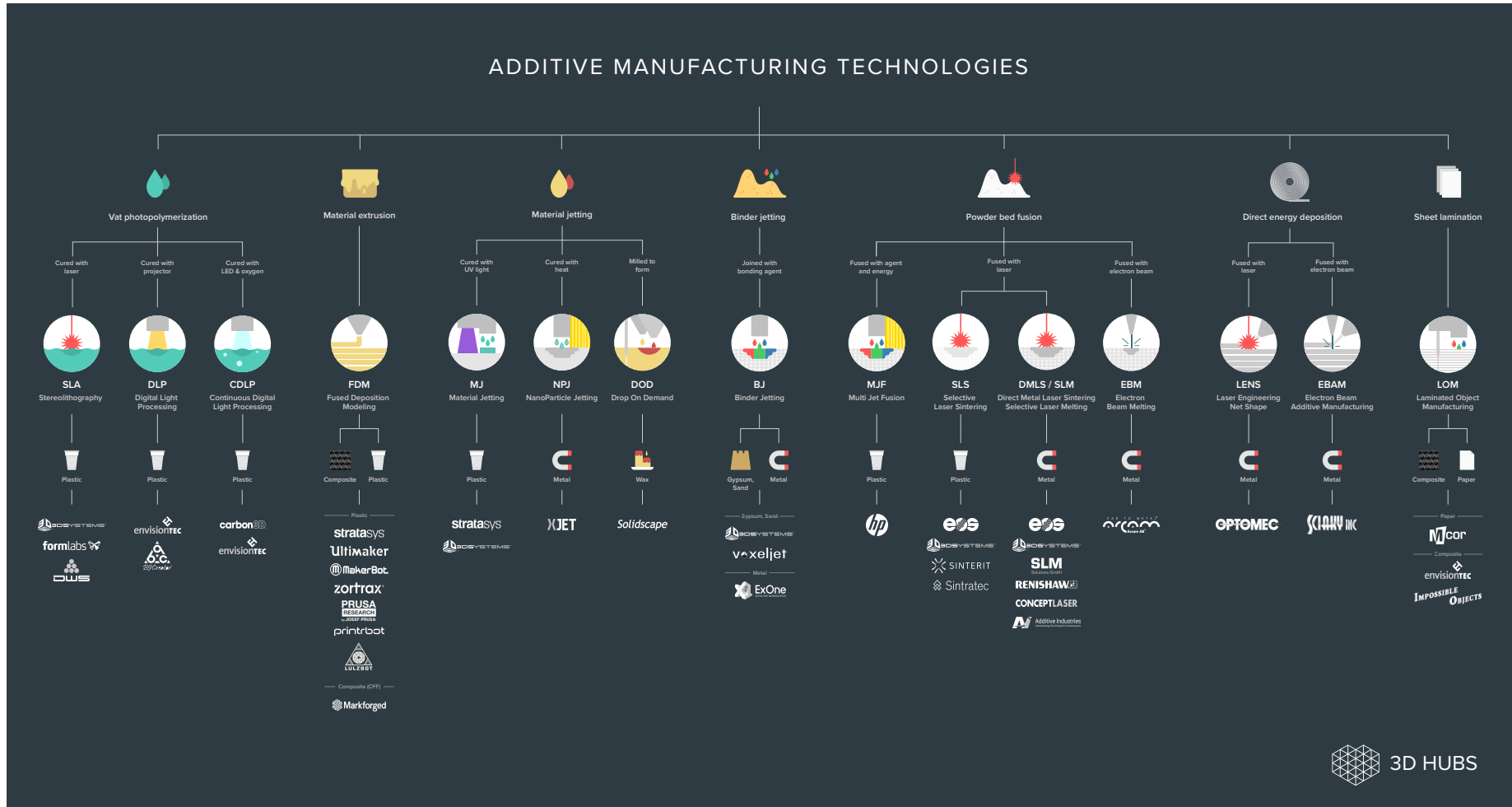


FIGURE 1.2: Additive manufacturing technologies scheme from [58]

### 1.3.1 3D printed pharmaceuticals

Considering Figure 1.2 it is clear that there are a significant number of techniques available for 3D printing. In selecting the most appropriate for a given task it is important to consider the advantages and disadvantages of each in the context of the outcome that one wishes to achieve as well as the properties of the materials involved, paying particular attention to active ingredients. As such, the aim of this section is to provide an overview of the most commonly available additive manufacturing technologies alongside practical examples from the literature and how they can be applied to solve the challenges faced by traditional tablet fabrication methods.

#### 1.3.1.1 Extrusion-based methods

Extrusion-based technologies are the most commonly available type of additive manufacturing due to being relatively inexpensive and a well established process in the field of pharmaceuticals. As the name suggest a formulation is extruded from a nozzle and deposited starting from the building plate and adding subsequent layers in a continuous motion. Based on the state of the material during the printing stage, extrusion based methods can be divided into two categories: extrusion of semisolids, which happens at room or elevated temperature, and extrusion of a molten thermoplastic.

#### Pressure-assisted microsyringes

Pressure-assisted microsyringes (PAM) belong to the semisolid extrusion family and became popular at the turn of the millennium because of their suitability for creating soft tissue scaffolds [59].

This extrusion methods consist of one or multiple microsyringes each connected to a pressure assisted piston [60]. The semisolid ink is loaded into the syringe and then extruded through the nozzle in a continuous manner onto a movable stage, after the first layer has been deposited the nozzle is lifted and the print can continue, the same process is repeated for each layer till the entire part is finished. Most printers allow for the nozzle and cartridge to be kept at room temperature or heated during extrusion to aid the material flowability. A schematic representation of the system is shown in Figure 1.3. The final part is then moved to a finished station where it is cured using heat, IR, UV light or any other post processing step necessary to guarantee the solidification of the material.

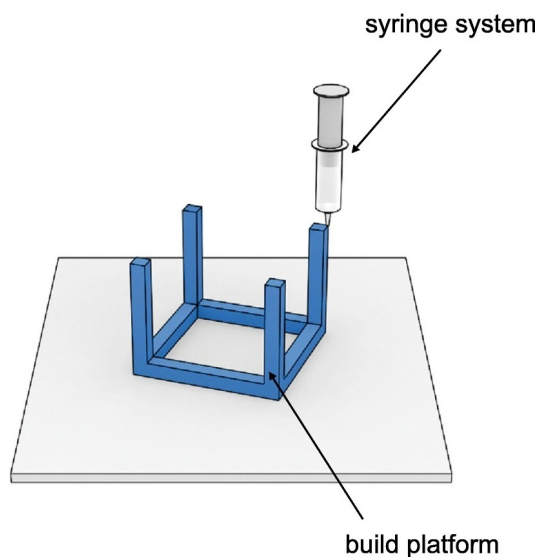


FIGURE 1.3: Pressure-assisted microsyringes, adapted from [14].

A potential disadvantage is that formulations can be difficult to print and suitably solidify. Inks for pharmaceutical use are frequently prepared by mixture of active ingredients, excipients and solvents, since many commonly used solvents are toxic the printing process must be followed by a curing and post processing step during which the solvents are completely removed and their absence is ensured [61]. This extra step while necessary is problematic, expensive and time consuming and represents the main drawback of this technique if a solvent free or safe solvent cannot be used. In addition the semisolid paste must satisfy a series of strict prerequisites, in particular it must not leak from the nozzle until pressure is applied, be dense enough to produce a continuous strand while extruded, be able to support the weight of subsequent layers without spreading or collapsing and lastly it must be compatible with the drying process without altering the active ingredient stability [62, 63]. Furthermore, since the print resolution is defined by the lateral dimension of the printed track, ink choice determine not only the property of the final solid dosage form, but also the resolution of the print. It is thus clear how material formulation represents the most significant challenge in pressure-assisted microsyringes 3D printing.

Despite these difficulties this technology also presents multiple strong points, firstly it offers an opportunity to print gel materials at room temperature without the risk of degradation or solvent loss, particularly suitable for creating soft tissue scaffolds [59]. Secondly it is compatible with extremely high drug loadings. For example, Kahled and coworkers produced an immediate release paracetamol tablets with a 80% drug load [64]. Lastly, by

mounting more than one syringe it has the potential for the production of complex multi-material design including tablets comprising more than one active ingredient to produce controlled release profiles for patient centric therapies [62, 63].

In 2015, after a series of successful results [65, 66] Khaled et al. devised a method to utilise pressure-assisted microsyringes 3D printing extrusion technique to sequentially manufacture a five-in-one pill [67]. The tablet was characterised by both immediate and sustained release and its geometry is described in Figure 1.4.

The printable paste used to form the barrier for the sustained release actives method prepared by mixing the powder mixture: cellulose acetate (hydrophobic membrane/shell), D-mannitol (a filler), and polyethylene glycol (PEG 6000) (plasticiser) with the binder: acetone and dimethyl sulfoxide (DMSO). Powders of atenolol, pravastatin, and ramipril were separately blended with the required excipients and ultra-pure water was added to the powder to form the active pastes. Lastly the immediate release layer was composed of aspirin and hydrochlorothiazide (active ingredients), sodium starch glycolate (disintegrant), and polyvinylpyrrolidone (PVP K30) (binder) again mixed with ultra-pure water to form a smooth and soft paste. All the pastes were loaded into separate ink cartridges for extrusion and the product was printed layer by layer starting with the enhanced release compartments. For this product the author adopted a segmented tablet strategy, ensuring that the actives were separated, and independent control of their release as proven in dissolution tests. With this paper the authors were able to clearly demonstrate their ability to create complex drug delivery systems with multiple dissolution behaviours. This device, with its highly tunable drug release profiles based on modifying the drug and excipient composition in the separate compartments, introduces a new definition of flexibility in the production of 3D printed polypills.

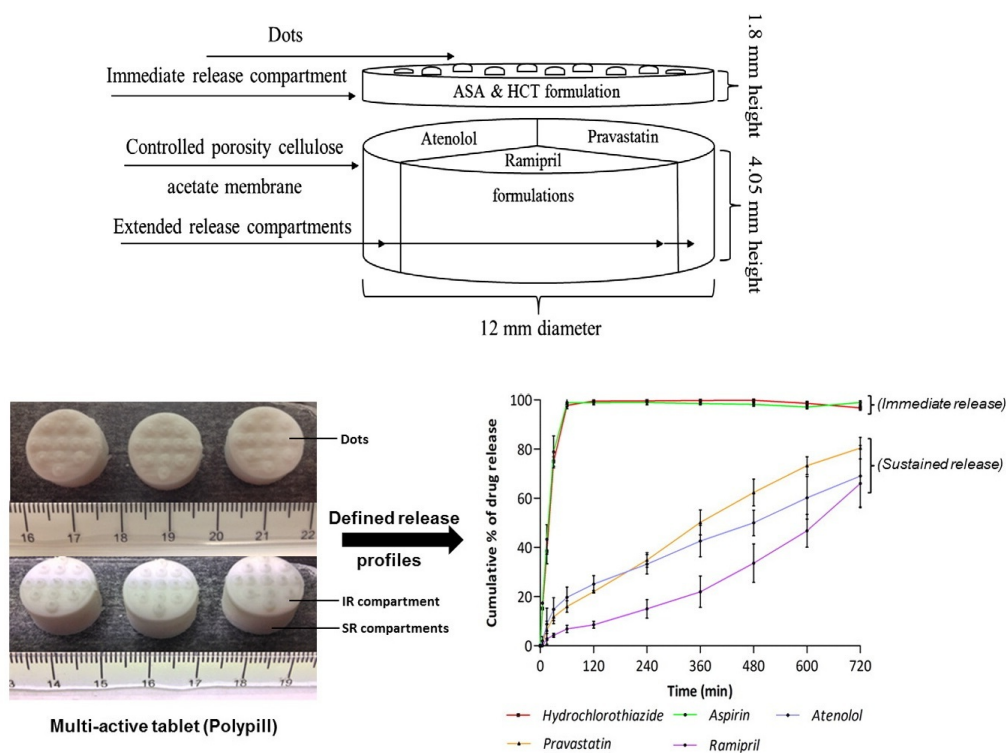


FIGURE 1.4: Schematic structural diagram of the polypill design, showing the aspirin and hydrochlorothiazide immediate release compartment and atenolol, pravastatin, and ramipril sustained release compartments. Figure from Reference [67].

### Fused-deposition modelling

In fused deposition modelling (FDM) a thermoplastic filament is pushed via a gear system into the back-opening of a nozzle, in this first area it is heated at a constant rate and brought to a semi molten state and is then extruded and deposited onto the substrate. A schematic representation is shown in Figure 1.5. Similarly, to what was done for the PAM systems the distance between the nozzle and the printing stage is adjusted after each layer by lowering the printing stage, to accommodate the extra height of the freshly deposited material [68]. Unlike PAM, FDM does not require an external curing step since cooling acts as a solidification process, indeed as soon as the filaments leaves the nozzles it starts to solidify removing the need for a curing stage.

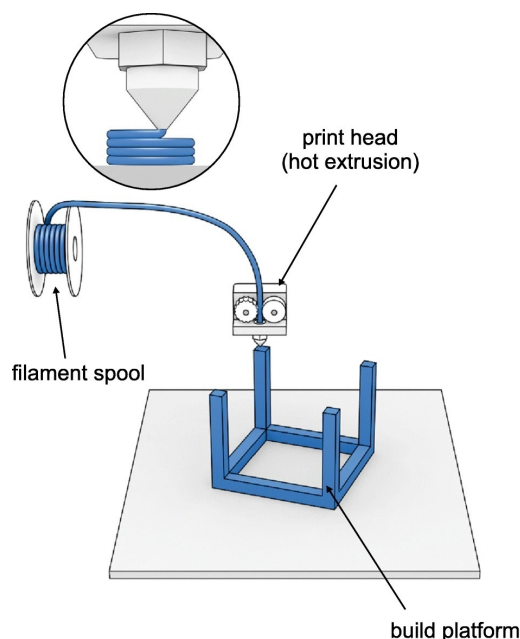


FIGURE 1.5: Fused deposition modelling, adapted from [14]

FDM popularity in the pharmaceutical field is due to the number of advantages that it offers, first and foremost availability, ease of use and low cost [69]. In addition, changing materials during printing is relatively simple, by just interrupting the previous filament and start a new one or producing a mixed material filament. This makes for a direct way of producing multi-material solid dosage forms without the need for complex machine design. What is also interesting is the possibility that FDM offers to solve the major drawback of PAM: the necessity to use a solvent. The use of temperature based method to guarantee printability instead of relying on the presence of a solvent makes it possible to produce readily available printlet that do not require any post processing step for solvent removal, potentially cutting the time and cost of production while not compromising on safety.

However, no machine is without limitation and FDM is no exception, in particular the elevated working temperature (on average around 200 °C) may cause degradation of pharmaceutical active ingredient or excipient. While a temperature based solidification mechanism represents an advantage when it comes to formulation it may constitute a problem in relation to surface roughness. Indeed since each layer starts to solidify as soon as it is extruded there is not complete fusion between subsequent layers resulting in clear demarcation lines.

Goyanes et al 2015 works are prime example of how FDM can be used to produce complex geometries and that, depending on the shape of the drug delivery system, it is possible to control the drug dissolution profile [70, 71,

72]. In Figure 1.6 are shown the digital and Raman images of the multi-material tablets with multilayer and sectioned DuoCaplet design from the paper: "3D printing of medicines: engineering novel oral devices with unique design and drug release characteristics".

Two sets of filaments were prepared using a combination of commercial poly(vinyl alcohol) (PVA) combined with either Paracetamol or caffeine (5 and 10% w/w). The mixture was then extruded via a single-screw filament extruder. The printing stage was obtained by alternating between the filament until the final part was produced.

In this work the authors implemented two different geometries in order to better understand the effect of tablet geometry and drug localisation on drug release. The analysis of the Raman images confirmed that each drug is localised in the desired region. Tablets incorporating a multilayer design showed similar release profiles for both drugs with faster release at higher concentrations, on the other side the DuoCaplets showed an initial release only from the paracetamol locate in the outer shell while the caffeine is released following an initial delay. Suggesting that the outer shell works as a masking material to the core and that the printing process was successful in producing such design.

The authors were thus able to demonstrate that FDM is a suitable technique to manufacture different structured objects with tailored drug dissolution profiles.

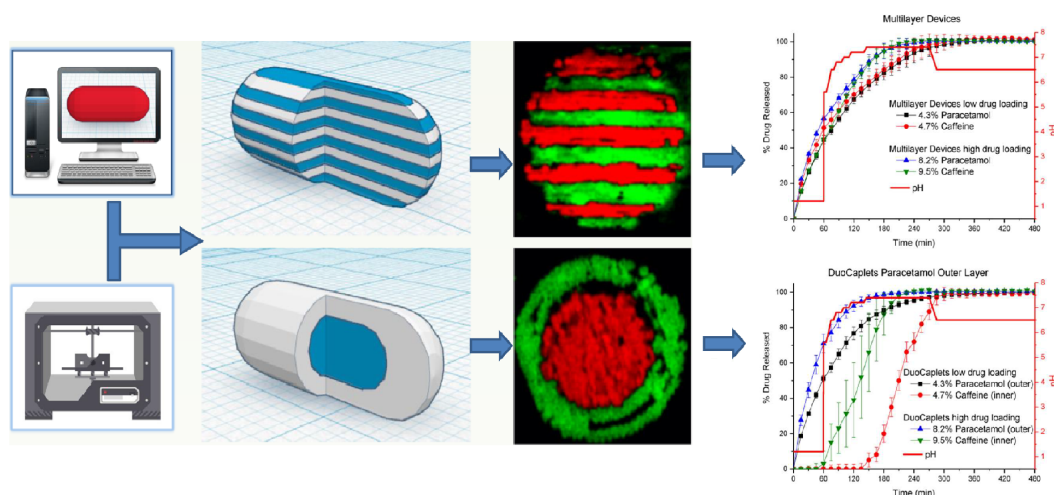


FIGURE 1.6: Digital and Raman images alongside with their dissolution profiles of the multi material tablets with multilayer and sectioned DuoCaplet design, white paracetamol–PVA and blue caffeine–PVA [71].

### 1.3.1.2 Laser based systems

Laser based 3D printing includes all additive manufacturing technologies for which a laser is a key element of the printing process. Specifically it represents the curing mechanism through which the material in a state of a liquid or a powder is made to coalesce and solidify in order to produce a 3D object. Two main types of AM technologies fit this profile, laser sintering (SLS) and stereolithography (SLA).

#### Selective laser sintering

SLS is a powder bed fusion AM processes, a thin layer of material is spread across the printing bed, once the powder layer is dispersed the material is solidified by exposure to a high power scanning laser which heats the powder particles close to their melting point. As a result neighbour particles that have been affected by the laser are fused together forming the layer design [73, 74, 75]. The printing bed is then lowered and a new layer of powder is spread across the printing bed using a levelling blade ready for the layer design. The final object is obtained by repeating these steps in a layer by layer fashion. Once the print is finished the part is removed from the powder and cleaned while the powder sieved and placed in the powder delivery system. Figure 1.7 shows a schematic representation of SLS.

SLS is able to work with a variety of compatible materials, however due to the working principle at the base of this technique the material formulation must be in powder form and must be able to withstand the working temperature. Even more important, objects produced with this technology are subjected during printing to elevated thermal stresses potentially causing the part to shrink or deform. In addition, the use of a single powder formulation further reduces the complexity of the printed part limiting the freedom to only geometrical variations and is lacking in this regard comparatively to other competitor technologies.

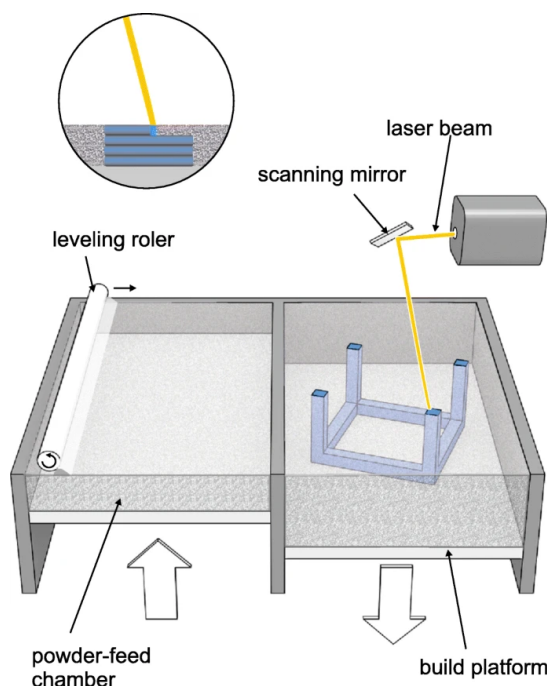


FIGURE 1.7: Selective laser sintering schematics (SLS) [14].

Despite the disadvantage it is possible to find instances in the literature where this technology was used to produce tablets for pharmaceutical applications[76].

In 2018 Fina and co-worker showed how laser scanning speed can affect the printed part porosity and consequently, in the case of solid dosage forms, their ability to release the active components. For this purpose, the authors designed two sets of prints at three different rasterising speeds ( $100 \text{ mm s}^{-1}$ ,  $200 \text{ mm s}^{-1}$  and  $300 \text{ mm s}^{-1}$ ) and two powder compositions: 5% Paracetamol, 3% of Candurin® Gold Sheen and 92% HPMC (hydroxypropyl methylcellulose) or kollidon as matrix material. The addition of the colorant Candurin® Gold Sheen to the mixture was necessary to enhance energy absorption. After completion the printlets were removed from the printing bed and the excess powder was simply brushed off.

For both sets of tablets compositions a higher laser scanning speed showed faster drug release during the dissolution test in an acidic medium, as a consequence of the variation in structure porosity due to the processing speed. Specifically at high speed the laser quickly scans over the particle causing them to not fully melt and thus to form looser connections creating a more porous structure, which allows for easier access for the dissolution medium as well as facilitating break down. As visible in Figure 1.8 in the case of Kollidon matrices the lowest laser scanning speed achieved complete dissolution within the first hour, while higher speeds of  $200 \text{ mm s}^{-1}$  and  $300 \text{ mm s}^{-1}$

managed to achieve the same goal in only 10 min.

HPMC based tablet showed an overall slower release rate with complete drug delivery reached in four hours for the 100 mm s<sup>-1</sup> tablets, three hours for the 200 mm s<sup>-1</sup> tablets and two hours for the 300 mm s<sup>-1</sup> tablets.

This shows that SLS is indeed capable of producing solid dosage forms with tailored release profiles, however the constraints in geometries achievable and in the materials available strongly limits the number of pharmaceutical cases for which the use of this technique can be beneficial. As a result, this technology is often disregarded in favour of other additive manufacturing methods..

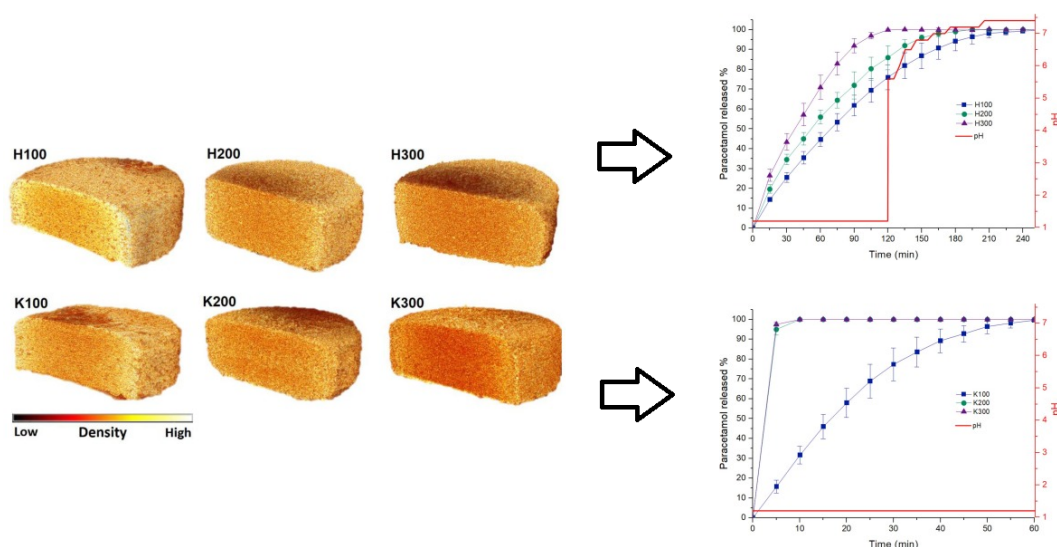


FIGURE 1.8: Image and dissolution study of tablets composed of 5% Paracetamol, 3% of Candurin® Gold Sheen and 92% HPMC (TOP) or kollidon (BOTTOM) [76].

### Stereolithography

Stereolithography is an additive manufacturing system where a photoactive resin is exposed to a focused light source (UV or high energy light) to induce photo-polymerisation [77, 78]. The photosensitive thermoset polymers are in a liquid form and are stored in a vat container, the printing platform is lowered into the resin leaving a small gap equivalent to one layer height between the transparent bottom and the platform itself. Focused light is then shined through the base to selectively curing and solidifying the photopolymer as visible in Figure 1.9. The platform is then lifted to allow resin to re-coat the bottom, a sweeper blade might be used to aid the process. The platform is once again lowered and the process repeated as many time as required by the digital design. By the end of the printing process the part is

only partially cured and requires further post processing. The first step is to lift the printing stage out of the vat and remove the leftover uncured resin by washing the part in an appropriate solvent, the next step would then be to finish curing the part under UV light.

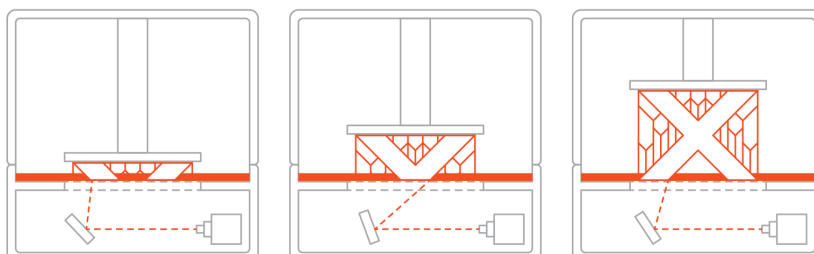


FIGURE 1.9: Stereolithography schematics (SLA) [58]. A laser selectively illuminates the transparent bottom causing resin solidification, the printing bed then lift to allow space for the next layer.

An advantage of this technology is that it offers the possibility to fabricate tablets with high resolution ( $30\ \mu\text{m}$  to  $40\ \mu\text{m}$ ) while avoiding the need to use high temperatures. However, it only works with crosslinkable polymeric matrices and is intrinsically mono-material since only one material per vat is allowed.

Recently Robles-Martinez et al. designed a method to enable multi-resin printing. This was achieved by pausing mid-print, removing the resin tray, and replacing the resin formulation [79].

Photosensitive resins were obtained by mixture of the pharmaceutical ingredient in liquid PEGda and PEG300 when applicable, as model drugs were selected paracetamol, acetylsalicylic acid, naproxen, chloramphenicol, and caffeine.

From Figure 1.10 Left it is clear that the authors were successful in producing multi material printlets with both a disc and ring geometry, furthermore the analysis of the dissolution profiles (Figure 1.10 Right) shows that not only all drugs can be released from the tablet, but also that their release can be tailored thanks to the printlet geometry.

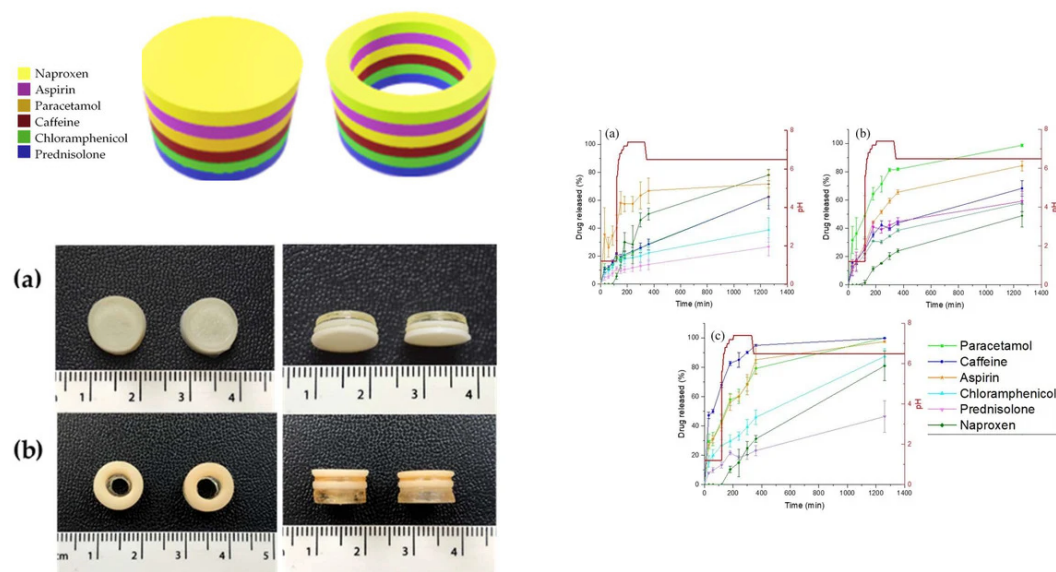


FIGURE 1.10: Left) Digital and optical images of disc and ring printlets produced using multi-material SLA. Right) Drug dissolution profiles of (a) cylindrical polypill; (b) ring-shaped polypill; and (c) ring-shaped polypill+PEG 300. [79].

### 1.3.1.3 Jetting systems

Inkjet printing identifies the category of printers which recreate digital images through the controlled formation and placement of ink droplets onto a substrate. Two types of inkjet 3D printers exist: drop-on-demand (DoD) inkjet printing and continuous inkjet printing (CIJ) [80].

Figure 1.11 left shows the CIJ method and how it exploits Rayleigh instability of a column of liquid for droplet generation, this results in a continuous stream of droplets that cannot be interrupted without compromising their production. To avoid this issue and to guarantee precise spatial deposition, the droplets are charged at the nozzle and a deflector is positioned downstream interrupting the flow by diverting the undesired droplets into a gutter collector and then into a vat for recycling. On the other hand DoD allows to produce droplets only when necessary reducing wastes, this is achieved by creating a pressure pulse in the fluid behind the printing nozzle. Two different mechanisms have been designed for this purpose. The first one is a thermal inkjet process (Fig.1.11 middle), when a droplet is required a heating element is activated causing a rapid raise in temperature of the ink and consequent formation of a bubble, which results in a large pressure increase, causing droplet ejection. Lastly, piezoelectric DoD units (Fig.1.11 right) exploit the ability of piezoelectric materials to respond to electric stimuli, when

a voltage is applied the piezoelectric actuator respond by dilating, generating a pressure pulse which forces a droplet out of the nozzle.

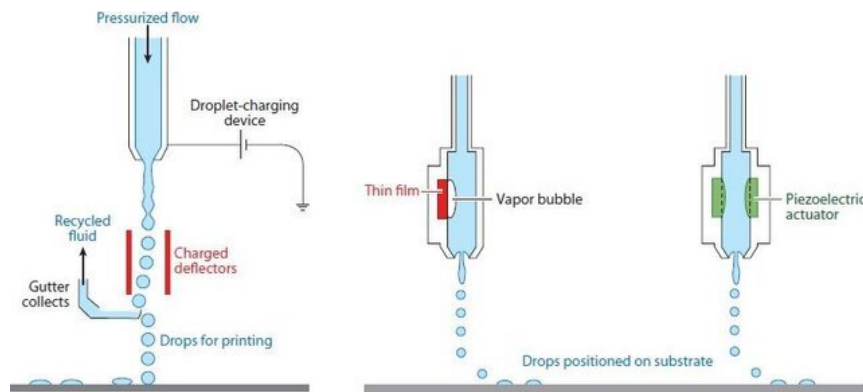


FIGURE 1.11: Schematic diagram of a continuous inkjet (CIJ) printer (Left), and a drop on demand (DoD) inkjet printing system, (middle) is the thermal inkjet and (right) is the piezoelectric inkjet [80].

Although all these techniques are very similar and require control over drop formation velocity and fluid viscosity, only DoD inkjet printers find common use in the pharmaceutical field, and more generally in the material science field. This is because the CIJ system uses a continuous stream of ink, even when it is not printing, making the process extremely wasteful. While the unused ink can be reused, the recycled material is at risk of environmental contamination. Moreover, within the DoD inkjet printers, piezoelectric print heads are usually preferred over the thermal print heads because more versatile and can be used with a larger range of inks, since the drop formation mechanism is independent from the ink properties and its capability to produce suitably sized bubbles to guarantee large enough pressure to produce droplet ejection. [81, 82]. DoD inkjet printers fall into two sub-categories: drop-on-powder and drop-on-drop. As can be gleamed from the name, the drop-on-powder procedure uses a powder 'bed' combined with a binder ink 'drop' to build a solid structure in a layer-wise manner. Drop-on-drop printers on the other hand deposit pre-formulated droplets on top of each other to produce a solid layer of the building material [80].

### Drop-on-powder deposition

Similarly to SLS, drop on powder is a powder bed fusion AM process where a layer of powder is spread across the printing bed, droplets of binder ink are then deposited on top to recreate the digital design. After a layer has been successfully printed the bed is lowered and a new layer of free powder is spread on top by a roller or blade. The process is then repeated in a layer by

layer fashion till the entire part is produced [80]. In these types of process the unbound powder acts as a support material preventing from collapsing of overhang or porous structure [14]. Once the final object is ready the part can be removed from the powder and finished by brushing away the excess. For pharmaceutical applications an additional drying step is usually necessary to ensure the complete removal of solvents that would otherwise compromise the part safety. As we have previously seen this could be problematic, since it is expensive, time consuming and could compromise part integrity [83].

The key feature of the drop-on-powder process is its ability to provide accurate dosing through the spatial deposition of the active pharmaceutical ingredients while simultaneously granting the ability to produce complex structures through regulation of the binder deposition on the powder bed [84, 80].

This technique can be effective in the production of printlets by dissolving the drug into the liquid binder and creating the powder base from the matrix material, however this approach is not precise enough when well-defined modulation in drug release is desired. This is because it is difficult to control both the dosage and the binder amount due to the limited void space in the spread powder layers. This is especially so for poorly-soluble drugs, which must be solubilised in the binder before loading. For this reason, in 2007 Yu et al. [85] decided to reverse their approach and start including the active component in the powder bed and using a release-retardation binder solution. For this purpose, they designed a tablet composed of four concentric sections (Figure 1.12) displaying different drug concentrations in order to obtain a gradient effect, this central section was topped and bottomed with an inert layer that was impermeable both to water penetration and drug diffusion.

The central part of the tablet was made by printing a binder solution of 2.0% w/v of EC solution in 90% v/v of ethanol into the bed powder. The mixed powder for this section was composed of APAP, HPMC E50, PVP K30, and colloidal silicon dioxide according to a ratio of 80:15:4.8:0.2 in weight. In order to grant the gradient distribution in this middle section, from the periphery to the centre, the concentration of the release-modulated materials was progressively decreased, while the void space was increased in small increments. Since the top and bottom of the tablets were formed by depositing droplets of liquid binder (4.0% w/v EC in 90% v/v ethanol) onto the manually spread EC powder, the dissolution of the drug loaded layer can happen only along the horizontal plane making it easier to control the release. The

printed tablets had to be dried after each pass and, at the end of the overall process, overnight at 35 °C under vacuum prior to use. Thanks to this geometry the erosion of the volume of the tablet was constant over time. This is because as the tablet is eroded, the available surface area for drug release diminishes which in turn causes an acceleration in the erosion process. The end result is a zero-order system with a linear drug release profile that can deliver 98% of the active component within 12 h of dissolution. Including the drug inside the powder bed not only improves control over the dissolution, but also increases the maximum concentration that can be achieved compared to the core-shell structure that we have seen up to this point (70% w/v compared to 20% w/v [86, 87]).

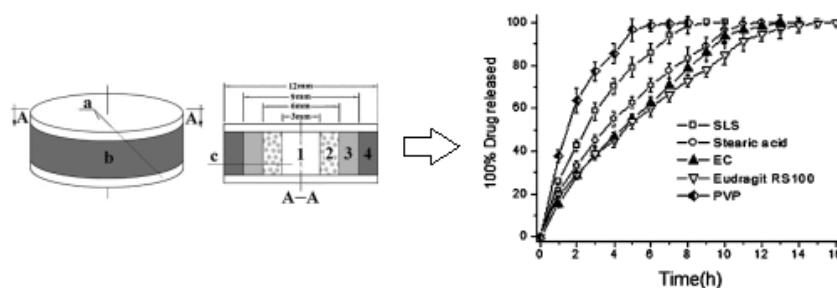


FIGURE 1.12: Left) Schematic representation of the concentric tablets with material gradients by Yu et al. Right) Drug dissolution profile [85]

### Drop-on-drop deposition

As the name suggests drop on drop systems do not require the use of a powder base, ink droplets are ejected from the nozzle and deposited on a printing bed covered with a suitable substrate, the most common being PET and glass slides. The choice of substrate is based on the desire for it to be easily available, low cost, capable to withstand relatively high temperatures, compatible with pharmaceutical applications and most importantly allow the release of the part after printing. As a result the choice of PET film and glass slides as substrates should not come as a surprise since they both fit all criteria. Additionally, it is desirable for the substrate to present a smooth surface to allow for easy removal of the final part and to prevent the imprint of the substrate topography onto the bottom surface of the printed solid dosage form.

The bed can be kept at room temperature or heated as necessary to ensure cohesion between subsequently deposited droplets. Each layer is cured either by cooling or in presence of a high energy light, UV or IR [80, 84]. Before

the next layer can be printed the initial one has to be cured enough to support the follow up layers and to avoid collapsing underneath their weight. The inclusion of multiple ink dispersing units within one printer allows for multi-material printing where the second material could be used as integral part of the final object or as a disposable support material [88]. As a result, the quality of printed product as well as its chemical-mechanical properties are dependent mainly on the choice of material.

While drop-on-powder deposition is well-suited for producing macro-structures it is not so useful for developing micro-structures [89]. Drop-on-drop deposition however, provides an elegant tool for the design and production of microscopic drug delivery systems with high drug loading capacities and complex geometries. In general each droplet has a mean diameter that ranges between 50  $\mu\text{m}$  and 100  $\mu\text{m}$ . One of the most challenging sides to this approach is the choice of the ink, this must contain both the active ingredient and the matrix material and can be prepared with or without the use of a solvent depending on the curing process selected without compromising the stability of the end result [80, 90, 91].

Drop on drop technology can be further divided into two sub categories depending on the type of curing mechanism: solvent-free which use heat as a curing mechanism and solvent based which require UV or IR light for curing.

The latter are the most commonly used in pharmaceuticals thanks to the availability of commercial printers[92, 93, 94]

In 2017 Clark and co-workers produced printlet containing ropinirole HCl, poly(ethylene glycol) diacrylate (PEGDA) and Irgacure 2959 as photo-initiator, to avoid undesired curing during the printing process the tablets were prepared in a low oxygen environment. The ink material was cross-linked using UV light, the result was amorphous solid dispersion showing sustained release of ropinirole HCl for up to 6 h [92]. It is clear that in a solvent base technique the removal of the unbounded polymer and photo-initiator is a key step to make the printlets safe for human use. Toxicity thus plays a key part in the choice of components and should be kept to a minimum when designing the tablet formulation.

A possible solution to this is the use of hot-melt printing drop on drop inkjet system, this technique relies on maintaining the ink in its liquid form by heating it past its melting point inside the printing unit which is kept at constant temperature. After deposition the ink material is allowed to cure at room temperature eliminating the need for solvents and post processing steps. To date only one application of this technique has been reported for

pharmaceutical use. In 2017 Kyobula et al. explored the use of beeswax as a carrier for the production of Fenofibrate drug delivery system, and how tablet geometry can be used to tailor the drug release profile [95].

By creating printlets with honeycomb geometries and different infill ratio they showed that effect of cell diameter on material wettability and the correlation to the dissolution profile, as visible in Figure 1.13. Specifically, an increase in the amount of drug released with the surface to volume ratio. Furthermore, they established that for the smallest set of cells the buffer solution surface tension plays a key role in preventing the liquid to infiltrate the channels. Kyobula and co-workers suggest that this mechanic can open the doors for the production of personalized medicines.

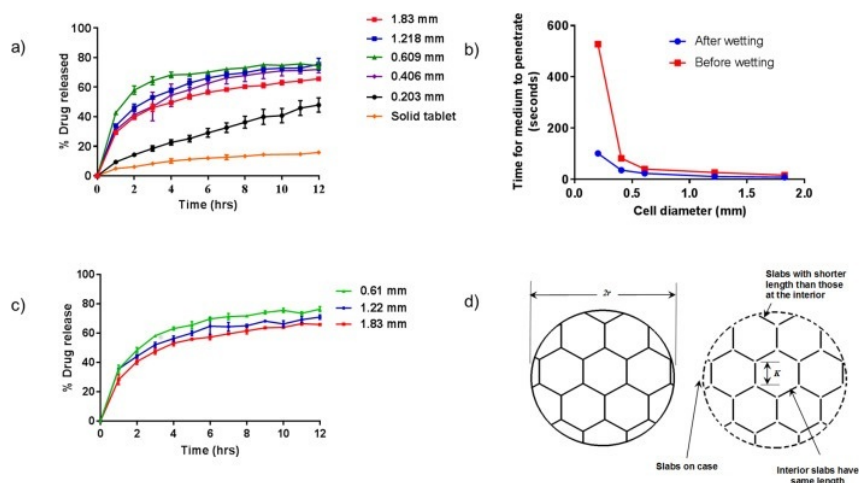


FIGURE 1.13: Dissolution profiles for the printed solid tablet and honeycomb like tablets with constant weight and various cell size [95].

## 1.4 Contribution of the present work

From the study of the traditional manufacturing methods of tablet production, section 1.2.1, it is evident the need for a simple and convenient process that is capable of producing solid dosage forms with complex and intricate design features capable of delivering patient specific therapy. Thanks to its versatility, 3D printing offers an elegant solution to this problem by enabling the production of tablets with highly customisable geometries and compositions. Indeed, in the past decade it has been demonstrated that 3D printers can produce printlets of enormous geometric complexity and with specially tailored characteristics like permeability, porosity or functionality. A large variety of additive manufacturing techniques exist today including laser writing, material extrusion and inkjet printing, however as highlighted in table 1.1 each techniques has its advantages, disadvantages and challenges. The choice of manufacturing technique has thus become integral to the tablet design. Indeed, while most methods have seen high interest and intense studies, inkjet printing is still in its infancy when it comes to pharmaceutical application. While being extremely promising in terms of resolution, speed and scalability, IJP suffers from a severely limited selection of useable active components and excipients due to the strict requirements of surface tension and viscosity. Furthermore, not all printer types are equipped to support multi-material deposition. This thesis work aims to advance prior research into this topic by focusing on hot-melt inkjet 3D printing. Hot-melt inkjet printing puts an interesting twist on the typical solvent based system. In this case the ink is stored in a reservoir above the print head and heated at a temperature above its melting point. No solvent is thus required to keep the ink in its liquid form eliminating the need for a rigorous post-processing solvents removal step. In addition, of particular interest is the possibility to utilise non thermoplastic materials and most specifically lipids as the main excipients for the solid dosage forms. Lipid-based formulations are known in traditional tableting for their capability to improve drug absorption [96], in particular when considering drugs with a low therapeutic index [97]. Indeed, a 2004 study showed how up to 70% of all developing chemical entities have low water solubility, hindering their capability to be absorbed correctly and ensure therapeutic efficacy [98]. The use of lipids can help enhance drug absorption via different mechanisms including promotion of lymphatic transport [99, 100], by increasing GI membrane permeability [101]. While it is easy to see the benefit of lipid-based formulation products, both traditional

tableting methods and most AM technologies are extremely slow or even incompatible with their manufacturing [96]. In this sense thermal jetting represents a great opportunity to produce lipid-based solid dosage forms in an efficient, fast and customisable way.

In this study, we want to develop a double reservoir system capable of co-printing two different materials while preserving the same depositional precision shared by all inkjet systems (approximately 50  $\mu\text{m}$ ). The introduction of a second ink reservoir will increase the geometrical freedom of the tablet design, helping in the production of complex tailored release profiles. In parallel we aim to expand the library of inks available in order to widen the field of applications. To our knowledge, there is no record of this technique being used in a multi-material set-up for producing solid dosage forms.

#### 1.4.0.1 Aims and objectives

The aim of this work is the design and development of a 3D system capable of fabricating multi-material solid dosage forms showing tailored release profile produced in a single additive process. Based on the information gathered in the literature review it was decided to use a hot-melt inkjet printing co-depositional approach, this would allow for a solvent free method capable of producing multi-material printlets while preserving the high geometrical freedom offered by inkjet printing. To achieve this, the following list of objectives was established.

##### **Design and development of a multi-material hot-melt 3D inkjet system.**

- Identification of the key features of multi-material hot-melt technology and creation of a digital copy of the system to aid the planning process.
- Implementation of the digital plan using a combination of commercially available and in-house manufactured components.
- Adaptation of the control code in charge of ink deposition and pattern generation.
- Assessment of the system capabilities via the production of multiple geometries starting with simple disc before moving up to complex structures with fine details.

##### **Development of a library of suitable excipients.**

- Characterisation of the chemical and physical properties of candidate pharmaceutically graded materials to guarantee compatibility with hot-melt jetting. These properties include: density, viscosity, chemical composition, crystallinity, degradation temperature and melting point.
- Evaluation and optimisation of their printability as single material or as inks obtained by combination with a test drug (Fenofibrate).
- Assessment of the effect of the printing process on the inks physical and chemical properties.
- Analysis of the functional performance of the solid dosage forms produced using ink (excipient plus API) relatively to their drug release capabilities.

#### **Production of multi-material tablets with tailored release profile**

- Identification of a test carrier material on the base of the knowledge built in the previous sections.
- Design of various geometries including multiple material to showcase tailored release.
- Build proof-of-concept tablets and test their drug release ability in the interest of validating the capabilities of the system.

TABLE 1.1: Advantages and disadvantages of 3D printing techniques. In the Ref. section are reported some key examples for each of the techniques.

AM techniques	Advantages	Disadvantages	Ref.
<b>FDM</b>	<ul style="list-style-type: none"> <li>• Low cost</li> <li>• Ease of use</li> <li>• Easy to access technology</li> <li>• Supports multi-material printing</li> <li>• Capable of solvent free</li> <li>• Printlet are readily available</li> <li>• No post processing step necessary</li> </ul>	<ul style="list-style-type: none"> <li>• High temperatures</li> <li>• High mechanical compression stress</li> <li>• Rough surface finishing</li> <li>• Slow printing process</li> <li>• Stair stepping effect in the z-direction</li> <li>• Warping and minor shrinking during curing</li> </ul>	<p>[102]</p> <p>[69]</p> <p>[103]</p> <p>[104]</p>
<b>PAM</b>	<ul style="list-style-type: none"> <li>• Supports multi-material printing</li> <li>• Cartridge temperature control</li> <li>• Print of gel material</li> <li>• Compatible with high drug loading ( 80%)</li> </ul>	<ul style="list-style-type: none"> <li>• Solvent removal step</li> <li>• Stair stepping effect in the z-direction</li> <li>• Rough surface finishing</li> <li>• Shrinking and Warping during solvent removal</li> </ul>	<p>[65]</p> <p>[67]</p> <p>[66]</p>
<b>SLS</b>	<ul style="list-style-type: none"> <li>• High number of compatible materials</li> <li>• High precision</li> <li>• Large build area</li> <li>• Good mechanical strength</li> <li>• Relatively low cost</li> <li>• High geometrical freedom, powder acts as support material</li> </ul>	<ul style="list-style-type: none"> <li>• Shrinkage and deformation during print</li> <li>• Extensive post processing step</li> <li>• powder agglomeration</li> <li>• Thermal stress</li> <li>• Improper powder feeding</li> <li>• Rough surface finish</li> </ul>	<p>[75]</p> <p>[73]</p> <p>[74]</p>

<b>SLA</b>	<ul style="list-style-type: none"> <li>• Supports multi-material printing(complex)</li> <li>• High geometrical freedom</li> <li>• Can print extremely fine features (&gt;20 <math>\mu\text{m}</math>)</li> <li>• Smooth surface finish</li> <li>• Minimal stair stepping effect</li> </ul>	<ul style="list-style-type: none"> <li>• Extensive post processing step</li> <li>• Low tensile strength</li> </ul>	<p>[77]</p> <p>[79]</p> <p>[78]</p>
<b>Drop-on-powder</b>	<ul style="list-style-type: none"> <li>• Supports multi-material printing</li> <li>• Fine features(&gt;50 <math>\mu\text{m}</math>)</li> <li>• Insignificant stair stepping effect</li> <li>• High geometrical freedom, powder acts as support material</li> </ul>	<ul style="list-style-type: none"> <li>• Binder bleeding</li> <li>• Powder agglomeration</li> <li>• low mechanical strength</li> <li>• Improper powder feeding</li> </ul>	<p>[81]</p> <p>[82]</p> <p>[83]</p> <p>[14]</p>
<b>Drop-on-drop binder</b>	<ul style="list-style-type: none"> <li>• Supports multi-material printing</li> <li>• High geometrical freedom, one of the material can be used as support</li> <li>• No post processing step required</li> <li>• Fine features(&gt;50 <math>\mu\text{m}</math>)</li> <li>• Insignificant stair stepping effect</li> </ul>	<ul style="list-style-type: none"> <li>• Bleeding</li> <li>• Extensive post processing step, including curing and solvent removal</li> <li>• Slow</li> </ul>	<p>[92]</p> <p>[93]</p> <p>[94]</p> <p>[91]</p> <p>[90]</p>
<b>Drop-on-drop hot-melt</b>	<ul style="list-style-type: none"> <li>• Insignificant stair stepping effect</li> <li>• No post processing step required</li> <li>• Fine features(&gt;50 <math>\mu\text{m}</math>)</li> <li>• High geometrical freedom, self supporting material</li> </ul>	<ul style="list-style-type: none"> <li>• Thermal stress</li> <li>• Warping during solidification</li> <li>• do not support multi-material printing</li> </ul>	<p>[95]</p>

## Chapter 2

# Platform development and understanding

The previous chapter highlighted the capabilities and importance of hot-melt technologies as a safe and cost effective way to produce solid dosage forms using FDA approved materials with the innate lack of need for a rigorous post-processing solvents removal step. Moreover, the freedom of geometry provided by the inkjet 3D printer could allow the tailoring of drug release profile by controlling tablet geometry and thus surface area available for interaction with dissolution media.

To expand this concept and the range of profiles achievable, we set up to design and construct a dual unit system capable of jetting two different materials during the same print. For pharmaceutical applications this translates into the possibility of tailored drug release, including delayed and pulsatile, achieved by combining drug enriched cores and drug free shell structures.

The first step to achieving this goal was to identify the key elements necessary for the development of a functional dual material hot-melt deposition system capable of producing 3D objects with bespoke, complex geometry. This implies that the system must support three dimensional movement, precise material deposition and a feedback system which allows the user to verify the printed part and droplet formation. On the basis of these ground basic assumptions and by comparison with pre-existing systems the following features were identified as essential:

- **Two hot-melt inkjet dispersing units**, each comprising of an inkjet print-head capable of withstanding high temperatures, a heater and a high temperature reservoir.
- **Power supply and temperature control** to correctly operate the dispersing unit.

- **Unit support**, necessary to attach the printing units to the main stage. This must showcase the following capabilities:
  - two hot-melt units.
  - a rigid support that leaves no space for lateral movement of the printing head in order to limit the effect of mechanical vibration during printing.
  - modular design to guarantee easy access to all printing parts for quick assembly and ease of maintenance.
  - allow for fine adjustment in the z direction in order to guarantee parallel alignment between the printing bed and the dispersing head.
- **Linear stage and printing bed** with precise three dimensional movement. Ideally the linear motors will display  $\leq 50 \mu\text{m}$  minimum step size to ensure printability of designs with  $50 \mu\text{m}$  resolution.
- **Position control, path optimisation and jetting management**. These controls are generally carried out by the main software associated with the system. It should thus, be able to manage material jetted from the print-head's nozzle in a controlled drop-on-demand fashion with minimal electronic delay in order to deliver a functional 3D object. Moreover, the software should be capable of optimising the drop deposition pattern in order to reduce the time and number of passages necessary to produce each individual layer. Lastly, it should allow for user defined parameters such as print speed, frequency and resolution.
- **Substrate securing system**, to avoid potential misalignment due to unintentional movement of the substrate film during jetting.
- **Controlled environment**, this is of particular importance when using hot-melt units since temperature control represents the main curing mechanism. A change in the ambient temperature or the presence of air current might negatively impact the printing process compromising the integrity of the end product. A closed casing around the printer is also useful to protect the printed part from potential chemical contamination and particle/dust inclusion. Additionally, the use of a case reduces the risks for the user.

- **Cameras**, a top view camera is necessary to calibrate the printheads and check on the part during printing. It can also be used for the calibration of the printing bed. A side view camera is also fundamental in order to optimize the printing parameters so to produce droplets showcasing the correct speed and shape when reaching the substrate.

Multiple approaches were considered on how to tackle the development of such a system, including the design of a printer *ex novo* and the adaptation of pre-existing commercially available 3D printers. The first method, however, represents an extreme mechanical and computational challenge, including but not limited to moving in three dimensions, maintaining consistent temperature through the entire dispersing system and control every single nozzle's deposition pattern individually. Seeing that the focus of this thesis work was pharmaceutical and not engineering, the natural solution was indeed to modify a commercially available machine. The choice was between a Dimatix (Fujifilm, USA) and a PiXDRO LP50 (Meyer Burger, Netherland), visible in Figure 2.1 A and C respectively. The first would have represented a poorer choice as it lacks a native dual head system, an open software and additional power ports to feed the cartridge temperature control. Making the adaptation process likely extensive and time consuming. So, the LP50 was the preferred choice, even more so since it can mount a dual head unit (not hot-melt) and has open software. Moreover, Meyer Burger offers a single compatible hot-melt unit [105]. Finally, the type of dispersing unit to use and the hardware and software modifications required needed to be defined. The LP50 selected has an in-house built support system that allows mounting and control of two Dimatix's cartridges, however, as visible in Figure 2.1 B this type of cartridges do not have a heated reservoir and therefore heating elements to both reservoirs and a temperature control unit were required.

This proved problematic, however, as the geometry and materials of the cartridge are not compatible with a high temperature approach (summarised in Appendix A.3). It was hence decided to focus effort working with the Meyer Burger's original hot-melt unit, Figure 2.1 D. In this case the main modification involved changing the geometry of the support case in order to host two units instead of one, adding a temperature control unit to power the second reservoir and lastly adapting the software so to manage the new prototype.

In the following sections the reader is guided through the conversion process and its functionality, in particular with detail of both the original system,

highlighting the elements fundamental to the project, and the modifications made by the author.



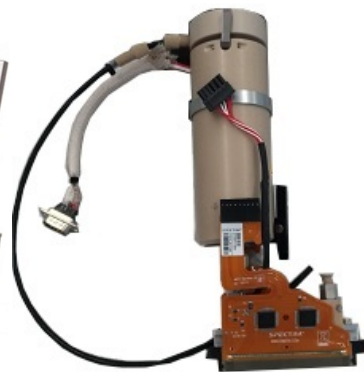
(A)



(B)



(C)



(D)

FIGURE 2.1: Schematic of the PiXDRO LP50, Dimatix printers and the respective cartridges. Dimatix (Fujifilm, USA) (A) and Dimatix printhead (Fujifilm, USA) (B), PiXDRO LP50 (Meyer Burger, Netherland) (C) and LP50 hot-melt printhead unit (D). Images (A) and (B) has been taken from Fujifilm's official website [106] while (C) was taken from Meyer Burger's website [105], lastly figure (D) was taken by the author.

## 2.1 Commercially available systems

### Printer: PiXDRO LP50

As mentioned in the previous section the printer of choice was the PiXDRO LP50 developed by Meyer Burger (Netherlands). This is a desktop inkjet printer designed for research and development of inkjet processes and applications, as well as evaluation and development of inkjet materials. As such it already shares a number of the features we were looking for in our system.

Among these it allows **motion** along the traditional X, Y, Z axis, and also rotation of the substrate table (S) and printhead (P). Moreover, the overall system accuracy and precision, as determined by the motors minimum step, are  $\pm 20 \mu\text{m}$  and  $\pm 5 \mu\text{m}$  respectively. Both are in good agreement with our starting requirements. Accuracy and precision relate to the capacity of the printer to produce repeatable and reliable results consistent with the digital design. Given a set of repeated measurements of a single droplet deposition onto a predefined position, accuracy is defined as the closeness of the deposited droplet to the target position, while precision is the closeness of the repeated droplets to each other.

The Y axis (representing the axes of motion of the printing bed as visible from Figure 2.2 A) mounts an ironless linear motor that can reach a top speed of  $400 \text{ mm s}^{-1}$ . In contrast stepping motors are used to control all other axes of motion and rotation and in this case the top speed achievable is  $200 \text{ mm s}^{-1}$ . This matches with the shared standard of preferring print bed motion over assembly movement during print. Such a decision is based on the desire to minimise undesired lateral movement of the printhead that might result in deviations from the deposition pattern. The print assembly is, however, still required to raise along the Z direction to guarantee 3D capability.

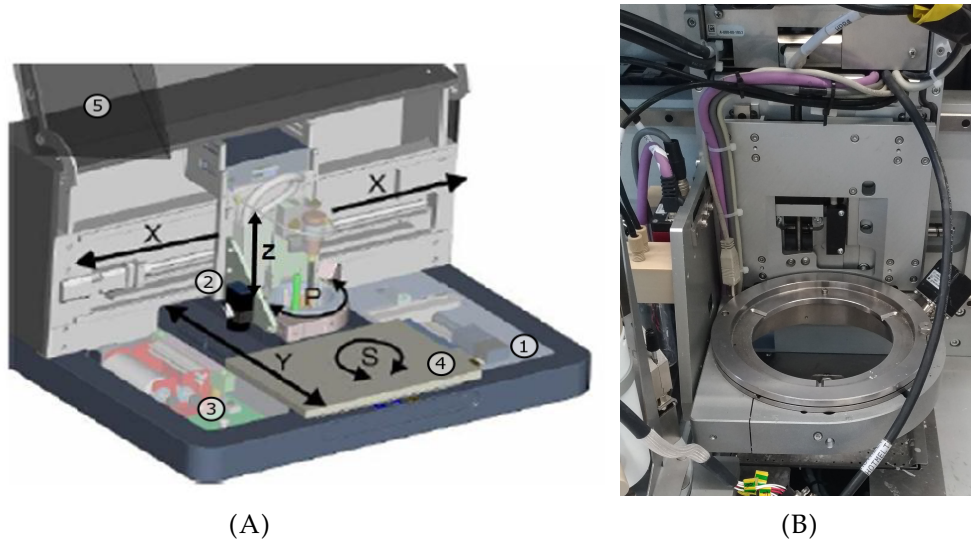


FIGURE 2.2: (A) Schematic of the LP50 machine including its major features. The motion system has been highlighted using directional arrows along the axes of motion, specifically the main printing axes (X, Y and Z), the rotation axis of the print unit (P) and the substrate tilting capability (S). Numbers were used to identify the remaining features of interest including the dropview (1) printview (2) cameras, the cleaning station (3), the printing bed (4), and the protective lid opened (5). The image was taken from PiXDRO Handout 2009 and modified by the author. (B) Detail picture of the magnetic mounting ring.

The **magnetic mounting ring** visible in Figure 2.2 B allows the attachment of the printing assembly to the printer's main body, providing accurate positioning while allowing for the unit to disengage in case an obstacle is encountered during motion guaranteeing the nozzle plate safety.

The **printing bed** consist of a metallic stage on which a suitable substrate ( $\leq 2.5$  mm thick) can be hosted and held flat via a vacuum suction created by a negative pressure through a series of 1 mm holes in the platform. Despite the overall stage dimension being  $227 \times 327$  mm the available printing volume is  $210 \times 310 \times 80$  mm due to fiducial alignment. Of particular importance for our application is the presence of a thermistor and a heater integrated into the stage platform allowing setting of the temperature up to  $90^\circ\text{C} \pm 1^\circ\text{C}$ .

The printer is equipped with two separate monochromatic **cameras** to provide top down and transversal views.

The top down camera, or *printview*, is attached to the assembly support as visible in Figure 2.2 A and is paired with a coaxial and ring light to cover for different illumination necessities. This recording system is used to inspect the pattern deposited on the substrate, its main application being for printhead,

print assembly and print bed alignment and calibration. When necessary it can also be used for nozzle selection when combined with the correct print design recipe.

The transversal, or *dropview* camera, is designed to monitor the drop formation, Figure 2.2 A. It is paired with a stroboscopic red LED synced with the printing signal. This enables the acquisition of pictures of the droplet in-flight after a specific time interval following ejection. While only one nozzle/droplet can be analysed at a time, the software is capable of acquiring subsequent pictures, one per nozzle, and stitch them together to create a complete vision of the printhead behaviour. This system is of particular importance for printing parameter optimisation since it provides a real time feedback including a snapshot of the analysed droplet alongside informations such as head speed, approximated volume and deviation from the nozzle vertical axis. This information is of particular interest for the user in understanding how the printer responds to changes of the printing pulse intensity and duration as well as printing frequency and nozzle temperature. It is possible to also analyse the effect of changes in the reservoir temperature, however due to its dimensions this is a slow process since the entirety of the reservoir and material need to reach a stable temperature. The key information for material optimisation are drop shape, volume and speed of ejection. For ease of use this set up can be controlled via Advanced Drop Analysis (ADA) software, which provides an automated picture acquisition for each set of user defined parameters. For each printing characteristic it is possible to input a range of interest and the program will automatically scan it without any further contribution from the user.

Meyer Burger provides a customised **software** to work with the LP50. The system comes with three nested levels of accessibility. The layered structure allows for different degrees of user intervention and modification while preserving the integrity of software core.

At the core of the software is a series of sub-routines that cannot be modified by the user. These include all the algorithms necessary to print, such as reading of digital files (only 2D file formats), pattern optimisation, movement control and droplet deposition. These functions are also in charge of controlling the pressure inside the print reservoir and to create the substrate's vacuum clamping.

While these routines cannot be modified it is possible to call them selectively via suitable scripts that in the context of this application are called *recipes*. A

*recipe* is a script that allows the programmer to feed parameters to the core functions in order to obtain the desired outcome, that being the printhead moved to a determined location, material deposition et cetera. This set of scripts are written in C#.

The last important layer of the software is the Human Machine Interface (HMI). This is a user-friendly graphic interface that enables the user to interact with the machine without having to change the code directly. In particular it supports parameter input and beginning/ending the print job without having access to the back end code. To make this possible the original recipe designs are paired with a corresponding .HML file allowing the use of Visual Basic for storage and handling. This simple visual interface reduces the chances of input errors, since it is simple to double check.

Of particular interest is also the possibility provided to the user to exclude non-performing nozzles, this favours higher quality prints while at the same time extending the print head life. In this scenario pattern optimisation will have to take into account the reduced nozzle availability and recalculate the output accordingly.

In addition to the aforementioned capabilities the LP50 presents some auxiliary inputs and outputs (I/O) port that can be used by the researcher to communicate with auxiliary systems.

In Table 2.1 are summarised the PiXDRO LP50 technical information.

TABLE 2.1: PiXDRO LP50 technical data [105]

Maximum printing envelope	210×310×80 mm
Max. substrate thickness	25 mm
Substrate hold	Vacuum clamping
Substrate heat	$\leq 90\text{ }^{\circ}\text{C}\pm 1\text{ }^{\circ}\text{C}$
Stage accuracy	$\pm 20\text{ }\mu\text{m}$
Stage precision	$\pm 5\text{ }\mu\text{m}$
Motion	Linear: Y Step: X, Z Rotation: substrate table, printhead
Print speed	X: $\leq 200\text{ mm s}^{-1}$ Y: $\leq 500\text{ mm s}^{-1}$
Maximum load:	2.5 kg
Printhead maintenance	Purging, capping, wiping
Print view	Pixel area: $656\pm 492\text{px}$ Field of view: $1.99\times 1.74\text{ mm}$
Drop view	Pixel area: $656\pm 492\text{px}$ Field of view: $1.1\times 0.7\text{ mm}$
Image formats	Bitmap, Gerber, postscript, png and PDF
Integrated post processing	UV pinning or curing

### **Hot-melt assembly**

At the beginning of this chapter, and specifically in Section 2, a briefly mentioned of Meyer Burger's hot-melt set up was provided. Here, more detail is provided on how it differs from a traditional inkjet unit and what are the benefit and downsides in relation to this thesis work.

As visible in Figure 2.3, the hot-melt unit shares all key aspects of a traditional inkjet one including the presence of a reservoir, a printhead heating unit and a printhead, however, it also allows the entire unit to be heated and not only the nozzles.

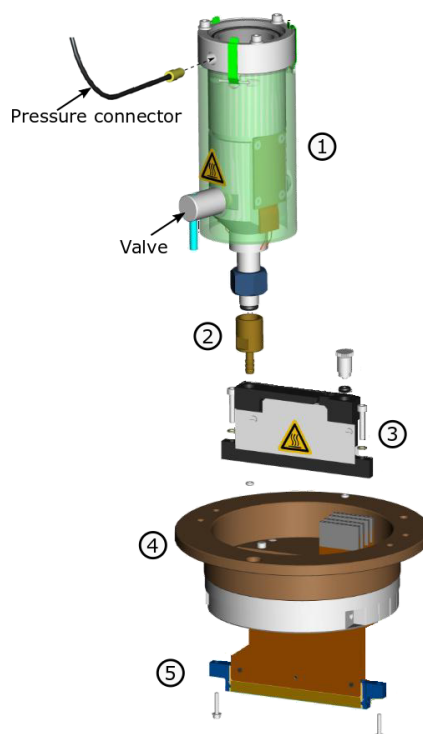


FIGURE 2.3: Schematic of the hot-melt inkjet assembly for PiXDRO LP50 printer. Highlighted the ink reservoir (1), metal connector(2), printhead heating element (3), metal holder (4), spectra head SE-128 (5). The image has been adapted by the author from (PiXDRO B.V. 2011) [105].

Specifically the 15 ml capacity reservoir can be heated up to 90 °C and is attached rigidly to the printhead heater via a metal connector and sealing o-rings. This is to be preferred over chemically resistant tubing, generally employed for traditional inkjet assays, since it guarantees heat diffusion between the reservoir and the heater minimising temperature gradients in the ink while flowing through the system. On the downside it adds an extra degree of difficulty in the design of the dual head system, since the unit is rigidly connected to the reservoir and therefore cannot be offset representing a strict geometrical constrain. The printhead of choice for this work was the Spectra SE-128 printheads (Fujifilm, Japan) visible in Figure 2.4 A. This is a piezoelectric unit designed for deposition of low viscosity materials in the range of 8-20 cP. This unit has a series of beneficial qualities, compared to other commercially available heads, that make it ideal for this project including a high number of nozzles (128), drop volume (30 pL) and high rate of operation (up to 40 kHz). The high nozzle density allows for a faster printing process by covering a wider transversal area in a single pass comparatively to less dense heads. In addition the high rate of operation allows for fast droplet

delivery increasing production speed. Lastly, while requiring a longer depositional process the use of small droplet volumes grants greater resolution due to the smaller foot print and consequently enables finer details. While droplet size can be influenced by the printing process it is mainly determined by the nozzle geometry and it is provided as a printhead parameter provided by the manufacturer. Moreover, it showcases a compact design compared to others. It indeed houses all 128 nozzles in only  $102 \times 5 \times 104$  mm and for a total weight of 25 g without sacrificing resolution. The compact design is particularly interesting for our project given the strong geometrical limitations, particularly in the X, Y plane. The nozzles are  $35 \mu\text{m}$  in diameter and  $508 \mu\text{m}$  apart from each other leading to a native resolution of 50 DPI. Spectra SE 128 is part of a printhead line from Fujifilm that contains also similar print heads with larger nozzle diameters. This resolution can be further reduced by rotating the printing angle and allowing for staggered deposition from the nozzles to account for the reference change. Specifically:

$$\begin{aligned} DPI_{Nat} &= \frac{1}{W_{Nat}} \\ W_{Prj} &= W_{Nat} \cos \alpha \\ DPI_{Prj} &= \frac{DPI_{Nat}}{\cos \alpha} \end{aligned} \quad (2.1)$$

Where  $DPI_{Nat}$  is the original DPI,  $W_{Nat}$  is the native nozzle spacing in inches,  $DPI_{Prj}$ ,  $W_{Prj}$  are the projected DPI and nozzle spacing and  $\alpha$  is the angle between the original and the final position. An illustrative scheme of such approach is visible in Figure 2.4 B

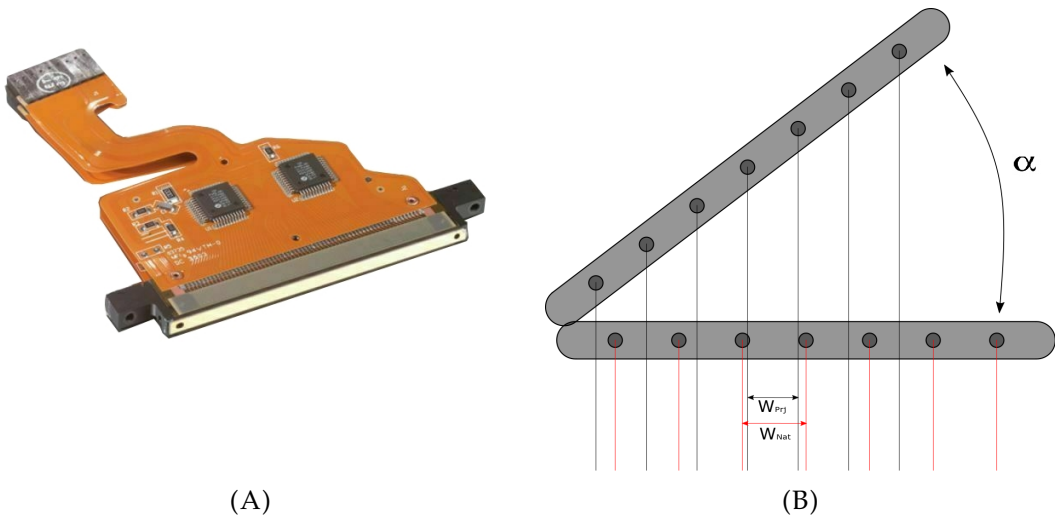


FIGURE 2.4: Spectra head Se 128 [106] (A) and DPI tilt (B).

Furthermore, the main reservoir can be connected to a pressure pump in order to aid ink stability. Specifically, a negative pressure ( $-30$  mPa to  $0$  mPa) is used to assist the formation of a stable meniscus at the nozzle by compensating the hydrostatic pressure and to avoid nozzle plate flooding. On the other side a positive pressure pulses up to  $250$  mPa used to purge the system either before ink substitution or in the attempt of resolving nozzle blockages.

Lastly in Table 2.2 are summarised the printhead characteristics.

TABLE 2.2: Hot-melt unit product data [106]

<b>Reservoir plus lid</b>	
Size	diameter 50 mm 211 mm
Weight	784 g
Operating temperature range	$\leq 90$ °C
Operational capabilities	manual on/off valve pressure tube connector
<b>Heater</b>	
Size	$90 \times 10 \times 59$ mm
Weight	117 g
Operating temperature range	$\leq 90$ °C
<b>SE 128 AA</b>	
Size	$102 \times 5 \times 104$ mm
Weight	25 g
Nozzle spacing	$508$ $\mu$ m
Nozzle diameter	$35$ $\mu$ m
Drop size	$30$ pL $\pm 4$ %
Operating temperature range	$\leq 90$ °C
Fluid viscosity range	8- 20 cP
Maximum operating Frequency	40 kHz

## 2.2 Hardware implementations

The aim of this work was to develop a support system able to host two printhead-heater-reservoir units whilst also being able to fit into the ring holder inside the Pixdro LP50. For this reason all the original unit's supports and attachments had to be redesigned. This project offered many challenges, largely due to the spatial and weight constraints imposed by the machine geometry and motor's power. In particular, the rigidity of the depositional unit meant that the reservoir cannot be delocalised with respect to the printhead. This, combined with the small dimensions of the ring holder and the generally limited space available to house the assembly inside the printer, greatly constrained the size of the base support of the set-up.

The consequent challenges and relative solutions are listed below.

The new **supports system** needed to be able to house two hot-melt units, each including a reservoir, a heating element and a printhead all rigidly connected. Moreover, it had to allow for quick and secure assembly with no room for undesired movements, while at the same time granting access to all parts for easy substitution and maintenance if necessary. To address these issues a modular design, inspired by Ledesma's work [107], was adopted as visible in Figure 2.5 including multiple detachable support parts, instead of a singular rigid structure [107]. Firstly, it was fundamental to understand the maximum **volume available** for the prototype inside of the printer. After a thorough examination of the assembly's housing it was realised that the holder actually consists of not one, but two concentric metal rings (respectively 109 mm and 139 mm of inner diameter), of which only the external one is secured directly to the printer. The double ring is a safety measure to allow the fast disengagement of the assembly if an obstacle is encountered during printing. By sacrificing the internal ring it was possible to increase the space available for the dual reservoir unit. In the Z direction the constraints are much less strict since the maximum height recommended is 230 mm and the total unit's height inclusive of reservoir, reservoir's cap, metal connector, heater and printhead is 211 mm.

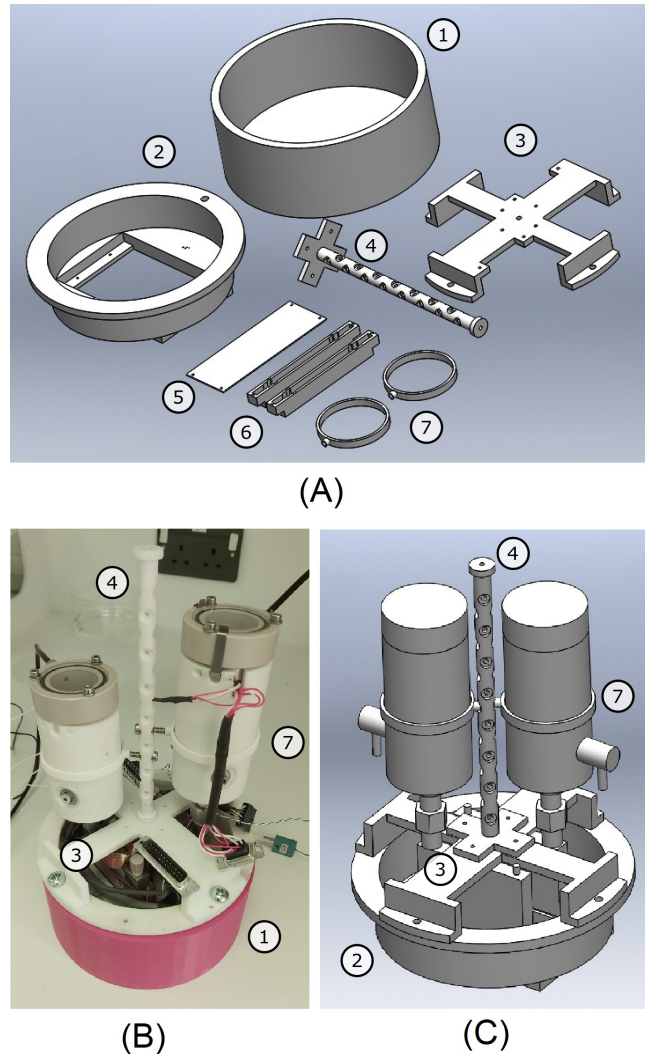


FIGURE 2.5: Top (A):Rendered image displaying of the main supports parts: assembly resting holder (1), base support (2), top case (3), central anchoring structure (4), bottom cover (5), printhead holder (6), reservoir holder (7). Bottom: Photo (B) and rendered image (C) of the assembled prototype.

Both the inner metal ring and the base support of single unit assembly share the same **magnetic kinematic mounting system** seen in Section 2.1 consisting of a series of hemispheres and holes matching the slots and pin of the main ring. Thus, to preserve the same safety levels after the removal of the ring, our prototype base support was designed to mimic the original one replicating the same sets of hemispheres and holes. In addition 4 neodymium disc magnets (N701-RB, Eclipse Magnetics Ltd, UK) were positioned to strongly secure the support to the printer. These help prevent lateral movement and vibrations during printing while at the same time allowing for fast disengagement if any pressure is put on the printhead by an obstacle. Moreover, by reproducing the original mount design it was possible to reflect the same zero-position. This is of particular importance for the head calibration and to

guarantee full range of motion especially the rotation (P) around the assembly's axis as visible in Figure 2.2 A, its maximum range being 94° compared to the zero-position.

Understanding how to best arrange the two units in the space available and designing a set of **supporting attachments** represented the most significant challenge due to the number of limitations both from the geometrical and mechanical point of view. As mentioned above the main spatial limitation is the ring hole diameter 139 mm while the main features of the printing units are the reservoir diameter 50 mm and the printhead footprint 102 mm × 5 mm. As noticeable from Table 2.2 the majority of the printing unit weight is related to the reservoir, resulting in a top heavy ensemble, meaning that it is prone to vibrations and mechanical misalignment. Thus, the reservoir needed to be rigidly attached to the support structure with little room for mobility since any movement will be transferred directly to the printhead disrupting the droplet's pattern of deposition. To reduce load imbalance and to guarantee rotational freedom, and in order to accommodate different printing angles, axial symmetry of the design was pursued.

The result is a *base support* that mimics the original, but that can fit in the new found space while allowing for the fit of two print units. Since it was our goal to make this prototype as modular as possible the base shows a series of anchoring points for the printheads so that the user can adapt the system to its needs without having to remake it. While designing this part particular attention was paid to replicating the anchoring system and to maintain the position at which the nozzles are sitting compared to the mounting ring for ease of calibration and safety of movement.

Keeping the same idea in mind, the *top cover* was made in the shape of a cross that attaches directly to the base with four bolts, at the centre a hollow column is used to secure the reservoirs via the tightly fitted ring shaped supports. The column presents a series of orthogonal off-centred threaded holes to adapt to the users needs. The resulting support is pictured in Figure 2.5.

During the first stages of the research it quickly became evident that the **Spectra head's mounting supports** represented a clear weak point. These were extremely delicate and broke with ease when the smallest stress was applied to them while being mounted. This is an expensive and wasteful limitation of the Spectra heads that needed to be taken into consideration while planning our prototype. To address this issue while at the same time

providing a stronger and more stable attachment to the base, it was decided to model a support case that encloses the printhead completely and that will then be mounted onto the base support directly, in this way removing the need to use the original printhead supports. Furthermore, this has a wider footprint on the anchor point reducing tilting to a minimum. The design can be seen in Figure 2.6.

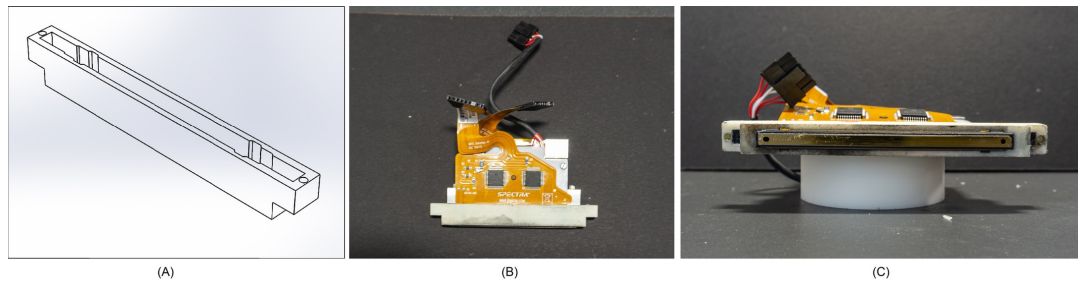


FIGURE 2.6: Detail of the print head holder. Namely the rendered image (A) and photos of the side (B) and bottom (C) view.

The last obstacle faced during the design phase was the **weight limitation** imposed by the maximum load supported by the stepping motors, nominally 2.5 kg. The original mount support in the Meyer Burger design used steel, making the supports not only hard to modify, but also heavy. For this reason it was decided to model the system using SolidWorks (Dassault Systèmes, Term), a solid modelling computer-aided design, and exploit our in-house Additive Manufacturing capability to manufacture it. This allowed us, not only to swap the original steel for much lighter nylon, but allowed a greater geometrical freedom and smart design such as a hollow column. As a result of these choices the support weight was cut by 63.5%. All parts were manufactured using an in-house laser sinter 3D printer, specifically a P-100 Formiga (EOS GmbH Electro Optical Systems, Germany) loaded with Nylon PA12. The prints were then cleaned with a brush and exposed to a grit blast, rinsed in water and dried in an oven for 2 h at 40 °C. Nylon PA12's data sheets reports its melting point at 172–180 °C and the softening point at 163 °C. Since our system maximum operational temperature of 90 °C it is safe to assume that the material is suitable for our application. The final set of supports is visible in Figure 2.5.

Excluding the side supports the majority of the printing unit's weight resides in the reservoir itself. As a result, it was necessary to try and reduce it. To do so a copy of the original reservoir was created from aluminium instead of steel, the overall height was also reduced by 1.5 cm decreasing the overall weight but also the ink volume to 10 ml, enough for the production of a full

printing bed of samples. To achieve this new design a digital replica of the original part was created, using SolidWork, including the main body, the isolating shaft and the valve system. The part was then machine turned by Andrew Plummer in the in-house workshop. The shaft and valve were adapted to fit the new design and reassembled including a new set of heat plates. The end result was a  $294 \pm 2$  g reservoir resulting in a reduction in weight of 60% in comparison to the original unit (Figure 2.7). Despite the clear benefit of our new reservoir this presents an issue, as it was not possible to recalibrate the LP50 temperature control system to account for the change in material conductivity and heating pads. As a result, the reservoir temperature needed to be controlled via an external control system. For this reason and thanks to the reduction in weight achieved using nylon supports and one aluminium unit, it was decided to still mount one of the traditional reservoirs and control it via the main software. Hence, the final assembly weighed 1.70 kg, safely inside the capabilities of the stepping motors and only 324 g more than the single unit. The final assembly can be seen in Figure 2.5 B.



FIGURE 2.7: Comparison between the original hot-melt reservoir from Meyer Burger (Right) and our redesigned version (Left).

## 2.3 Software implementations

To support all the alterations made to the system a re-evaluation and appropriate revision of the supporting software became necessary.

This is of particular importance given the addition of the extra hot-melt unit and the changes in geometry that resulted from it. Notably it was also desirable to include in the software the possibility of using, during one print, ink materials with different layer heights with minimal input from the user so as to minimise human error. While this represents its own computational challenge it was believed to be essential in order to make the prototype functional and versatile past the limits of this thesis work.

### 2.3.1 LP50 software adaptations

In section 2.1 were introduced the LP50 basic features including the control software provided by Meyer Burger in association with the machine. While access to the core code is denied to users it is possible to call it via suitable scripts that in the context of this application are called *recipes*. The selected programming language for this set of script is C# and the parameter handling was performed by Visual Basic both for GUI and recipe scripts. Thus, tailored printing routines were developed by building upon these pre-existing structures, whilst adapting them to our specific needs. In particular the user interface and respective handling were split into separate sections. One being in management of each individual printhead and one in charge of the specific print. The former, known as *head profile*, behaves similarly to the original recipe in the way that it holds all the information relative to a specific printhead and ink configuration. In contrast, this does not contain any detail regarding the specific print generation function that is generally within the domain of the original recipe. Multiple profiles can be created relative to separate printheads or for different inks with the same printhead. This allows the establishment of a library of profiles that can be later paired to create the desired 3D object via the *Printing* script. The introduction of a library eliminates the need for the user to re-establish all parameters every time they decide to switch materials, this not only helps speeding up the setting up of the print but also to reduce input errors since the user has to only record the correct profile instead of a long list of parameters.

The *Printing* script was conceived, as mentioned, to minimise human error and to speed up the process of setting for a print. The user only needs to select the head profiles and to provide a correctly sliced and named set of 2D

maps, the *printing recipe* will then pair each BMP map with the relative *head profile* calling them in the correct order so to create the optimal deposition pattern. In the following sections it will be discussed more in detail some of these steps. In Appendix A.1 is reported the core code for the *Head profile* and *Printing*.

### 2.3.2 Temperature control

As in Section 2.2 the hardware and software limitations and in particular the lack of a fourth power port to the heater of the second reservoir meant the development of a supplementary temperature control system was needed. The reservoir was equipped with two polyimide thermofoil heaters, one on each side, kept in position by aluminium plates. A K-thermocouple was also attached to the main body of the reservoir with high temperature resistant polyimide tape and covered evenly with non-silicone heat transfer paste (HTC10S, Electrolube, UK) to ensure an homogeneous thermal distribution. A circuit, including the following electronic components, a IRZF44N MOSFET, a 10 k $\Omega$  resistor, a BC337-25 transistor and a MAX31855 module pinboard, all mounted on a small circuit board and connected to the heating pads, the thermocouple, a power supply and a microcontroller (Arduino Uno, Adafruit). By means of the corresponding software: Arduino 1.8.11 a Proportional, Integral and Derivative (P.I.D.) loop control routine was designed capable of reading the thermocouple output which provides the temperature inside the reservoir and hence manages the power supplied to the heating pads, in order to firstly bring the system to temperature and subsequently to maintain it stable. To minimise errors a three stream P.I.D. controller chain produces an actuating signal aimed to engage the heating pads as necessary and provide a feedback path. The *Proportional* section of the control produces an actuating signal that is proportional to the error term, this allows the temperature to be quickly raised when the system is turned on, and then slowing down the heating when approaching the desired temperature. While sufficient in many cases it can cause a steady state error that makes it impossible for the system to reach the desired temperature. For this reason, it was necessary to introduce the *Integral controller*, which sums up the input signals over time and keeps a running total, when added to the signal coming from the proportional path this overcomes the impasse caused by the

steady state error. Lastly the *Derivative controller* measures the rate of change of the error and is added to control the speed of change of the temperature to prevent overshooting. The system was calibrated using the Ziegler–Nichols method [108] which set to optimise the value of the gains in an heuristic way. Specifically, I (integral) and D (derivative) gains are initially set to zero, while P (proportional) gain is increased until the output shows stable oscillations. The oscillation gain value and period are then used to set the P, I, and D gains on the base of the Ziegler–Nichols as reported in the literature [108]. The parameter are then micro optimised until the desired behaviour is obtained.

### 2.3.3 Calibration

There are two main approaches to calibrating a two head system, the first puts more strain on the support design while in the second the stress is placed on the software. The former is based on having the capability of adjusting the position of one head with respect to the other so that the two can be made perfectly parallel to each other. It is then necessary to calibrate only one of the two via the software since the other will have the same calibration parameters, but shifted by a factor equal to the distance between the two heads. This can be achieved by introducing a set of movable parts in the base support to allow mechanical adjustment. However, this causes a bulking up of the structure which, due to the tight working space, is incompatible with our desire of modularity. Moreover, the inclusion of additional moving parts increases the chances of vibration during print. Considering part stability and reduction of lateral movement are key objectives the second option of calibrating the heads separately was chosen. Firstly, a frame of reference was created by establishing the fiducial and edge alignment for the printing platform, so each printhead of our prototype could be finely tuned with respect to the same point. Then, the calibration was performed exploiting the pre-existing routines used for the single unit. This procedure involves printing a series of known patterns such as lines and squares and investigating the printed part taking advantage of the integrated vision system. Any observable deviation has to be addressed and compensated for by tailoring the *printhead offset parameters*. The successful calibration allowed us to create multi materials complex patterns without depositional errors. An example is shown in Figure 2.8.

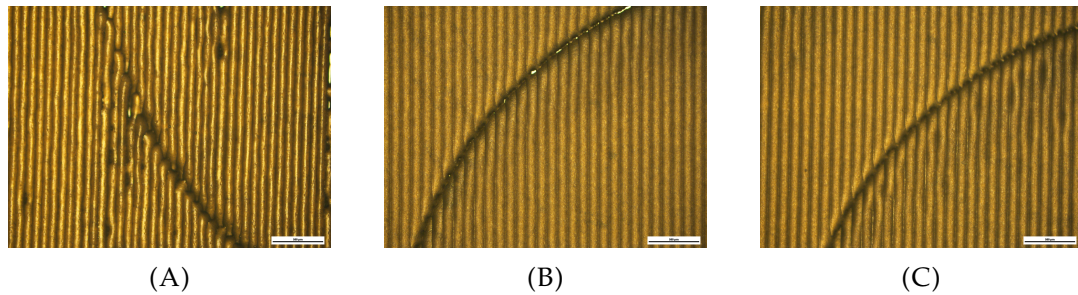


FIGURE 2.8: Microscope images of multi-material depositions where the material on the right and on the left were printed respectively with our in-house control unit and the original Meyer Burger one. The pictures represent the result of errors in the printhead calibration (A), (B) and a well calibrated setup (C).

### 2.3.4 3D object design and slicing

A key advantage of any additive manufacturing technique over traditional processing is its capability to produce complex three dimensional objects and hot-melt inkjet printing is no exception. As such at the base of any work there is the design of the 3D object via a CAD software, the resulting file includes all the geometrical detail necessary. However, it does not contain any information regarding the properties of the material to be used. Specifically, it is lacking key details such as layer height and drop spacing. Most companies will overcome this limitation by providing an inbuilt option for 'slicing' the file into a stack of layer patterns with user specified height and DPI (Drop Per Inches). However, as seen in section 2.2, the original LP50 software can only read 2D patterns and does not provide the user with a slicing option. Meaning that it is the user who prepares the stack of 2D designs such that they will contain all the desired detail, including layer heights and drop spacing, in such a manner that when combined in a layer by layer fashion they will form the desired 3D solid form. This is a non-trivial problem and makes the process highly susceptible to human error. This becomes more evident when working with complex geometries including multiple materials with different layer heights. It was hence developed an in-house slicing routine in Matlab (Mathworks, USA) capable of accepting any .stl file and slicing it into the correct stack of bitmaps (BMP), not only reducing human error and time necessary to process the original 3D file, but also increasing part consistency. The program requires from the user some key parameters including resolution in terms of DPI, layer thickness and relative .stl files for each material. The outcome is a stack of .png files named in accordance with our new sets of recipes (see section 2.3) and saved in a folder indicated by the user.

### 2.3.5 Material deposition conditions

After designing a functional set of recipes and routines to correctly manage part slicing, head movement and tilting; their precise performance is dependent on the material deposition conditions.

The main parameters under user control are: z-rise between layers, temperature of the fluid and of printbed, material deposition order, ink pressure and printing pulse applied by the piezoelectric actuator.

When considering z-rise the increment along the Z-axis was identified after each layer deposition to ensure consistent distance (or gap) between the nozzle plate and the substrate, each increment corresponding to the expected layer thickness input by the user.

An error in this value might lead to one of two possible scenarios. If the layer thickness had been underestimated over time it is possible to observe a decrease in the distance between the nozzle plate and the printing layer itself, which in extreme cases can result in the printhead touching it, compromising print integrity. Alternatively, an overestimation of this parameter causes an increase in nozzle plate to printing layer distance. Since the time of flight is constant during the entire print a change in the nozzle distance might over-time translate into drop depositional errors and again a compromised print.

This work requires a control ink temperature, as such it is clearly a key component amongst the printing conditions. As mentioned this not only allows us to maintain the material in a liquid state but also the capability to tailor its viscosity. Similarly, the heating functionality of the printing bed was exploited to maintain the material in a semi-solid state after deposition in order to improve adhesion between sequential droplets while at the same time limiting spreading. To determine the best performing print bed temperature a series of single layer square prints were performed at increasingly high temperature while maintaining all other printing parameters constant. Each print was removed from the print bed before raising the temperature and performing the next print. The results were observed under the microscope and ranked on the base of the smoothness of the top surface and the sharpness of the edges, aiming at eliminating the scalloping effect. The best performing temperature was selected for future prints.

The order in which the different materials are deposited is defined by either spreading or layer height. Specifically, fluids with a smaller footprint on the substrate will be deposited first to create a well-like condition for the second material to be deposited in. Similarly, in order to avoid a 'mountain' effect at the contact edge the material with the thinnest layer height should be deposited first.

As mentioned in Section 2.1 the role of pressure in the IJP is to avoid fluid leakage and nozzle plate flooding in between firing signals. This is achieved by establishing a negative pressure to compensate for the hydrostatic thrust.

Lastly, is the printing pulse applied to the piezoelectric actuator and used to actuate drop formation and deposition. This pulse can in general have different shapes to accommodate diverse materials, however in the case of the LP50 the shape is fixed to the trapezoidal one. Figure 2.9, shows two regions of fast voltage change and discharge (rise and falling edge) and a constant central region (peak time). It also has an inactive voltage threshold (low voltage) and an active voltage level (high voltage). The optimal pulse conditions are those in which the majority of the energy is transferred to the droplet and not wasted in vibrational energy and consequent heat formation. Since the energy is used only to overcome the jetting barriers arising from surface tension all the remaining energy is transferred to the drop in the form of kinetic energy. This means that the easiest way to determine the optimum pulse is to identify the fastest stable drop that does not present long tails or satellites.

For user ease all the mentioned parameters can be tested independently or together via the Advanced Drop Analysis (ADA) software, which provides an automated picture acquisition for each set of user defined parameters. The use of ADA also allows for the identification of underperforming nozzles, that can then be excluded.

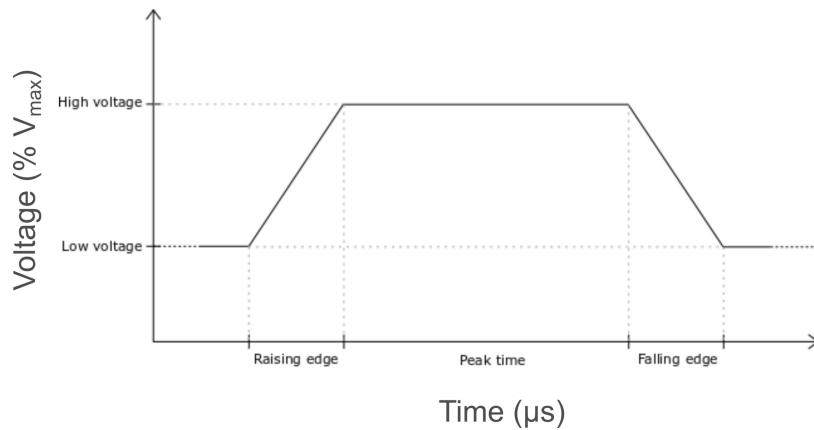


FIGURE 2.9: Piezoelectric actuator trapezoidal printing pulse, highlighted: rising edge, peak time, falling edge, threshold and maximum voltage.

## 2.4 Final set-up

To conclude, in this chapter it was shown the process behind the development of the new dual reservoir hot-melt inkjet printing platform. In Figure 2.10 is presented the final prototype resulting from all the modifications here described. It includes the newly designed functional multi-material printing assembly 2.10 B for which a modular approach was adopted allowing for quick and secure assembly of two printing units. While the support system allows for the inclusion of diverse printing systems for the scope of this thesis two hot-melt inkjet printing units were mounted, each comprising of an inkjet print-head capable of withstanding high temperatures (Spectra SE-128 printheads, Fujifilm, Japan), a heater and a high temperature reservoir.

By manufacturing all part using a in-house laser sinter 3D printer, P-100 Formiga (EOS GmbH Electro Optical Systems, Germany) loaded with Nylon PA12, it was possible to produce high temperature resistant, light weight parts without sacrificing sturdiness. In addition, to further reduce the weight strain on the printer motors a lighter and smaller aluminium copy of the original reservoir was produced reducing the weight by 60%. The final assembly weighed 1.70 kg, safely inside the capabilities of the stepper motors and only 324 g more than the single unit. It is thus clear that 3D printing was not only the key focus of this work, but also an essential support system allowing the creation of complex parts that would have been either impossible or very costly to produce by other means.

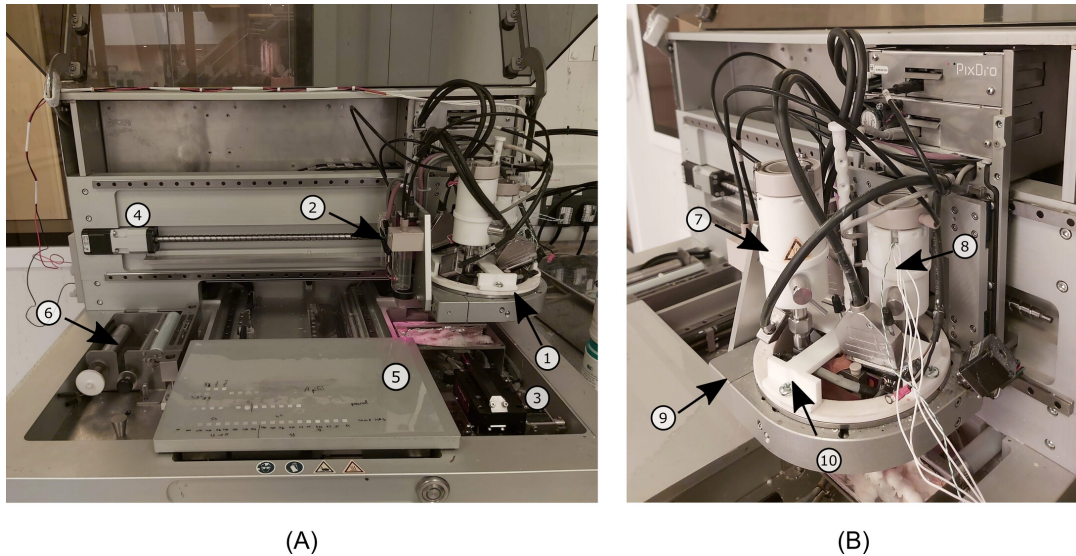


FIGURE 2.10: Final the dual hot-melt system set-up. Left: Photo of LP50 machine including its major features. (1) Dual hot-melt unit, (2) printview and (3) dropview cameras, (4) stepper motors, (5) the printing bed and substrate, (6) maintenance station. Right: close up of the printing unit (7) original and (8) custom made reservoirs, (9) ring holder (10) custom made support.

In this chapter was also explored the development of a temperature control system to support the second heated reservoir, which included the addition of an external power supply controlled via an Arduino (Adafruit, Arduino uno) which enables continuous monitoring and control of the unit temperature via a dedicated software.

Lastly, to complement the new setup the original machine software was modified to manage both the individual printhead separately and as a unit, particular attention was paid to their depositional interaction both an a 2D and 3D level, taking into consideration both droplet overlap, material interaction and layer variations native to the material or the pattern.

## Chapter 3

# Materials and methods

The following chapter contains the information on the active pharmaceutical ingredient (API), excipients and primary experimental techniques used. The aim is to provide an understanding of the working principle of the most common experimental techniques and a general overview of the current and historical application of the API (Fenofibrate) and excipients of interest. More information regarding the material selection process and the specificity of the experimental procedures used at the different stages of the research can be found in the chapters that follow, specifically Chapter 4 and Appendix A.2. In particular, Chapter 4 includes an in depth analysis of the thermo, chemical and mechanical property of the printable candidates. While a complementary summary of the remaining unsuccessful materials alongside with their main property is provided in Appendix A.2.

### 3.1 Materials

#### 3.1.1 Fenofibrate

Fenofibrate ( $C_{20}H_{21}ClO_4$ ), shown in Figure 3.1 is a drug of the fibrate class and it is the most commonly prescribed among them. It finds application in the treatment of hypertriglyceridemia [109], mixed dyslipidemia [110] and hyper-cholesterolemia [111]. It works by reducing plasma levels of blood triglyceride, cholesterol, and low-density lipoprotein cholesterol in healthy subjects and patients with hyperlipoproteinaemia.

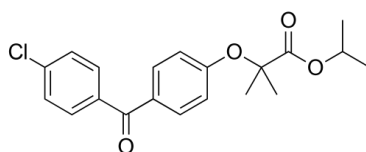


FIGURE 3.1: Chemical structure of Fenofibrate( $C_{20}H_{21}ClO_4$ ).

Fenofibrate is a BSC class II drug with very low oral solubility and high permeability [112, 113] and hence can require formulation strategies to improve bioavailability. Traditionally other commonly employed approaches to enhance drug bioavailability include the use of silica based formulation [114], nano suspension [114], nanocrystals [115], micro emulsions [116] liposome formulations [113] and micronisation [113]. Despite the extensive studies only a relatively few formulations can be found on the market using these approaches due to challenges associated with equipment handling, processing and material selection [117, 118].

### 3.1.2 Candelilla

Candelilla Wax is a natural wax derived from the leaves of the candelilla shrub and consisting of about 20-29% wax esters, 12-14% alcohols and sterols, 49-50% hydrocarbons, 7-9% free acids, 2-3% moisture and 1% mineral matter [119, 120]. It is a hard and brittle wax, yellow in colour, opaque to translucent and aromatic with a sweet sent to it. Its melting point is reported in the range between 68 °C and 72 °C [210]. In addition, it is emulsifiable and has excellent gelling and oil retention properties. Thanks to its properties Candelilla finds a wide application in both the cosmetic and food industry, but can also be encountered in car varnish. [121]

In the recent years Candelilla has also attracted the attention of the pharmaceutical field for the production of micro emulsion, taste masking, as an excipient in antifungal and antioxidant bioactive film. [122, 123, 124, 125]

As a food additive, candelilla wax has the E number E 902 and is used as a glazing agent [126], edible coating agent to prolong food items shelf life [127], texturiser for chewing gum base [128], carrier for food additives (including flavours and colours) [129] and clouding agent [130].

In cosmetic industry, it is used as a component of lip balms and lotion bars. [131]

### 3.1.3 Apifil CG

Apifil CG is a PEG-8 enriched beeswax produced by Gattefossé as a O/W emulsifier and is the result of alcoholysis and esterification reactions of natural beeswax [132]. Beeswax has a complex chemical structure including various organic compounds, among which the main components are: unsaturated and saturated hydrocarbons, monoesters, diesters, triesters, hydroxymonoesters, hydroxypolyesters, free fatty acids, acid monoesters and acid

polyesters. However, the composition is highly influenced by the bleaching procedure and the region from which it was sourced [133, 134]. From beeswax Apifil CG inherits its opaqueness and aromaticity, in contrast it is white in colour. It presents a melting point in the range between 59 °C and 70 °C [132]. Apifil CG finds application mainly in the cosmetic industry where it is appreciated as an emulsifier and for its long-lasting moisturising effect. Nevertheless, in the last decade it has been investigated as an excipient and a potential carrier for lipophilic drugs, such as N,N-diethyl-m-toluamide, and vitamin K [135, 136]. This material was chosen to be tested for this project on the base of the results obtained using the parent material: Beeswax. The latter was successfully printed by M. Kyobula [137] utilising the same commercially available single head hot-melt ink-jet printer on which the newly developed dual head system was based on.

The Apifil CG used in this project is of pharmaceutical grade donated by Gattefossé.

### 3.1.4 Compritol 888 ATO

Glyceryl behenate (Compritol® 888 ATO) is a hydrophobic fatty acid ester of glycerol (as shown in Fig.3.2), as such it presents a relatively low melting point, low HLB (hydrophile-lipophile balance) value and have excellent plastic properties [138]. It is neutral in flavor and odorless, more importantly it is chemically inert and safe for human consumption (FDA approved). Its reported melting temperature is in the range from 65 °C to 77 °C [138]. In addition Compritol 888 ATO is compatible with standard excipients, flavoring agents, polymers, plasticizers and surfactants making it the perfect candidate for our project.

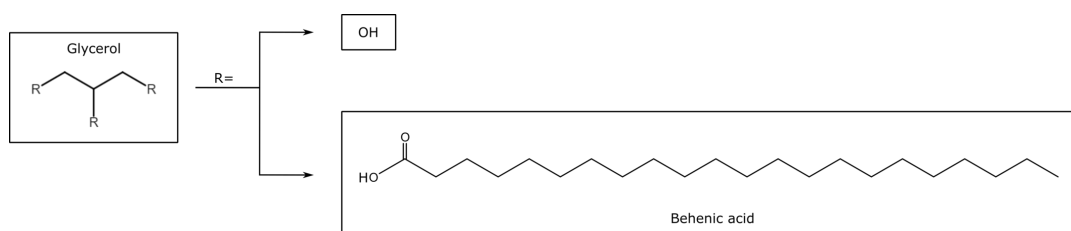


FIGURE 3.2: Chemical structure of Compritol 888 ATO.

Originally introduced as a lubricant for compression tablets [139, 140, 141], it has recently reached a wide application as a hot-melt coating agent for sustained-release formulations [142, 142, 143, 144] and as a binder in dosage forms prepared by melt pelletization [145, 146]. It is commonly found in

concentrations that ranges between 1% and 3% when used as a lubricant or binding agent, while in excess of 10% when employed as a sustained release excipients [141].

Compritol 888 ATO has also been reported to be successfully used as a lipophilic matrix-forming agent in the manufacture of sustained-release tablets [147], in this case its concentration was raised above 30% of the total tablet weight.

The Compritol 888 ATO used in this project is of pharmaceutical grade and was donated by Gattefossé.

### 3.1.5 Compritol HD5 ATO

Compritol HD5 ATO consists of mono, di- and triglycerides and PEG-8 mono- and di- esters of (C22) behenic acid [148] (the structure is visible in Fig.3.3). It is a mixture of Compritol 888 ATO and polyethylene glycol (PEG) behenate where the latter represents more than 50% of the total mass. It is white in colour, opaque and it is neutral in flavor and odorless and its melting point is in the range from 60 °C to 67 °C [148].

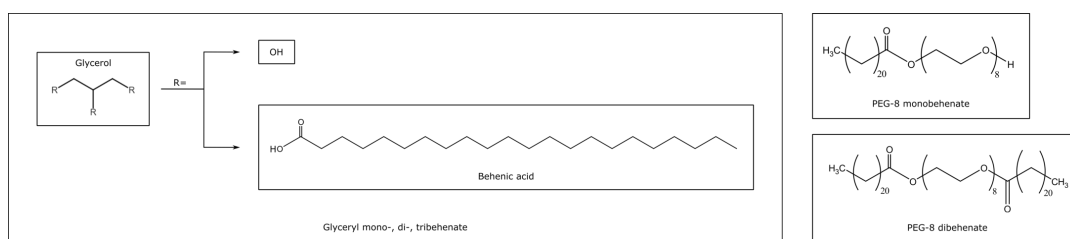


FIGURE 3.3: Chemical structure of Compritol HD5 ATO.

Compritol HD5 ATO is an amphiphilic substance with a hydrophilic-lipophilic balance (HLB) value of 5, (Compritol® 888 ATO HLB = 2). As a result, this excipient has been reported to exhibit excellent lubricant properties [139, 149] and has been proved to enhance the solubility and dissolution rate of poorly soluble drugs [150]. In contrast with what seen in the previous section for Compritol 888 ATO, Compritol HD5 has yet to be explored as a lipid matrix former, and its capability to enhance the dissolution properties of poorly soluble API in aqueous solvents or to adjust drug release from matrix systems has not yet been adequately evaluated.

### 3.1.6 Precirol ATO 5

Glyceryl palmitostearate (Precirol ATO 5) consists of mono-, di- and triglycerides of palmitic (C16) and stearic (C18) acids (structure presented in Fig.3.4), with the diester fraction being predominant [151]. It is a white in colour, opaque and with a neutral taste and its melting point is in the range from 50 °C to 60 °C [148]..

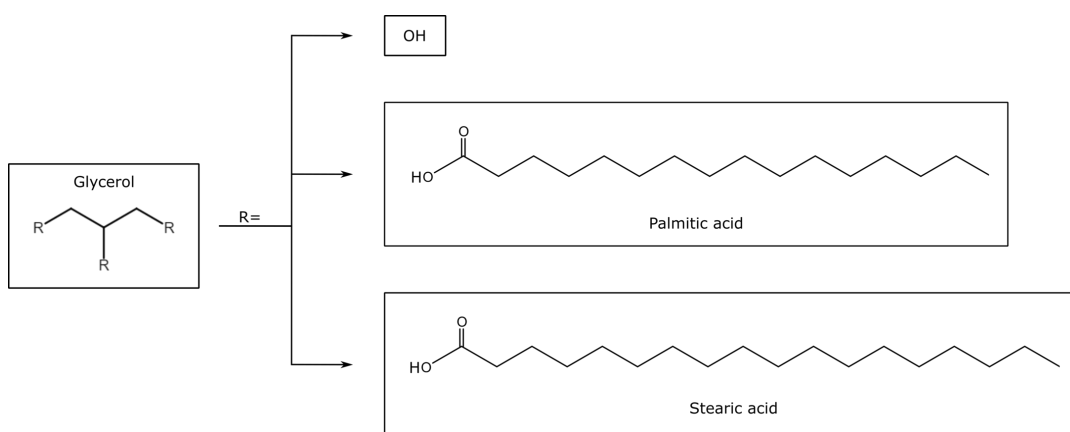


FIGURE 3.4: Chemical structure of Precirol ATO 5.

Precirol ATO 5 is traditionally used as a lipid vehicle for sustained release formulations [152, 153], as taste-masking agents for bitter tasting drugs [154, 155] and for capsule filling due to its low friction properties [141]. Furthermore Precirol ATO 5 finds application in the formulation of lipid nanoparticles as vehicles for topical delivery [156]. However due to its highly hydrophobic nature the use of Precirol ATO 5 as the only carrier can lead to the drug release being too slow. As a result in literature it is frequently found in association with Compritol 888 ATO. Hamdani's study from 2002 [145] demonstrated that a short time prolonged release of phenylephrine hydrochloride can be achieved utilising an appropriate mixture of Precirol ATO 5 and Compritol 888 ATO.

### 3.1.7 Flexible polyethylene terephthalate film

Polyethylene terephthalate (PET), structure visible in Figure 3.5, is a general-purpose thermoplastic polymer which belongs to the polyester family. Depending on its fabrication it finds applications in multiple fields from fibres for clothing, to containers for liquids and foods, and in combination with glass fibre even in the production of engineering resins. With the advent of 3D printing thin films of polymers such as PET have grown in interest for

their application as printing substrate due to their optical, thermal and mechanical properties. Their optical transparency, flexibility and low cost being highly appreciated in the production of electrical components at the price of their poor insulations capability [157, 158, 159].

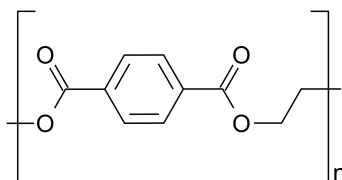


FIGURE 3.5: Chemical structure of polyethylene terephthalate ( $[\text{C}_{10}\text{H}_8\text{O}_4]_n$ ).

For the sake of this project was selected a thin film of flexible PET (Plastics ltd Hereford, Type 6, 200  $\mu\text{m}$  thickness). At the base of this choice was the desire for a inert material that could prevent sample contamination while at the same time allowing for heat diffusion from the printing plate. For the work here described the maximum working temperature was kept lower than 45  $^{\circ}\text{C}$ , below the 130  $^{\circ}\text{C}$  maximum recommended working temperature for the PET film. In addition, the use of PET films provided a smooth top surface reducing geometrical artefacts on the finished product and facilitating the removal step. The solid dosage form was popped off the film without causing any damage by gently flexing the substrate. Additionally, the film flexibility guarantees adhesion to the printing plate thanks to the vacuum action generated by the latter, and as a result producing a flat surface for the print.

## 3.2 Methods

### 3.2.1 Statistical analysis

In order to provide statistical relevance to the results each measurement was recorded multiple times ( $N \geq 3$ ). Direct measurements are noted as *value*  $\pm$  *instrument precision*, if the latter was not provided by the manufacturer it was assumed to coincide with the smallest discernible interval on the instrument scale. Amongst these are measurements obtained from precision scale, caliper and micrometer. Whenever possible, value acquisitions were randomised to minimise bias and experimental errors. With regard to indirect measurements it is safe to assume that the errors present are systematic, linked to instrument precision and accuracy. As a result it is possible to assume a standard distribution of the recorded measurements and apply the relative statistic. In this category fall all the thermo, chemical and mechanical measurements such as melting point, degradation temperature, material density and drug loading. Assuming normal distribution of the data the average result for each set of measurements was calculated according to equation 3.1 as the weighted median value of the set and was paired with the relative standard deviation (eq. 3.2) and Student t-test calculated as per equation 3.3, was used as a method to identify confidence intervals and express compatibility between results.

$$\bar{x} = \frac{\sum_{i=1}^N \bar{x}_i / \sigma_i^2}{\sum_{i=1}^N 1 / \sigma_i^2} \xrightarrow[\text{have the same error}]{\text{if all measurements}} \bar{x} = \frac{\sum_{i=1}^N \bar{x}_i}{N} \quad (3.1)$$

$$\sigma_{\bar{x}} = \sqrt{\frac{1}{\sum_{i=1}^N 1 / \sigma_i^2}} \xrightarrow[\text{have the same error}]{\text{if all measurements}} \sigma_{\bar{x}} = \frac{\sigma}{\sqrt{N}} \quad (3.2)$$

Providing that the measurements are independent from each other, errors associated to indirect measured quantities were calculated by propagation of uncertainties using the following formula:

$$\sigma_f = \sqrt{\sum_{i=1}^N \left( \frac{\delta f}{\delta x_i} \sigma_i \right)^2} \quad (3.3)$$

Least squares regressions was deployed in the case of dependent measurements and their validity assessed using the  $R^2$  test as a correlation value.

All statistical analysis were performed using OriginPro (OriginLab Corporation) unless otherwise specified.

### 3.2.2 Ink preparation

Following what can be found in the current literature [137, 65, 160], four different drug loading concentration per excipient were explored alongside the pure base materials, namely: pure, 5% w/w, 10% w/w, 20% w/w and 30% w/w.

All materials were used as provided by the manufacturers without further purification and within their shelf life. All dry components were weighed beforehand using weighing boats and a precision balance (Kern ALS Analytical Balance).

The ink mixtures were prepared by loading the excipient into a glass vial containing a magnetic stirrer and positioned on a hot plate. The temperature was set at 100 °C and at least 10 °C higher than the material's melting point to ensure the removal of crystal memory. Particular attention was put in to ensuring that, at each step of the process, the temperature of the mixture was below the degradation point of both the excipient and the API. As the material started to melt the magnetic stirrer rotation was activated and set to 50 rpm.

The material was left to stir until it appeared completely melted to the naked eye, at which point it was left on the hot plat for an additional 10 min to ensure homogeneous melting and temperature distribution. A suitable quantity of Fenofibrate was then added to achieve the desired concentration. The compound was left to stir for 30-40 minutes allowing the drug to melt completely and form an homogeneous mixture. The resulting ink was placed aside to cool to room temperature (18 °C) in a controlled environment (desiccator). The now ready ink material was subsequently stored in a desiccator at 18 °C  $\pm$  2 °C until use. In order to provide the most faithful representation of the material behaviour during and after printing the drug-free samples used for material characterisation was subjected to a similar procedure as the mixtures. It was heated up to 100 °C while being stirred at 50 rpm till completely melted and then allowed to cool at room temperature in a desiccator.

For most of an ink's thermo, chemical and mechanical studies samples were collected by scraping the material from the vial using a nickel lab spatula and directly transferred onto sample trays or pans as required by the

specific instrument. More information about sample loading and preparation will be provided in the relative analytical technique section.

To load the ink into the printer the vial containing the preparation of interest was transferred once again onto the hotplate and heated at 90 °C until fully melted, the stirrer was kept at steady 50 rpm rate to guarantee homogeneity. The ink was then poured into the preheated assigned reservoir where was allowed to acclimatise and reach the desired printing temperature. The cooling of the material did not cause any problem during the loading phase. Indeed, the material did not have the time to solidify before being transferred. Any left over material was further scraped and placed in the reservoir. Here the material was allowed to rest long enough for it to reach a complete and stable melted state at the desired temperature.

### 3.2.3 Density studies

The bulk density of base materials was calculated by depositing a set of known volumes, namely round discs with constant diameter  $\varnothing = 10$  mm and increasing height  $h = 1, 2, 3, 4, 5$  mm. After deposition the solidified volumes dimensions were measured using a micrometer (RS PRO External Micrometer) and a caliper (RS PRO Digital Caliper) and an analytical laboratory balance (Kern ALS Analytical Balance) was used to determine their weight. The results are fitted using linear regression and the density value was obtained from the slope. The study of the material density was furthermore employed to confirm the correct loading of Fenofibrate within the ink formulations, which was done by comparing the actual solid form weight with the expected value obtained from the linear combination of the individual components' densities.

Specifically, an ink density can be estimated as follow:

$$\rho_{\text{ink}} = C_d \cdot \rho_d + C_e \cdot \rho_e, \quad (3.4)$$

where  $\rho$  indicates the density,  $C$  the concentration and the subscripts  $d$  and  $e$  refer to drug and excipient respectively. By multiplying for the volume, it was possible to estimate the total tablet weight:

$$W_{\text{exp}} = \rho_{\text{ink}} \cdot V \quad (3.5)$$

where  $V$  is the volume and  $W_{\text{exp}}$  is the resulting weight.

Compatibility between the expected value  $W_{\text{exp}}$  and the measured one  $W_{\text{meas}}$  was assessed according to section 3.2.1

### 3.2.4 Differential Scanning Calorimetry

Developed in the early 1960s, Differential scanning calorimetry (DSC) is a thermal analysis technique, used to determine the energies of phase transitions and conformational changes by measuring thermodynamic properties of thermally induced transitions [161, 162].

A DSC instrument consist of two independent small furnaces to hold a sample and reference respectively. The sample is placed in a suitable pan and sits in the DSC analysis cell on top of a platinum disc paired with a thermocouple, which allows for the sample's temperature measurement 3.6B.

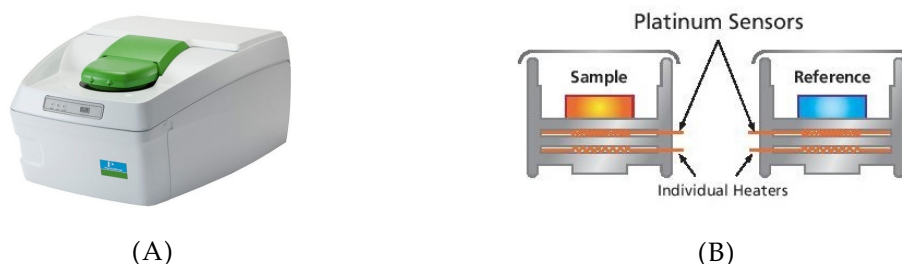


FIGURE 3.6: Differential Scanning Calorimeter system (A) Perkin Elmer DSC 8000 and (B) furnace schematics: images from Perkin Elmer's catalogue [163]

An empty reference pan is positioned in the symmetric analysis cell. The differential heat flow required to maintain both the sample and reference pans at the same temperature is measured.

A change in the heat flow can be observed when the sample undergoes a phase transition (endothermic or exothermic) as a result of the temperature discrepancy between the sample and reference arising during such event. The adjustment of the heat flow is necessary to remove the temperature difference [164, 165]

A thermogram can be obtain by plotting the heat flow variation against the temperature change. Peak in the graph will then correspond to thermal adjustment associated with sample phase transitions such as melting (endothermic) and conformational changes like crystallisation (exothermic) and glass transition.

For the purpose of this work all standard DSC measurements were carried out using a DSC 8000 (Perkin Elmer, Waltham, MA) visible in Figure 3.6A. All samples were weighted (between 5 mg and 10 mg) using a high precision

scale (Kern ALS Analytical Balance) and encapsulated in hermetically sealed aluminium pans to retain the volatile component of the sample. The reference pan was prepared using the same hermetically sealed aluminium pans (TA standard aluminium sample pans and lids). Calibration was performed automatically by the system using inside reference materials, specifically Indium ( $T_m = 156.6\text{ }^\circ\text{C}$ ,  $\Delta H_f = 28.50\text{ } \text{J g}^{-1}$ ) and Zinc ( $T_m = 419.5\text{ }^\circ\text{C}$ ,  $\Delta H_f = 108.37\text{ } \text{J g}^{-1}$ ).

Sample measurements were acquired in the  $20\text{ }^\circ\text{C}$  to  $120\text{ }^\circ\text{C}$  range at a heating rate of  $10\text{ }^\circ\text{C min}^{-1}$  in a nitrogen enriched environment at a steady flow rate of  $20\text{ mL min}^{-1}$ . The sample temperature was lowered to  $20\text{ }^\circ\text{C}$  prior to the beginning of the run, during the data acquisition the temperature was maintained constant for 1 min at the end/beginning of each ramp to guarantee sample stability.

An initial data collection was carried out to determine a baseline, in this case an empty reference pan was used in place of the sample, the spectrum was collected under the same set of conditions.

Data collection and data analysis was performed using Pyris DSC software and OriginPro respectively. The baseline was automatically subtracted by the Pyris DSC software during data acquisition, the thermograms were further normalised by the sample's weight, the instrument transient was also removed to simplify data analysis. [166]

### 3.2.5 Thermogravimetric Analysis

Thermogravimetric Analysis (TGA) is a method of thermal analysis in which sample mass loss is recorded as a function of temperature or time. The main application of TGA is to determine the characteristic decomposition patterns of a sample to obtain information about its chemical-physical transitions such as phase change, absorption, thermal decomposition, and solid-gas reactions such as oxidation and reduction. [167, 168, 169]

The TGA instrument consists of a crucible positioned on top of a precision balance inside a furnace with programmable temperature, as visible in Figure 3.7B. The sample chamber atmosphere and pressure can be tailored to the specific sample needs. These include inert gas, the most common being nitrogen, vacuum and ambient air, or reactive gas such as oxidizing/reducing, corrosive or carburising gases and "self-generated atmosphere" [167, 168, 169]. In addition pressure can be controlled to achieve high vacuum, high pressure, or constant pressure.

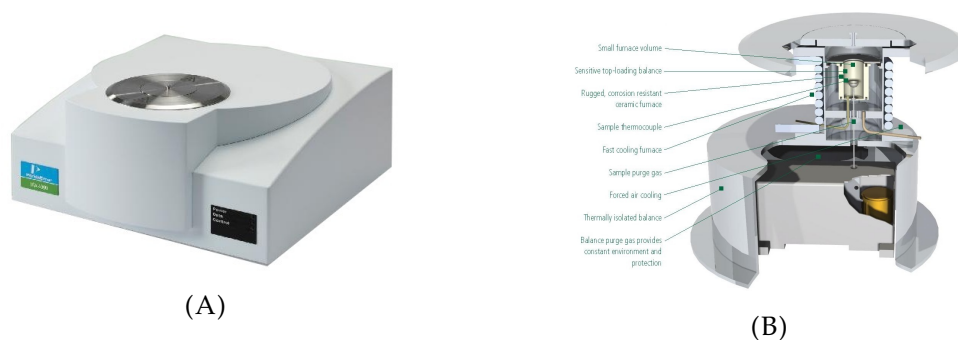


FIGURE 3.7: Thermogravimetric Analyzer system (A) Perkin Elmer TGA 4000 and (B) furnace schematics: images from Perkin Elmer's catalogue [163]

Most thermogravimetric analysers can be operated in three different modes: static, quasi-static and dynamic. In static (also isothermal) thermogravimetry the temperature is kept constant and the sample weight is recorded as a function of time. Quasi-static thermogravimetry get its name from its sequential nature, in this case temperature is risen progressively via a series of isothermal plateaus at increasingly higher temperatures. Each plateau is maintained till sample mass stabilisation. Lastly for the dynamic thermogravimetry the sample temperature is linearly increased at a steady rate.

For this work a Thermogravimetric Analyser (TGA 4000, Perkin Elmer, USA) as shown in Figure 3.7A was used in ambient air. Samples of approximately 7 mg to 10 mg were loaded onto the crucible and tested at a heating rate of  $40\text{ }^{\circ}\text{C min}^{-1}$  in the  $30\text{ }^{\circ}\text{C}$  to  $700\text{ }^{\circ}\text{C}$  temperature range. The maximum temperature at which the materials are subjected during printing and preparation is  $100\text{ }^{\circ}\text{C}$  much lower then the range here considered, however testing at such high temperature allows to better understand the degradation patterns of both the pure API and the mixed inks, which in turn affects their chemical and mechanical stability.

The original TGA curve have been plotted alongside with their first derivative (DTG) to determine inflection points.

Data collection and data analysis was performed using Pyris software and OriginPro respectively.

### 3.2.6 Shear viscosity characterisation

A rheometer is a device used to measure flows of a fluid in response to applied forces. There are two distinct types of rheometers, the rotational or shear rheometers that control the applied shear stress or shear strain and the extensional rheometers that apply extensional stress or extensional strain.

From the knowledge acquired in Chapter 2 of the basic working principle of an inkjet printer, it is understood that material viscosity plays an essential role in drop formation and ejection. During the printing procedure the ink material is pushed through a series of internal tubing and ultimately through the micrometric nozzle, the material experience growth in shear rate as the pipes diminish in diameter up to the point of ejection. Here, given the size of the conduct and the ejection velocity, the shear rate can reach values up to  $10^5 - 10^7 \text{s}^{-1}$  [170, 171, 172].

For this project the printhead of choice was the Spectra SE-128 printheads (Fujifilm, Japan), which is a piezoelectric unit designed for deposition of low viscosity materials in the 8 cP to 20 cP range. Recalling the information from Table 2.2 which states that for the printhead in consideration the nozzle diameter is  $35 \mu\text{m}$  and drop size is  $30 \text{pL} \pm 4\%$  and combining it with the average printing impulse of  $8 \mu\text{s}$  it is possible to calculate the shear rate to which the material is subjected in the moment of ejection.

$$\dot{\gamma} = \frac{4V}{\pi R^3 t} \sim 10^7 \text{s}^{-1} \quad (3.6)$$

As a result, the candidate material for jetting needs to display stable viscosity in the 8 cP to 20 cP range at high shear rates up to  $10^7 \text{s}^{-1}$ .

It is clear that given the intent of this work the rotary rheometer was preferred, on the downside, traditional rotary rheometer has a maximum shear rate range of  $10^3 \text{s}^{-1}$  which is 2 to 4 orders smaller than the maximum experienced by the material in our system. In case of Newtonian fluids this does not represent an issue, indeed for these materials the viscosity is independent from the shear rate meaning that it is safe to extrapolate from the medium share rates to the higher limit. In the case of non-Newtonian fluids though, it is not as simple, materials belonging to this category present a high dependence from the shear rate that causes the insurgence of shear-thinning or shear-thickening behaviour based on the nature of the specific material in consideration. Regardless, for high enough values of shear rate all materials are expected to reach a Newtonian plateau where the material viscosity stops being dependent on the shear rate and the materials assumes a Newtonian behaviour [173, 174]. As a result, if the material of interest shows enough evidence to have reached the plateau it can then be considered to behave as a Newtonian fluid at higher shear rates and it is justified to extrapolate from medium shear rates to the upper range. Noticeably, while in the Newtonian plateau range the viscosity value becomes independent from shear rate and

time it is still susceptible to temperatures and pressures variation. With regard to the latter a pressure in the order of MPa is required [173, 174] to cause a significant effect on the fluid behaviour, in an inkjet printing system, such values are never reached and thus, with the assumption of fluid incompressibility, it is reasonable to assume that it is not a parameter that has to be taken into consideration in this study. However, temperature plays a key role in our system and as such it is fundamental to explore its effect on the potential inkjet material taken into consideration for this project.

Rotational rheometers can operate in two different modes: controlled shear rate or controlled shear stress. The first is used to emulate applications that are flow velocity or volume flow rate dependent, the second is used to simulate system where torque or shear stress are the main driving forces. It is possible to convert the torque into shear stress and velocity into shear rate using simple conversion factors. For the sake of this work a shear rate guided approach was selected.

For a standard rotational rheometer, a typical set-up includes a base (called cup) which holds the sample and a matching measuring component (called bob) placed in such a way that the sample results sandwiched between the two.

Depending on which part is made to rotate the system works under the Searle or Couette principle. In the former case, the cup is fixed and the bob is rotated, in the latter, the roles are reversed and the cup rotates while the bob is kept at rest. An extensive quantity of different measuring cups and bobs are available on the market to serve the various types of materials. For Searle systems, the most common are coaxial cylinders, parallel plates, and cone-plate geometries.

A cone and plate geometry guarantees a constant shear rate throughout the sample providing a significant advantage allowing for the measurement of absolute viscosity values, as such it was chosen for this set of experiments. Given the geometry visible in Figure 3.8 A the shear rate can be calculated as follow:

$$\dot{\gamma} = \frac{v}{h} \xrightarrow{\alpha \ll 4^\circ} \dot{\gamma} = \frac{r\omega}{r\alpha} = \frac{\omega}{\alpha} \quad (3.7)$$

where  $r$  is the distance from the centre,  $\omega$  is the rotation rate,  $\alpha$  is the angle between the cone and plate in radian [175] Moreover, the relationship between shear rate and torque can be written as:

$$\sigma = \frac{3T}{2\pi a^3} \quad (3.8)$$

Where  $\sigma$  is the shear stress,  $T$  is the torque and  $a = 2R$  is the diameter of the cone.

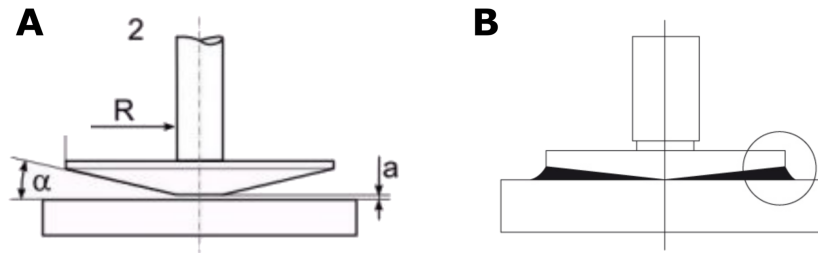


FIGURE 3.8: (A) Cone-plate geometry used for rotational rheometer with truncated cone, radius  $R$ , cone angle  $\alpha$  and gap  $a$ . (B) Sample loading on cone-plate system after gap setting [174].

The cone structure is usually placed on top to allow the fluid to rest on a flat surface. To reduce wear and to help in the zeroing process the tip of the cone is truncated, this does not cause any change in the practical functionality of the system but allows to work with fluids containing small suspended particles provided that they are smaller than 0.2 times the gap between cone and plate. The usual gap range is between  $50\ \mu\text{m}$  to  $210\ \mu\text{m}$ . A small gap is indeed necessary to minimise fluid instabilities and specifically the generation of secondary flows and radial sample migration. Based on Newtonian behaviour it is possible to define a critical rotational speed ( $\omega_c$ ) for secondary flow establishment.

$$\omega_c = \frac{10\eta}{\rho\alpha^2 a^2} \quad (3.9)$$

where  $\eta$  is the viscosity,  $\rho$  is the density. Given that  $h = \alpha r$  for small angles it is clear that smaller gaps correspond to more stable results. Similarly for the case of radial sample migration it is possible to identify an expression for the critical value of the shear rate ( $\dot{\gamma}_c$ ) dependent on surface tension ( $\sigma$ ).

$$\dot{\gamma}_c = \frac{\omega_c r}{a} = \sqrt{\frac{20\sigma}{3\rho a^3}} \quad (3.10)$$

Again, it is clear that more stable results correspond to smaller gaps.

To carry out the analysis of the candidate material for 3D printing a Kinexus Pro (Malvern Instruments Ltd., UK, visible in Figure 3.9) was employed. The system was equipped with a cone-plate geometry ( $\theta = 4^\circ$ ), a gap of  $200\ \mu\text{m}$ , and a heated plate. A heat trap was used in conjunction with the

cone-and-plate geometry to reduce the environmental contribution, to avoid sample contamination, and to minimise temperature gradient, creating a stable environment inside the chamber around the spinning disc.



FIGURE 3.9: Kinexus Pro Rheometer: images from Malvern's catalogue [176]

Each sample was carefully loaded onto the pre-heated cup base material, where it was allowed to reach temperature and melt before the bob was lowered to the 200  $\mu\text{m}$  gap. Any excess fluid was then cleaned up to reach the optimal loading spreading, see Figure 3.8 B. The heat hood was then closed and the sample was brought to the starting experimental temperature. Each sample was tested over a range of six different temperatures from 75  $^{\circ}\text{C}$  to 95  $^{\circ}\text{C}$  every 5  $^{\circ}\text{C}$ , variations within this range was based on samples melting points, the machine range of operation and consistency between materials. Each measurement was performed in shear rate range of  $1\text{ s}^{-1}$  to  $10^3\text{ s}^{-1}$ , at a stable temperature with variation equal to  $\pm 0.01\text{ }^{\circ}\text{C}$ . Every point was captured under steady-state conditions where a value was accepted with a 5% tolerance for 10s.

To correctly understand and interpret the obtained results it was necessary to determine a suitable model for data interpretation.

Fluid behaviour can be classified on the base of their response to variation of shear rate. If the viscosity remains constant across all values then the fluid has known as Newtonian, otherwise as non-Newtonian [173].

Figure 3.10 shows a general overview the most common rheological behaviour. Of particular interest is to notice that materials undergoing shear thinning are the most common, as the shear rate increases a reduction in viscosity is visible due to the molecules aligning with the flow of the fluid. In contrast, fluids showing a shear-thickening trend as the shear rate increases experience the formation of aggregate breaking the pre established flow. It is

not uncommon for material in this category to show an initial shear-thinning behaviour followed by a shear-thickening one.

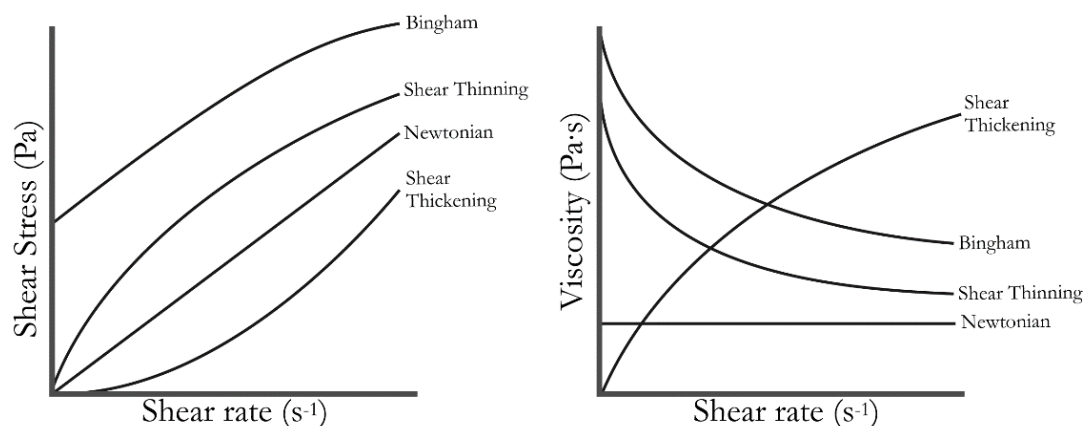


FIGURE 3.10: Rheological behaviour of Newtonian and non-Newtonian fluids as viscosity (left) and shear stress (right) when exposed to a wide range of shear rates. [177]

Lipids are known to behave as rigid solids until the shear stress exceeds the yield value when they start to behave like a viscous liquid [177]. Since viscosity can be seen as the interaction between the components of the fluid when subjected to a stress, this low temperature plasticity can be explained by the polymorphism of the lipid network and the complex molecular packing in the crystals [178, 179]. Then, once a breaking point is reached, the original arrangement is disrupted causing variations in the internal interactions and with the molecules now able to move and align with the flow. Fluid showcasing a Newtonian behaviour after the applied stress surpasses its apparent yield stress are described as Bingham plastic [177].

Pseudoplastics are especially useful in applications such as 3D printing, where a fluid coming from a reservoir has to be extruded or ejected through a smaller pipe. The lower viscosity at higher shear rates, allows for the use of lower pressures during the printing process while the higher viscosity at low shear rates favours droplet stability after deposition.

Over the decades multiple mathematical models have been developed to fit non-Newtonian flow curves.

The most general description of time-independent shear-thinning fluids is the Cross model [180]:

$$\frac{\eta_0 - \eta}{\eta - \eta_\infty} = (K' \dot{\gamma})^m \quad (3.11)$$

Where  $K'$  and  $m$  are constants,  $\eta_0$  the asymptotic values of the viscosity at very low shear rates and  $\eta_\infty$  at very high ones.

However, this is a model approach that finds application only in the theory since practical measurements impose limitations on  $\eta_0$  and  $\eta_\infty$ . For a practical application it is safe to assume  $\eta \ll \eta_0$  and  $\eta \gg \eta_\infty$ . After parameter redefinition the result is the Herschel–Bulkley model:

$$\eta = \frac{\eta_0}{(K'\dot{\gamma})^m} = K\dot{\gamma}^{n-1} \quad (3.12)$$

where  $K \propto \eta_\infty$  is the new constant and  $n$  the power-law index. Interestingly, when  $n = 0$  the equation is reduced to the Bingham model [173].

On this basis, for the present section the Herschel–Bulkley and Cross model have been employed as necessary to best fit the specific material flow profile. Particular attention was used to ensure that the model of choice was offering the best fitting in the region of higher shear rates which best approximates the range of interest for the printing process. To ensure this the minimum  $\chi^2$  method was employed. As seen at the beginning of this section, in order to be printable a material needs to display stable viscosity in the 8 cP to 20 cP range at high shear rates up to  $10^7 \text{s}^{-1}$ , however the Kinexus Pro Rheometer can only reach shear rates up to  $10^3 \text{s}^{-1}$ . As such, data fitting and behavioural analysis play a key role in estimating the viscosity values at high shear rates. In particular, when working with Bingham plastic, by showing that the material has reached a Newtonian state within the range analysed it is correct to assume that such value will remain constant regardless of the increasing shear rate and can thus be use as an indicator for ensuring the material printability. All results were analysed using OriginPro.

### 3.2.7 Scanning electron microscopy and Energy Dispersive X-ray Spectroscopy

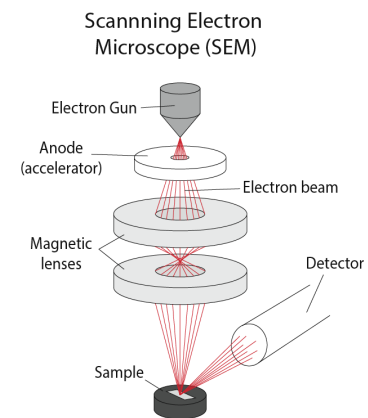
Scanning electron microscopy (SEM) is a technique used to produce extremely high definition images (resolution greater than 1 nm) by rastering the sample surface using a focused electron beam [181, 182].

The primary electron beam is produced by thermo-ionic emission from an electron gun fitted with a tungsten filament cathode and collimated thanks to a series of magnetic lenses as seen in Figure 3.11 B. When the primary electrons interact with atoms within the sample, the following set of effects is produced: secondary electron emission and back-scattering, X-ray emission, Bremsstrahlung, IR, visible e UV radiation due to cathodoluminescence, Auger electron emission and electrons scattering, transmission or absorption. The capability to use a collector-scintillator-photomultiplier system to detect

the low-energy (<50 eV) secondary electrons is at the base of the most commonly used SEM mode [181, 182]. The latter are produced as consequence of inelastic scattering interaction of the sample with the primary beam and the subsequent emission of electron from the sample's conduction or valence bands. By collecting such electrons it is possible to obtain a two-dimensional intensity distribution across the sample's scanned surface. Besides due to the specific geometry of the system steep surfaces and edges tend to be brighter than flat surfaces, which results in images with a well-defined, three-dimensional appearance. SEM microscope can work in a variety of conditions however, the most commons are in high vacuum, low vacuum or wet conditions in variable pressure or environmental SEM, more specialised instrument can also work at a wide range of cryogenic or elevated temperatures depending on the necessity of the specific sample.



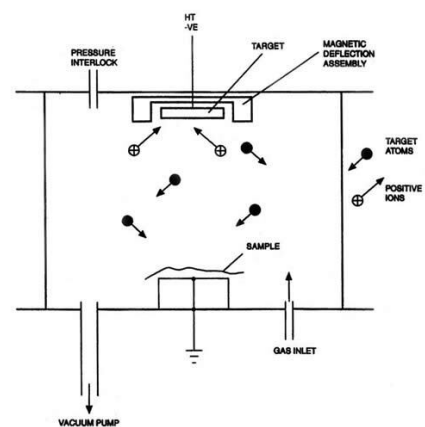
(A)



(B)



(C)



(D)

FIGURE 3.11: (A) Scanning electron microscope: Hitachi TM3030 equipped with Debem Sprite stage controller and (B) its schematic diagram [183]. (C) Sputter coater: 108 Manual Sputter Coater, Ted Pella, ink. alongside with (D) its schematic diagram [184].

SEM is commonly paired with an Energy Dispersive X-Ray Analyzer (EDX) which is used to provide elemental identification and quantitative compositional information about the sample. In this case the effect exploited for the material characterisation is the production of X-rays. Due to their electromagnetic nature they obey the Lambert-Beer law producing a unique set of peaks in the emission spectrum [185].

A key aspect of successful imaging is for the sample to be electrically conductive, at least at the surface, and grounded to prevent the accumulation of electrostatic charge. Samples that are non-conducting have thus to be coated with an ultra-thin layer of electrically conducting material, deposited on the sample either by low-vacuum sputter coating or by high-vacuum evaporation.

As visible in Figure 3.11 D a sputter coater consists of a cathode tube filled with inert gas. When a current is applied ionization occurs by collision of electrons with gas atoms causing what is commonly known as Townsend discharge [186]. When a current is applied and the voltage across the tube exceeds the breakdown potential, a self-sustaining glow discharge occurs. In such conditions the ion bombardment of the cathode material causes its erosion and consequent deposition of the sputtered atoms on the surface of the anode surface and work chamber. In the case of a sputter coater gold is usually utilised as a cathode sputter material while the sample is mounted in such a way to work as an anode. This process allows for a ultra-thin and uniform gold coating of the sample surface.

For this project images were obtained using a variable pressure scanning electron microscope (Hitachi TM3030, Fig. 3.11 A) equipped with a multi axis stage controller (Debem Sprite) in a high vacuum at an accelerated voltage ranging between 10 kV and 20 kV depending on the specific sample.

Each sample was prepared by breaking the initial tablet into small pieces. The sections were then mounted onto an aluminium stubs (Agar Scientific, UK) lined with carbon discs (Agar Scientific). Particular attention was paid in order to arrange the sample such that the surface of interest would be presented to the beam. The samples were then transferred into the Sputter Coater (108 Manual Sputter Coater, Ted Pella, ink.) visible in Fig. 3.11 C. Ambient air was removed from the main chamber and substituted with Argon gas the pressure was then reduced to 0.06 mbar and coated with gold for 90 sec with a current of 26 mA to 29 mA.

### 3.2.8 Attenuated Total Reflection-Fourier Transform Infrared Spectroscopy

Fourier Transform Infrared Spectroscopy (FTIR) is a third generation IR spectrometer, which allows measurement of all infrared frequencies simultaneously via the use of an interferometer as visible in Figure 3.12 A. This technique is used to identify or quantify a material composition by measuring its IR absorption spectrum since every molecule exhibit a specific IR fingerprints that can be identify as a signature pattern in the spectrum [187, 188]. By pairing it with a Attenuated total reflection (ATR) crystal it is possible to examine solid or liquid state samples directly, without the need for further preparation. As shown in Figure 3.12 B a beam of infrared light is shined through the ATR crystal, by exploiting the total internal reflection property of the crystal it is possible to produce an evanescent wave which reflects least once off the internal surface in contact with the sample. This reflection forms the evanescent wave which extends into the sample. The beam is then collected by a detector as it exits the crystal [189]. The number of reflections and penetration depth are dependent on sample opacity, angle of incidence and wavelength of light.

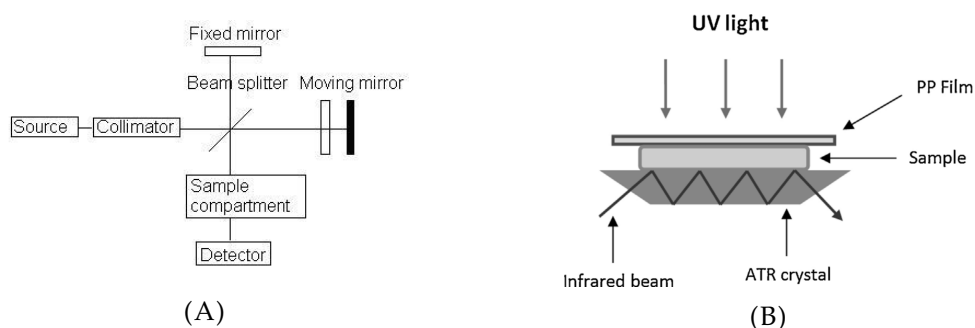


FIGURE 3.12: Block diagram of an Fourier Transform Infrared Spectroscopy (FTIR) A) spectrometer [190] and B) ATR [191].

FTIR spectroscopy was here used to verify the content of drug inside the ink materials before printing, in the printed solid dosage forms and in the remains after dissolution. All spectra were obtained using a FTIR Routine Spectrometers Alpha (Bruker), Figure 3.13 equipped with an ATR crystal. Each sample was loaded individually onto the analysis plate ensuring to centre it with respect to the crystal. The press was then lowered allowing the sample material to come in contact with the crystal and tightened in order to maximise the sample-crystal contact surface. Spectra were collected over the range  $4000\text{ cm}^{-1}$  to  $700\text{ cm}^{-1}$ .

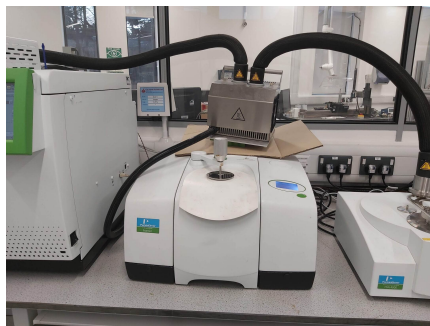


FIGURE 3.13: Fourier Transform Infrared Spectrometer: Perkin Elmer FT-IR Spectrometer Frontier [163]

In this range Fenofibrate presents two characteristic set of peaks associated respectively to the carbon rings and to the Chlorine bond. The C-C stretch (in ring) is characterised by two distinct peaks at  $1600\text{ cm}^{-1}$  to  $1650\text{ cm}^{-1}$  while the  $720\text{ cm}^{-1}$  to  $765\text{ cm}^{-1}$  peaks are associated with the C-Cl stretch [192, 193]. The  $765\text{ cm}^{-1}$  C-Cl stretch peak was selected as a marker to identify the presence of Fenofibrate due to the fact that it present only inside of the drug molecule and cannot be found in any of the matrix materials.

### 3.2.9 Raman Spectroscopy

Raman spectroscopy is a light scattering technique that dates back to 1928 and Professor C.V Raman. Based on Raman scattering, inelastic scattering of photons see Figure 3.14 D, it is an extremely information rich spectroscopic technique, useful for chemical identification, characterization of molecular structures, effects of bonding, environment and stress on a sample [172, 194, 195].

To induce the Raman shift in the sample molecule, it is illuminated with a laser beam, the most commonly used are in the visible, near infrared, or near ultraviolet spectra however X-ray wavelengths may also be deployed [172].

As shown in Figure 3.14 C the electromagnetic radiation from the illuminated spot is then filtered through a monochromator and a frequency filter, either a notch filter, edge pass filter, or a band pass filter to exclude the laser back scattering lines (intense Rayleigh scattered laser light). The light coming from the dispersive single-stage spectrographs is then collected in a detector, CCD being the most common although Fourier transform (FT) spectrometers also find application for use with NIR lasers.

While the most commonly used type of Raman spectroscopy is vibrational Raman many other variations exist including surface-enhanced, resonance, tip-enhanced Raman, polarized, stimulated, transmission, spatially-offset and hyper Raman.

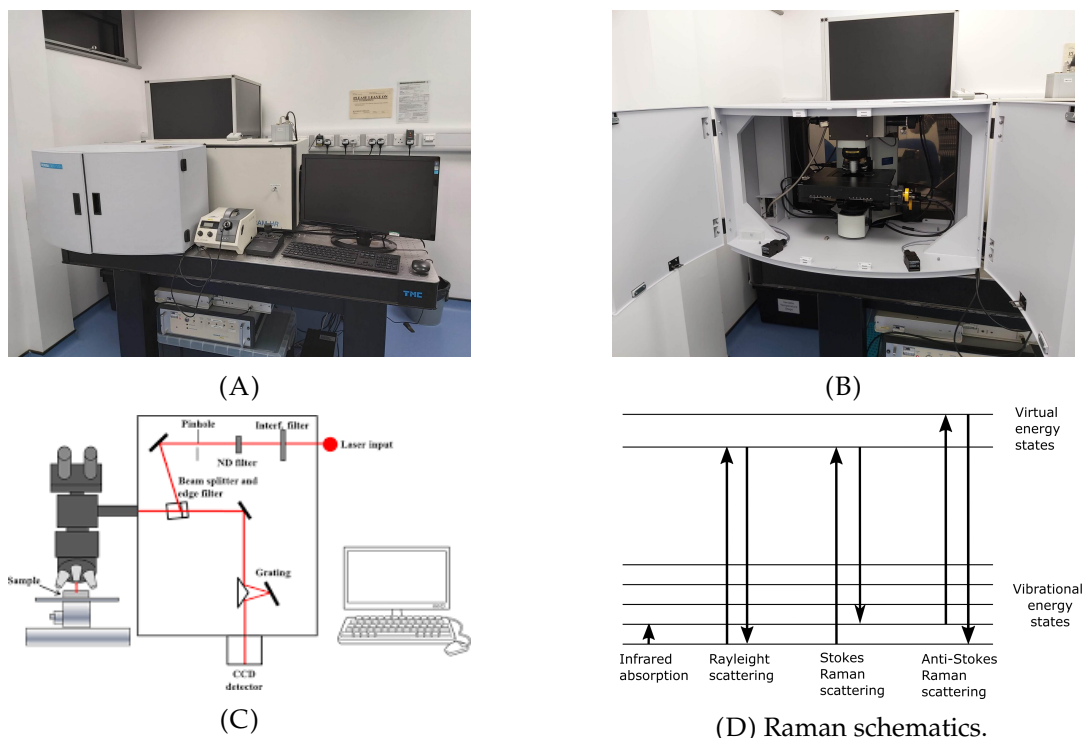


FIGURE 3.14: Raman system: HORIBA Jobin Yvon LabRAM HR spectrometer (A,B). Block schematics of Raman instrument [196] (C), Raman shift (D).

A HORIBA Jobin Yvon LabRAM HR spectrometer (Fig. 3.14 A) was used to perform the Raman analysis of our raw ink materials and printed parts. The spectrometer comes equipped with an automated Märzhäuser xyz stage that can be controlled manually or via an external joystick (Fig. 3.14 B) and a KL 2500 LCD(SCHOTT) as a light source to navigate the sample surface and to help with the focusing process. The system is controlled via a computer and a dedicated software: LabSpec6.

The samples were loaded one at the time, and the laser beam focused on the surface with the aid of a microscope. The light intensity and colour temperature was then adjusted for each sample in order to maximise contrast and ease of focus.

All spectra were collected using a 785 nm laser at 25 mW power, a  $50\times$  objective, a  $300\ \mu\text{m}$  confocal pinhole and a 300 lines/mm diffraction grating. For spectra acquisition a SYNAPSE CCD detector (1024 pixels) was adopted

and thermoelectrically cooled to  $-60^{\circ}\text{C}$ . A silicon sample (Si 100) with reference band at  $520.7\text{ cm}^{-1}$  was used as a standard to calibrate the instrument before spectral acquisition. Single spectra acquisition was performed in the range between  $100\text{ cm}^{-1}$  and  $3300\text{ cm}^{-1}$ . Data were collected for 5 seconds and 16 accumulations per spectral window. Mapping was carried out with the same acquisition conditions across a  $80\text{ }\mu\text{m}$  line at  $10\text{ }\mu\text{m}$  intervals for a total of 9 spectra. The line was located such that the zero of the x-axis fell on the interface line separating the core and shell region. During the measurements, samples were kept at room temperature ( $20^{\circ}\text{C}$ ) and in ambient air.

Raman spectroscopy was used to determine the API content and distribution inside the ink material before printing and in the printed solid dosage forms. Of particular interest was the capability of the spectrometer to acquire sequential spectra along the x or y direction. This allowed us to study the distribution of the API at the interface core/shell in the multi material tablets. As for the FTIR technique we decided to use the unique peaks linked to the C-Cl bond ( $1.580\text{-}1610\text{ cm}^{-1}$ ) as a marker to identify the presence of Fenofibrate. All spectra were analysed and all peaks were identified and compared with the theoretical ones. The spectra were then normalised and the marked peaks were compared. All data was analysed using OriginPro.

### 3.2.10 X-ray Powder diffraction

X-ray diffraction spectrometry (XRD) is based on the capabilities of crystalline substances to act as three-dimensional diffraction gratings for X-ray wavelengths. As a result, XRD is a common technique used for the study of crystal structures and atomic spacing [197, 198, 199]. In Figure 3.15 B is visible how the X-rays are generated in a cathode ray tube and forced to go through a monochromator and a collimator before reaching the sample surface. A CCD detector is used to collect the diffracted ray. Which is the result of constructive interference of the incident X-rays with crystalline sample following Bragg's Law ( $n\lambda = 2d \cdot \sin\theta$ ). All sample's lattice diffraction directions are scanned by rastering the sample through a range of  $2\theta$  angles. Each substance bares a unique set of diffraction peaks and relative d-spacing (distance between atomic planes characterised which yields a diffraction peaks) allowing its identification via XRD analysis.

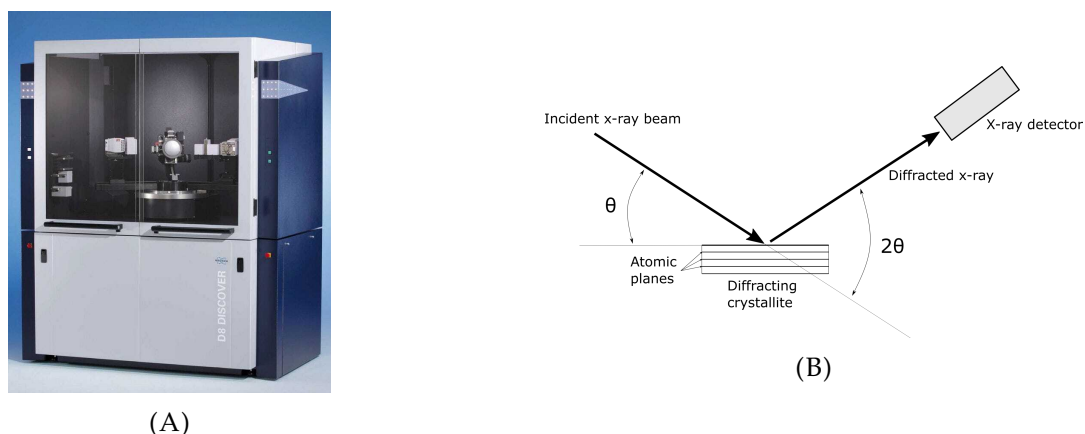


FIGURE 3.15: XRPD D8 Advance DaVinci (Bruker) spectrometer (A) and block schematics(B).

For this work XRD analysis was performed using an XRD D8 Advance DaVinci (Bruker Fig. 3.15 A) using  $\text{Cu K}\alpha$  radiation (40 kV and 40 mA) and an Ni filter with a scanning speed of  $0.02^\circ 2\theta\text{s}^{-1}$  with the divergence slit set to  $0.3^\circ$ . The anti-scatter slit was set at 5.2 mm, which is fully open, as required for fast scanning with the detector in 1D mode. Spectra were collected at room temperature and in the 3 to  $70 2\theta$  range.

Samples were prepared by crushing the printed tables utilising a mortar and pestle into a fine powder, which was then transferred into a shallow PMMA sample holder (8.5 mm height and  $\varnothing = 25$  mm, from Bruker). Once loaded the sample was pressed and the top surface smoothed using a glass slide, sample was added until a perfectly smooth surface was achieved. Any loose material present on the rim of the disc holder was removed using a Isopropanol imbued tissue.

### 3.2.11 Advanced Drop Analysis

Advanced Drop Analysis (ADA) is a native analytical function of the Pixdro LP50 (Meyer Burger, Netherlands) and it is used to analyse material jettablity and optimisation of the printing conditions.

In Figure 3.16 a schematic of the system is presented and its key components, namely the camera shutter, jetting head and LED are highlighted.

As the name suggests ADA main goal is to allow fast and efficient optimization of jetting performance for specific inks and printheads in order to achieve best printing results.

ADA makes use of the integrated high-speed CCD camera to analyse drop formation, while varying the jetting settings, such as wave form time

and intensity, frequency and pressure, while recording their effect on the drop formation and jettability [200]. Thanks to the printing unit motors it is possible to access any of the printhead nozzles individually or in sequence, making ADA an invaluable instrument not only for printing optimisation, but also for routine maintenance of the printhead ensuring top performance during printing.

In this work ADA was exploited for both purposes. It was initially used to determine printability and droplet formation optimisation of the ink compounds, firstly the working temperature was set on the base of the properties of the individual material. The pressure within the system was then made to vary  $-30$  mbar to  $0$  mbar until a stable meniscus was formed at the air/ink interface at the nozzle, which prevents nozzle plate flooding during idle times. The remaining parameter optimisation was performed by cycling over all parameters possibilities within the range selected and ensuring a velocity of  $4 \text{ m s}^{-1}$  to  $8 \text{ m s}^{-1}$  [80]. Specifically:

- rise time:  $1 \mu\text{s}$  to  $5 \mu\text{s}$ ,
- fall time:  $1 \mu\text{s}$  to  $5 \mu\text{s}$ ,
- peak time:  $3 \mu\text{s}$  to  $7 \mu\text{s}$ ,
- voltage:  $90 \text{ V}$  to  $110 \text{ V}$ .

Each test was performed on a nozzle in the middle of the printhead to avoid extremity bias. The validity of the final set of parameters was then checked through the entire printhead to confirm its applicability to the entire printing unit. Through our experience we noticed that the first and last 5 nozzle of each printing head are never performing as well as the rest, and were then systematically removed from the analysis pool.

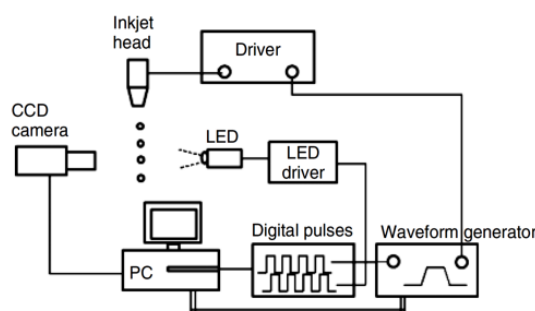


FIGURE 3.16: Advanced Drop Analysis (ADA) schematics, including CCD camera, printhead and LED. Figure from "Vision monitoring" [200].

### 3.2.12 Hot-melt inkjet 3D printing

The printing process of hot-melt inkjet printing has been already discussed in detail in the previous two chapters 2 and 1, here I briefly present the ink loading and printer set up used during printing. Firstly, the printer is calibrated, checking that all motors are moving correctly and that the printhead and substrate are correctly aligned. Then the temperature of the printing unit is set to 90 °C and the substrate to 40 °C. While the printer is left to reach temperature (approximately 30 min) the ink mixtures are selected and placed to melt on a hotplate at 90 °C and 50rpm. When the inks are completely melted and the machine has reached a stable temperature the inks are transferred into the reservoirs where are left to acclimate for a minimum of 15 min to ensure a stable temperature through both system and material. The material is then flushed through the pipe to eliminate air from the tubing and ensuring their complete wetting. Once the correct recipe and printing conditions are selected on the base of the specific material, a printhead maintenance run is performed, as described in the previous Section 3.2.11, to identify and remove any potentially problematic nozzle from the printing set. Once the set of nozzles have been selected and the printing parameter entered, the last step included loading of the design to be printed, placing the substrate onto the platform plate and selecting the starting point for the print, the input value will correspond to the bottom left corner of the bitmap design. Last thing to do is to press start and wait. Once the print was finished it was allowed to remain on the printing bed at the bed printing temperature for an additional 30 min and then removed alongside with the substrate and placed in a dessicator at 4 °C where it remained for a minimum of 4 h. The samples were then simply removed from the substrate by bending the latter and allowing the samples to detach. The printlets were stored in a glass petri dish and in a dessicator at 4 °C until needed. All samples were used as close the production time as possible and always within a week from printing to avoid changes in the drug crystallinity and maintain consistency between results.

### 3.2.13 *In vitro* drug release

*In vitro* dissolution testing is a standard method for measuring the rate of drug release from a given oral dosage form. It is an essential requirement throughout the product development cycle for drug release optimisation and stability testing. The testing conditions are tailored to the specific dosage form, the time in the product development cycle, and the intended route of

administration [201, 202]. A dissolution test usually includes a vessel kept at constant temperature, either by partially immersing it in a water bath or by using a jacket and a stirring element necessary to maintain the concentration of the active ingredient uniform throughout the buffer contained in the vessel. A single solid dosage is placed in each vessel. The industry standard to investigate solid dosage forms are the United States Pharmacopoeia (USP) apparatuses: baskets (UPS 1), paddle (UPS 2), reciprocating cylinders (UPS 3), flow-through-cell (UPS 4), paddle-over-disc (UPS 5), cylinder (UPS 6) and reciprocating holders (UPS 7) [203]. USP Apparatus 2 (paddle) is the most commonly used for immediate, modified, and extended release however the use of a sinker or a USP 1 (baskets) might be required if the solid forms are prone to float. Known volumes of buffer sample are collected at predetermined time intervals and replaced with an equivalent amount of fresh buffer. The samples were then analysed via UV-Vis spectroscopy or High-performance liquid chromatography (HPLC) to determine the content of drug in each sample.

The dissolution test machine used in this work is the Copley Dissolution Test Dis8000 visible in Fig. 3.17, this consists of a temperature regulated water bath with enough space for eight one litre round bottom glass vessels surmounted by a control unit and motor system.



FIGURE 3.17: Copley scientific Dissolution Test Dis8000, image from Copley scientific's catalogue [204]

Each vessel is paired with a stirring rod equipped with a type 2 UPS paddle. Before each dissolution session the paddle height was checked using a calibration ball ensuring uniformity between vessels. The rods are then lifted and each vessel filled with 500 mL of buffer solution consisting of 0.1 M phosphate with 0.05 M sodium lauryl sulphate at PH7.4. The choice of buffer was

based on the literature review to maximise wettability [137, 152, 205]. When the desired temperature is reached the samples are loaded into a helix wire sinker to prevent the sample from floating and positioned at the bottom of the vessels. The paddles are then quickly lowered and the measurement timer started. Over the entire duration of the test the paddles are kept in motion at a constant speed of 50 rpm. Even sample volumes (5 mL) of buffer solution is withdrawn from each vessel at regular intervals and filtered via 0.45  $\mu\text{m}$  MF-millipore membrane filter (MILLEX HA). An equivalent amount of fresh buffer kept at the same temperature is reintroduced. The amount of drug released into the medium as a function of time is obtained by analysing the collected samples using UV-visible spectrophotometry. All dissolution tests were done in triplicates.

These conditions were used consistently throughout the entirety of this work, however an exception was made for the pulsatile release tablet. The changes have been introduced to ensure separation of the two burst release peaks. In this case the samples were collected every 15 min for the entire duration of the experiment and the buffer solution was completely removed and substituted with a fresh one after every sampling session. This again was performed in triplicate.

Test conditions are summarised in Table 3.1.

TABLE 3.1: Dissolution test conditions. Where all values are expressed in terms of mean value  $\pm$  standard error over five measurements.

<b>Buffer</b>	
Composition	0.1 M phosphate buffer with 0.05 M sodium lauryl sulphate
pH	7.40 $\pm$ 0.02
Temperature	37 $\pm$ 0.2 $^{\circ}\text{C}$
Volume	500 mL
<b>Sample collection</b>	
Volume	5 mL
Filter	0.45 $\mu\text{m}$ MF-Millipore membrane filter (MILLEX $\text{\textcircled{R}}$ HA)
Total collection time	10 h
Collection intervals or	5, 15, 35, 70, 120, 240, 360, 480, 600 min every 15 min

### 3.2.14 UV-Visible spectrophotometry

UV-Visible spectrophotometry is a technique based on the ability of molecules (containing  $\pi$ -electrons or non-bonding electrons) to absorb photons. It takes into consideration the interaction of molecular species with radiation in the ultra violet (200-400 nm) and visible (400-800 nm) regions of the light spectrum, hence the name of the technique. Figure 3.18 shows a schematic representation of a typical spectrometer [206, 207].

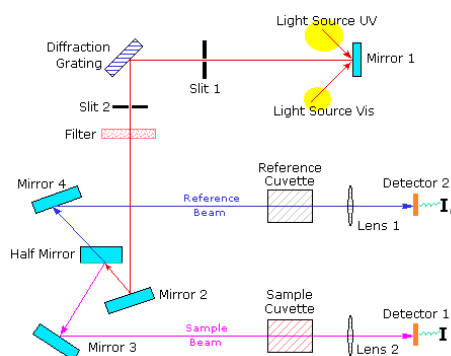


FIGURE 3.18: Schematics of UV-Visible spectrophotometer [208].

A beam of light from a visible and/or UV light source is separated into its component wavelengths by a prism or diffraction grating. The beam then passes through a cuvette or well (small transparent container) and the intensity of the outgoing beam is collected by electronic detectors (photodiodes). The spectrometer automatically scans all the component wavelengths. In order to obtain a sensible measurement it is necessary to firstly collect a ground spectrum of the solvent alone, afterwards it is possible to substitute the material in the cuvette with the sample to be analysed. The intensity of the ground spectrum is referred as  $I_0$ . The intensity of the sample beam is defined as  $I$ .

Given a certain wavelength if the sample does not absorb light  $I = I_0$ , however if there is an absorption effect  $I$  comes out to be lower than  $I_0$  and it is possible to obtain an estimation of the absorption in terms of absorbance defined as  $A = \log_{10} \frac{I_0}{I}$ . The wavelength of maximum absorbance is a characteristic value relative to the specific compound, indicated as  $\lambda_{max}$ . The result is a graph of absorbance versus wavelength [206].

For further interpretation the Beer-Lambert law is used:

$$A = \log_{10} \frac{I_0}{I} = \epsilon lc \quad (3.13)$$

where  $l$  is the light path length and is a fixed parameter of the cuvette dimension,  $c$  is the concentration of the absorbing molecules and  $\epsilon$  is the molar absorptivity. The molar absorptivity is characteristic to the absorbing molecules and its a measure of how strongly a chemical species attenuates light at a given wavelength. Thus, by measuring the absorbance of a sample it is possible to determine the concentration of a compound in the solution.

For this project was used a Spark Microplate Reader (Tecan Trading AG, Switzerland) equipped with a deuterium - tungsten light source. The  $\lambda_{max} = 290$  nm peak of maximum absorbance for Fenofibrate was used as a reference in the analysis of all samples. Measurements were collected after a settling time of 50 ms and for a total of 10 flashes. All results were analysed using OriginPro.

## Chapter 4

# Carrier selection and solid dosage forms print.

An integral part of this research project was the creation of a library of suitable materials readily available for the production of 3D printed solid dosage forms for the pharmaceutical industry using hot-melt inkjet 3D printing technology. For this purpose a wide number of materials were taken into consideration, including both traditionally employed excipients and FDA approved materials that are not commonly used in the pharmaceutical field.

A thorough literature study for compatible candidates revealed that lipid materials had a range of properties that could make them attractive for 3D printing and yet are relatively little explored in this application. They comprise of fatty acids and their derivatives, including substances related biosynthetically; as such it is not uncommon to find lipidic compounds which are solid at room temperature and with a melting point below 100 °C. Additionally lipids are renowned in making excellent pharmaceutical excipients due to their being inexpensive, biodegradable and generally nontoxic. [209]

They commonly find applications in controlled release dosage forms as enhancer of the solubility and permeability of drugs with poor oral bioavailability, in the preparation of gastric floating dosage forms due to their low densities, in reducing irritation in the gastrointestinal tract, and as taste-masking agents for bitter tasting drugs. [154, 155, 96]

Lipids are also reported to be used for hot-melt extrusion/ spheronization process, showing that such materials can be successfully employed in hot-melt techniques which, as for our case, requires the complete melting of the lipids at a raised temperature and its solidification at room temperature for a much desired solvent-free extrusion/ spheronization.

Excipients for this study were selected on the basis of nominal melting point, availability, price and existing applications; this included both natural and synthetic derived waxes. The selected materials were then screened to

ensure adherence to the strict printing conditions dictated by the nature of the process and the limitations imposed by the choice of components used to build the dual material system (see Chapter 2).

Compliance of the carrier to the thermo-mechanical properties of interest is though not enough to guarantee printability and to ensure the quality of the end product in terms of surface finish, stability and handleability, particularly when drug-loaded ink materials are taken into consideration.

Thus, before attempting to produce any 3D structures, for each ink composition it is necessary to optimise the jetting conditions and the 2D deposition as well as understanding layering and solidification effects.

Following this approach, this chapter is divided into two sections. The first (Section 4.1) includes the thermal, chemical and mechanical properties of both pure materials (pure carriers and API) and the composite inks. The second section (Section 4.2) is dedicated to the 3D deposition of solid dosage forms. This was investigated in two different stages, in the first part the focus was on the study of drop formation and deposition (Section 4.2.1). In the second part (Section 4.2.2) the focus was on the 3D deposition of functional solid dosage form and the characterisation of their mechanical and chemical properties as well as the evaluation of their functionality as drug delivery systems.

For conciseness, and to not lose track of the main goal of this work, only the results for the excipients which were identified as suitable candidates based on their compatibility with the printhead requirements (melting point  $\leq 90$  °C, viscosity 8 mPa s to 20 mPa s) and could ultimately be successfully printed are presented. A summary of the remaining materials that were considered during the selection stage is provided in Appendix A.2.

## 4.1 Results and discussion: Ink characterisation

In this section, the characterisation of the pure materials and the ink compounds is presented.

As highlighted in Chapters 1 and 2 temperature plays a key role in the success of the printing process. It controls not only the post deposition solidification process, but also the material printability, making it possible to maintain the ink in a liquid state within the printing chamber while at the same time tailoring its mechanical property such as its viscosity. As such, the characterisation of the thermal-mechanical properties of the candidate excipients and ink mixtures was critical. For this purpose the following techniques were utilised: Thermogravimetric Analysis (TGA), Differential scanning calorimetry (DSC) and temperature dependent Rheological analysis. Other key characteristics such as density, drop formation and deposition have been studied utilising traditional technologies such as a high precision balance, optical microscopy and optical spectroscopy.

In order to ease the comparison between the different materials while maintaining a clear understanding of the overall direction of this chapter the results are organised by characterisation technique or property analysed.

### 4.1.1 Density studies

Figure 4.1 shows the results of the study for the determination of the density values of the pure carrier materials.

The data clearly show a high degree of linearity across the different volumes as well as a good agreement with the available values reported in literature (Table 4.1). The density values were obtained from printed samples, as described in Section 3.2.3, meaning that these findings do not only provide essential information about the single materials, but also suggest that the depositional method is consistent in producing defect free solid dosage forms. As a result, errors such as air bubble entrapment and misfire which are sources of weight variations and consequent density evaluation errors are not significant and can be considered negligible.

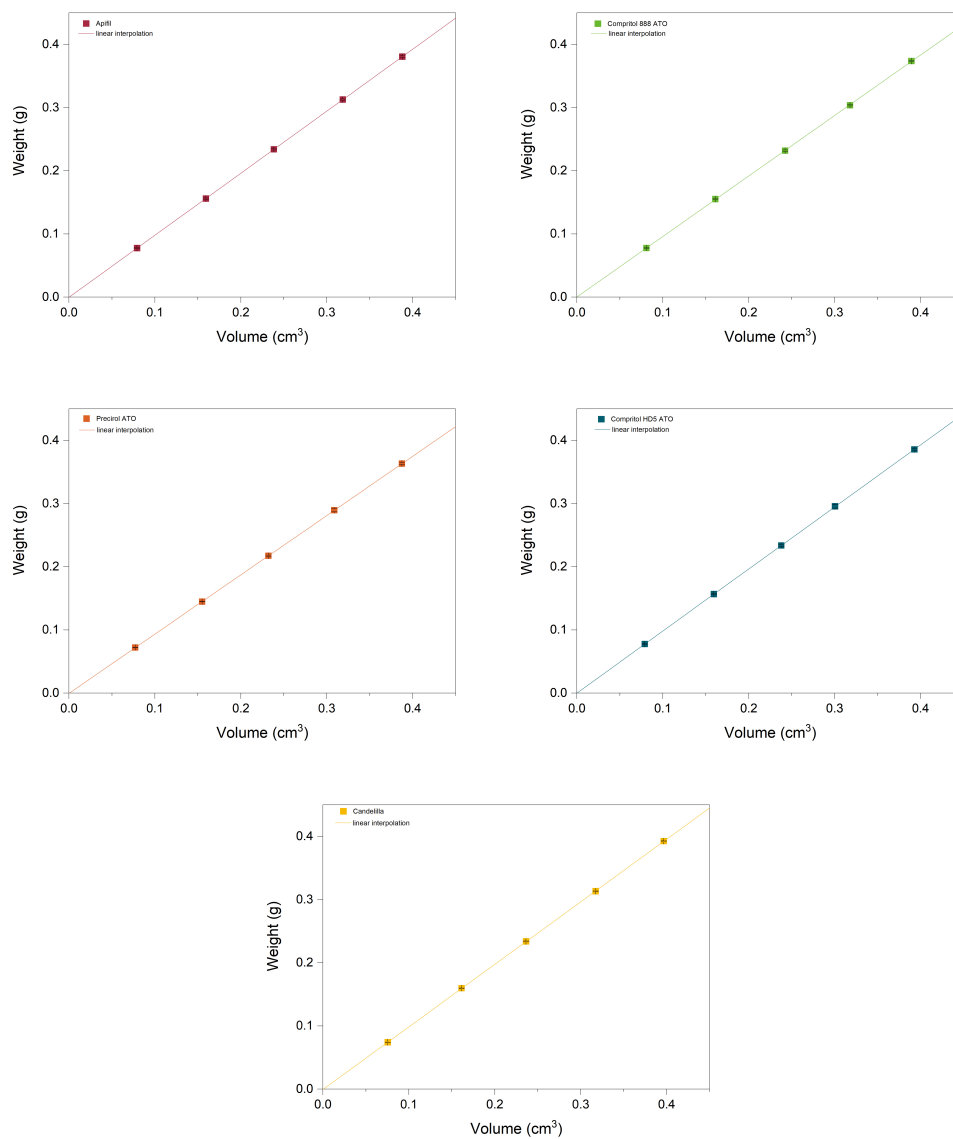


FIGURE 4.1: Density determination via linear regression of the data obtained by weighting known volumes of each fluid. High linearity and negligible y-axis intercepts are observed.

TABLE 4.1: Linear regression parameters for density determination. In the case of data fit all errors come from the fitting procedure and the value of the density was identified with the slope of the linear regressions from Figure 4.1.

Sample	Density [g/ml]	Intercept [g]	$R^2$
<i>Apifil</i>			
Literature	n.a.		
Mean	$0.9806 \pm 0.0015$		
Fit	$0.9892 \pm 0.0031$	$0.0002 \pm 0.0005$	0.99
<i>Candelilla</i>			
Literature	0.988 [210]		
Mean	$0.9881 \pm 0.0015$		
Fit	$0.9902 \pm 0.0013$	$0.0004 \pm 0.0002$	0.99
<i>Precirol ATO 5</i>			
Literature	$1.00 \pm 0.02$ [211] <sup>a</sup>		
Mean	$0.9370 \pm 0.0015$		
Fit	$0.9383 \pm 0.0045$	$0.0004 \pm 0.0007$	0.99
<i>Compritol 888 ATO ATO</i>			
Literature	n.a.		
Mean	$0.9594 \pm 0.0014$		
Fit	$0.9580 \pm 0.0030$	$0.0002 \pm 0.0006$	0.99
<i>Compritol HD5 ATO</i>			
Literature	n.a.		
Mean	$0.9834 \pm 0.0015$		
Fit	$0.9823 \pm 0.0038$	$0.0001 \pm 0.0006$	0.99

<sup>a</sup> The original value was recorded in  $kg/m^3$  [211] and was converted using the following relation  $1000 kg/m^3 = g/ml$ .

The results for the combination inks containing increasing amount of active ingredient are reported in Table 4.2 and grouped based on the main carrier. Once again the results are compatible with a linear regression and are in good agreement with the theoretical prediction obtained from the linear combination of the raw components. This suggests that the ink preparation method was successful, and the inks were composed of the correct and expected ratio of drug to carrier. Moreover, it demonstrates that the printing

process does not likely affect the ink composition since the correct density is found in the printed dosage forms.

TABLE 4.2: Density determination of drug loaded inks. Where 'calculated' identifies the estimated density value calculated from the linear combination of the density of the single components, while 'Measured' is the density of the final product calculated as  $\rho = W/V$  (weight over volume). Errors are obtained by propagation.

Sample	Matrix (%)	Drug (%)	Density (g/ml)	
			Calculated	Measured
Apifil	95	5	0.992±0.001	0.993±0.001
	90	10	1.003±0.001	1.003±0.001
	80	20	1.024±0.001	1.025±0.001
	70	30	1.046±0.001	1.047±0.001
Candelilla	95	5	0.999±0.001	0.997±0.001
	90	10	1.009±0.001	1.010±0.001
	80	20	1.031±0.001	1.032±0.001
	70	30	1.052±0.001	1.051±0.002
Precirol	95	5	0.950±0.001	0.956±0.004
	90	10	0.963±0.001	0.963±0.004
	80	20	0.990±0.001	0.987±0.003
	70	30	1.016±0.001	1.011±0.002
Compritol 888	95	5	0.971±0.001	0.973±0.004
	90	10	0.983±0.001	0.985±0.003
	80	20	1.007±0.001	1.008±0.001
	70	30	1.032±0.001	1.032±0.001
Compritol HD5	95	5	0.994±0.001	0.999±0.002
	90	10	1.005±0.001	1.022±0.009
	80	20	1.027±0.002	1.011±0.002
	70	30	1.048±0.001	1.050±0.005

### 4.1.2 Differential Scanning Calorimetry

DSC was employed to study the thermal properties of Apifil CG, Candelilla, Compritol HD5 ATO, Compritol 888 ATO and Precirol ATO 5 as pure materials components and the ink preparations obtained by including different concentrations of Fenofibrate. The aim was to ensure that all materials would be completely melted at a temperature that is equal or lower than the system

working temperature (90 °C) as well as obtaining an initial understanding of carrier and active ingredient interaction, specifically testing for Fenofibrate crystallinity.

### Fenofibrate

A representative Fenofibrate thermogram shown in Fig. 4.2 reveals a single sharp endothermic peak at  $84.7 \pm 0.2^\circ\text{C}$  [212] consistent with the distinctive melting point previously observed for Form I, which is the most stable crystalline form. Around 65 °C and 70 °C two smaller peaks are visible (<3%) and indicate the minor presence of the metastable Forms II, which in the literature has been found to co-exist with Form I in the right conditions [213].

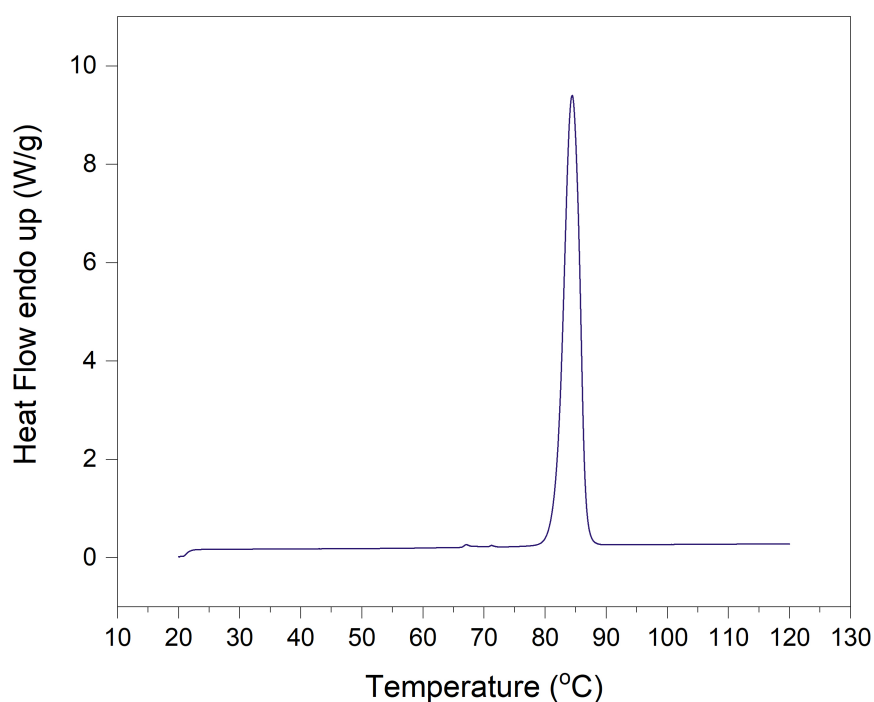


FIGURE 4.2: Differential Scanning Calorimetry heating curve of pure Fenofibrate.

### Compritol HD5 ATO

Figure 4.3 shows the thermograms for pure Fenofibrate, Compritol HD5 ATO, and their mixtures including 5%, 10%, 20% and 30% (w/w) of drug. The thermogram of pure Fenofibrate is included for reference. Compritol HD5 ATO thermogram is characterised by the presence of two endothermic peaks at  $57.4 \pm 0.1^\circ\text{C}$  and  $66.1 \pm 0.3^\circ\text{C}$ . This is consistent with the crystalline

nature of the two lipid families constituting the material. Specifically in Section 3.1.5 it was reported how Compritol HD5 ATO consists of mono, di- and triglycerides of (C21) behenic acid and PEG-8 mono- and di- esters of (C21) behenic acid.

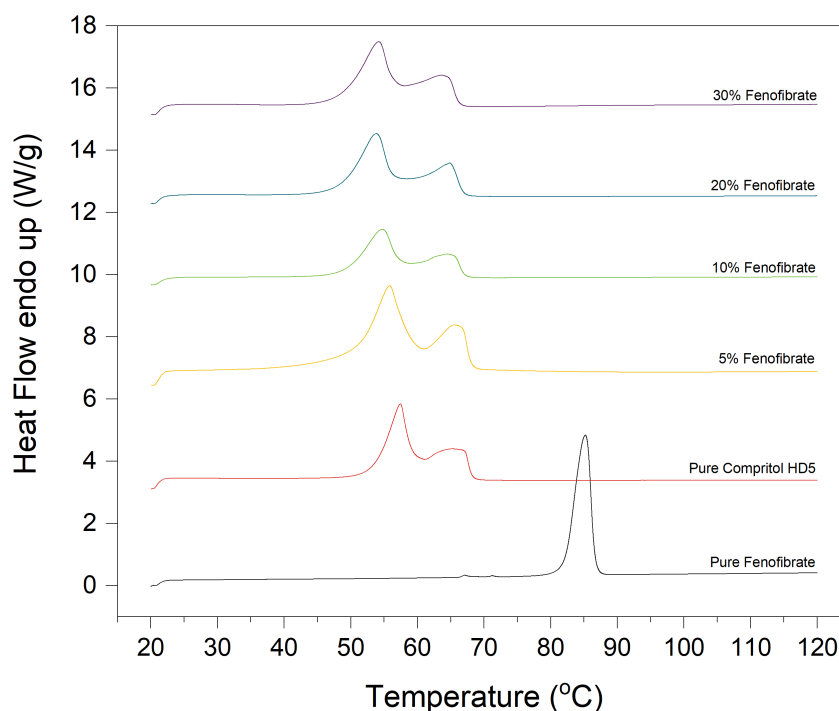


FIGURE 4.3: Differential Scanning Calorimetry of pure Fenofibrate, Compritol HD5 ATO and mixture of the two at 10%(w/w), 20%(w/w) and 30%(w/w). The spectra have been offset on the y-axis for clarity.

It should be noted that even at higher concentrations, the DSC thermograms of Fenofibrate-loaded inks did not show a melting endotherm of the drug and minimal variation in the position of endothermic peaks associated to the carrier. This suggests that the drug remains largely in an amorphous state and that there is no detectable interaction between the active ingredient and the excipient.

Table 4.3 summarises the temperatures of the main endotherm transitions. The analysis suggests a reduction of the onset temperature and melting peak. While unexpected, this behaviour is compatible with what has been observed by Karolewicz and co-worker [214]. Here they reported that Pluronic F127 and Fenofibrate formed an eutectic mixture, in particular they highlighted how while Pluronic F127 melting temperature decreased as expected, the fenofibrate melting peak was detectable only at high drug concentrations.

$\geq 40\%$ . Thus, it is reasonable to assume that a similar logic could be used to explain the behaviour shown by Compritol HD5.

Most importantly, from the analysis of the thermograms, it is evident that all materials completely melted below the printer working temperature of  $90\text{ }^{\circ}\text{C}$  confirming Compritol HD5 ATO as a candidate carrier material for printing.

TABLE 4.3: Identification of endothermic peaks for Compritol HD5 ATO based inks.

Sample	Matrix (%)	Drug (%)	Peak transitions ( $^{\circ}\text{C}$ )	
			I	II
Compritol HD5	100	0	$57.4 \pm 0.2$	$66.1 \pm 0.3$
	95	5	$56.3 \pm 0.5$	$66.2 \pm 0.2$
	90	10	$54.6 \pm 0.1$	$64.5 \pm 0.1$
	80	20	$53.8 \pm 0.1$	$64.9 \pm 0.1$
	70	30	$54.2 \pm 0.1$	$64.0 \pm 0.2$

### Compritol 888 ATO

The DSC scan of Compritol 888 ATO, Figure 4.4, shows one main endotherm peak overshadowing a second smaller transition at lower temperature. This behaviour can be attributed to the complex multi ester nature of Compritol 888 ATO, which includes mono- di- and tri- esters of (C21) benenic acid as seen in Section 3.1.4. Moreover, the thermograms result in good agreement with what previously reported in the literature [215, 216, 217].

The analysis of Figure 4.4 highlights how the inclusion of Fenofibrate in the ink materials causes a change in the response of the samples to heating, resulting in a shift of the endothermic peaks towards lower temperatures accompanied by the separation of the two transitions.

Of particular interest is the suggested presence of thresholds, indeed the primary transition appears to shift both when the drug is added and then noticeably when the Fenofibrate content exceeds  $10\%$  (w/w).

While the lack of a drug endotherm indicates that the Fenofibrate has been successfully dispersed within the matrix material (at least below the sensitivity of DSC), the observable shift implies an interaction between the two materials, most likely in the form of a eutectic mixture [218].

As visible in table 4.4, the results once again confirm that all ink compounds are melted below  $90\text{ }^{\circ}\text{C}$ , the material thus complies with the printing conditions.

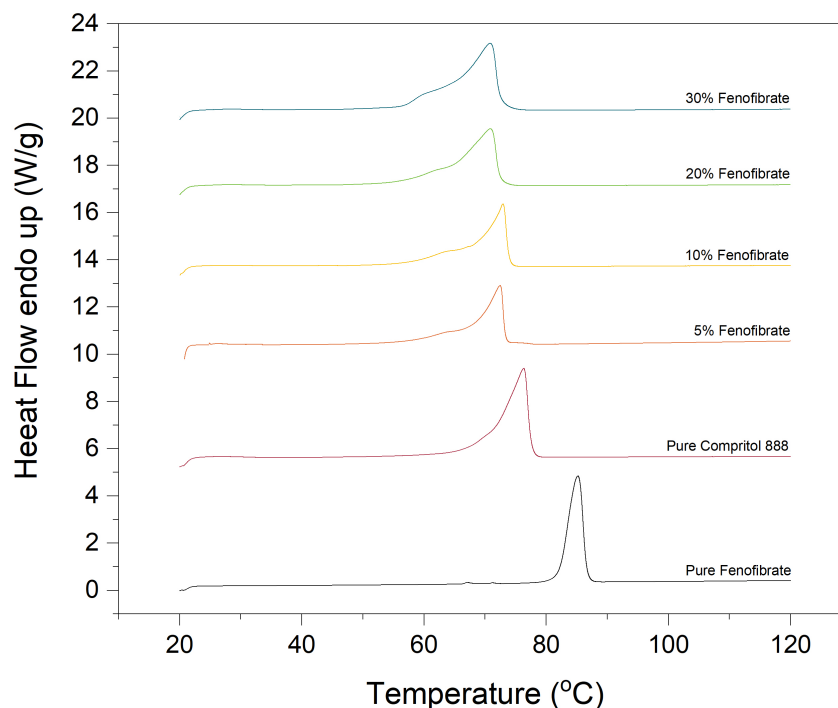


FIGURE 4.4: Differential Scanning Calorimetry heating curve of pure Fenofibrate, Compritol 888 ATO and mixture of the two at 5%(w/w), 10%(w/w), 20%(w/w) and 30%(w/w). The spectra have been offset on the y-axis for clarity.

TABLE 4.4: Identification of endothermic peaks for Compritol 888 ATO based inks.

Sample	Matrix (%)	Drug (%)	Peak transitions [°C]	
			I	II
Compritol 888	100	0	71.7± 0.3	76.4± 0.1
	95	5	64.9± 0.4	72.4± 0.1
	90	10	68.5± 0.3	72.9± 0.1
	80	20	64.1± 0.1	70.9± 0.1
	70	30	63.3± 0.6	70.6± 0.1

### Apifil CG

The DSC analysis of Apifil CG, visible in Figure 4.5, shows a complex thermogram with multiple overlapping endotherms. Two main groups are distinguishable, the first one is a double peak at approximately 50 °C and 53 °C while the second is constituted by one main peak at 61 °C followed by a really small shoulder at approximately 69 °C to 72 °C. As presented in

Section 3.1.3 Apifil CG is a compound mixture of beeswax and PEG-8 resulting in a complex combination of both amorphous and crystalline structures which explains the complexity of the thermogram.

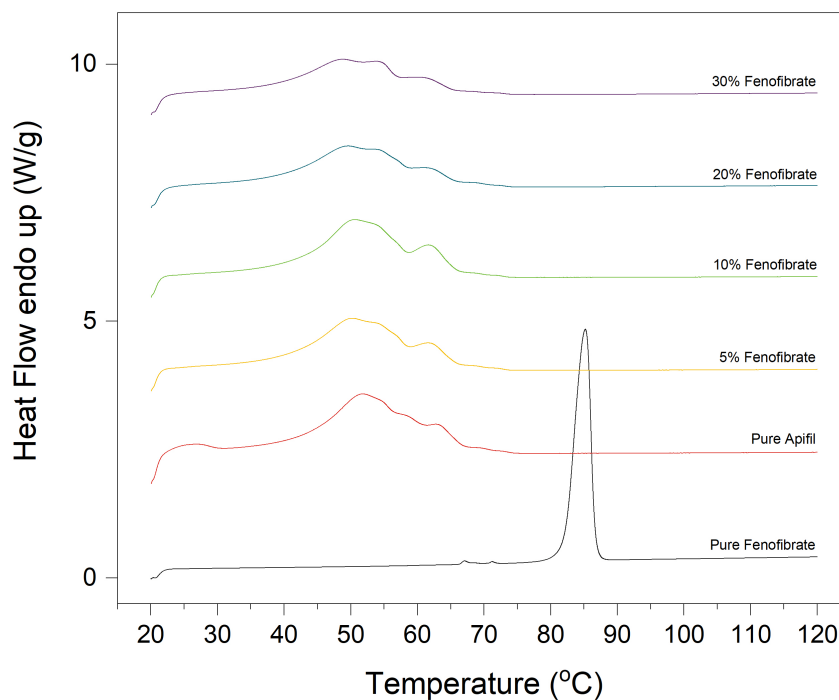


FIGURE 4.5: Differential Scanning Calorimetry of pure Fenofibrate, Apifil CG and mixture of the two at 10%(w/w), 20%(w/w) and 30%(w/w).The spectra have been offset on the y-axis for clarity.

The comparative analysis of all thermograms shown in Figure 4.5 is summarised in Table 4.5. The results suggests that the introduction of Fenofibrate causes a shift of the entire thermogram of approximately 2°C. It is furthermore noticeable a decrease in peaks height both overall and relative to each other. These data combined with the absence of the Fenofibrate peak at 84°C are indicators of an interaction between the matrix material and the API. While also suggesting that the majority of the Fenofibrate is still in an amorphous phase.

Lastly, it is important for the current work to highlight that regardless of the drug content all inks were melted below 90°C.

TABLE 4.5: Identification of endothermic peaks for Apifil CG wax based inks.

Sample	Matrix (%)	Drug (%)	Peak transitions [°C]		
			I	II	III
Apifil	100	0	51.9± 0.1	56.6± 0.1	62.1± 0.1
	95	5	50.3± 0.4	53.2± 0.3	60.8± 0.3
	90	10	50.2± 0.2	52.2± 0.2	61.6± 0.1
	80	20	50.4± 0.2	52.9± 0.5	60.5± 0.2
	70	30	50.0± 0.1	53.1± 0.2	61.3± 0.1

### Candelilla

The pure Candelilla thermogram in Figure 4.6 shows a broad peak centred at  $67.1\pm 0.1^\circ\text{C}$  and onset at  $55.3\pm 0.2^\circ\text{C}$ . Three additional transitions appear masked by the main peak at approximately  $53^\circ\text{C}$ ,  $60^\circ\text{C}$  and  $75^\circ\text{C}$ .

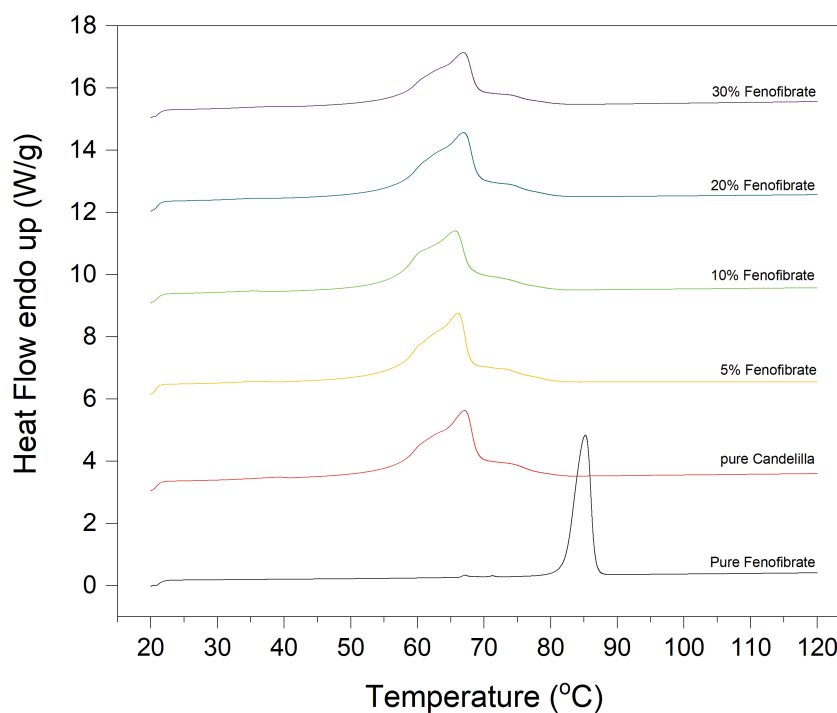


FIGURE 4.6: Differential Scanning Calorimetry heating curve of pure Fenofibrate, Candelilla and mixture of the two at 5%(w/w), 10%(w/w), 20%(w/w) and 30%(w/w).The thermograms have been offset on the y-axis for clarity.

Candelilla comprises of both amorphous and crystalline structures (Section 3.1.2). Hydrocarbon molecules and mono-esters crystallites tend to form orthorhombic structures, whilst the free acids and diesters form a monoclinic structure [95, 219]. The observed trace is in good agreement with the literature [126]. Similarly, to what was observed in the case of Compritol HD5 ATO once the Fenofibrate was added to the mixture its endotherm would not appear and the only Candelilla's peaks are evident. However in contrast with what was observed for the other materials present in this section, Candelilla does not show a shift in the melting point position suggesting that Fenofibrate is in an amorphous state. The endotherm transition temperature of the main melting steps are reported in Table 4.6.

Nevertheless, once again all compounds melt below the printer working temperature of 90 °C confirming Candelilla as a candidate for printing.

TABLE 4.6: Identification of endothermic peaks for Candelilla wax based inks.

Sample	Matrix (%)	Drug (%)	Mean Transition [°C]
Candelilla	100	0	67.1± 0.1
	95	5	67.9± 0.6
	90	10	66.7± 0.1
	80	20	67.1± 0.1
	70	30	67.3± 0.4

### Precirol ATO 5

The thermogram of the pure Precirol ATO 5, visible in Figure 4.7, shows a sharp peak centred at  $59.6\pm 0.2^\circ\text{C}$  and preceded by an underlying shoulder at  $53.9\pm 0.1^\circ\text{C}$ .

After the introduction of Fenofibrate a reduction of the main peak height can be observed accompanied by the shift towards lower temperatures of the shoulder peak as highlighted in Table 4.7. The main endotherm is subject to a minimal shift with a widening of the gap separating the two peaks which is proportional to the quantity of drug included.

Such behaviour resembles that of a eutectic mixture suggesting a potential interaction between the drug and the main excipient indicating a rearrangement of the crystalline structure of the two compounds [218]. Again all inks melted below 90 °C and are thus valid candidates for this work. Furthermore, it is important to notice that the onset point is below 40 °C suggesting

that the material could be found in a softened state in harsh environmental conditions. Regardless, due to the nature of this work as a foundation for future endeavours, it was decided to include Precirol ATO 5 in the pool of candidate carrier since it fulfils the thermo-chemical requirements to be printed.

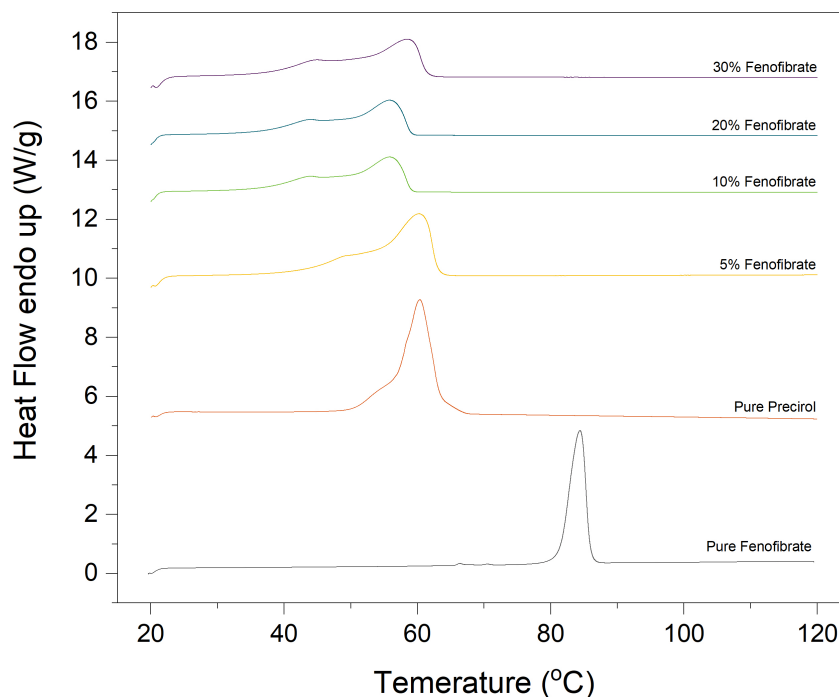


FIGURE 4.7: Differential Scanning Calorimetry heating curve of pure Fenofibrate, Precirol ATO 5 and mixture of the two at 5%(w/w), 10%(w/w), 20%(w/w) and 30%(w/w).The spectra have been offset on the y-axis for clarity.

TABLE 4.7: Identification of endothermic peaks for Precirol ATO 5 based inks.

Sample	Matrix (%)	Drug (%)	Peak Transition (°C)	
			I	II
Precirol	100	0	$59.6 \pm 0.2$	$54.0 \pm 0.1$
	95	5	$49.8 \pm 0.3$	$60.4 \pm 0.1$
	90	10	$47.9 \pm 0.3$	$59.3 \pm 0.1$
	80	20	$44.2 \pm 0.1$	$56.6 \pm 0.1$
	70	30	$44.9 \pm 0.1$	$58.1 \pm 0.1$

### 4.1.3 Thermogravimetric analysis

Thermogravimetric Analysis (TGA) was used to understand the effect of temperature on sample thermal stability and any degradation processes. Specifically, the interest was on verifying the capability of the carriers, API, and ink mixtures to withstand the temperatures of the printing process without undergoing degradation. For this reason in addition to the study of the transitions onset, outset and decomposition peak temperature ( $T_d$ ) the focus was placed on the identification of key parameters such as the temperature at which a 5% mass loss is achieved ( $T_{5\%}$ ) and the mass variation, expressed in terms of mass retained compared to the initial weight ( $\Delta m_T = \frac{m_T}{m_{init}}$ ), respectively at 90 °C ( $\Delta m_{90}$ ) and 100 °C ( $\Delta m_{100}$ ). These parameters, reported in Table 4.8, help determine the compatibility of both API and carriers with the printing method of choice. Recalling what we have seen in the previous sections all material need to maintain their integrity up to 100 °C, the temperature at which the inks are prepared. The study of each component will be discussed individually or in conjunction with other relevant ones, a schematic overview of the results found in this section is presented in Table 4.8.

TABLE 4.8: Main Thermogravimometrical parameters expressed in terms of mean value  $\pm$  standard error.

Sample	Onset I [°C]	Onset II [°C]	Outset [°C]	$T_d$ I	$T_d$ II [°C]
Apifil	167	332	357	214	380
Candelilla	304	365	462	352	418
Precirol	225	402	447	283	403
Compritol 888	396	–	449	430	–
Compritol HD5	408	–	466	445	–
Fenofibrate	256	324	355	294	348

Sample	$T_{5\%}$	$\Delta m_{90}$	$\Delta m_{100}$
Apifil	196	99.99	99.99
Candelilla	285	99.98	99.97
Precirol	275	99.81	99.80
Compritol 888	354	99.98	99.98
Compritol HD5	355	99.61	99.60
Fenofibrate	248	99.96	99.95

### Fenofibrate

The TGA curve of Fenofibrate alongside its derivative (DTG) is shown in Figure 4.8. The analysis of the DTG shows a two-stage degradation process, in agreement with what reported by Shi and colleague in their work [220].

Furthermore, it is possible to identify the two peak temperature associated with the decomposition stages observable in the TGA graph, respectively 294 °C and 348 °C. The first transition is characterised by an early onset at 256 °C ( 324 °C for the second one), which is above the working temperature of the 3D printing process investigated in this thesis.

By examining the material behaviour at high temperatures and particularly past the outset point (355.16 °C) it is possible to conclude that the material is completely since it achieves a total 99% weight loss before 385 °C.

Finally, the values of  $\Delta m_{90} = 99.96\%$  and  $\Delta m_{100} = 99.95\%$  confirm Fenofibrate as an optimal choice as active ingredient, since it results stable in the temperature range of interest.

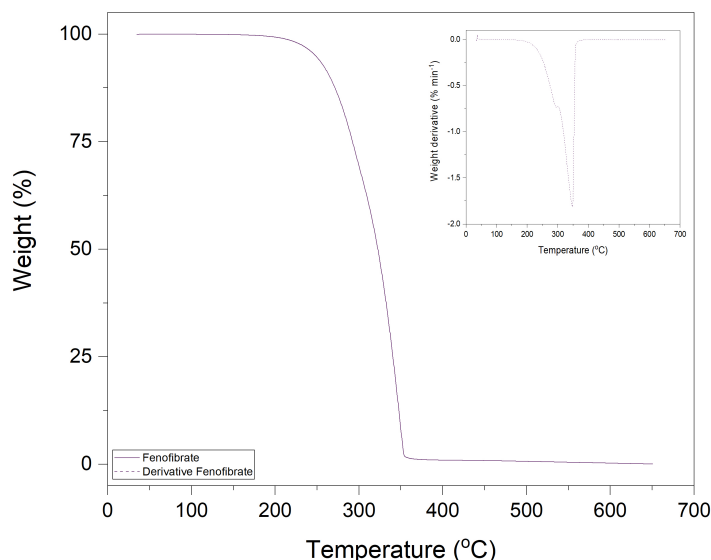


FIGURE 4.8: Thermogravimetric curves of pure Fenofibrate. The inset shows its DTG curve.

### Apifil CG, Candelilla and Precirol ATO 5

Apifil CG, Candelilla and Precirol ATO 5 show a dual transition profile similarly to what was observed for the Fenofibrate. However, while similar, each material presents its own peculiar behaviour.

Figure 4.9 shows how **Apifil CG** is the first component to undergo degradation. In this case the first transition starts at 166.72 °C with a  $T_d = 213.95$  °C

and progresses quickly till the onsets of the second transition at 332.22 °C characterised by  $T_d = 380.43$  °C. The outset is sharp and happens at 356.57 °C. Despite the early onset the material still results stable at the temperature of interest with  $\Delta m_{90} = 99.99\%$  and  $\Delta m_{100} = 99.99\%$ .

**Precirol ATO 5** degradation curve occurs over a much wider range of temperatures compared to Apifil CG, approximately 220 °C, starting at 224.94 °C and terminating at 402.40 °C. In opposition the initial slope, the second transformation happens at a much faster pace over only approximately 40 °C centred at  $T_d = 403.23$  °C. Lastly, **Candelilla** shows the sharpest degradation curve with both transitions happening over a narrow range with initial onset at 303.52 °C and outset at 462.10 °C. While the distinction between the two degradation stages does not jump to the eye when looking at the TGA curve it becomes obvious when analysing the DTG curve. In the latter two peaks are easily distinguishable, with the local maxima at 352.13 °C and 418.02 °C.

As expected as all materials are organic there is a 99% weight loss just above 480 °C.

All three material are hence stable at both 90 °C and 100 °C with a total remaining mass >99.8%. As a result it is possible to conclude that all material are valuable candidates for the use as carrier in a pharmaceutical formulation.

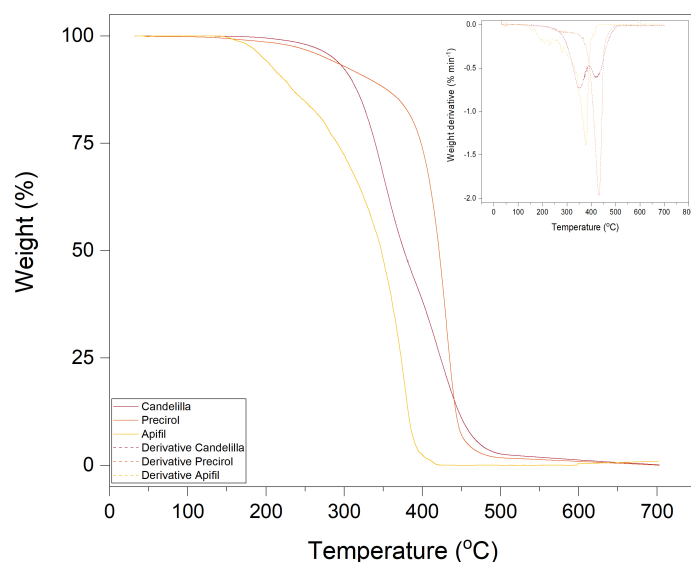


FIGURE 4.9: Thermogravimetric curves of pure Apifil CG, Candelilla and Precirol. The inset shows its DTG curves.

### Compritol HD5 ATO and Compritol 888 ATO

For this section Compritol HD5 ATO and Compritol 888 ATO have been grouped together allowing for a direct comparison between the original material, Compritol 888 ATO, and its derivative, Compritol HD5 ATO. In Figure 4.10 can be observed that the introduction of PEG-8 esters causes a shift of the TGA curve towards higher temperatures while maintaining the original shape. Both Compritol inks, show a single sharp thermo-oxidative decline with onset respectively at 395.86 °C for Compritol 888 ATO and 408.23 °C for Compritol HD5 ATO and outset at 448.50 °C and 465.54 °C.

The analysis of the DTG curve visible in the inset of Fig. 4.10, made also possible to identify the characteristic temperature of these transitions:

$T_d = 430.23$  °C for Compritol HD5 ATO and 445.01 °C for Compritol 888 ATO.

For both material complete degradation (>99%) was reached before 500 °C confirming their organic nature.

Lastly, the attention was focused on determining the degradation of the samples at the temperature of interest for the printing process and ink preparation. It was found that in the range of interest less than 0.4% was lost, indicating that both carriers are stable and suitable for hot-melt inkjet printing.

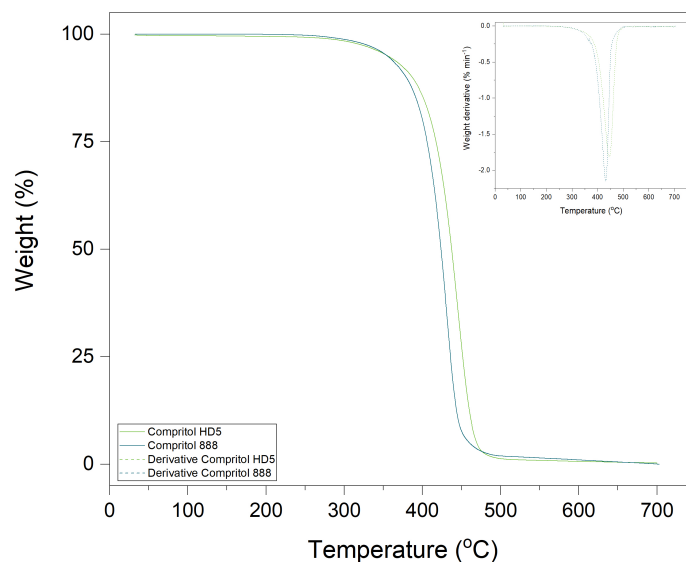


FIGURE 4.10: Thermogravimetric curves of pure Compritol 888 ATO and Compritol HD5 ATO. The inset shows its DTG curves.

Lastly, to better understand the behaviour of not only the single carrier,

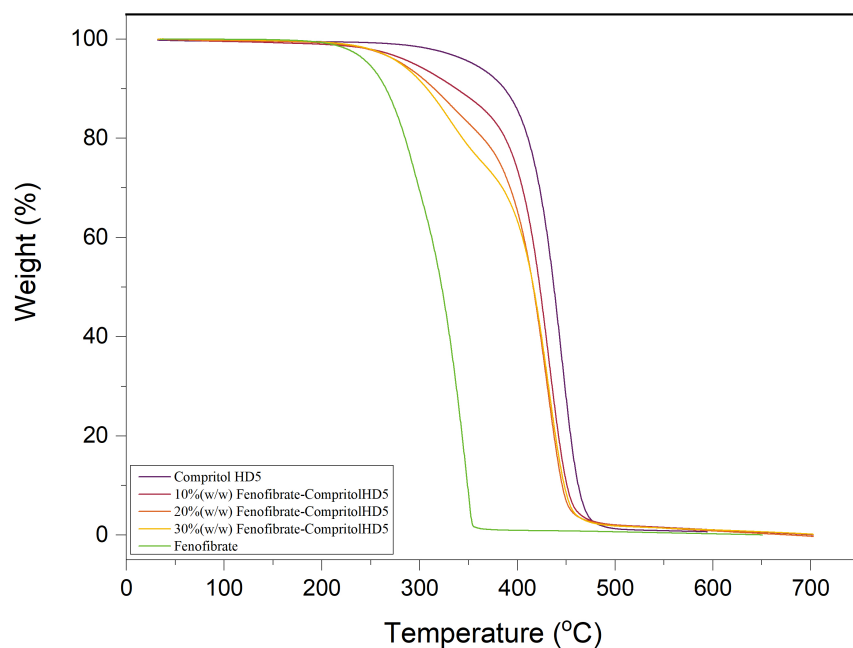
but also of the composite inks, Compritol HD5 ATO was selected as test material alongside three different concentrations of Fenofibrate: 10%, 20%, and 30% (w/w). The results are presented in Figure 4.11A, B where the thermograms of the composite inks are plotted in conjunction with the pure materials to work as reference.

It can be observed that in contrast to the pure carrier all drug-loaded materials present two main mass loss stages, Figure 4.11A. The DTG curves in Figure 4.11B highlight the dual nature of the decomposition process showing two distinctive peaks for each of the inks. By comparing the  $T_d$  values of the different drug concentration mixes to the main transition of the original constituents it becomes clear that they correspond to the direct combination of the two original constituents. All key parameters are summarised in Table 4.9. This effect results are even more evident when considering the peaks relative height which is proportional to the concentration of each component. Such behaviour is in good agreement with what seen in the previous section 4.1.2 indicating the formation of homogeneous mixture or a solid dispersion of the drug and matrix material. Noticeably only the main Fenofibrate peak shows in the combined inks, this could be linked to an overshadowing effect where the resolution of the data collection is not enough to distinguish the two peaks and the main one overshadows the other.

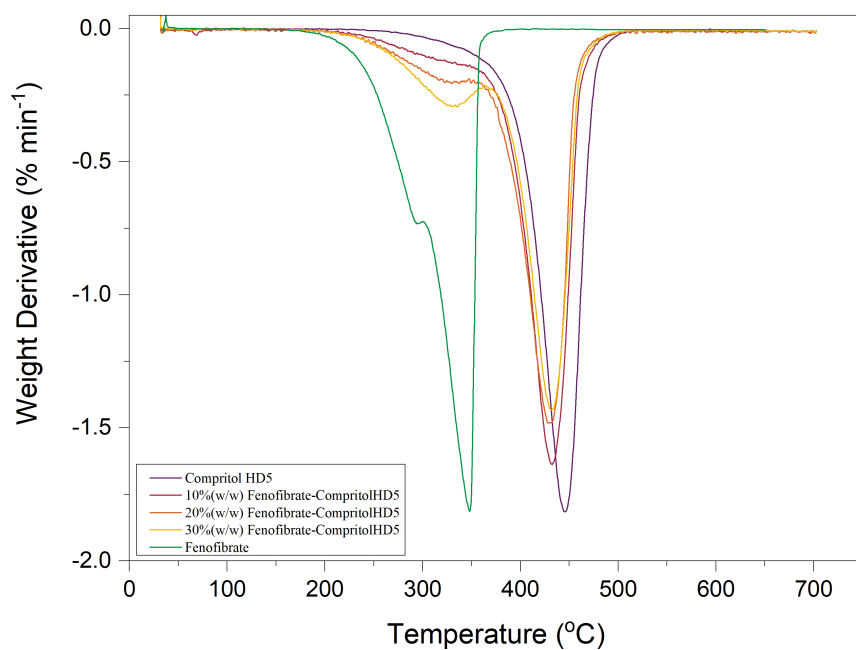
In conclusion it is possible to infer that not only the pure carrier and API are compatible with the printing process, but also in combination.

TABLE 4.9: Compritol HD5 ATO Thermogravimetical parameters expressed in terms of mean value  $\pm$  standard error.

	Compritol HD5 [°C]	10%(w/w) [°C]	20%(w/w) [°C]	30%(w/w) [°C]	Fenofibrate [°C]
onset I	–	–	–	–	256
onset II	–	274	270	267	324
onset III	408	401	399	406	–
outset	465	455	450	453	355
$T_d$ I	–	–	–	–	294
$T_d$ II	–	331	329	324	348
$T_d$ III	445	433	430	432	–



(A)



(B)

FIGURE 4.11: Thermogravimetric curves (A) and their derivatives (B) of pure Fenofibrate, Compritol HD5 ATO and mixture of the two at 10%(w/w), 20%(w/w) and 30%(w/w). (C) shows the height of the two derivative peaks of interest (namely 348 °C and 408 °C) in relation to the drug concentration.

#### 4.1.4 Shear viscosity characterisation

As seen in the previous sections 1 and 3.2.6 the main goal of the study of the inks rheological properties is to ensure drop formation and ejection from the printing head. Specifically, given the choice of printhead (Spectra SE-128 printheads, Fujifilm, Japan) the inks must show a low viscosity in the 8 mPa s to 20 mPa s range. The range of temperatures examined for this section were selected to reflect the working temperature of the 3DP apparatus ( $\leq 90^\circ\text{C}$ ) in addition to the restriction imposed by the melting point of each individual raw material. In the case of ink compounds the lower range limit was matched with the API's one, since it happens to be higher than all the carriers'.

During the data analysis it was possible to appreciate the effect the increase in drug concentration on the ink's viscosity. Most notably, two distinct behaviours became evident. In the first case the effect was a gradual drop in the material viscosity while in the second the opposite behaviour was observable. As a result, in the next section the materials have been grouped on the base of their response. The Fenofibrate (API) is presented separately since it constitutes a category of its own.

##### Fenofibrate

In Figure 4.12 it is easily noticeable that Fenofibrate shows an almost Newtonian behaviour plateauing at high shear rates for all the temperatures examined. The averaged experimental data are presented in Figure 4.12 (dots) alongside their respective Cross fit flow curve (full line) calculated as described in section 3.2.6. From the data it is clear that the model represents the experimental data well with  $\chi^2 > 0.97$ . Furthermore, it is appreciable that in the range of temperatures tested with exception of  $80^\circ\text{C}$  the estimated viscosity at the highest rates ( $\eta_\infty$ ) is within the range of interest. The results are summarised in Table 4.10.

Notably the lowest temperature,  $80^\circ\text{C}$  is not suitable for the pure material to be printed. Indeed, while the material is in a softened state it has yet to reach its complete melting point (see Section 4.1.2). It was decided to include the test to provide a bench mark for the behaviour of the ink composites.

TABLE 4.10: Fenofibrate  $\eta_{\dot{\gamma} \rightarrow \infty}$  obtained from the fitting using Cross model.

Temperature [°C]	Viscosity $\eta_{\dot{\gamma} \rightarrow \infty}$ [mPa · s]
80	20.15 ± 0.04
85	15.77 ± 0.02
90	12.58 ± 0.03
95	10.27 ± 0.03

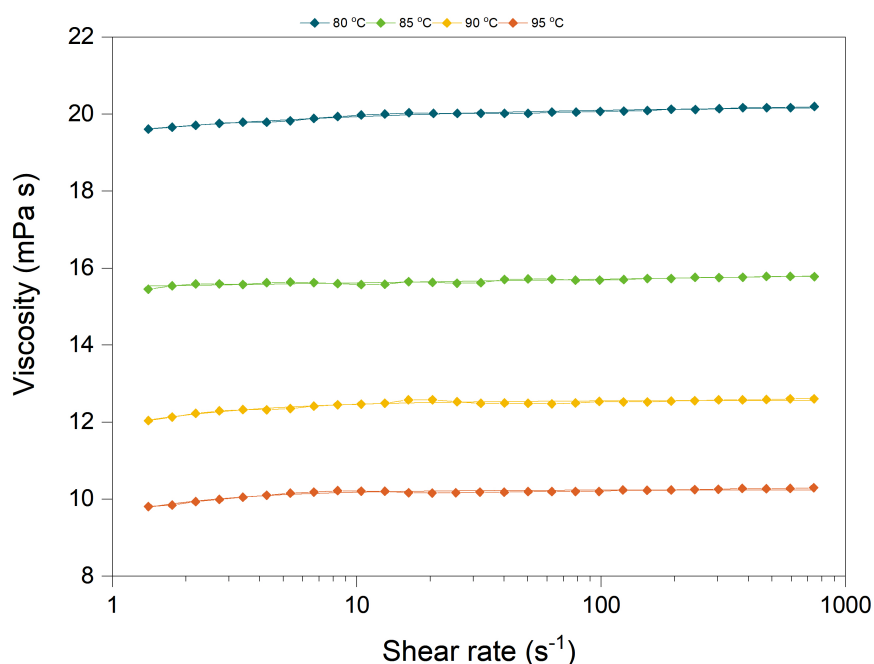


FIGURE 4.12: Flow curves of Fenofibrate at 80 °C, 85 °C, 90 °C and 95 °C. The solid symbols represent the averaged experimental data from a rotary rheometer while the lines represent the Cross fit. The fit is in good agreement with the measured values.

### Candelilla, Compritol 888 ATO and Precirol

All materials here presented show the expected shear thinning behaviour typical of most lipids [177, 221], see plots 4.13A, 4.14A and 4.15A. At low temperatures, a rapid decrease in viscosity was observed in response to an increase in the shear rate, before an almost-Newtonian behaviour was reached. Notably at higher temperature an easing of initial viscosity gradient is visible. As a result, the stable state is also reached more quickly. Following what can be found in the literature all flow curves were fitted using the Cross model (continuous line) by minimising the  $\chi^2$ . From the analysis of the plots 4.13A, 4.14A and 4.15A it is clear that the method best fits the data profiles at

higher temperatures where  $\chi^2 > 0.99$  while at lower temperatures the value drops to  $\chi^2 \leq 0.96$ .

To form the ink compounds Fenofibrate was added to the carrier materials in the desired concentrations (5%, 10%, 20% and 30% w/w). For all the materials here considered the viscosity of the pure carrier is comparable or higher than the Fenofibrate at temperatures above 80 °C. Thus, the addition of Fenofibrate causes a decrease in the inks viscosity, compared to the pure carrier, which is proportional to the content of API. This behaviour is easily appreciable in Figures 4.13C, 4.14C and 4.15C. Lastly, it is important to notice that while it strongly influences the response to the shear rate, the addition of the drug does not have major effect on behaviour when it comes to temperature, see Figures 4.13B, 4.14B and 4.15B. The results are summarised in Table 4.11 As a result all ink mixes are compatible with the operative range of the printhead and are thus, suitable for printing. Amongst the pure carrier Candelilla is the only one for which a temperature restriction is needed, specifically 80 °C has to be excluded.

TABLE 4.11: Fenofibrate, Candelilla, Compritol 888 ATO and Precirol ATO 5 comparative table of  $\eta_{\dot{\gamma} \rightarrow \infty}$  values organised by temperature and drug concentration. The coefficients are given as average  $\pm$  standard error.

API (w/w)	80 °C	85 °C	90 °C	95 °C	
Fenofibrate	20.15 $\pm$ 0.04	15.77 $\pm$ 0.02	12.58 $\pm$ 0.03	10.27 $\pm$ 0.03	
Candelilla	pure	23.04 $\pm$ 0.24	19.95 $\pm$ 0.09	17.41 $\pm$ 0.03	13.08 $\pm$ 0.03
	5%	18.47 $\pm$ 0.09	16.04 $\pm$ 0.03	14.20 $\pm$ 0.02	12.80 $\pm$ 0.02
	10%	17.80 $\pm$ 0.02	15.63 $\pm$ 0.02	13.91 $\pm$ 0.02	12.44 $\pm$ 0.01
	20%	18.64 $\pm$ 0.42	16.19 $\pm$ 0.33	14.12 $\pm$ 0.26	12.59 $\pm$ 0.17
	30%	17.76 $\pm$ 0.01	15.69 $\pm$ 0.03	13.46 $\pm$ 0.06	12.09 $\pm$ 0.02
Compritol 888	pure	18.86 $\pm$ 0.27	16.32 $\pm$ 0.57	15.07 $\pm$ 0.73	14.07 $\pm$ 0.19
	5%	18.05 $\pm$ 0.09	15.63 $\pm$ 0.04	13.73 $\pm$ 0.04	12.17 $\pm$ 0.01
	10%	17.04 $\pm$ 0.05	15.14 $\pm$ 0.06	13.21 $\pm$ 0.02	11.76 $\pm$ 0.03
	20%	16.91 $\pm$ 0.05	14.73 $\pm$ 0.03	13.09 $\pm$ 0.03	11.50 $\pm$ 0.04
	30%	15.59 $\pm$ 0.24	13.40 $\pm$ 0.14	11.76 $\pm$ 0.10	10.49 $\pm$ 0.07
Precirol	pure	14.94 $\pm$ 0.04	13.03 $\pm$ 0.02	11.59 $\pm$ 0.02	10.32 $\pm$ 0.02
	5%	14.70 $\pm$ 0.02	13.3 $\pm$ 0.03	11.22 $\pm$ 0.02	10.21 $\pm$ 0.02
	10%	14.40 $\pm$ 0.01	12.64 $\pm$ 0.03	11.17 $\pm$ 0.03	10.07 $\pm$ 0.03
	20%	14.14 $\pm$ 0.02	12.47 $\pm$ 0.02	10.89 $\pm$ 0.01	9.64 $\pm$ 0.02
	30%	11.84 $\pm$ 0.01	10.67 $\pm$ 0.02	9.65 $\pm$ 0.01	9.26 $\pm$ 0.02

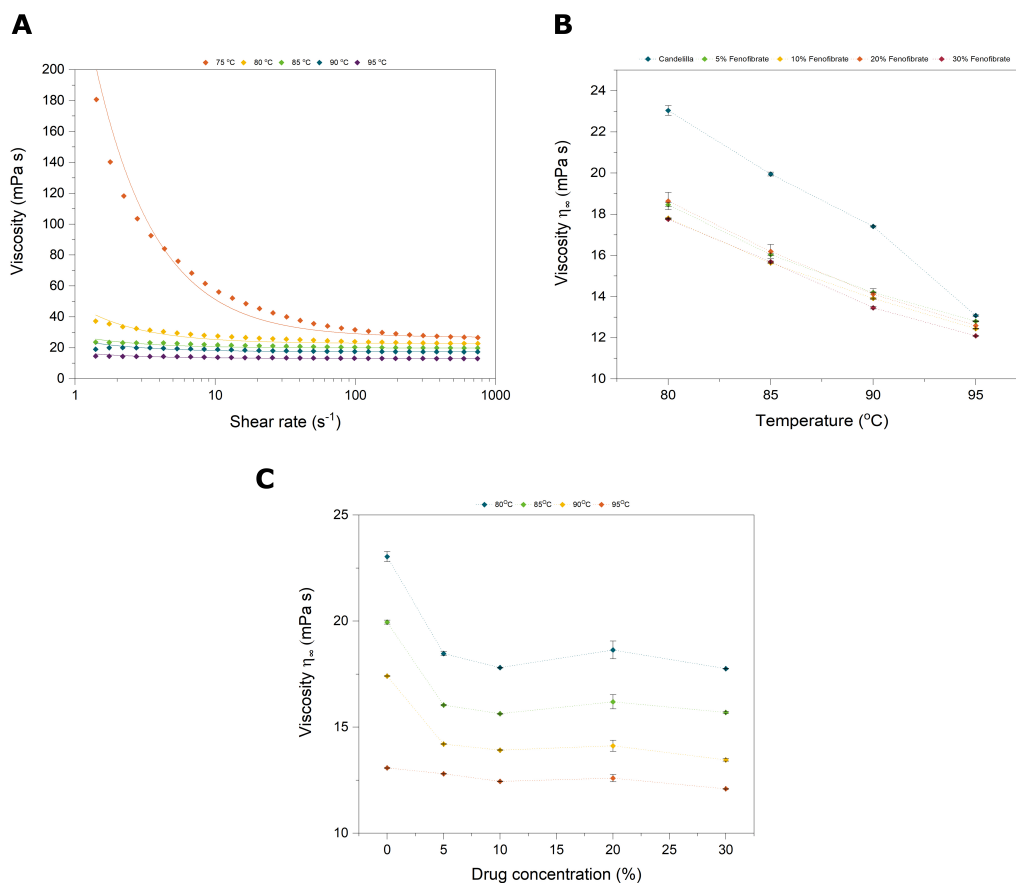


FIGURE 4.13: A) Flow curves of pure Candelilla at 75 °C, 80 °C, 85 °C, 90 °C and 95 °C. The solid symbols represent the averaged experimental data from a rotary rheometer while the lines represent the Cross fit. The fit is in good agreement with the measured values. B) Effect of Temperature on ( $\eta = \eta_{\infty}$ ) value evaluated at five different concentrations 0%, 5%, 10%, 20% and 30%. C) Effect of Fenofibrate content on ( $\eta = \eta_{\infty}$ ) value evaluated at four different temperatures 80 °C, 85 °C, 90 °C and 95 °C.

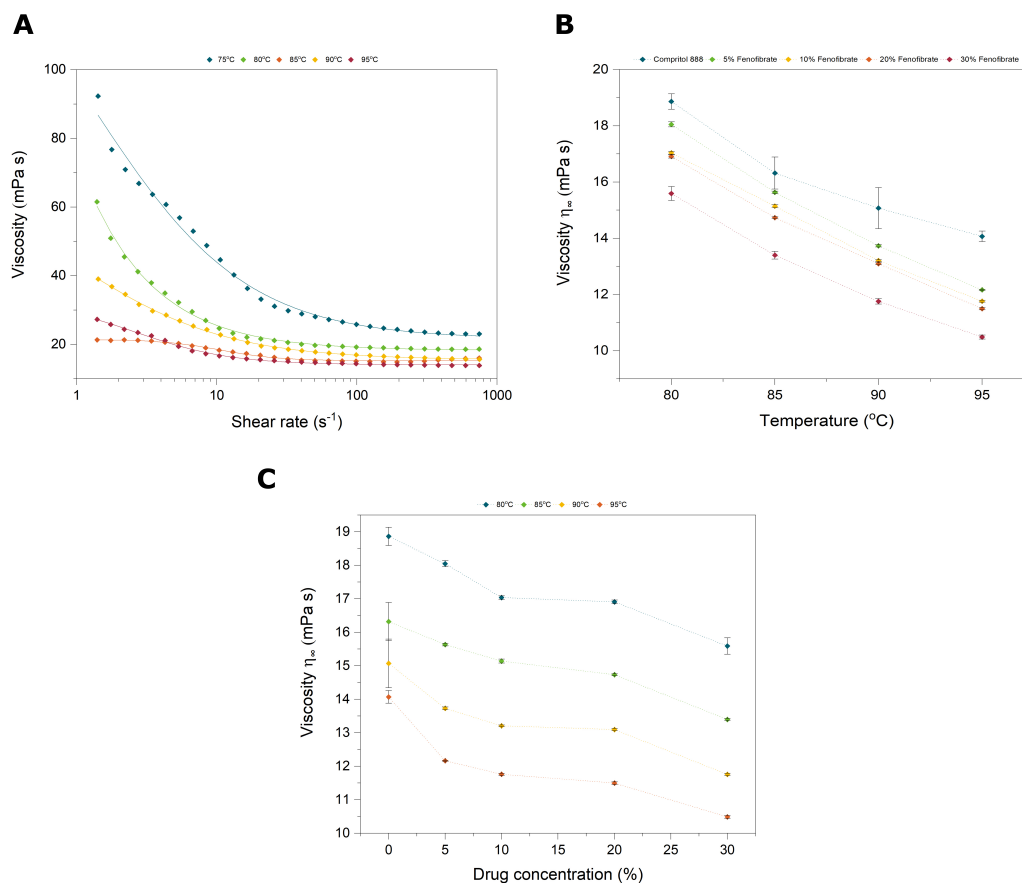


FIGURE 4.14: A) Flow curves of pure Compritol 888 ATO at 80  $^{\circ}C$ , 85  $^{\circ}C$ , 90  $^{\circ}C$  and 95  $^{\circ}C$ . The solid symbols represent the averaged experimental data from a rotary rheometer while the lines represent the Cross fit. The fit is in good agreement with the measured values. B) Effect of Temperature on ( $\eta = \eta_{\infty}$ ) value evaluated at five different concentrations 0%, 5%, 10%, 20% and 30%. C) Effect of Fenofibrate content on ( $\eta = \eta_{\infty}$ ) value evaluated at four different temperatures 80  $^{\circ}C$ , 85  $^{\circ}C$ , 90  $^{\circ}C$  and 95  $^{\circ}C$ .

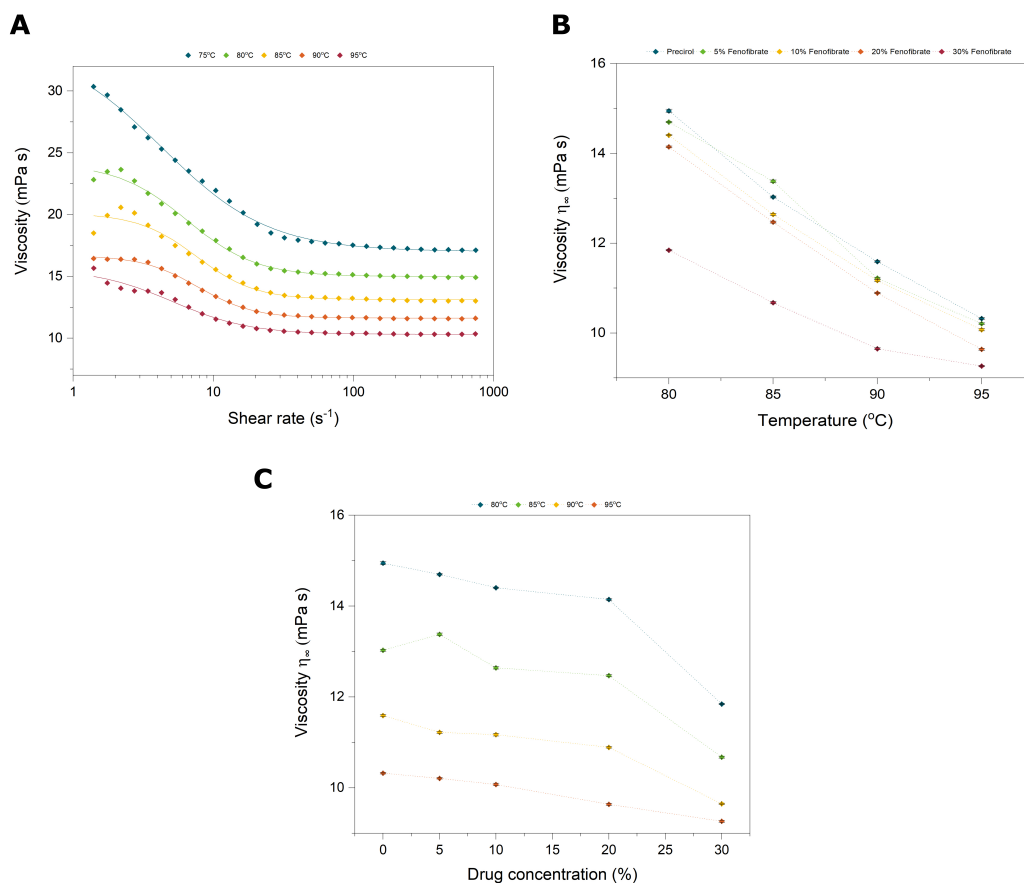


FIGURE 4.15: A) Flow curves of pure Precirol ATO 5 at 80 °C, 85 °C, 90 °C and 95 °C. The solid symbols represent the averaged experimental data from a rotary rheometer while the lines represent the Cross fit. The fit is in good agreement with the measured values. B) Effect of Temperature on ( $\eta = \eta_{\infty}$ ) value evaluated at five different concentrations 0%, 5%, 10%, 20% and 30%. C) Effect of Fenofibrate content on ( $\eta = \eta_{\infty}$ ) value evaluated at four different temperatures 80 °C, 85 °C, 90 °C and 95 °C.

### Compritol HD5 ATO and Apifil CG

The data collected from the flow curve measurement alongside with their fit for the Apifil CG and Compritol HD5 ATO are displayed in Figure 4.16 and 4.17 respectively.

The viscosity curves for Compritol HD5 ATO are plotted in Fig. 4.17A and reveal a shear-thinning behaviour. Notably  $\eta_{\gamma \rightarrow \infty}$  is inversely proportional to the temperature of collection, with 95 °C showing the lowest flow curve and 75 °C presenting the most unstable trend. As we have previously seen this behaviour is compatible with the lipidic nature of Compritol HD5 ATO.

In contrast, Apifil CG shows an unexpected shear-thickening behaviour (Fig. 4.16A). This might be explained by the complexity of the Apifil CG composition, which includes a mixture of both long and short organic chains. At

high shear rates this might form aggregates with high cross-linker density due to slow chain diffusion resulting in transversal flows and the resulting raised viscosity [222]

When the API is added to the mixture both Apifil CG and Compritol HD5 ATO show a similar behaviour where the viscosity of the ink increases with the Fenofibrate content and is higher than the combined viscosity of the original materials as highlighted in figures 4.16C and 4.17C. Notably, despite the increase in viscosity all materials retain the same behaviour when it comes to temperature as seen in figures 4.16B and 4.17B. The results are summarised in Table 4.12.

What differentiates these two carriers from those previously analysed and a possible explanation for the observed behaviour is the presence of PEG esters. This assumption is supported by the behaviour of Compritol. Specifically, in this work both Compritol HD5 ATO and 888 have been studied offering a comparison. Indeed, the only thing that separates the two is the presence of a PEG ester in the HD5 sample, starting with the comparison of the flow curve it can be noted that they do not greatly differ from one another. However, when it comes to comparing results for the ink compounds containing the API the behaviour is quite different with the change in viscosity moving in opposite directions. As a result of this trend, combined with the difference in composition alongside with reports in the literature [223], it is reasonable to suggest that PEG and Fenofibrate are capable of forming localised agglomerates which in return would disrupt the original flow and cause the observed increment in viscosity. Regardless, all Apifil CG preparations approach a Newtonian behaviour at high shear rates with  $\eta_{\dot{\gamma} \rightarrow \infty}$  within the range of interest for the hot-melt 3D printing application. In the case of Compritol HD5 ATO, in the range of temperatures analysed, all inks show Newtonian behaviour at high shear rates and the resulting viscosities are compatible with the 3D printing process with the exception made for 20% (w/w) and 30% (w/w) which require temperature  $\geq 85^\circ\text{C}$ . In Figure 4.17A low temperature rheological curves have been included for completion. However, it is clear that at these temperatures are too close to the material melting point and as a result present a problematic behaviour at small shear rates. Furthermore, they are not capable to achieve a Newtonian state within the interval analysed. As a result these two temperatures have been excluded from further analysis.

TABLE 4.12: .

Fenofibrate, Compritol HD5 ATO and Apifil CG comparative table of  $\eta_{\dot{\gamma} \rightarrow \infty}$  values organised by temperature and drug concentration. The coefficients are given as average  $\pm$  standard error.

API (w/w)		80 °C	85 °C	90 °C	95 °C
Fenofibrate		20.15 $\pm$ 0.04	15.77 $\pm$ 0.02	12.58 $\pm$ 0.03	10.27 $\pm$ 0.03
Compritol HD5	pure	18.61 $\pm$ 0.07	16.49 $\pm$ 0.05	14.74 $\pm$ 0.03	13.24 $\pm$ 0.01
	5%	18.41 $\pm$ 0.06	16.33 $\pm$ 0.07	14.47 $\pm$ 0.07	13.04 $\pm$ 0.06
	10%	19.63 $\pm$ 0.05	17.45 $\pm$ 0.07	15.51 $\pm$ 0.06	13.73 $\pm$ 0.03
	20%	21.06 $\pm$ 0.07	18.69 $\pm$ 0.07	16.59 $\pm$ 0.04	14.77 $\pm$ 0.03
	30%	21.54 $\pm$ 0.07	18.81 $\pm$ 0.09	16.69 $\pm$ 0.06	15.02 $\pm$ 0.05
Apifil	pure	13.42 $\pm$ 0.01	11.88 $\pm$ 0.01	10.66 $\pm$ 0.02	9.65 $\pm$ 0.01
	5%	13.20 $\pm$ 0.04	12.22 $\pm$ 0.03	10.74 $\pm$ 0.04	9.88 $\pm$ 0.04
	10%	13.54 $\pm$ 0.04	12.13 $\pm$ 0.05	10.90 $\pm$ 0.03	9.95 $\pm$ 0.03
	20%	14.83 $\pm$ 0.03	13.16 $\pm$ 0.02	11.54 $\pm$ 0.02	10.43 $\pm$ 0.01
	30%	18.01 $\pm$ 0.02	15.62 $\pm$ 0.06	13.96 $\pm$ 0.12	12.54 $\pm$ 0.02

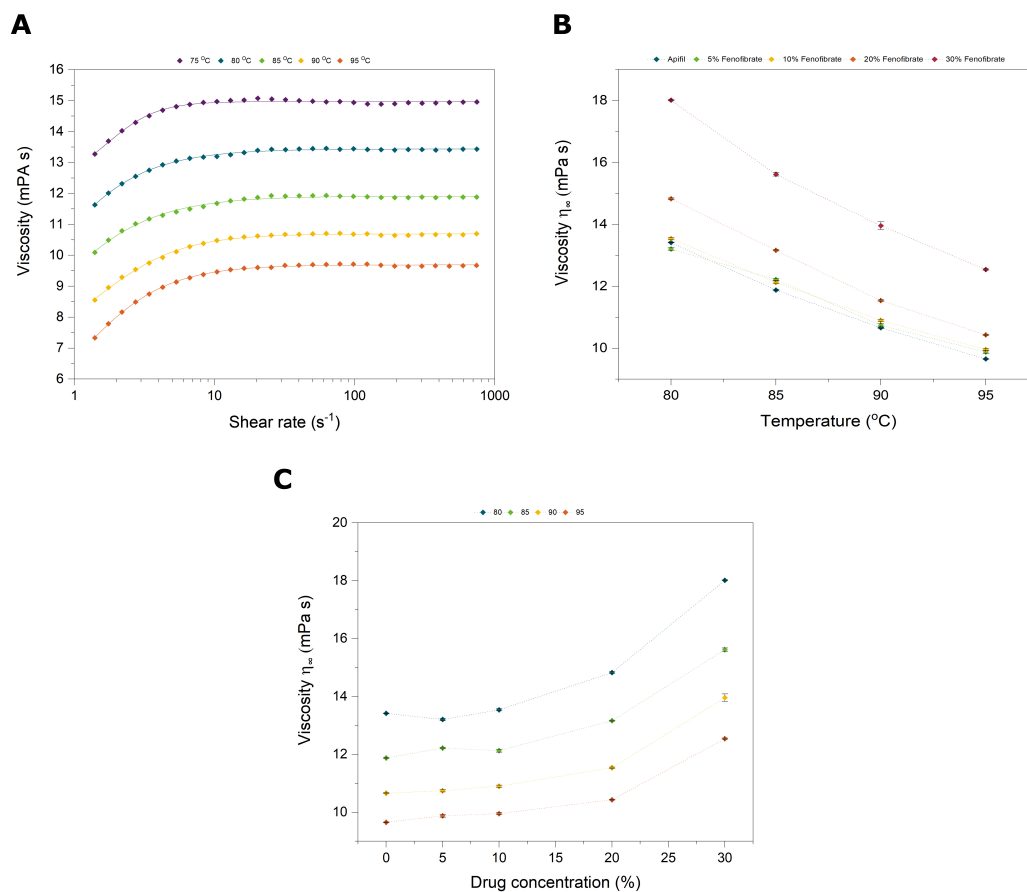


FIGURE 4.16: A) Flow curves of pure Apifil CG at 80 °C, 85 °C, 90 °C and 95 °C. The solid symbols represent the averaged experimental data from a rotary rheometer while the lines represent the Cross fit. The fit is in good agreement with the measured values. B) Effect of Temperature on ( $\eta = \eta_{\infty}$ ) value evaluated at five different concentrations 0%, 5%, 10%, 20% and 30%. C) Effect of Fenofibrate content on ( $\eta = \eta_{\infty}$ ) value evaluated at four different temperatures 80 °C, 85 °C, 90 °C and 95 °C.

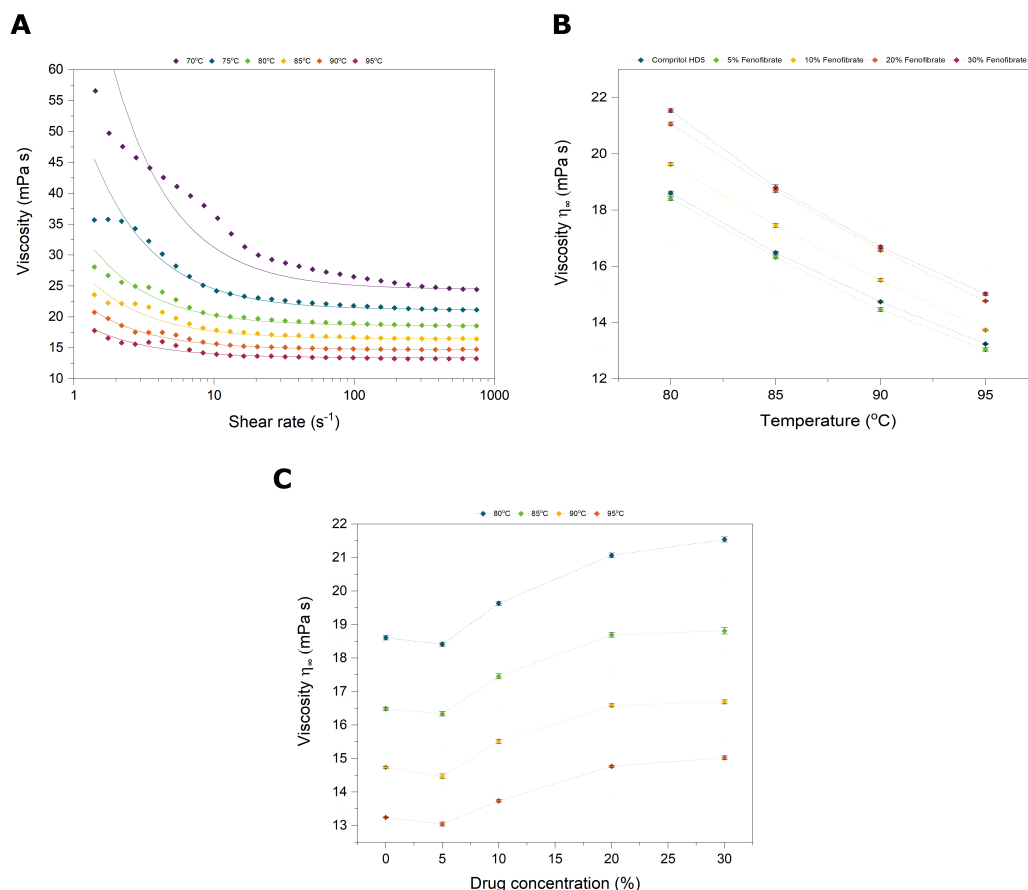


FIGURE 4.17: A) Flow curves of pure Compritol HD5 at 80 °C, 85 °C, 90 °C and 95 °C. The solid symbols represent the averaged experimental data from a rotary rheometer while the lines represent the Cross fit. The fit is in good agreement with the measured values. B) Effect of Temperature on ( $\eta = \eta_{\infty}$ ) value evaluated at five different concentrations 0%, 5%, 10%, 20% and 30%. C) Effect of Fenofibrate content on ( $\eta = \eta_{\infty}$ ) value evaluated at four different temperatures 80 °C, 85 °C, 90 °C and 95 °C.

#### 4.1.5 Fourier Transform Infrared Spectroscopy

Here Fourier Transform Infrared Spectroscopy was used to confirm the presence of Fenofibrate within the ink preparation and to obtain a qualitative understanding of the amount of API contained in each of them, in such a way to confirm our capability to reliably produce the desired concentration.

Figure 4.18 shows the spectra obtained for each of the samples, grouped on the base of the matrix material.

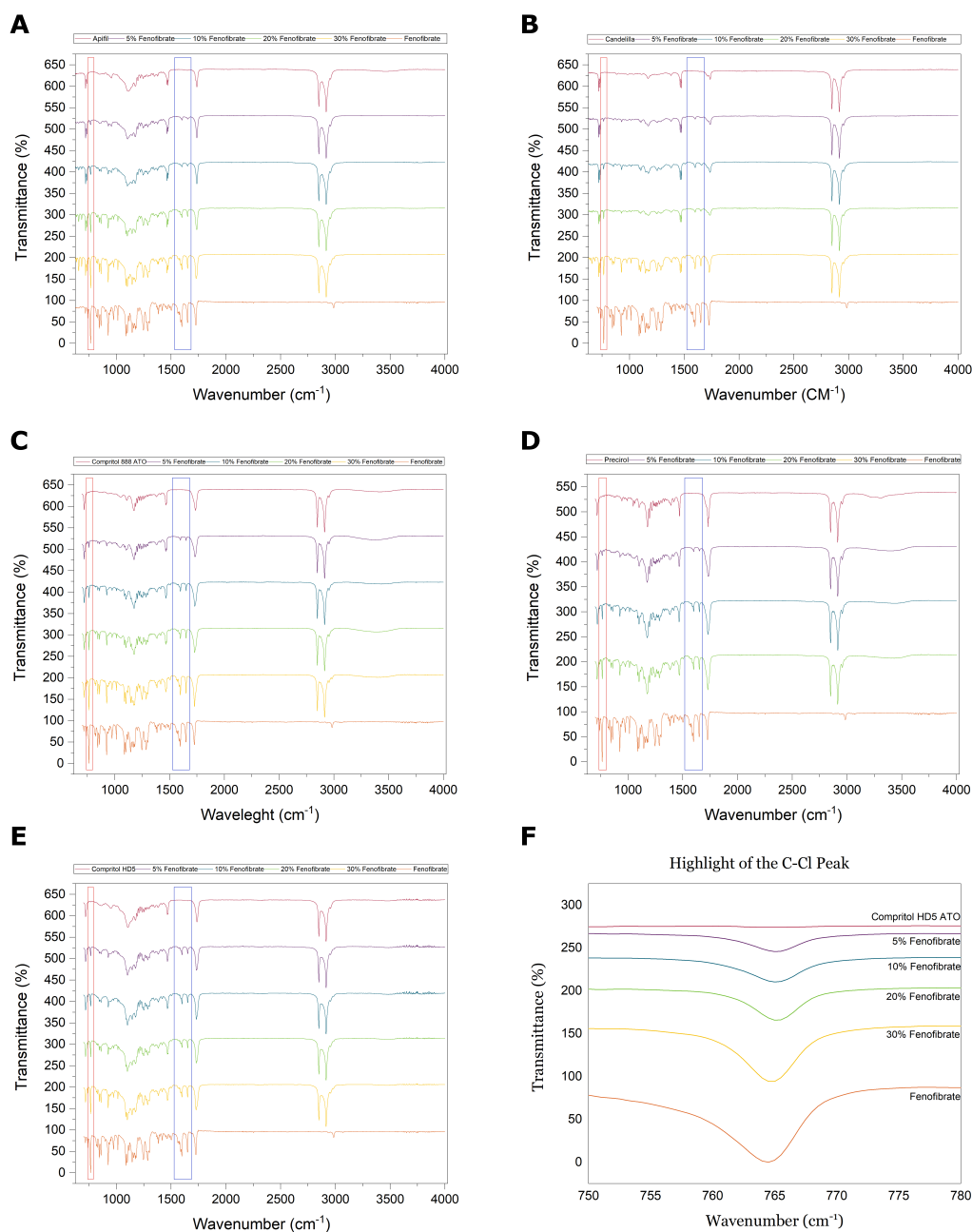


FIGURE 4.18: Fourier Transform Infrared Spectroscopy analysis of pure carriers and ink samples with Fenofibrate concentrations of 5%, 10%, 20% and 30% (w/w). A) Apifil CG, B) Candelilla, C) Compritol 888 ATO, D) Precirol, E) Compritol HD5 ATO and F) Highlight of the C-Cl peak of Compritol HD5 ATO. In all instances the blue box highlights the two C-C stretch (in ring) peaks at  $1600\text{ cm}^{-1}$  and  $1650\text{ cm}^{-1}$ , while the red highlights the  $765\text{ cm}^{-1}$  peak associated with the C-Cl stretch.

In the range here considered Fenofibrate presents two characteristic set of peaks associated respectively to the carbon rings and to the Chlorine bond. The C-C stretch (in ring) is characterised by two distinct peaks at  $1600\text{ cm}^{-1}$  to  $1650\text{ cm}^{-1}$  while the  $765\text{ cm}^{-1}$  peak is associated with the C-Cl stretch [192, 193]. In the graphs the blue and red boxes highlight respectively the carbon

rings and the Chlorine bond peaks. Although both sets of peaks are characteristic of the presence of Fenofibrate, the  $765\text{ cm}^{-1}$  peak is more reliable since the C-Cl bond can be found only in the Fenofibrate molecule, the latter was chosen as the main focus in the pursuit of a validation method.

From Figure 4.18 and the respective Table 4.13, it is clear that all materials present satisfyingly larger features in correspondence to the higher concentrations of Fenofibrate as expected, meaning that the peak intensity scales with the concentration.

TABLE 4.13: FTIR characterisation of Immediate release tablets via the intensity of the Fenofibrate characteristics,  $765\text{ cm}^{-1}$  and  $1600\text{ cm}^{-1}$  to  $1650\text{ cm}^{-1}$ . The intensities values are given as average  $\pm$  standard error.

	API (w/w)	C-Cl [%]	C-C stretch (in ring) [%]	
		$765\text{ cm}^{-1}$	$1600\text{ cm}^{-1}$	$1650\text{ cm}^{-1}$
Apifil	5%	$21.3 \pm 2.0$	$10.9 \pm 0.7$	$8.6 \pm 1.0$
	10%	$29.9 \pm 1.6$	$11.0 \pm 0.8$	$9.0 \pm 1.0$
	20%	$56.5 \pm 0.8$	$21.0 \pm 0.7$	$19.0 \pm 0.4$
	30%	$80.1 \pm 1.0$	$35.4 \pm 0.4$	$32.9 \pm 0.2$
Candelilla	5%	$13.2 \pm 0.4$	$8.5 \pm 0.2$	$5.5 \pm 0.1$
	10%	$17.3 \pm 0.2$	$13.8 \pm 0.1$	$8.2 \pm 0.2$
	20%	$23.8 \pm 0.5$	$9.9 \pm 0.3$	$8.1 \pm 0.2$
	30%	$42.6 \pm 8.7$	$34.5 \pm 0.2$	$27.2 \pm 0.5$
Compritol 888	5%	$28.4 \pm 0.6$	$11.5 \pm 0.7$	$12.0 \pm 0.7$
	10%	$38.6 \pm 1.6$	$20.6 \pm 1.6$	$20.4 \pm 1.9$
	20%	$51.4 \pm 0.4$	$24.8 \pm 0.1$	$23.5 \pm 0.3$
	30%	$83.4 \pm 0.2$	$48.8 \pm 0.2$	$44.7 \pm 0.2$
Compritol HD5	5%	$23.6 \pm 2.8$	$20.9 \pm 2.5$	$17.9 \pm 3.0$
	10%	$37.0 \pm 3.5$	$39.1 \pm 1.1$	$37.4 \pm 3.1$
	20%	$42.5 \pm 2.9$	$28.8 \pm 2.0$	$18.4 \pm 6.2$
	30%	$70.5 \pm 0.1$	$31. \pm 0.2$	$31.6 \pm 0.2$
Precirol	5%	$28.2 \pm 0.3$	$10.9 \pm 0.1$	$10.8 \pm 1.0$
	10%	$38.6 \pm 1.6$	$20.7 \pm 1.6$	$20.4 \pm 1.9$
	20%	$50.6 \pm 0.9$	$26.6 \pm 2.6$	$25.5 \pm 2.9$
	30%	$83.4 \pm 0.2$	$48.4 \pm 0.4$	$44.0 \pm 0.8$

Moreover, it was possible to successfully fit the values of the peaks intensities using a linear regression strengthening the belief that the correct amount of drug was loaded into the ink preparations, the fit parameters are visible in table 4.14. All the carriers here taken into consideration display similar chemical structure including mixtures of mono-di- and tri- glycerides esters of long chain lipids. It is thus reasonable to expect similar slope values.

In conclusion, although qualitative, this analysis strengthens the validity of the previous assumptions on the amount of drug loaded into each ink.

TABLE 4.14: Parameters of the linear regression of the FTIR intensities associated to the  $765\text{ cm}^{-1}$  peak.

Carrier	intercept	slope	$\chi^2$
Apifil	$7.6 \pm 1.5$	$2.42 \pm 0.1$	0.997
Compritol 888	$16.1 \pm 5.8$	$2.1 \pm 0.3$	0.960
Compritol HD5	$3.3 \pm 1.8$	$2.2 \pm 0.1$	0.933
Precirol	$16.9 \pm 0.3$	$2.2 \pm 0.1$	0.992

#### 4.1.6 Conclusions

In this section the density, melting point, viscosity and drug loading capabilities of the five carrier materials used in this work were characterised and discussed.

All materials presented in this section showed properties that are within the range of printing requirements. Firstly, combining the use of FTIR with a density study it was possible to confirm that the ink preparation method was successful and the inks were composed of the correct ratio of drug to carrier. Furthermore, via the TGA and the DSC analysis it was possible to determine that the material can successfully survive the temperature required for printing without undergoing degradation. In addition it was also shown that it is possible to find a range of temperatures within the working range of the printhead for which the inks are completely melted allowing for ejection.

Lastly, the study of Rheological properties allowed to gain an initial insight into the inks behaviour when subjected to shear stress. In particular it was shown that if the correct temperature is selected all inks can flow with a Newtonian behaviour at high shear rate, as it is expected for a successful print.

Thus, it is possible to conclude that all materials presented are suitable candidates for 3D printing and in the future for multi-material 3D printing.

## 4.2 Results and discussion: 3D deposition of solid dosage forms

The scope of this Section is to explore the possibility of producing drug releasing solid dosage forms via hot-melt inkjet 3D printing using the materials described in Section 4.

3D printing technologies follow a layer-by-layer approach, as a result before attempting to produce 3D structures, it is crucial to optimise each material for 2D depositions. This includes understanding drop sizing, drop spacing (dpi) and single layer thickness. While the first two are necessary to guarantee a dense 2D geometry, the latter determines the resolution in the z direction. Furthermore, the combination of droplet density and native layer height decides the time and energy necessary to produce the final product.

The initial investigation was focused on establishing a set of printing parameters capable of guaranteeing the production of solid 2D designs for each of the selected inks. Based upon insights from this study, the second part is focused on the production and characterisation of 3D objects. Specifically, a set of honeycomb geometries were produced to test the printer capability to manufacture intricate designs without losing resolution. A simple disc geometry was also employed to study the effect of drug loading on drug release from the printlets. Lastly X-ray Powder Diffraction (XRPD) analysis was deployed, when possible, to better understand the crystalline state of the printed material.

### 4.2.1 Drop formation and deposition

The material of section 4.1 were loaded into the main chamber of the printing unit and their printability was evaluated via the use of the ADA analytical function by varying the printing parameters such as temperature, firing pulse shape and applied pressure while monitoring the output as described in Section 3.2.11.

The drop formation was observed by recording still frames of droplets during/after ejection near the nozzle while the printing settings were made to vary. For this purpose a set of reliable nozzle in the centre of the printing unit have been selected for the test.

During this calibration phase particular attention was used in the analysis of the drop tail. Specifically, the droplet needed to show separation from the nozzle and clean tail formation within the frame of acquisition in order

to guarantee recoil before impact on the substrate. Such behaviour is necessary to ensure a round footprint upon deposition and thus avoiding printing imperfections. Furthermore, a longer tail might result in tail separation and satellite formation, which are detrimental to the production of a dense, smooth and highly detailed 2D layer. Indeed, once a satellite is detached from the main drop body the weight of the latter is modified causing a change in its trajectory and consequently a displacement in its landing position that will not coincide with the original design. Besides, the newly formed satellite will have its own flight path determined by its mass ( $\ll$  droplet mass), the velocity of separation and the tail recoil force [80]. The result is a course that is completely different from the one of the original droplet, but which might still bring the satellite to land within the printing pattern causing an imperfection in the print. In the case of satellites landing outside of the region of interest some of the material from the main part is now lost causing a deficit in the end result. Lastly a clean separation from the nozzle is necessary not only to ensure the desired drop speed, but also because it is a key point in the maintenance of a clean working nozzle, assuring that at the moment of separation there is no material pooling on the plate causing misfire, which ultimately dictates the repeatability of the process.

Concurrently the droplet footprints after deposition were analysed to obtain their printed diameter, which was then used establish the print 2D resolution in terms of droplets per inches (DPI).

Once the printing conditions for 2D patterns were established sets of discs with increasing number of layers were produced in order to determine the layer thickness and the consequent native resolution of each material along the z-axis.

#### 4.2.1.1 Drop formation

The establishment of a working set of printing parameter was done exploiting the capabilities of the native ADA program, which allows to cycle over different sets of parameters conditions so to obtain all possible pairing combinations.

The printer was set to work at a constant negative pressure of  $-20$  mbar which prevents nozzle plate flooding during idle times by maintaining a stable ink meniscus at the air/ink interface at the nozzle, preventing jet instability. The Temperature restrictions imposed by both the maximum working temperature of the printheads unit ( $T_{nozzle} \leq 90$  °C as seen in Section 3.2.12) and the melting point of the chosen materials for which  $T_{melt} \geq 85$  °C (see

Section 4.1.2), the range of temperatures available was extremely limited. In order to ensure flowability and thus maximise the ejection rate of success the initial experiments were run at the higher limit of the range, 90 °C. This ensures that all ink compounds are well within the range of viscosity set by the manufacturer, as seen Section 4.1.4. Frequency was adjusted to the shutter frame of the camera and set to  $\sim 900$  Hz and was not representative of the printing firing speed. As a result, the focus was on the determination of the printing pulse parameters (Fig. 4.19), specifically: rising edge, peak time, falling edge and maximum voltage. The aim was to obtain well formed droplets with velocity in the  $3 \text{ m s}^{-1}$  to  $8 \text{ m s}^{-1}$  range, aiming for the higher limit in order to expedite the printing process while retaining precision of deposition. The upper limit is imposed by the maximum moving speed of the printhead and the distance between the substrate and the nozzle, higher velocity would force lower firing rates to guarantee to the same level of precision.

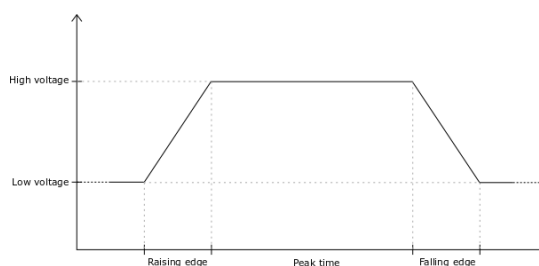


FIGURE 4.19: Piezoelectric actuator trapezoidal printing pulse, highlighted: rising edge, peak time, falling edge, threshold and maximum voltage.

During the optimisation phase the parameters of interest were made to vary one at the time and until all possible combinations were tested. For each cycle the best performing conditions were noted based on the criteria described in the example below. The best results were then compared, and the optimal set of condition selected.

Figures 4.20 shows an example of the optimisation process for Compritol HD5 ATO. Values were made to vary one at a time to understand their effect on droplet formation and ejection.

A similarity in drop behaviour in response of changes in the rise and fall time is clearly visible in Fig. 4.20A and B. Short impulse times  $\leq 1 \mu\text{s}$  are not able to generate a viable drop. As the time interval increases so does the droplet size and velocity until a maximum is reached at  $3 \mu\text{s}$ . Further increment in the inset/outset time causes slower contraction/expansion cycles for the piezoelectric actuators imparting less velocity. A similar reasoning

can be applied to the peak time behaviour where the maximum is reached at  $5 \mu\text{s}$  (Fig. 4.20D).

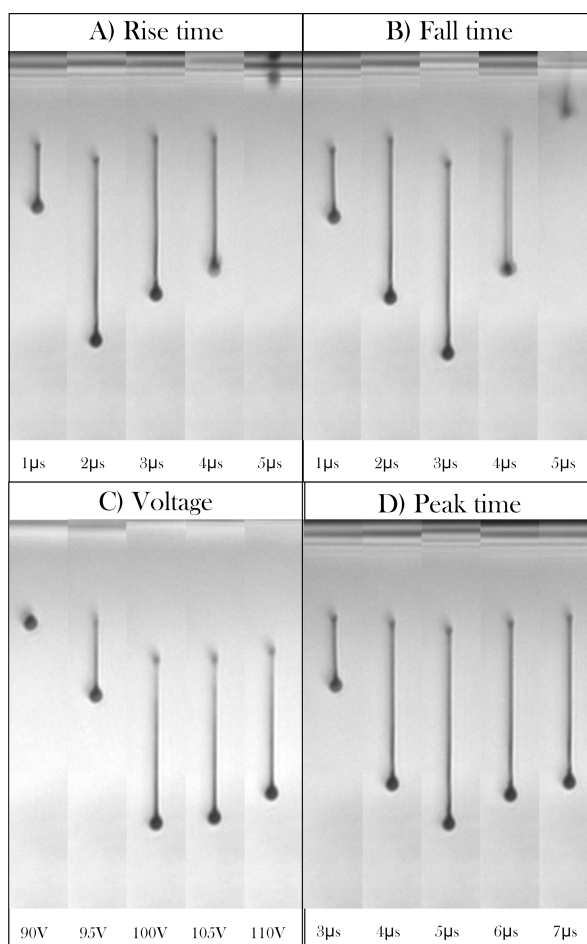


FIGURE 4.20: Printing parameters optimisation via Advance Drop Analysis of Compritol HD5 ATO. The images show the image acquisition of in-flight droplets  $20 \mu\text{s}$  after ejection. A) rise time, B) fall time, C) printhead voltage and D) peak time. The scale of the images is  $1.56 \mu\text{m px}^{-1}$ . The results were obtained as the mean value of five separate acquisitions. The average was rounded to the closest integer. The error provided is calculated as the standard deviation and is here included to provide a measure of the precision associated with each parameter choice.

During the Voltage study it became evident that above a threshold value the increase in voltage power causes minimum variation to the droplet ejection behaviour. The choice of working parameter was thus made on the base of the lowest value providing the highest speed and volume. In this case it was 100 V.

The same process was repeated for all materials and the results are reported in Table 4.15. Notably, minor differences are recorded between inks sharing the same carrier but different drug loading, suggesting that the same

parameters can be used and that the addition of Fenofibrate do not effect printability within the concentration range considered.

TABLE 4.15: Optimised printing waveform parameters.  $T_R$  rise time,  $T_F$  fall time,  $T_P$  peak time, V voltage and u speed.

	<b>Apifil-Fenofibrate (w/w)</b>				
	100-0%	95-5%	90-10%	80-20%	70-30%
$T_R$ [ $\mu\text{s}$ ]	$2 \pm 0.5$	$2 \pm 0.9$	$2 \pm 0.9$	$2 \pm 0.5$	$2 \pm 0.5$
$T_F$ [ $\mu\text{s}$ ]	$2 \pm 0.5$	$2 \pm 0.5$	$2 \pm 0.8$	$2 \pm 0.8$	$2 \pm 0.8$
$T_P$ [ $\mu\text{s}$ ]	$5 \pm 0.5$	$5 \pm 0.5$	$5 \pm 0.5$	$5 \pm 0.6$	$5 \pm 0$
V [V]	$90 \pm 3.2$	$90 \pm 3.2$	$90 \pm 2.6$	$90 \pm 3.2$	$90 \pm 0$
u [ $\text{m s}^{-1}$ ]	$5.15 \pm 0.15$	$5.11 \pm 0.23$	$5.05 \pm 0.14$	$5.04 \pm 0.14$	$5.08 \pm 0.20$
	<b>Candelilla-Fenofibrate (w/w)</b>				
	100-0%	95-5%	90-10%	80-20%	70-30%
$T_R$ [ $\mu\text{s}$ ]	$4 \pm 0.52$	$4 \pm 0.82$	$4 \pm 0.97$	$4 \pm 0.00$	$4 \pm 0.82$
$T_F$ [ $\mu\text{s}$ ]	$4 \pm 0.52$	$4 \pm 0.51$	$4 \pm 0.00$	$4 \pm 0.52$	$4 \pm 0.82$
$T_P$ [ $\mu\text{s}$ ]	$6 \pm 0.63$	$6 \pm 0.82$	$6 \pm 0.82$	$6 \pm 0.82$	$6 \pm 0.00$
V [V]	$100 \pm 4.08$	$100 \pm 4.83$	$100 \pm 4.08$	$101 \pm 4.83$	$100 \pm 3.16$
u [ $\text{m s}^{-1}$ ]	$4.45 \pm 0.24$	$4.40 \pm 0.29$	$4.38 \pm 0.19$	$4.33 \pm 0.19$	$4.30 \pm 0.19$
	<b>Compritol HD5-Fenofibrate (w/w)</b>				
	100-0%	95-5%	90-10%	80-20%	70-30%
$T_R$ [ $\mu\text{s}$ ]	$3 \pm 0.82$	$3 \pm 0.00$	$3 \pm 0.00$	$3 \pm 0.52$	$3 \pm 0.52$
$T_F$ [ $\mu\text{s}$ ]	$3 \pm 0.52$	$3 \pm 0.52$	$3 \pm 0.63$	$3 \pm 0.52$	$3 \pm 0.52$
$T_P$ [ $\mu\text{s}$ ]	$5 \pm 0.52$	$5 \pm 0.52$	$5 \pm 0.52$	$5 \pm 0.63$	$5 \pm 0.00$
V [V]	$100 \pm 3.16$	$100 \pm 3.16$	$100 \pm 0.00$	$100 \pm 4.83$	$100 \pm 2.58$
u [ $\text{m s}^{-1}$ ]	$6.01 \pm 0.10$	$6.03 \pm 0.16$	$6.04 \pm 0.15$	$6.07 \pm 0.14$	$6.12 \pm 0.21$
	<b>Compritol 888-Fenofibrate (w/w)</b>				
	100-0%	95-5%	90-10%	80-20%	70-30%
$T_R$ [ $\mu\text{s}$ ]	$3 \pm 0.97$	$3 \pm 0.00$	$3 \pm 0.26$	$3 \pm 0.52$	$3 \pm 0.82$
$T_F$ [ $\mu\text{s}$ ]	$3 \pm 0.63$	$3 \pm 0.52$	$3 \pm 0.52$	$3 \pm 0.52$	$3 \pm 0.82$
$T_P$ [ $\mu\text{s}$ ]	$5 \pm 0.63$	$5 \pm 0.52$	$5 \pm 0.00$	$5 \pm 0.63$	$5 \pm 0.00$
V [V]	$100 \pm 3.16$	$100 \pm 2.58$	$100 \pm 0.00$	$100 \pm 5.16$	$100 \pm 2.58$
u [ $\text{m s}^{-1}$ ]	$6.096 \pm 0.09$	$6.05 \pm 0.15$	$6.07 \pm 0.20$	$6.04 \pm 0.13$	$6.12 \pm 0.14$
	<b>Precirol-Fenofibrate (w/w)</b>				
	100-0%	95-5%	90-10%	80-20%	70-30%
$T_R$ [ $\mu\text{s}$ ]	$3 \pm 0.82$	$3 \pm 0.00$	$3 \pm 0.00$	$3 \pm 0.52$	$3 \pm 0.52$
$T_F$ [ $\mu\text{s}$ ]	$3 \pm 0.52$	$3 \pm 0.52$	$3 \pm 0.63$	$3 \pm 0.52$	$3 \pm 0.52$
$T_P$ [ $\mu\text{s}$ ]	$6 \pm 0.63$	$6 \pm 0.82$	$6 \pm 0.63$	$6 \pm 0.52$	$6 \pm 0.82$
V [V]	$105 \pm 2.58$	$105 \pm 3.16$	$105 \pm 4.08$	$105 \pm 2.58$	$105 \pm 4.08$
u [ $\text{m s}^{-1}$ ]	$5.4 \pm 0.19$	$5.52 \pm 0.20$	$5.52 \pm 0.19$	$5.42 \pm 0.34$	$5.52 \pm 0.12$

#### 4.2.1.2 Drop deposition, 2D and 3D resolution

The main goal of the drop deposition study was to determine the x, y and z resolution achievable for each material. Specifically, the former two are determined by the working DPI which allows for a smooth and dense 2D layer. The latter is defined by the single layer thickness.

The DPI of a material was determined as the number of droplets necessary to obtain a 1 inch long continuous line with constant width.

However, when two droplets come in contact a change in the overall shape takes place and can cause the displacement of one or both the original droplets depending on the boundary conditions. Therefore, in order to fully optimise the 2D deposition it is necessary to understand not only the impact size of a single droplets, but also fluid interactions between droplets deposited sequentially.

"Drawback" effect refers to the withdrawal of the droplets edges along the axis joining the centres causing a shrinkage of the overall footprint of the combined drops compared to the initial individual ones [224]. This effect becomes more pronounced if the first droplet have had the time to cool and solidify before the impact of the second. The former will then withdraw less causing asymmetry. To avoid this for the experiments here presented the substrate temperature was kept at a stable 40 °C, to ensure merging between subsequent drop depositions while allowing curing between layers. Ideally, to form lines it should be enough to deposit consistently spaced overlapping droplets, however due to drawback this might not lead to the desired outcome and instead cause line interruption or scalloping depending on droplet pacing.

After determining the single droplet size via microscope analysis, a series of single lines with increasing drop spacing was printed with the aim to identify the best DPI to obtain a continuous and homogeneous printed line. To best understand the material behaviour two key parameters were identified,  $\lambda$  and  $\theta$ . The former defines the extent of overlap between two droplets and can be written as:

$$\lambda = 1 - \frac{L}{D_s} \quad (4.1)$$

where L is the center-to-center distance between two consecutive droplets and  $D_s$  is the single droplet diameter after impact and solidification on the substrate measured from photographs.

The drawback index is indicated with  $\theta$  and can be calculated as follows:

$$\theta = \frac{D_y}{D_s + L} \xrightarrow{D_y = \sqrt[3]{2}D_s} \theta_{eq} = \frac{\sqrt[3]{2}}{2 - \lambda} \quad (4.2)$$

where  $D_y$  is the real measurement and can be approximated to  $D_y = \sqrt[3]{2}D_s$  when the two droplet system reaches the equilibrium.

The relationship between the two determines the capability of the material to form a continuous un-broken line. Specifically Li and coworker [224] determined the existence of a critical condition:

$$\theta = \frac{2(1 - \lambda)}{2 - \lambda} \quad (4.3)$$

which divides the  $\lambda - \theta$  plane into two separate regions (breakup and non-breakup) as visible in Fig. 4.21.

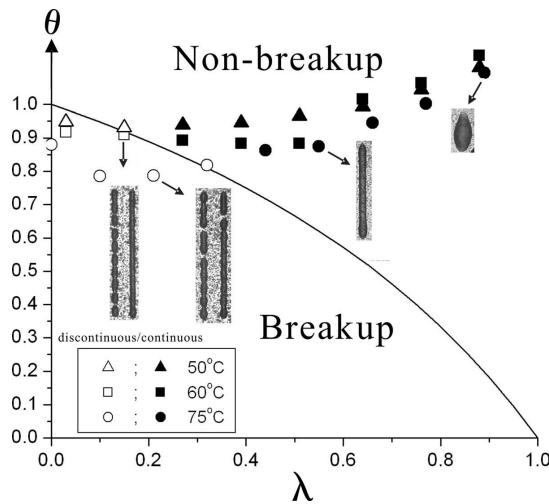


FIGURE 4.21: Equation 4.3 is plotted as a curved line that divides the first quadrant into break-up and non-break-up regions. Figure from "Drawback during deposition of overlapping molten wax droplets"[224]

Combining our results with the non-breakup condition it was possible to optimise the printing resolution on the X-Y plane. The final results for the pure carrier materials are reported in Table 4.16.

Along the Z-axis the resolution is equivalent to the minimum layer height, which was easily obtained by printing a set of five discs each with an increasingly higher number of layers. The overall part height was then measured using a caliper (HILKA TOOLS Digital Calipers) and divided by the number of layers. The obtained values were then averaged to determine the set layer thickness. The process was then repeated five more times and the results averaged and reported in Table 4.16.

TABLE 4.16: Optimised depositional parameters. The values are reported as mean value  $\pm$  standard deviation when resulting from direct measurements, otherwise the error were calculated by propagation.

<b>Apifil</b>				
$D_s$ [ $\mu\text{m}$ ]	$\lambda$ [%]	$\theta$	Layer thickness [ $\mu\text{m}$ ]	DPI [ $\text{inch}^{-1}$ ]
$73.56 \pm 0.31$	$63.65 \pm 1.70$	$0.92 \pm 0.32$	$72.63 \pm 1.24$	950
<b>Candelilla</b>				
$D_s$ [ $\mu\text{m}$ ]	$\lambda$ [%]	$\theta$	Layer thickness [ $\mu\text{m}$ ]	DPI [ $\text{inch}^{-1}$ ]
$61.05 \pm 0.61$	$60.37 \pm 2.00$	$0.90 \pm 0.25$	$68.23 \pm 0.18$	1050
<b>Compritrol HD5</b>				
$D_s$ [ $\mu\text{m}$ ]	$\lambda$ [%]	$\theta$	Layer thickness [ $\mu\text{m}$ ]	DPI [ $\text{inch}^{-1}$ ]
$62.64 \pm 0.36$	$61.38 \pm 3.74$	$0.91 \pm 0.49$	$67.57 \pm 0.37$	1050
<b>Compritrol 888</b>				
$D_s$ [ $\mu\text{m}$ ]	$\lambda$ [%]	$\theta$	Layer thickness [ $\mu\text{m}$ ]	DPI [ $\text{inch}^{-1}$ ]
$64.28 \pm 0.38$	$62.37 \pm 2.12$	$0.91 \pm 0.29$	$68.84 \pm 0.45$	1050
<b>Precitol</b>				
$D_s$ [ $\mu\text{m}$ ]	$\lambda$ [%]	$\theta$	Layer thickness [ $\mu\text{m}$ ]	DPI [ $\text{inch}^{-1}$ ]
$76.00 \pm 0.53$	$62.86 \pm 2.23$	$0.92 \pm 0.45$	$65.77 \pm 0.47$	900

## 4.2.2 3D functional deposition

Here the knowledge gathered in the previous section is used to create functional 3D tablets for the delivery of Fenofibrate. The goal is to select the best performing carrier amongst the one selected, which will then be used in the following chapter to showcase the present and future capabilities of the multi-material approach proposed in this work. The carriers' performance evaluation was based on two properties, their capability to produce high precision design, fundamental in the production of complex geometries, and their ability to release the drug. To assess drug delivery capacity a standard circular tablet design was implemented (10 mm diameter and 5 mm height), see Fig. 4.22A. In addition three honeycomb geometries were selected to investigate the quality of the printed dosage forms (cell diameter: 0.6 mm, 1.22 mm and 1.83 mm). The digital design is shown in Fig. 4.22B, C,

D. For each geometry and carrier material tablets containing Fenofibrate at 5% (w/w), 10% (w/w), 20% (w/w) and 30% (w/w) were printed utilising the optimised set of printing conditions and working parameters found in Sections 4.2.1.2 of this chapter.

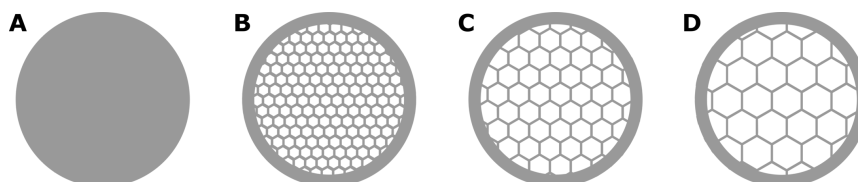


FIGURE 4.22: Digital design of 3D functional tablets. Top view of A) full disc (100% infill), B) honeycomb with cell diameter of 0.60 mm (45% infill), C) 1.22 mm (24% infill) and D) 1.83 mm (17% infill).

While variation in tablets geometry and specifically the use of a honeycomb design offer a series of benefits including higher surface area to volume ratio, in this section their use will be limited to test for the printing capability of each ink to produce complex geometries.

In the next Chapter 5 the benefit associated with this choice of geometry will be discussed in depth alongside an example of its application.

#### 4.2.2.1 Optical imaging

From a visual point of view all tablets were printed with the same degree of success regardless of the choice of carrier material or drug concentration, suggesting that given the correct set of printing parameters the drug content does not influence the printed results in this example. In Figure 4.23 a representative set of tablets are displayed per carrier type, specifically for 10% (w/w) Fenofibrate.

Each set includes three honeycomb structured samples (cell diameter: 0.6 mm, 1.22 mm and 1.83 mm) alongside with a conventional disc tablet all with diameter of 10 mm. By visual inspection all tablets are well-defined, with a smooth surface, free channels and without appreciable defects. Upon closer inspection printing lines typical of the 3D depositional process can be found on the top surface. Though undesired this feature does not compromise the functionality of the tablet or dissolution process and should thus not be considered a concern. In contrast to the top, surface of the bottom is smooth and even by virtue of the choice of substrate (PET) on to which the tablets were printed.

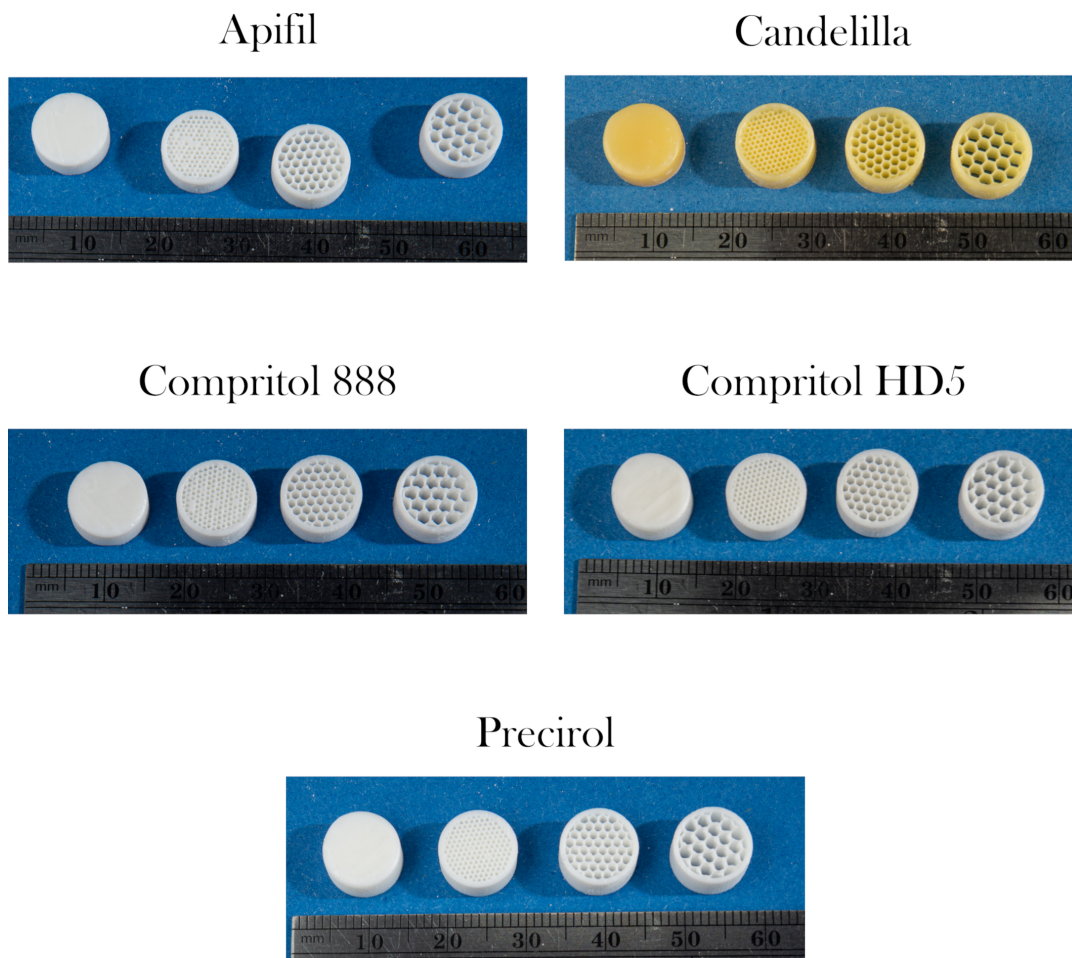


FIGURE 4.23: Photos of 3D printed tablets showing three honeycomb structured (cell diameter: 0.6 mm, 1.22 mm, 1.83 mm) alongside with a conventional disc tablet with diameter of 10 mm. Tablets are grouped based on carrier material, A) Apifil CG, B) Candelilla, C) Compritol 888 ATO, D) Compritol HD5 ATO and E) Precirol ATO 5.

Each set of tablets was prepared with 10% (w/w) Fenofibrate concentration.

#### 4.2.2.2 Drug loading evaluation

An essential step before the *in vitro* dissolution study was the determination of the drug content in each of the printed tablets. This was done with a double intent, firstly to validate hot-melt inkjet printing as a method for producing accurate dosing, secondly to accurately interpret the raw dissolution results.

To this end all tablets were weighted and the weight of the active ingredient calculated on the basis of the density of the constituents as determined in Section 4.1.1. While drug weight is most commonly calculated by % assay by High Performance Liquid Chromatography (HPLC), this method could not be applied in this situation. Indeed, the carrier materials here utilize are not

easily dissolvable and have Chloroform as their main solvent, which is incompatible with the HPLC technology. The results are reported in Table 4.17.

TABLE 4.17: Study of the Fenofibrate content in 3D printed derived from density calculations.

	Fenofibrate (w/w)	Tablet's weight [mg]	Fenofibrate's weight [mg]
<b>Apifil</b>	5%	354.7 ±0.8	17.7±0.4
	10%	356.1±0.9	35.6±0.6
	20%	367.7±0.6	73.5±0.3
	30%	380.8±1.6	114.2±0.5
<b>Candelilla</b>	5%	362.5 ±0.9	18.1±0.9
	10%	358.5±1.6	35.8±0.6
	20%	370.4±1.5	74.1±1.5
	30%	382.4±1.8	114.7±0.4
<b>Compritol 888</b>	5%	347.5 ±1.3	17.4±0.4
	10%	348.6±0.9	34.9±0.5
	20%	357.1±0.8	71.4±0.2
	30%	366.2±1.7	109.9±0.4
<b>Compritol HD5</b>	5%	352.9 ±2.0	17.7±2.0
	10%	358.7±1.7	35.9±1.7
	20%	363.2±1.4	72.6±1.4
	30%	370.4±1.3	111.1±1.3
<b>Precirol</b>	5%	348.9 ±2.3	17.4±2.3
	10%	342.8±1.3	35.9±1.3
	20%	354.5±0.5	70.9±0.5
	30%	366.0±1.4	109.8±1.4

To further confirm the results found using the density approach one of the printed tablets from each batch was selected to be analysed using FTIR. As previously seen in Section 4.1.5 the  $765\text{ cm}^{-1}$  peak is uniquely associated with the C-Cl and was here employed as a marker to judge the quantity of Fenofibrate within each tablet.

In Table 4.18 a comparison of peak intensities from the tablet samples to the reference value previously recorded for the ink materials is shown. The

results are consistent, within the error, and suggest that the printing process does not effect ink composition. Furthermore, since samples for FTIR analysis were taken from different regions within the tablets, but yield consistent results it is possible to infer that Fenofibrate is homogeneously distributed throughout the tablet.

TABLE 4.18: FTIR characterisation of Immediate release tablets via the intensity of the Fenofibrate characteristic  $765\text{ cm}^{-1}$  peak.

	Fenofibrate (w/w)	Reference [%]	Tablet [%]
<b>Apifil</b>	5%	$21.3 \pm 2.0$	$21.0 \pm 0.6$
	10%	$29.9 \pm 1.6$	$29.9 \pm 0.7$
	20%	$56.5 \pm 0.8$	$63.7 \pm 2.3$
	30%	$80.1 \pm 0.8$	$80.6 \pm 0.5$
<b>Candelilla</b>	5%	$13.2 \pm 0.4$	$13.3 \pm 0.2$
	10%	$17.3 \pm 0.2$	$17.3 \pm 0.2$
	20%	$23.8 \pm 0.5$	$23.7 \pm 0.2$
	30%	$42.6 \pm 8.5$	$47.6 \pm 0.7$
<b>Compritol HD5</b>	5%	$23.6 \pm 2.3$	$22.7 \pm 0.7$
	10%	$37.0 \pm 3.4$	$38.7 \pm 3.0$
	20%	$42.5 \pm 0.9$	$44.9 \pm 4.4$
	30%	$70.5 \pm 0.6$	$70.5 \pm 0.8$
<b>Compritol 888</b>	5%	$28.4 \pm 0.5$	$28.4 \pm 0.4$
	10%	$38.6 \pm 1.6$	$38.3 \pm 0.4$
	20%	$51.4 \pm 0.4$	$51.3 \pm 0.3$
	30%	$83.4 \pm 0.2$	$83.4 \pm 0.2$
<b>Precirol</b>	5%	$28.2 \pm 0.3$	$28.8 \pm 2.0$
	10%	$38.6 \pm 1.6$	$36.8 \pm 0.9$
	20%	$50.6 \pm 0.9$	$49.5 \pm 0.5$
	30%	$83.4 \pm 0.2$	$83.1 \pm 0.8$

### 4.2.2.3 Drug crystallinity: X-ray Powder diffraction (XRPD)

Drug crystallinity plays a key role in molecular mobility and drug availability, with lower degrees of crystallinity associated with higher release rates and reduced physical stability [225, 226, 227, 228].

Thus, before the dissolution study it was important to understand the crystalline state of the 3D printed tablets. For this purpose samples were prepared by crushing the printlets using a mortar and pestle into a fine powder and analysed following the procedure described in Section 3.2.10. Unfortunately, only samples from Compritol 888 ATO, Compritol HD5 ATO and Precirol ATO 5 had the correct brittleness to allow grinding via mortar and pestle.

Fig. 4.24 shows the results for Compritol HD5 ATO, Fig. 4.25 for Compritol 888 ATO and Fig. 4.26 for Precirol ATO 5.

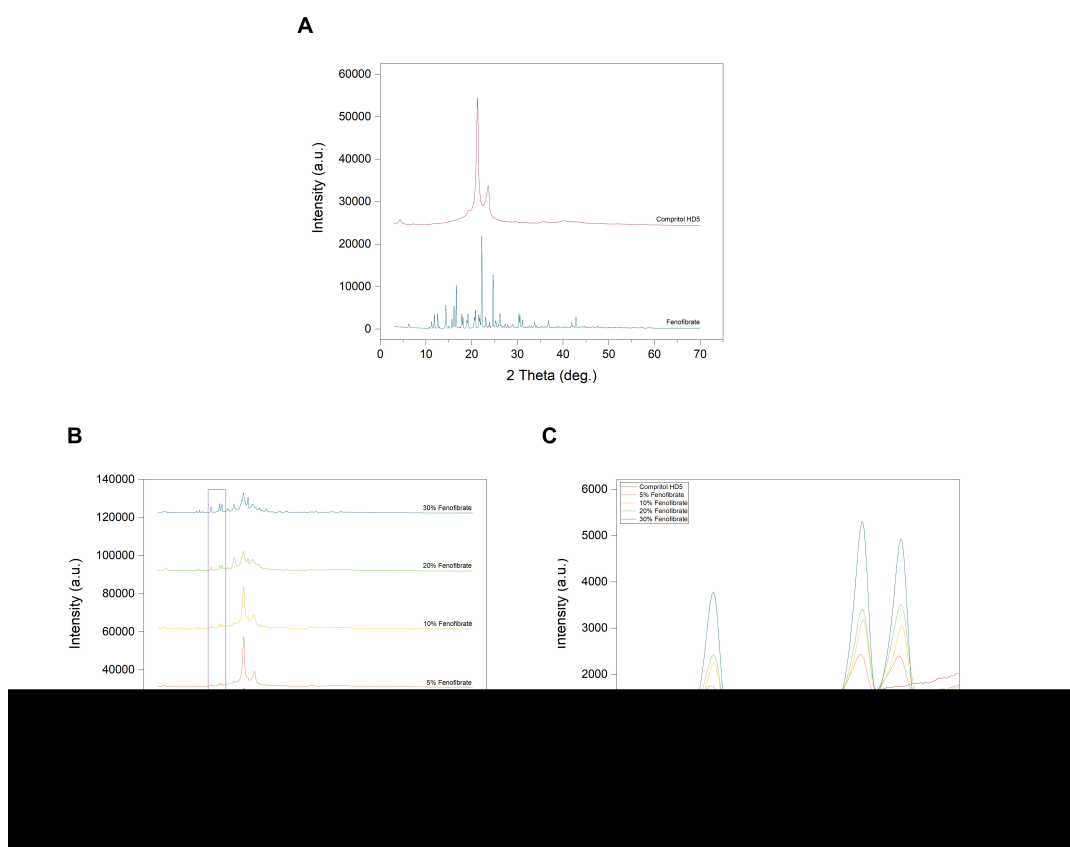


FIGURE 4.24: X-ray powder diffraction curves of A) pure Fenofibrate and Compritol HD5 ATO. B) Mixture of the two at 5%(w/w), 10%(w/w), 20%(w/w) and 30%(w/w) highlighted the region of interest which has been enlarged in figure C).

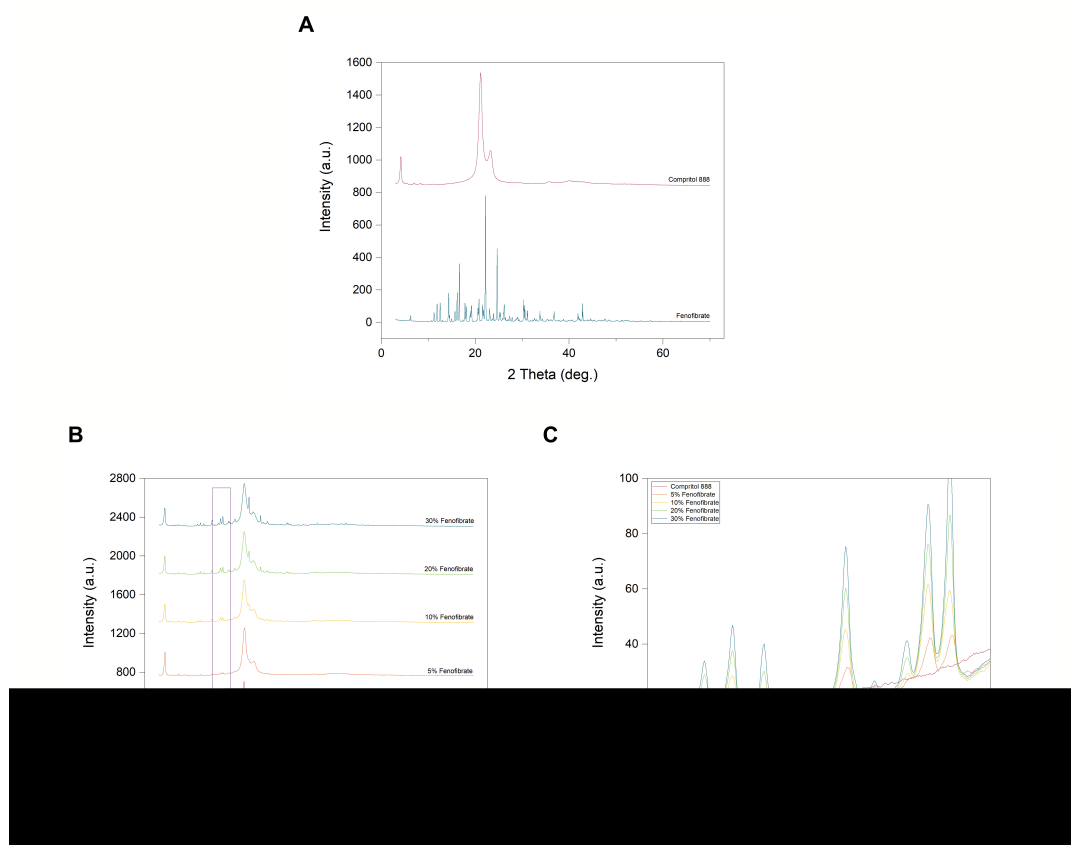


FIGURE 4.25: X-ray powder diffraction curves of A) pure Fenofibrate and Compritol 888 ATO. B) Mixture of the two at 5%(w/w), 10%(w/w), 20%(w/w) and 30%(w/w) highlighted the region of interest which has been enlarged in figure C).

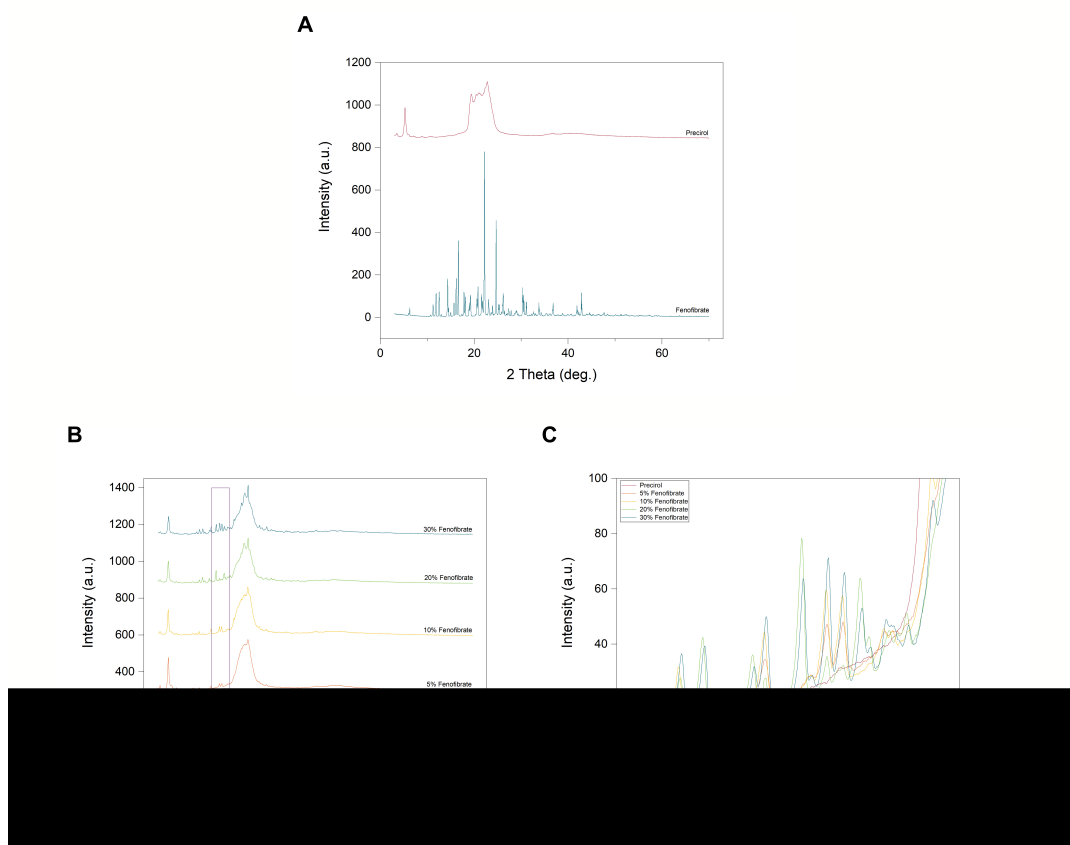


FIGURE 4.26: X-ray powder diffraction curves of A) pure Fenofibrate and Precirol ATO 5. B) Mixture of the two at 5%(w/w), 10%(w/w), 20%(w/w) and 30%(w/w) highlighted the region of interest which has been enlarged in figure C).

The PXRD scans of pure Compritol HD5 ATO, pure Compritol 888 ATO and pure Fenofibrate (Fig. 4.24A and Fig. 4.25A) revealed the presence of diffraction bands characteristic of crystalline substances. In the previous section it was seen that Compritol HD5 ATO differs from Compritol 888 ATO on the addition of PEG-8 mono- and di- esters of (C21) behenic acid, here it is visible that both material show similar spectra with the exception of a peak at  $\theta = 4$ . In particular, while XRPD scans for Compritol HD5 ATO and Compritol 888 ATO show sharp high-intensity peaks (Fig. 4.24A top, Fig. 4.25A top), Precirol ATO 5 instead (Fig. 4.26A) displays much broader peaks. Suggesting that all carriers form crystalline structures. Similar reasoning can be used for the analysis of the pure drug (Fig. 4.24A bottom) which clearly presents crystalline formations.

The diffraction pattern of the binary mixtures, Fenofibrate plus carrier, (Fig. 4.24 B-C, Fig. 4.25 B-C and Fig. 4.26B-C ) exhibit a number of reflection peaks which are consistent with the direct combination of the spectra

of the original components. Fenofibrate was therefore not molecularly dispersed within the carrier in these studies, but remained at least partially in a crystalline state. At a first glance these observations seems to contradict the results from the DSC analysis. A possible explanation to reconcile these contrasting findings, implies that while part of the Fenofibrate drug can be found in a crystalline form as shown in the PXRD, this must be below the detection limit of the DSC instrument (.ca 5% w/w) indicating that the remaining content must be in a disorderly state (non-crystalline) and thus justifying the absence of melting peak in the DSC figure. This hypothesis is furthermore supported by the initial assumption that Fenofibrate tends to form an eutectic mixture when combined with the carriers here analysed.

#### 4.2.2.4 *In Vitro* release study

*In vitro* drug dissolution studies are a fundamental technique used in understanding the drug release of oral dosage forms [229]. Here, samples were tested according to the procedure described in Section 3.2.13 and 3.2.14.

To correctly relate the absorbance intensity of the fenofibrate peak ( $\lambda_{max} = 290$  nm) in the UV-Vis spectrum with the drug content in the analysed sample a calibration curve was produced by dissolving known quantity of fenofibrate in a predetermined volume of buffer solution. Specifically the following concentrations were selected: (0, 1, 2, 5, 10, 20, 50, 500) $\mu\text{g ml}^{-1}$ , five samples per concentration were analysed.

The intensity of such samples were then determined, averaged and fitted using linear regression (equation 4.4) to determine the relation between the peak intensity and the drug quantity.

$$y = y_0 + m \cdot x \quad (4.4)$$

Where  $y_0$  is the intercept,  $m$  is the slope,  $x$  is the concentration and  $y$  the absorbance peak intensity. The fit parameters are reported in Table 5.6.

TABLE 4.19: UV-Vis Fenofibrate calibration curve parameters.

Intercept [ml/ $\mu\text{g}$ ]	Slope [a.u.]	$R^2$
$0.00141 \pm 0.00043$	$0.00669 \pm 0.00001$	0.999

The amount of drug released given a determined absorbance intensity is then obtained by rearranging Eq. 4.4, as follows,

$$x = \frac{y - y_0}{m} \quad (4.5)$$

Figure 4.27 displays the results of the *in vitro* drug release study for the disc tablet, grouped on the base of the carrier material (Apifil CG, Candelilla, Compritol 888 ATO, Compritol HD5 ATO and Precitrol) and colour coded on the base of drug content, respectively **red** for 5%, **yellow** for 10%, **green** for 20% and **blue** for 30%.

The release data show that the choice of carrier had a major effect on the release rate. So, while all formulations displayed sustained release over the period in consideration, the rate of release varied. Interestingly regardless of matrix material in all formulations the lowest drug loading tablets (5% and 10% w/w) showed the fastest release rate.

This behaviour is consistent with the XRD and DSC findings and the suggestion that Fenofibrate can be found in a crystalline and amorphous form within the tablets. In particular it can be expected that at higher drug loading a greater proportion of the drug will be in the crystalline state as only a limited amount of the drug is held in the amorphous/dispersed state and hence the higher the loading (i.e. more crystalline) the relatively slower the release [227, 228]. It is also important to understand that for Apifil CG, Candelilla, Compritol 888 ATO and Precitrol there was no observable swelling or change in shape that occurred during dissolution. In contrast, Compritol HD5 ATO underwent an erosion process.

From the data in Fig. 4.27 **Candelilla** displays the most limited dissolution behaviour regardless of active ingredient concentration, with a maximum release of 12% of the total amount within the first 10 h in the case of 10% (w/w) drug loading.

With respect to Candelilla, **Apifil CG** presents a sharp increase in release capability with almost four times the amount of drug delivered in the same time frame. Specifically, the tablets containing 5% (w/w) Fenofibrate delivered 40% of the initial drug loading, followed by 32% of the 10% (w/w) load and finally 13% and 7% of the 20% and 30% (w/w) drug content respectively.

Considering the relative release profiles of Compritol 888 ATO, Compritol HD5 ATO and Precitrol ATO 5 the latter two have the highest drug release amount during dissolution, followed closely by Compritol 888 ATO.

**Compritol 888 ATO** displays once again the fastest release rate behaviour for 5% and 10% drug loading, the latter reaching the maximum of 68% release of the initial content while the former only delivered 50%. In contrast the two highest loading were below 25% of delivery by the tenth hour.

While both Compritol HD5 ATO and Precirol ATO 5 displayed relatively fast drug delivery capabilities, Compritol HD5 ATO demonstrated the highest drug delivery and most importantly the highest release was achieved by the tablet containing 10% of active ingredient against the 5% of Precirol ATO 5. Allowing for the delivery of a greater amount of Fenofibrate within the same time frame.

Specifically **Compritol HD5 ATO** was capable of delivering up to 88% of its initial 10% loading, followed by 80% of the 5% loading.

**Precirol ATO 5** released 82% of drug content from the 5% tablet and only 59% of the 10% tablet.

In both cases the tablets including more than 20% of Fenofibrate were incapable of releasing more than 35% of the initial content within 10 h.

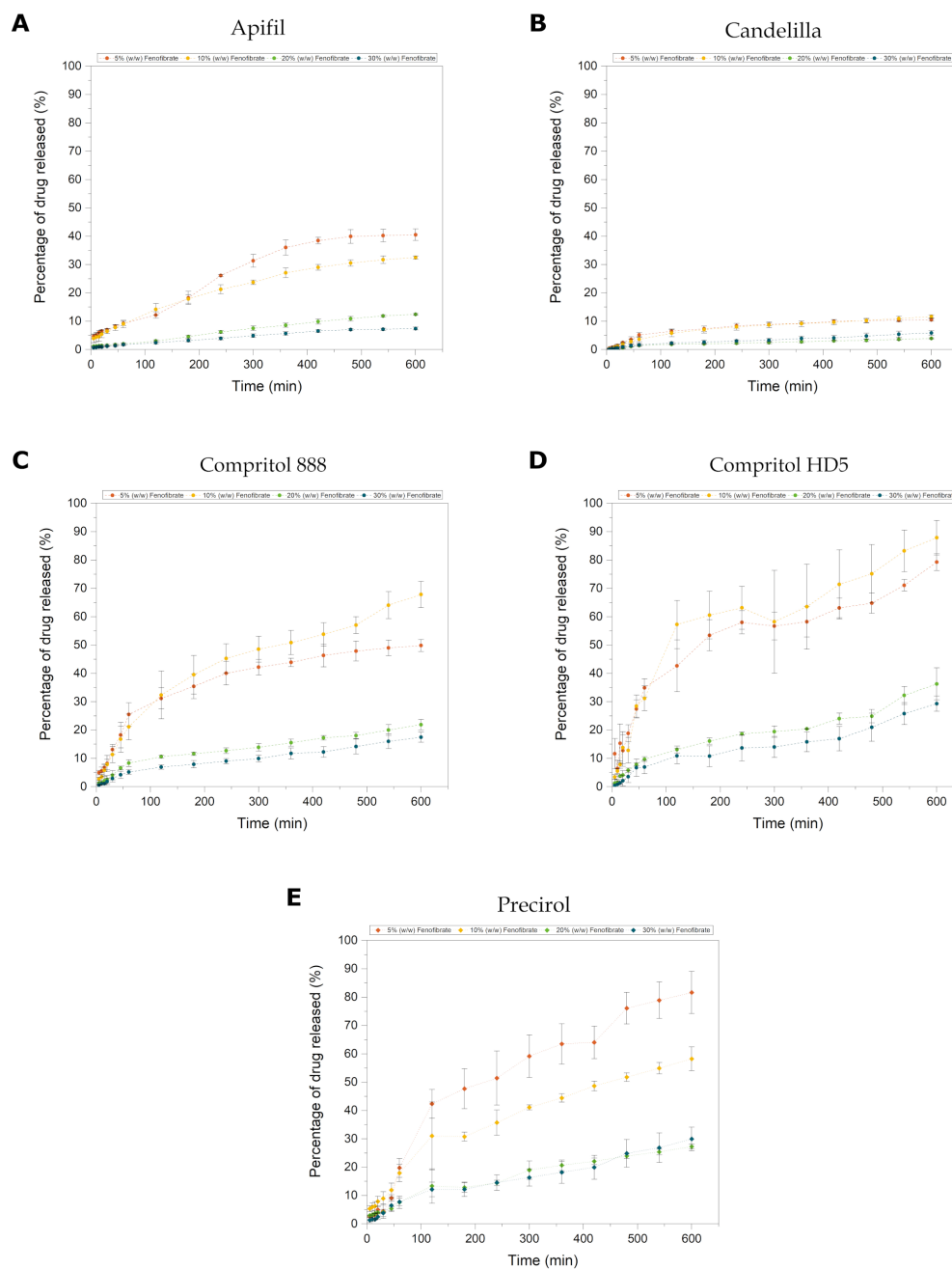


FIGURE 4.27: Dissolution profiles of printed circular tablets (10 mm diameter) as a function of time, drug concentration and carrier material,  $n=3$ . Data are grouped based on carrier material, A) Apifil CG, B) Candelilla, C) Compritol 888 ATO, D) Compritol HD5 ATO and E) Precirol ATO 5. For each matrix material tablets were prepared with four different drug loading concentrations namely 5%, 10%, 20% and 30% which are identified in the graphs respectively by the colours red, yellow, green and blue

### **Drug release kinetics**

To better understand the underlying drug release mechanisms displayed by the different formulations, the collected data were fitted accordingly to the most common models: Zero-order, First-order, Higuchi and Korsmeyer-Peppas kinetic models [230, 231, 232]. The  $R^2$  values of the data fits are summarised in Table 4.20, and in bold are highlighted the best results for each set of conditions.

In the case of both Apifil CG and Precirol ATO 5 two different behaviours can be seen depending on drug concentration. Lower API content are best fitted by the Higuchi model while at higher concentrations a first order model best represents the data suggesting that past a loading threshold and the amount of drug released is proportional to the amount of remaining drug in the matrix, suggests the drug is released primarily by diffusion [230]. Tablets prepared using Candelilla and Compritol 888 ATO as matrix materials showed single behaviour regardless of drug loading and were best fitted using the Higuchi model indicating diffusion as the main release mechanism. It is important to note that the tablets remained intact during the dissolution studies, and no observable swelling or change in shape occurred. These materials are expected to form an insoluble network structure, making diffusion the only method possible for fluid to penetrate within the tablet and subsequently extract the drug through the same method [233].

Compritol HD5 ATO based tablets showed a distinctly different behaviour to the rest of the test group, undergoing degradation during the dissolution process. Such behaviour is mirrored in the kinetic model fit, Korsmeyer-Peppas, with a release exponent  $n = 0.650-0.790$  which indicates that the release is non-Fickian or anomalous transport, and the mechanism of drug release is governed by diffusion and swelling or erosion [230, 234].

TABLE 4.20: Drug release kinetics study.  $R^2$  values of Zero-order, First-order, Higuchi and Korsmeyer-Peppas kinetic models of release data from 10h in vitro release of Apifil CG-Fenofibrate (5%, 10%, 20% and 30% w/w), Candelilla-Fenofibrate (5%, 10%, 20% and 30% w/w), Compritol 888 ATO-Fenofibrate (5%, 10%, 20% and 30% w/w), Compritol HD5 ATO-Fenofibrate (5%, 10%, 20% and 30% w/w) and Precirol-Fenofibrate (5%, 10%, 20% and 30% w/w). In bold the best fitting parameter.

	API	Zero order	First order	Higuchi	Korsmeyer-Peppas	n
	(w/w)	$R^2$	$R^2$	$R^2$	$R^2$	
Apifil	5%	0.957	0.966	<b>0.968</b>	0.952	0.52
	10%	0.959	0.973	<b>0.995</b>	0.982	0.502
	20%	0.995	<b>0.996</b>	0.964	0.935	0.567
	30%	0.983	<b>0.985</b>	0.98	0.973	0.554
Candelilla	5%	0.842	0.85	<b>0.954</b>	0.948	0.641
	10%	0.909	0.917	<b>0.987</b>	0.958	0.770
	20%	0.93	0.932	<b>0.982</b>	0.946	0.725
	30%	0.966	0.968	<b>0.984</b>	0.969	0.712
Compritol HD5	5%	0.873	0.937	<b>0.958</b>	0.924	0.473
	10%	0.851	0.933	0.944	<b>0.947</b>	0.655
	20%	0.958	0.960	0.965	<b>0.968</b>	0.650
	30%	0.954	0.953	0.95	<b>0.955</b>	0.790
Compritol 888 ATO	5%	0.844	0.892	<b>0.964</b>	0.960	0.528
	10%	0.924	0.972	<b>0.990</b>	0.977	0.677
	20%	0.931	0.944	<b>0.982</b>	0.964	0.609
	30%	0.966	0.972	<b>0.984</b>	0.975	0.665
Precirol	5%	0.921	0.979	<b>0.981</b>	0.959	0.844
	10%	0.943	0.978	<b>0.99</b>	0.978	0.561
	20%	0.966	0.975	<b>0.987</b>	0.969	0.515
	30%	0.97	<b>0.976</b>	0.973	0.975	0.670

#### 4.2.2.5 Conclusions

In this section were presented several printing resolution tests aimed at identifying the optimal printing conditions to guarantee successful 3D deposition of solid dosage forms. All five carrier materials identified in Section 4 (Apifil CG, Candelilla, Compritol 888 ATO, Compritol HD5 ATO and Precirol ATO 5) were here tested using a combination of Advanced Droplet Analysis and optical microscopy. Despite the differences in their properties it was possible to achieve good drop formation for all five materials. From the ADA study it was observed that the duration of the rise and fall time act symmetrically on droplet formation, extremely short impulse times  $\leq 1 \mu\text{s}$  are not strong enough to generate a satisfying drop while increment of the inset/outset time past the optimum point cause slower contraction/expansion cycles for the piezoelectric actuators imparting less velocity and causing slower droplets. Similar reasoning can be applied to the analysis of the peak time. Furthermore, all inks displayed speed in the  $4 \text{ m s}^{-1}$  to  $6 \text{ m s}^{-1}$  range which is ideal for inkjet printing [80], it is important to notice that the shown speed corresponds to the main body of the droplet.

Despite the differences in the nature, all materials achieved good 2D results when the overlap was set to approximately 60% of the droplet size. This observation is consistent with the upper limit of what previously reported [224, 95].

Such results were then used to produce 3D solid dosage forms with complex honeycomb geometry and disc shape tablets with variable drug loading. The results were well-defined tablets, with a smooth surface, free channels and without appreciable defects, validating hot-melt inkjet printing as a method of reliably producing printlets with complex 3D geometry.

FTIR analysis of samples before and after the printing process show no change in the material indicating that the printing process do not effect ink composition. Furthermore, both FTIR and XRD analysis showed that there was no detectable interaction between the chosen excipients and the drug, with the latter being partially in a crystalline and partially in a disorderly state.

The *in vitro* drug release of disc tablet made of diverse carrier and containing drug concentration ranging from 5% to 30% (w/w) Fenofibrate revealed that all carriers were capable of producing sustained drug release for the entire duration of the study regardless of drug loading. In particular it showed that Candelilla provides the slowest sustained release making it a candidate for implants or prolonged release. In contrast Precirol ATO 5 and Compritol

HD5 ATO produced the highest delivery rate. The former being an insoluble matrix releases the drug mainly by diffusion dependent upon the rate of solvent permeation and solubility of the drug compounds embedded in the matrix. In contrast drug release from Compritol HD5 ATO tablets is based on both diffusion and erosion mechanisms.

As a result, Compritol HD5 ATO was identified as the most suitable excipient for the further development of a multi-material design and the optimum drug loading was determined to be 10% w/w.

In conclusion the work in this chapter while pointing towards the later multi-material study, it here validated the use of hot-melt inkjet 3D printing as a feasible method to produce simple tailored medicines via the choice of excipient. In the next chapter, more complex 3D printed geometry with well-defined drug release profiles will be presented.

## Chapter 5

# Influence of 3D design on model drug release profiles.

The aim of this chapter is to show the effect of computational design of printed dosage forms on drug release and how the newly fashioned dual material hot-melt inkjet 3D printing system can aid in the process by adding a degree of freedom allowing multiple materials in one print without the need for ink swap. The knowledge regarding the selection and properties of the available ink materials gathered in Chapter 4 combined with the new system capabilities allowed to produce a series of tablets structures displaying immediate, extended, delayed and pulsatile drug release. These included single and multi-material complex 3D patterns with defined localised drug loading where the drug-free ink is used as a release-retarding material. The drug-free and drug-loaded materials can be positioned in a precise 3D geometry to obtain the desired release profile.

## 5.1 Material and Methods

### 5.1.1 Material

To maintain simplicity of manufacture it was decided to use the same matrix material as a base for the production of both drug-free and drug-loaded inks, so as to avoid the most challenging aspects of multi-material inkjet printing from both a geometrical and chemical point of view including mound/valley formations and chemical contaminations. Unplanned interactions between the jetted materials, can lead to physical and chemical reactions at the interface between regions leaving the potential for geometry distortions and functionality loss. By utilising temperature cooling as the main solidification path it is possible to exploit the deposition time to limit chemical diffusion

between adjacent materials. This is done by printing each single material region sequentially providing enough time for the first region to set before the second material section is filled in. By preventing the two jetted materials to come into contact while still liquid it is possible to greatly reduce the chances of cross contamination and chemical migration. Moreover, due to the nature of the system and to the choice of materials, all the inks used share the same solidifying conditions eliminating the risk of incompatible solidification steps. Lastly the decision to use the same matrix material for both the drug-loaded and the drug-free inks promotes layer height consistency, eliminating the need to layer match between different materials regions, reducing the chances of misalignments and consequent building defects.

In Chapter 4, Compritol HD5 ATO was identified as the best performing material, amongst those tested for a printable Fenofibrate containing formulation from a hot-melt inkjet printer. It was thus natural to select it as the matrix material for this more complex study. In the same chapter it was also determined that low drug concentration samples (5% and 10% w/w) displayed faster drug release dissolution profiles compared to higher concentrations (20% and 30% w/w). From this analysis, it would appear that 5% or 10% are the most appropriate drug loading concentrations.

It is necessary to highlight though, that the absolute amount of drug release would be correspondingly less at this low drug loading. Hence the 10% drug concentration was established as the standard for this work since the release profile from the 10% tablet is remarkably similar to that of the 5% tablet in percentage during the 10 hours duration of the test while providing double of the drug content. The higher loading also facilitates easier analysis by UV-vis spectroscopy.

In addition, to provide a complete overview of the effect of geometry on drug release, one geometry per dissolution type was selected to be tested with the different drug concentrations (5%, 10%, 20% and 30% w/w) to assess any behavioural change in response to geometrical modifications.

In the next session is presented a further discussion about tablets geometry and drug loading, a summary of all samples geometries and drug loading combinations is reported in Table 5.1.

## 5.1.2 Methods

### 5.1.2.1 Tablets structure design

As seen in Chapter 2 the new dual-material hot-melt inkjet 3D printing unit developed in this work is capable of precisely depositing micro metric droplets in a predetermined pattern to create solid dosage forms with precise geometrical, mechanical and compositional properties. For instance, not only can various materials be used to fabricate a part in a single process, but the transition between them can be designed to be gradual or sharp depending on the desired effect on release. In this chapter the aim is to investigate the capabilities of the modified LP50 hot-melt system in terms of tailored release and how the addition of an extra dispersing unit can be exploited to produce tuned drug release.

Building on the study of homogeneously loaded disc tablets in Chapter 4 it was decided to focus on addressing the following types of release profiles: immediate, sustained, delayed and pulsatile.

It was already observed that a 100% infill disk produces a **sustained drug release** for over 10 hours (Section 4.2.2.4), thus to address the **immediate drug delivery** design a disk tablet was developed containing a honeycomb infill as in Fig. 5.1. This choice was based on the desire to increase the surface area to volume ratio in order to enhance drug release by favouring the interaction between the tablet material and the buffer solution. This is a well known approach frequently used in traditional tableting, often to achieve zero order release [235, 236, 237, 238, 239, 240]. Naturally a similar approach has been adopted for 3DP which allows to manufacture tablets with complex bespoke shape with precision and ease, that would be challenging to create by powder compaction [95, 160, 70, 71]. However, this is, to our knowledge, the first time that this approach has been tested on the ink materials presented in this work. In the attempt to demonstrate the power of inkjet printing, while at the same time exploring different surface to volume ratio a modelling computer-aided design software (SolidWorks) was utilised to design three infill honeycomb geometries visible in Fig. 5.1 by varying the cell diameter, specifically achieving 45% infill with  $\varnothing = 0.60$  mm, 24% infill with  $\varnothing = 1.22$  mm and 17% infill with  $\varnothing = 1.83$  mm respectively.

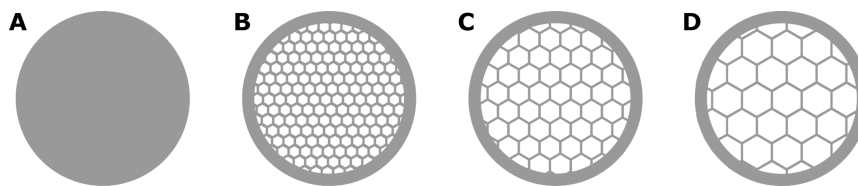


FIGURE 5.1: Digital design of immediate release tablets showing the honeycomb structures. Top view of A) full disc (100% infill), B) honeycomb with cell diameter of 0.60 mm (45% infill), C) 1.22 mm (24% infill) and D) 1.83 mm (17% infill).

Tablets designed to display **delayed release** were modelled to make use of the multi material jetting system to produce a precisely controlled local drug distribution within the tablet. As visible in Figure 5.2 the final geometry comprised a 100% infill drug loaded centre surrounded by a drug free shell acting as a rate-limiting barrier to active ingredient release. In such a barrier system drug release can happen only when, through degradation and erosion, the buffer comes into contact with the drug-containing core, therefore inducing the desired delay.

To understand the effect of shell thickness on the dissolution drug release profile, three geometrical standards were identified  $s_1 = 1$  mm,  $s_2 = 1.5$  mm and  $s_3 = 2$  mm where  $s$  represents the shell thicknesses. Since it is expected for surface area to volume ratio to effect drug release a fixed core geometry was selected as a mean to ensure that any behavioural adjustment recorded in the dissolution pattern were the result of the changes in shell thickness and not from the drug loaded region allowing the factors of interest to be isolated. The choice of external layer thickness was designed to keep the tablet size within the FDA recommended dimensions [241]; hence the core dimensions were set to  $\varnothing = 8$  mm,  $h = 2$  mm and consequently the tablet's overall size was made to vary between 10 mm and 12 mm.

In Figure 5.2 are presented the vertical and horizontal cross sections of the digital designs with the drug loaded regions in *grey* and the drug free shells presented in *white*.

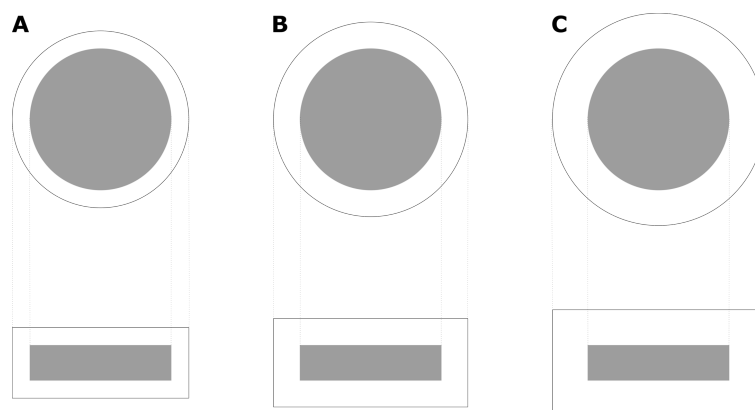


FIGURE 5.2: Digital design of delayed release tablets showing the horizontal and vertical cross section of the different shell structures. A) Thin 1 mm shell, B) medium 1 mm shell and C) thick 1 mm shell. The drug loaded region are identified in figure by the *grey* colour while the drug free shell is presented in *white*.

Based on the information gathered in Section 4.2.1.2, the relative distance between the core and the ring inner diameter was calculated, on the basis of drop spreading, solidification time and desired overlapping to ensure a smooth transition between regions and to avoid either mound or valley formation. Mound formation is an effect linked to the nature of the depositional process, indeed each section is printed sequentially and the part's edges are partially solidified when the next material is deposited. As a result, if the bitmaps are not correctly spaced the two materials will not smoothly overlap, but will instead build up on top of each other causing the afore mentioned mound effect. It is of particular importance for this to be avoided since it compromises form and structural integrity, and as a cumulative error it cannot be contained and has a disruptive effect on the final product.

A second set of tablets was established to explore the effect of drug concentration on drug release for tablets with fixed shell thickness, in this case the tablet geometry was maintained constant (core:  $\varnothing = 8$  mm,  $h = 2$  mm, shell:  $s = 1$  mm) and drug concentration varying between 5% (w/w) and 30% (w/w).

Lastly a multi-compartment dosage form strategy was chosen to investigate **pulsatile release**. For this section the goal was to design a product showcasing two separate drug burst releases with delayed onset.

While modelling, the focus was on designing a drug spacial placement such that it would be possible to distinguish between the different release bursts while at the same time keeping the tablet size within the FDA recommended dimensions. The resulting geometrical design is a tablet containing two nested drug-loaded regions encapsulated by inactive drug-free material.

In detail it consists of a drug loaded central disc region ( $\varnothing = 4$  mm,  $h = 2$  mm) surrounded by a 3 mm shell of drug free material that is furthermore circumscribed by a concentric ring (*thickness* = 1 mm,  $h = 7$  mm), one last 1 mm layer of drug free material encases the entire part. This can be seen in Figure 5.3 where the grey areas represent the API loaded regions while the white areas are drug-free, wax only. The final tablet dimensions are:  $\varnothing = 12$  mm,  $h = 9$  mm.

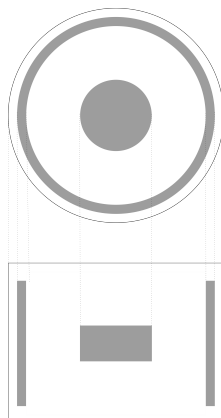


FIGURE 5.3: Digital design of pulsatile release tablets showcasing the horizontal and vertical cross section of the different embedded shell structures. The drug loaded region are identified in figure by the *grey* colour while the drug free shell is presented in *white*.

In table 5.1 is presented a schematic summary of all tablets types used in this chapter.

TABLE 5.1: Summary of the immediate, delayed and pulsatile tablets geometrical and compositional properties.

Immediate	Cell diameter and wall [mm]	Ring thickness [mm]	Tablet dimensions [mm]	Fenofibrate content (%)
$H_a'$	$\varnothing = 0.60, t = 0.18$	$t = 0.70$	$\varnothing = 10, h = 4.95$	5
$H_a''$	$\varnothing = 0.60, t = 0.18$	$t = 0.70$	$\varnothing = 10, h = 4.95$	10
$H_a'''$	$\varnothing = 0.60, t = 0.18$	$t = 0.70$	$\varnothing = 10, h = 4.95$	20
$H_a''''$	$\varnothing = 0.60, t = 0.18$	$t = 0.70$	$\varnothing = 10, h = 4.95$	30
$H_b$	$\varnothing = 1.22, t = 0.18$	$t = 0.70$	$\varnothing = 10, h = 4.95$	10
$H_c$	$\varnothing = 1.83, t = 0.18$	$t = 0.70$	$\varnothing = 10, h = 4.95$	10
Delayed release	Core dimensions [mm]	Shell thickness [mm]	Tablet dimensions [mm]	Drug loading (%)
$D_a'$	$\varnothing = 8, h = 2$	$t = 1$	$\varnothing = 10, h = 4$	5
$D_a''$	$\varnothing = 8, h = 2$	$t = 1$	$\varnothing = 10, h = 4$	10
$D_a'''$	$\varnothing = 8, h = 2$	$t = 1$	$\varnothing = 10, h = 4$	20
$D_a''''$	$\varnothing = 8, h = 2$	$t = 1$	$\varnothing = 10, h = 4$	30
$D_b$	$\varnothing = 8, h = 2$	$t = 1.5$	$\varnothing = 11, h = 5$	10
$D_c$	$\varnothing = 8, h = 2$	$t = 2$	$\varnothing = 12, h = 6$	10
Pulsatile release	Core dimensions [mm]	Ring dimensions [mm]	Tablet dimensions [mm]	Drug loading (%)
P	$\varnothing = 4, h = 2$	$t = 1, h = 7$	$\varnothing = 12, h = 9$	10

Note: when identifying a sample the capital letters specifies the type of release profile. Sets are defined as described in Section 5.1.2.1 H=immediate release, D=delayed release and P=pulsatile. The subscript letters indicates different geometries within a set and the appendix refers to the drug concentration (%) in the ink used to print the drug loaded regions.

### 5.1.2.2 3DP Tablet production

All inks were prepared following the procedure described in Section 3.2.2. Dry components were weighed beforehand using weighing boats and a precision balance (Kern ALS Analytical Balance). The ink mixtures were prepared by liquid mixing of the melted ingredients by adding a suitable quantity of Fenofibrate to the melted matrix material until the desired concentration was reached. The resulting ink was then transferred into one of the reservoirs attached to the printer ready to be used. The drug-free inactive ink was prepared by loading the Compritol HD5 ATO directly into the printer's other reservoir and melted *in situ*. Following the directions established in the previous section (Section 5.1.1) 5%, 10%, 20% and 30% w/w Fenofibrate inks were prepared alongside the pure Compritol HD5 ATO ink.

The original 3D designs described in Section 5.1.2.1 were sliced according to layer height using in-house slicing software (Section 2.3.4), the outcome being an ordered stack of LP50 compatible 2D bitmaps organised by layer number and material composition.

As a further precaution, for the composite tablets, a manual check was performed. Matching maps corresponding to the tablet middle cross section were identified and extracted from each material set, the combined result was then checked for misalignments, ensuring that all parts were concentric and that the desired gap between regions was consistent to accommodate for spreading.

The files were then loaded into the correct folder and the part printed using the dual unit system described in Chapter 2. The parameters were selected on the basis of the results obtained in Chapter 4 and are summarised in Table 5.2.

The adapted software discussed in Chapter 2 was then capable of pairing each 2D design to the correct printhead to produce the final 3D object.

The quality of the printed parts was assessed via spatial and chemical characterisation. For this purpose the following set of analysis was employed: Optical microscopy, Scanning Electron Microscopy, Fourier Transform Infrared Spectroscopy and Raman spectroscopy. Traditional techniques such as camera photography, precision balance, micrometer and caliper were also used.

TABLE 5.2: Summary of printing parameters.

Number of nozzles	variable <sup>a</sup>
Nozzle diameter	35 $\mu\text{m}$
Firing voltage	100 V
Hot melt chamber temperature	90 $^{\circ}\text{C}$
Printing head temperature	90 $^{\circ}\text{C}$
Substrate temperature	40 $^{\circ}\text{C}$
$T_R$	3 $\mu\text{s}$
$T_F$	3 $\mu\text{s}$
$T_P$	5 $\mu\text{s}$
Substrate	polyethylene terephthalate (PET) 200 $\mu\text{m}$

<sup>a</sup> The number of nozzles used was determined at the beginning of each session in order to optimise the end result by excluding any defective one.

### **Tablet preparation for Raman Spectroscopy**

Raman spectroscopy was used to determine the API content and distribution inside the printed solid dosage forms. In particular it was employed the capability of the instrument to acquire sequential spectra along the x or y direction to study the distribution of the API at the interface core/shell in the multi material tablets. Due to the nature of the technique it is of utmost importance to maintain the sample in focus at all times while performing the line mapping, thus to ensure the success of data collection and comparability of results [242, 243]. On account of this, solid dosage forms were produced with the middle cross section of the tablet exposed and with a minimum surface roughness. Hence the tablets were printed with the cross-section surface facing a PET substrate and built up from there, in a reverse approach compared to the one used for the SEM and FTIR samples. By printing the surface of interest directly onto the PET substrate it was possible to eliminate the ridges characteristic of 3D printing and guarantee a smooth result. Furthermore, since the rest of the part is built accordingly to the original design it ensures for part stability while at the same time replicating the chemical and spatial distribution found in the full tablet. In such a manner slicing can also be avoided eliminating the risk of sample breakages and smearing of materials into neighbouring regions that would invalidate the entire measurement.

The samples were mounted on glass slides, loaded onto the microscope slot and analysed according to the procedure described in Section 3.2.9. The  $1598\text{ cm}^{-1}$  peak, unique to the Fenofibrate, was established as a marker to identify the presence of the drug.

## 5.2 Results and discussion

### 5.2.1 Immediate release tablets

#### 5.2.1.1 Optical spectroscopy and printed tablets geometrical evaluation.

The honeycomb designs developed in Section 5.1.2.1 were successfully printed using the single head hot-melt unit. Noticeably, it was possible to consistently and reliably produce tablets with the desired cell diameter and drug composition. Indeed, to understand the effect of the ratio between surface area and volume on the drug release profile three sets of tablets were printed, each set included three honeycomb structured samples (0.6 mm, 1.22 mm and 1.83 mm) alongside a conventional disc tablet to be used as reference.

In conjunction, tablets with constant geometry (45% infill), but diverse drug concentrations of 5%, 10%, 20% and 30%, were printed with the same degree of success. In this instance each concentration sample was produced separately and in triplicate. Here the reference was a drug free tablet.

In photo Fig. 5.4 TOP it is possible to appreciate all three infill geometries alongside with the disc tablet (100% infill), by visual inspection all tablets are well-defined, with a smooth surface and without appreciable defects.

Similar results can be seen in tablets sharing the same geometry, but different drug loading. Fig. 5.4 BOTTOM displays solid dosage forms printed with the four concentrations of interest alongside with the reference produced using a pure Compritol HD5 ATO ink (0% drug content). The tablets result indistinguishable to the naked eye with well defined edges and smooth surfaces. No visible defects can be found, suggesting that drug content does not influence the printed results.

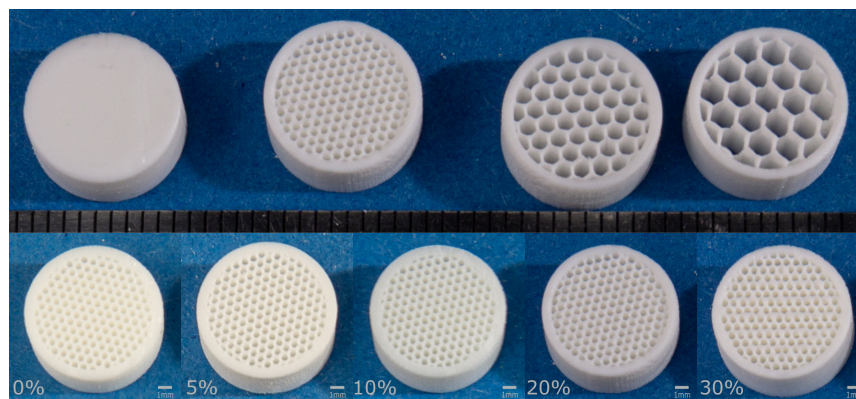


FIGURE 5.4: Photos of immediate release tablets showing the honeycomb structures. TOP) Tablets with constant drug loading (10%) and different geometries, respectively disc and honeycomb with cell diameter of 0.60 mm, 1.22 mm and 1.83 mm. BOTTOM) Tablets with constant geometry ( $\varnothing_{cell} = 0.60$  mm) and different drug loading concentration, namely 0%, 5%, 10%, 20% and 30%. The visible colour difference is an artefact due to difference in lightening conditions under which the pictures were acquired.

### Optical microscopy

Optical microscopy was used to investigate the surface quality of the dosage forms and to determine the size of the printed cells. Images of the top and bottom surfaces of all three honeycomb geometries were acquired using microscope and are presented in Fig. 5.5, from left to right  $\varnothing_{cell} = 600\mu m$ ,  $\varnothing_{cell} = 1220\mu m$  and  $\varnothing_{cell} = 1830\mu m$ .

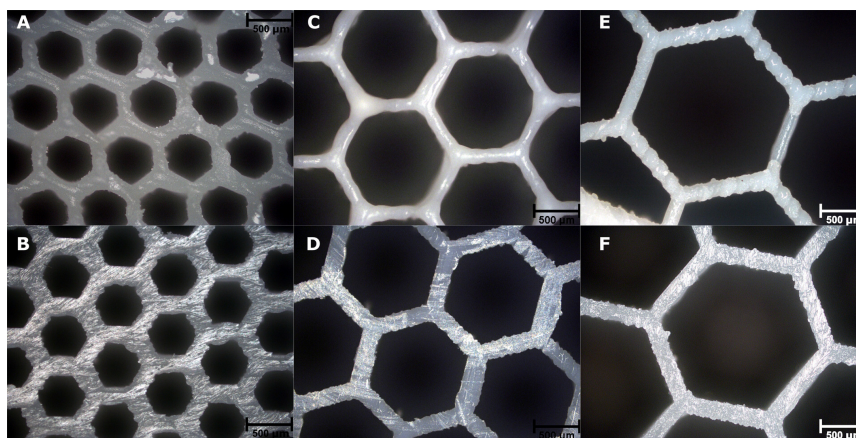


FIGURE 5.5: Optical microscope images of top and bottom surfaces of immediate release tablets showcasing the honeycomb structures with constant drug loading (10%) and different channel size. Respectively  $\varnothing = 0,60$  mm top (A) and bottom (B) surfaces,  $\varnothing = 1,22$  mm top (C) and bottom (D) surfaces and  $\varnothing = 1,83$  mm top (E) and bottom (F) surfaces.

In all three cases the bottom surface (Fig. 5.5 B, D, F) result smooth and defects free with channels diameters of respectively  $(585 \pm 20)\mu m$ ,  $(1214 \pm$

10) $\mu\text{m}$  and  $(1864 \pm 12)\mu\text{m}$ , all results are compatible with the theoretical value according to Student's t-test. Such an even and smooth surface was attained by employing a PET film as printing substrate.

In contrast the top surface, while smooth to the naked eye, presented the unmistakable printing lines often evident from a 3D printing processes, as such they can not be completely avoided, but only reduced and are to be accepted as part of the production method. Though, this feature does not disrupt the dissolution process, increased surface roughness is known to promote surface wettability and hence opens the potential in the future to exploit the process native flaw to help tailor the initial interaction with the buffer solution [244]. Lastly, from the analysis of the microscopy images (Fig. 5.5 A, C, E) it was possible to determine that channel diameters were consistent through the tablet height with less than 5  $\mu\text{m}$  variation between the top and bottom diameter, well within the measurement error range. Their compatibility was further confirmed by Student's t-test alongside their compatibility with the predicted values. All the results refer to the distance between two opposite vertices (diameter of the circumscribed circle ) and are summarised in Table 5.3.

TABLE 5.3: Channel diameter of immediate release tablets at constant drug loading concentration (10%).

Geometry <sup>a</sup>	$H_a$	$H_b$	$H_c$
Digital design [ $\mu\text{m}$ ]	600	1220	1830
Tablet top surface [ $\mu\text{m}$ ]	$588 \pm 25$	$1210 \pm 11$	$1869 \pm 12$
Tablet bottom surface [ $\mu\text{m}$ ]	$585 \pm 20$	$1214 \pm 10$	$1864 \pm 12$

<sup>a</sup> The notation here utilised to identify the different geometries is consistent with what previously established in Table 5.1.

### Scanning Electron Microscopy

Further analysis of the honeycomb channels was carried out using Scanning Electron Microscopy with a 150x magnification. A tablet (10% drug loading and  $\varnothing = 0,60mm$  channels) was broken and positioned such that the inside of the cells would be exposed to the electron beam. From the images in Fig. 5.6 it is clear that both the channels and the walls are well formed and for the most part free from imperfection. The horizontal lines, visible along the channel length correspond to the boundaries between subsequent layers deposited along the z-axis.

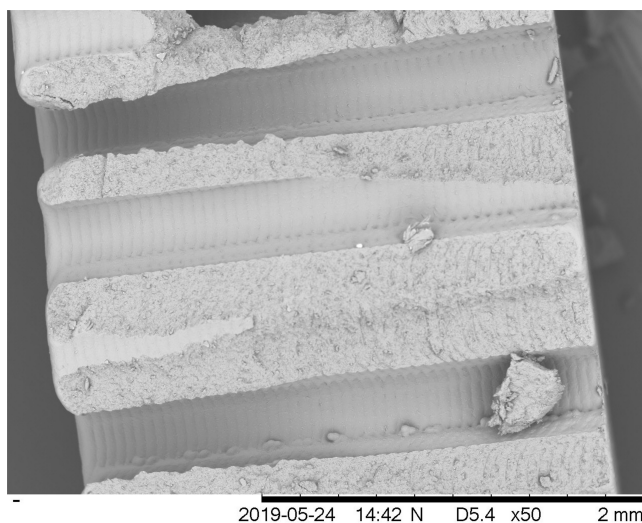


FIGURE 5.6: SEM images of 10% drug loading immediate release tablet with  $\varnothing = 0,60mm$  channels. The particle at the bottom right of the image is a result of the breaking process and it is not indicative of the printing.

#### 5.2.1.2 Content uniformity and weight variation

The drug content of each of the tablets was investigated using FTIR and weight variation. Five tablets per type were weighed and the results averaged. The outcomes were then compared with the estimated values obtained from the designed geometry and the calculated density studied in Section 4.1.1.

The theoretical values of volume ( $V$ ) and surface area ( $SA$ ) were determined from the digital design utilising a built-in feature of Solidworks, the weight of the tablets was then estimated as:

$$W = \rho_{ink} \cdot V \quad (5.1)$$

Where the overall density of the inks was estimated on the base of the density of the single components and their concentration:

$$\rho = C_c \cdot \rho_c + C_f \cdot \rho_f \quad (5.2)$$

where  $\rho$  indicates the density,  $C$  is the concentration and the subscript  $c$  and  $f$  refer to Compritol HD5 ATO and Fenofibrate respectively. The outcome of these calculations alongside the measured values are reported in Table 5.4. Given the high geometrical precision of the printed solid dosage forms, observed in the previous sections, it follows that the measured values are in great agreement with the digital version.

TABLE 5.4: Summary of the immediate release tablets geometrical and weight properties

	Tablet diameter [mm]	Tablet height [mm]	Weight [mg]	SA/V ratio [cm <sup>-1</sup> ]
<i>H<sub>a</sub></i> [ $\varnothing = 600\mu m$ , 10% Fenofibrate]				
Digital design	10	4.95	231.58 $\pm$ 4.39	6.93
Printed tablet	10.02 $\pm$ 0.04	4.93 $\pm$ 0.03	229.84 $\pm$ 0.52	
<i>H<sub>b</sub></i> [ $\varnothing = 1220\mu m$ , 10% Fenofibrate]				
Digital design	10	4.95	169.34 $\pm$ 3.21	6.78
Printed tablet	10.03 $\pm$ 0.04	4.94 $\pm$ 0.01	167.10 $\pm$ 0.63	
<i>H<sub>c</sub></i> [ $\varnothing = 1830\mu m$ , 10% Fenofibrate]				
Digital design	10	4.95	150.18 $\pm$ 2.85	6.26
Printed tablet	10.06 $\pm$ 0.09	4.93 $\pm$ 0.01	148.69 $\pm$ 1.22	
<i>H'<sub>a</sub></i> [ $\varnothing = 600\mu m$ , 5% Fenofibrate]				
Digital design	10	4.95	229.00 $\pm$ 4.64	6.93
Printed tablet	10.03 $\pm$ 0.04	4.93 $\pm$ 0.02	225.87 $\pm$ 1.42	
<i>H''<sub>a</sub></i> [ $\varnothing = 600\mu m$ , 10% Fenofibrate]				
Digital design	10	4.95	231.58 $\pm$ 4.40	6.93
Printed tablet	10.02 $\pm$ 0.04	4.93 $\pm$ 0.03	229.84 $\pm$ 0.52	
<i>H'''<sub>a</sub></i> [ $\varnothing = 600\mu m$ , 20% Fenofibrate]				
Digital design	10	4.95	236.74 $\pm$ 4.15	6.93
Printed tablet	10.01 $\pm$ 0.02	4.94 $\pm$ 0.01	234.88 $\pm$ 1.03	
<i>H''''<sub>a</sub></i> [ $\varnothing = 600\mu m$ , 30% Fenofibrate]				
Digital design	10	4.95	241.91 $\pm$ 3.42	6.93
Printed tablet	10.03 $\pm$ 0.05	4.95 $\pm$ 0.01	240.53 $\pm$ 0.44	

### Fourier Transform Infrared Spectroscopy

In using the Fourier Transform Infrared Spectroscopy technique, as described in Section 3.2.8, the goal was to further confirm the presence of Fenofibrate inside the printed tablets by recognising the C-Cl bond, which is characteristic of the Fenofibrate molecule. Figure 5.7 shows the spectra obtained for each of the samples, the blue and red boxes highlighting the major characteristic peaks of Fenofibrate, the C-C stretch (in ring) at  $1600\text{ cm}^{-1}$  to  $1650\text{ cm}^{-1}$  and the  $720\text{ cm}^{-1}$  to  $765\text{ cm}^{-1}$  peaks of the C-Cl stretch [192, 193]. In Figure 5.7 are reported the results referring to the set of tablets with the same geometry ( $\varnothing_{cell} = 600\mu\text{m}$ ) and drug content variation. To provide relevance to our findings, the same approach used in the previous Chapter 4.2.2.2, was adopted here with the attention focused on the  $765\text{ cm}^{-1}$  peak. By comparing the last results with the knowledge acquired on the base materials, it was possible to produce a qualitative interpretation of our findings. In Figure 5.7 B such peaks are highlighted and a comparison of the different tablets is presented. Satisfyingly larger features correspond to the higher concentrations of Fenofibrate as expected and the peaks intensities are compatible with the expected values as highlighted in Table 5.5.

A similar approach was utilised to examine the spectra collected from the tablets printed using the same drug concentration but different geometry, Figure 5.7C. The results are as to be expected compatible with each other and with the reference value from Chapter 4.2.2.2.

Although qualitative, this analysis strengthens the validity of the previous assumptions on the amount of drug loaded into each tablet.

TABLE 5.5: FTIR characterisation of immediate release tablets via the intensity of the Fenofibrate characteristic  $765\text{ cm}^{-1}$  peak.

	Channel	Fenofibrate	Tablet [%]	Reference [%]
$H_a$	$600\mu\text{m}$	10% (w/w)	$38.8 \pm 1.2$	$37.0 \pm 3.5$
$H_b$	$1220\mu\text{m}$	10% (w/w)	$38.6 \pm 0.7$	$37.0 \pm 3.5$
$H_c$	$1830\mu\text{m}$	10% (w/w)	$39.6 \pm 2.4$	$37.0 \pm 3.5$
$H'_a$	$600\mu\text{m}$	5% (w/w)	$24.0 \pm 1.2$	$23.6 \pm 2.8$
$H''_a$	$600\mu\text{m}$	10% (w/w)	$38.8 \pm 1.2$	$37.0 \pm 3.5$
$H'''_a$	$600\mu\text{m}$	20% (w/w)	$43.0 \pm 2.4$	$42.5 \pm 2.9$
$H''''_a$	$600\mu\text{m}$	30% (w/w)	$70.2 \pm 2.4$	$70.5 \pm 0.1$

<sup>a</sup> The notation here utilised to identify the different geometries is consistent with what previously established in Table 5.1.

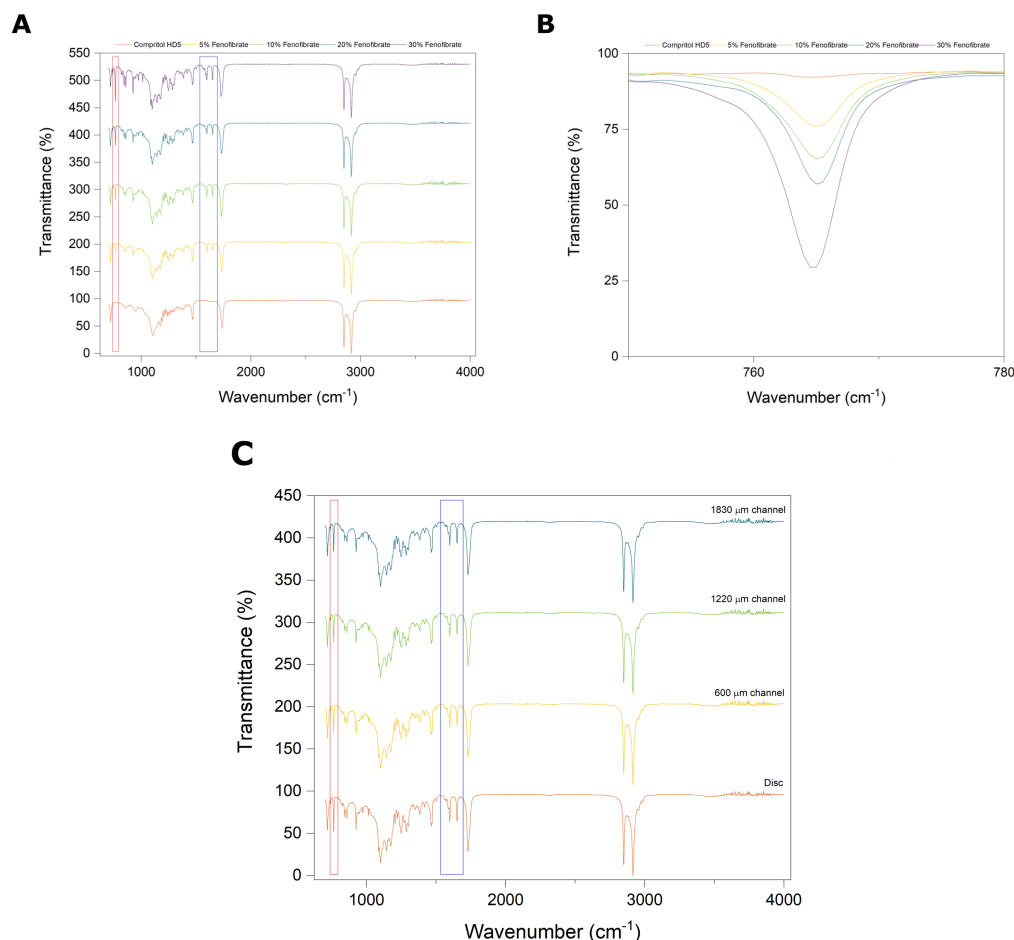


FIGURE 5.7: Fourier Transform Infrared Spectroscopy analysis of immediate release tablets with honeycomb structure of Compritol HD5 ATO and Fenofibrate mixture. A) constant geometry,  $\varnothing_{cell} = 0.60$  mm and different drug loading concentration namely 5%, 10%, 20% and 30% and B) highlight of the  $765\text{ cm}^{-1}$  peak. C) Constant drug loading (10%) different channel diameter: 0.60 mm, 1.22 mm and 1.83 mm.

### 5.2.1.3 *In vitro* drug release

As seen in the previous chapters *in vitro* drug dissolution study is a fundamental technique used in understanding the drug release of oral dosage forms [229]. To maintain the work consistency the same Copley's Dissolution Test Dis8000 and test conditions were used as in the previous experiments, Section 3.2.13.

The amount of drug released into the medium as a function of time was obtained by analysing the collected samples using UV-visible spectrophotometry. The amount of drug released given a determined absorbance intensity is obtained using Eq. 4.4.

$$x = \frac{y - y_0}{m} \quad (5.3)$$

Where the fit parameters are reported in Table 5.6.

TABLE 5.6: UV-Vis Fenofibrate calibration curve parameters.

Intercept [ml/ $\mu$ g]	Slope [a.u.]	$R^2$
$0.00141 \pm 0.00043$	$0.00669 \pm 0.00001$	0.999

All dissolution tests were done in triplicate. The disc tablets (100% infill) along with the solid dosage forms presenting honeycomb structures with cell diameters of 0.6 mm, 1.22 mm and 1.83 mm were used to investigate the effect of changes in the tablet geometry, specifically the surface area to volume ratio, on drug release rate.

The results are reported in Figure 5.8 A.

In accordance with what was previously reported in the literature [160, 70, 71, 137], the rate of drug dissolution from the tablet tends to increase with the surface area and the smallest cell diameter belongs to the best performing tablet while the full disk is the worst in the sense of drug release rate. The disc tablet is indeed capable of releasing 88% of its drug content in 10 hours. In striking contrast, the honeycomb tablet with the smallest cell diameter (0.60 mm) was able to achieve the same result after only three hours and released more than 98% of the content by the end of the sixth hour. The geometries with cell diameters of 1.22 mm and 1.83 mm sit in the region between the previous two curves, with the former releasing 90% by the sixth hour followed by the latter with an hour delay.

As the best performing geometry, the 0.60 mm cell diameter structure was selected to test the impact of the different drug concentrations. The aim was to assess if the trend observed for the solid disc Compritol HD5 ATO dosage forms in Chapter 4.2.2.4 is replicated when the geometry is changed. The resulting data is presented in Figure 5.8 B. As for the previous case, the low drug concentration samples (5% and 10% w/w) displayed faster drug release dissolution profiles compared to the higher concentration ones (20% and 30% w/w). Notably, the tablet containing just 5% w/w Fenofibrate displayed the fastest drug release profile, with more than 92% of the initial drug released by the third hour and more than 98% by the fourth. Interestingly the release profile of the 10% tablet does not differ greatly from the 5% one delivering more than 98% of the total load in 6 hours.

This behaviour is compatible with the result found for the disc tablet suggesting it to be a property of the ink material itself, and specifically drug crystallinity and to not be effected by the tablet geometry.

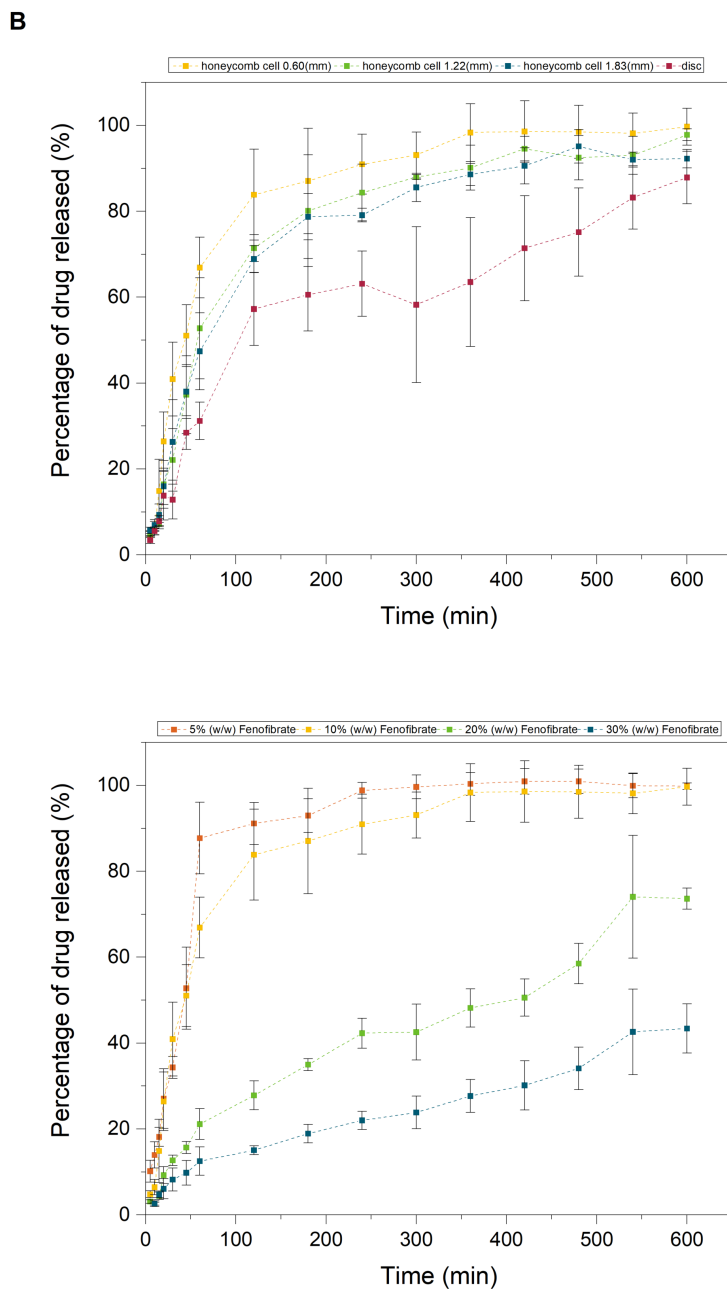


FIGURE 5.8: *In vitro* dissolution test of immediate release tablets with honeycomb structure of Compritol HD5 ATO and Fenofibrate mixture. A) constant drug loading (10%) and different geometries, respectively disc and honeycomb with cell diameter of 0.60 mm, 1.22 mm and 1.83 mm. B) constant geometry,  $\varnothing_{cell} = 0.60$  mm and different drug loading concentration namely 5%, 10%, 20% and 30%.

## 5.2.2 Delayed release tablets

### 5.2.2.1 Optical spectroscopy and printed tablets geometrical evaluation

Delayed release tablets are the first example of multi-material solid dosage form realised using the new dual unit hot-melt inkjet printer discussed in Chapter 2. This offers the possibility to not only appreciate the functionality of the system, but most importantly to take the first steps towards exploring its capabilities in providing an additional degree of freedom in tablet design.

The 2D bitmaps from the slicing process described in Section 5.1.2.2 were sequentially printed using the modified software capable of pairing the different files to the correct head in order to deploy the desired material at the correct time to produce the sought after high precision multi-material designs.

As visible from the photo in Fig. 5.9 the printed tablets appear visually homogeneous and well defined with only minor defects.

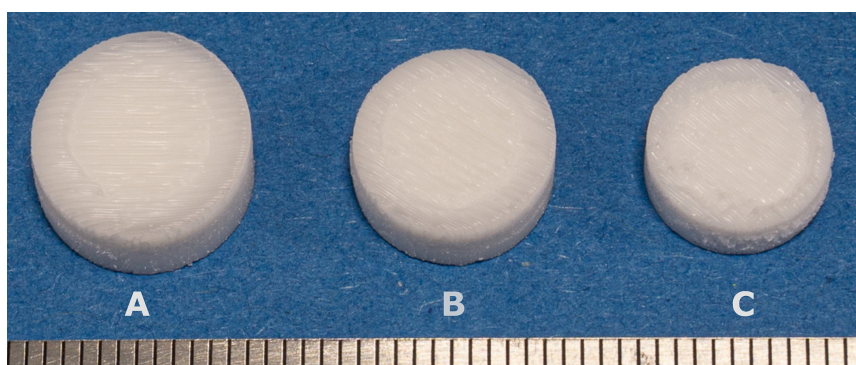


FIGURE 5.9: Photos of delayed release tablets, constant drug loading(10%) and different shell thickness, respectively 1 mm, 1.5 mm and 2 mm.

The top surfaces are smooth with the exception of a small indentation in correspondence of the outside edge of the central core, suggesting that the core/shell transition was not perfectly smooth. Nevertheless, the tablets were solid, well-defined and it was possible to consistently print all three shell size geometries, namely the 1 mm, 1.5 mm and 2 mm. It is clear that the printing technique was successful and that the printed product does not differ greatly from the computer design. As a such the dimensions of the printed solid dosage forms are in good agreement with the parameters of the digital version as highlighted in Table 5.7.

Similar results can be reached for tablets sharing the same thin shell geometry, but bearing different drug loading in the core region.

TABLE 5.7: Summary of the delayed release tablets geometrical and weight properties

	Tablet diameter [mm]	Tablet height [mm]	Weight [mg]
<i>D<sub>a</sub></i> [shell = 1mm, 10% Fenofibrate]			
Digital design	10	4.00	309.19 ± 4.51
Printed tablet	10.00 ± 0.04	4.04 ± 0.03	297.09 ± 2.17
<i>D<sub>b</sub></i> [shell = 1.5mm, 10% Fenofibrate]			
Digital design	11	5.00	466.51 ± 8.00
Printed tablet	11.00 ± 0.01	5.02 ± 0.01	435.65 ± 2.80
<i>D<sub>c</sub></i> [shell = 2mm, 10% Fenofibrate]			
Digital design	12.00	6.00	665.26 ± 12.18
Printed tablet	12.00 ± 0.01	6.05 ± 0.03	653.614 ± 1.36
<i>D'<sub>a</sub></i> [shell = 1mm, 5% Fenofibrate]			
Digital design	10	4.00	308.07 ± 4.51
Printed tablet	10.00 ± 0.01	4.04 ± 0.02	294.15 ± 4.72
<i>D''<sub>a</sub></i> [shell = 1mm, 10% Fenofibrate]			
Digital design	10	4.00	309.19 ± 4.51
Printed tablet	10.00 ± 0.04	4.04 ± 0.03	291.36 ± 2.17
<i>D'''<sub>a</sub></i> [shell = 1mm, 20% Fenofibrate]			
Digital design	10	4.00	311.43 ± 4.51
Printed tablet	10.00 ± 0.01	4.07 ± 0.04	303.97 ± 3.41
<i>D''''<sub>a</sub></i> [shell = 1mm, 30% Fenofibrate]			
Digital design	10	4.00	313.68 ± 4.51
Printed tablet	10.00 ± 0.01	4.07 ± 0.04	309.44 ± 1.50

### Optical microscopy

Optical microscopy was used to further investigate the interface between the inner core and the outer ring shell.

To this end a print was stopped half-way through revealing the middle cross section, the sample was then analysed using a Nikon Eclipse Lv 100ND microscope with NIS Elements software with a 50x objective. For all three shell thicknesses the result are visible in Fig. 5.10, from left to right large (2 mm), medium (1.5 mm) and small (1 mm) shell thickness. The surfaces show the familiar printing lines and a well-defined interface between the inner core and the outer ring shell showing apparently good cohesion and separation between regions while avoiding the mound effect.

With the exclusion of shell thickness there are no other significant differences between the tablets, in agreement with what was observed in the previous section.

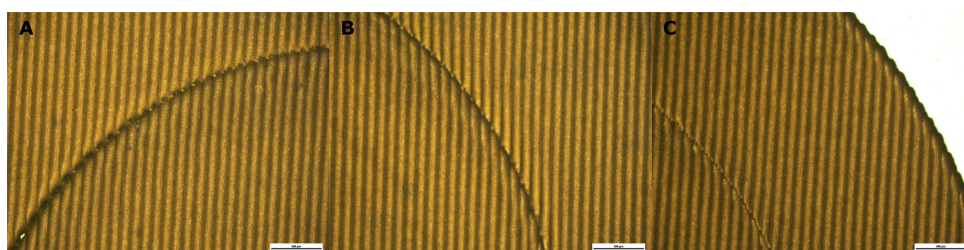


FIGURE 5.10: Optical microscope images of delayed release tablets, interface between the inner core and the outer ring shell. Respectively A) thick shell (2 mm), B) medium shell (1.5 mm) and C) thin shell (1 mm).

### Scanning Electron Microscopy

In addition to optical microscopy, Scanning Electron Microscopy was employed to study the interface between the inner core and the outer ring shell. A thin shell, 10% drug loaded core tablet was prepared as previously by interrupting the print at the mid-point. The sample was then mounted on an aluminium stand and exposed to the imaging electron beam. A 150x magnification was used to examine the materials junction. In Fig. 5.11 are highlighted two separate regions, B) shows a smooth well formed connection with a minor mound effect while A) is focused on a problematic area. The existence of these defects is at the base of the imperfections observed on the top surface. Regardless, it is evident that both core and shell regions are well formed and for the most part free from imperfection.

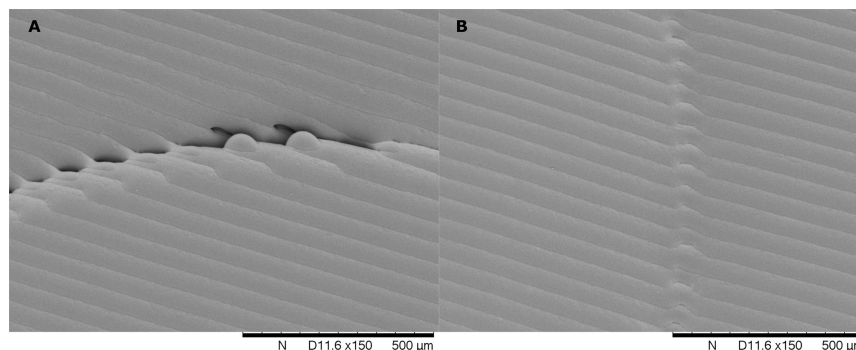


FIGURE 5.11: SEM images of the junction between the inner core and the outer ring shell in a delayed release tablet with 1 mm shell thickness and 10% drug loaded core.

A) Junction defect and B) well-formed connection with minor mound effect.

### **Fourier Transform Infrared Spectroscopy**

Fourier Transform Infrared Spectroscopy was utilised to provide supplementary information with regard to drug localisation within the printed tablet and to further confirm the presence of Fenofibrate only inside the central core. For the first investigation the tablets were broken and samples of the core and shell region were collected separately, for each region three separate samples were acquired, the results were then averaged and are shown in Figure 5.12 and Figure 5.13. The  $765\text{ cm}^{-1}$  peak was once again utilised as a marker to identify the presence of the API. In Figure 5.12 are presented the results for printed dosage forms with constant core drug loading (10%) and different shell thickness. It is clear that the drug was contained only inside the core and it is absent in the external layer.

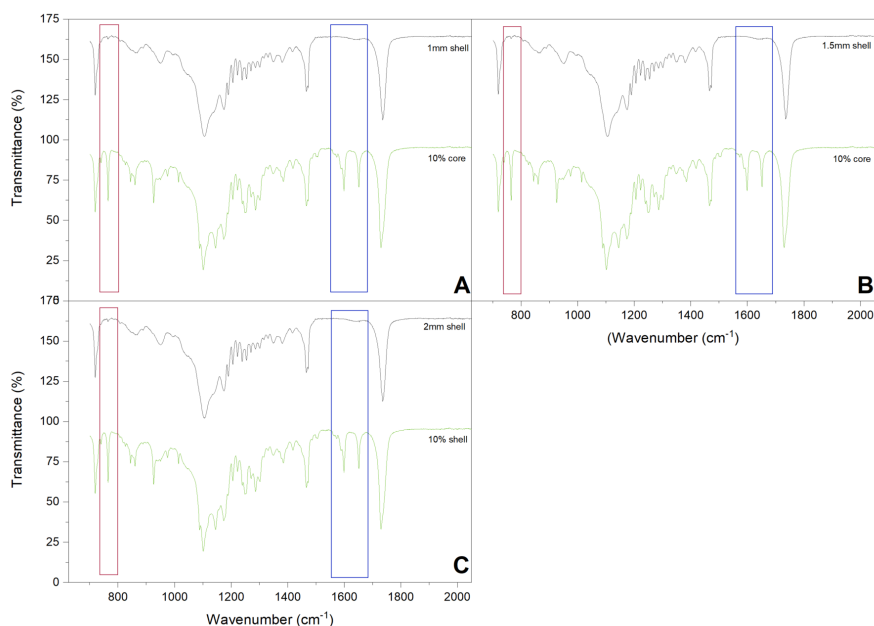


FIGURE 5.12: Fourier Transform Infrared Spectroscopy analysis of delayed release tablets with constant core geometry and drug loading (10%) and different shell thickness, namely 1 mm (A), 1.5 mm (B) and 2 mm (C). Highlighted in red the  $765\text{ cm}^{-1}$  C-Cl peak, in blue the  $1600\text{-}1650\text{ cm}^{-1}$  C=C peaks linked to Fenofibrate presence.

A similar behaviour is visible in Figure 5.13 where the drug content was varied while the geometry was maintained constant. Notably, for both analysis the peaks intensities are in good agreement with the expected values, confirming once more that not only I was capable of producing tablets with localised drug, but also to successfully tailor the drug concentration. Highlighted in red the  $765\text{ cm}^{-1}$  C-Cl peak, in blue the  $1600\text{-}1650\text{ cm}^{-1}$  C=C peaks linked to Fenofibrate presence. The results for both sets of tablets are reported in Table 5.8.

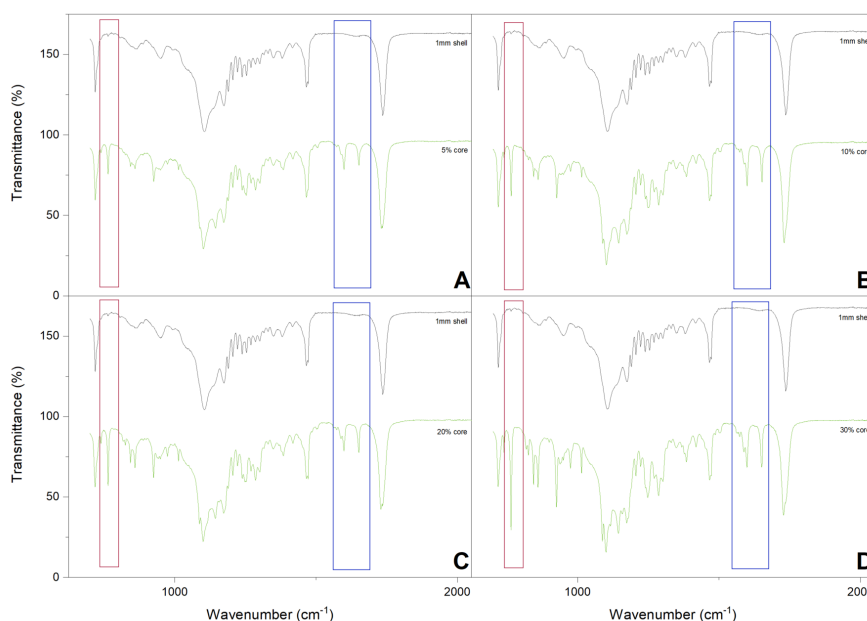


FIGURE 5.13: Fourier Transform Infrared Spectroscopy analysis of delayed release tablets with constant core geometry ( $\varnothing_{core} = 8mm$ ,  $t_{shell} = 1mm$ ) and different drug loading concentration namely 5% (A), 10% (B), 20% (C) and 30% (D). Highlighted in red the  $765\text{ cm}^{-1}$  C-Cl peak, in blue the  $1600\text{-}1650\text{ cm}^{-1}$  C=C peaks linked to Fenofibrate presence.

TABLE 5.8: FTIR characterisation of immediate release tablets via the intensity of the Fenofibrate characteristic  $765\text{ cm}^{-1}$  peak.

	Shell thickness[mm]	Fenofibrate	Tablet[%]	Reference[%]
$D_a$	1	10% (w/w)	$36.8 \pm 1.8$	$37.0 \pm 3.5$
$D_b$	1.5	10% (w/w)	$37.6 \pm 2.0$	$37.0 \pm 3.5$
$D_c$	2	10% (w/w)	$37.9 \pm 1.6$	$37.0 \pm 3.5$
$D'_a$	1	5% (w/w)	$23.6 \pm 1.9$	$23.6 \pm 2.8$
$D''_a$	1	10% (w/w)	$36.8 \pm 1.8$	$37.0 \pm 3.5$
$D'''_a$	1	20% (w/w)	$43.1 \pm 1.1$	$42.5 \pm 2.9$
$D''''_a$	1	30% (w/w)	$70.5 \pm 0.6$	$70.5 \pm 0.1$

### 5.2.2.2 Raman spectroscopy

Raman line scans were acquired to produce a chemical characterisation across the core shell interface accordingly to the procedure described in Section 3.2.9. The study was carried out on one day old tablets and the line of analysis was

positioned astride the separation line between the core and shell region, as a consequence the "zero" value of the x-axis corresponds to the interface, the negative numbers to the core and the positive to the shell. The graph 5.14 A clearly show well definite separation between the core and the shell, suggesting the presence of Fenofibrate in the core of the tablet with little signs of it diffusing into the shell.

Such distribution is furthermore confirmed when analysing region of the sample further away from the interface. It is clear from Fig. 5.14 B how the core spectrum is compatible with the presence of Fenofibrate while the shell show little sign of it. Nevertheless, minor traces of the API can be found also in the shell region close to the separation line suggesting the possibility of some minor chemical diffusion of Fenofibrate from the main areas of interest to the adjacent shell.

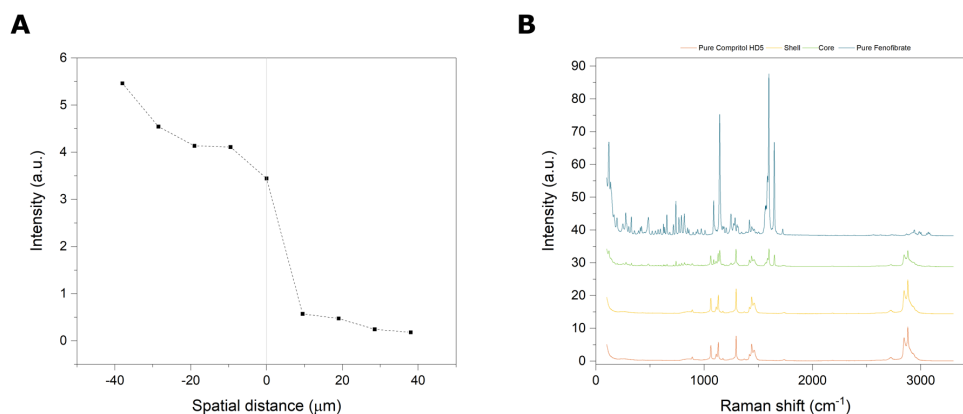


FIGURE 5.14: Raman spectra and linear mapping of the core shell interface in delayed release tablets. A) Raman linear map of the chemical characterisation of the core shell interface. Where on the x-axis "zero" corresponds to the interface, the negative numbers move into the core region and the positive into the shell section. B) Spectra of reference Compritol HD5 ATO (orange), printed shell far from the interface (yellow), printed core at far from the interface (green) and reference Fenofibrate(blue).

### 5.2.2.3 *In vitro* drug release

Drug dissolution studies were performed to assess the efficacy of a drug-free shell layer in preventing drug release from the tablet's core. As for the immediate release tablets a Copley's Dissolution Test Dis8000 was used with the same test conditions described Section 3.2.13.

Thus, the first set of samples to be tested included solid dosage forms with fixed core geometry and shell thickness variation. As to be expected all tablets displayed a delayed release with a lag time proportional to the shell

thickness, specifically a 15, 20, 30 min lag time was observed respectively for 1 mm, 1.5 mm and 2 mm, Fig. 5.15 A and B. After the initial delay the drug release was prompt and continued for the remaining 12 h. This is consistent with the literature [71, 102, 160], proving that the drug-free shell induces a delay in the drug release and that shell thickness has a significant influence on dissolution profile. Notably the thickness of the external layer does not only prevent dissolution for the initial delay time, but has a long lasting effect on the dissolution rate. From Fig. 5.15 A it is clear how the red curve corresponding to the 2 mm geometry shows a slower release profile compared to the green curve (1 mm shell thickness) delivering just over 20% of the drug load in 12 h despite being delayed only 15 min comparatively. As already observed for the disc tablets in Section 4.2.2.4 also in this case the tablets dissolved mainly by degradation and erosion. As a result the release of the drug through the exterior shell is mediated by the same mechanisms. In addition the degradation of the material weakens the structural integrity of the outer shell causing it to eventually separate and expose the main core directly to the medium. Provided it displayed the fasted release profile the thinner shell geometry was also tested with multiple Fenofibrate concentrations to ensure that the delayed behaviour was replicable and it was not linked to the specific drug loading. As expected, tablets displayed the same delayed release of 15 min and afterwards developed a similar dissolution pattern to the one seen for both the disc and honeycomb tablets, where the fastest dissolution was achieved by the lowest concentrations. Suggesting that delay induced by the drug-free shell is independent from drug loading and it is purely linked to the geometry.

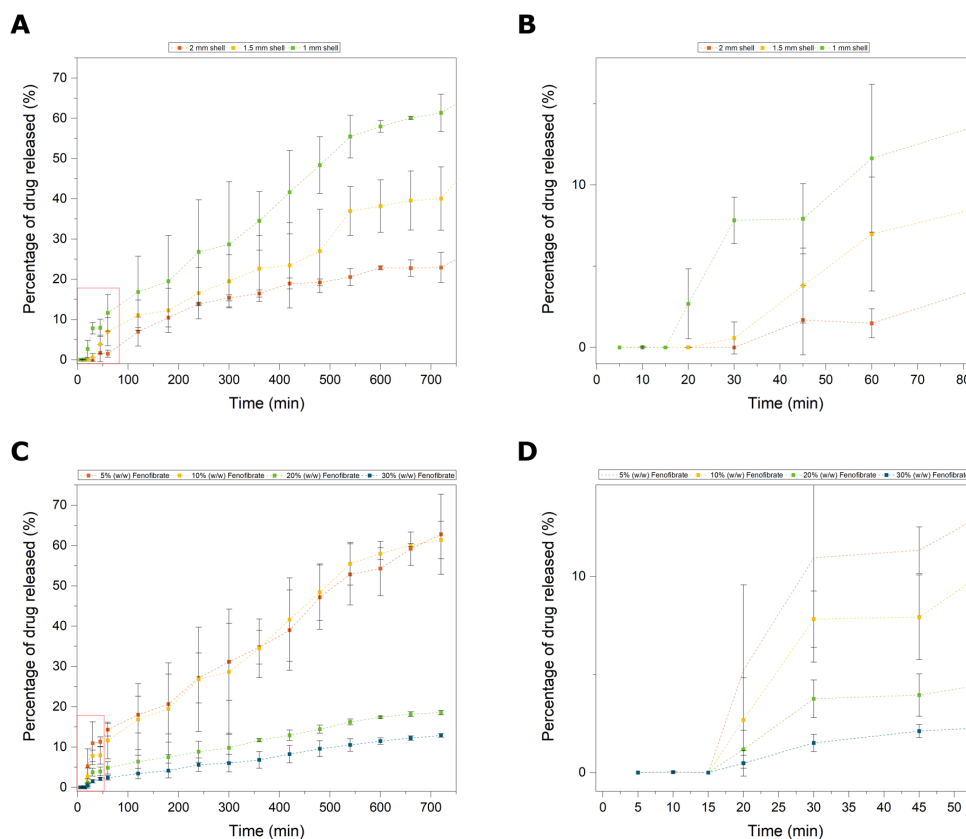


FIGURE 5.15: *In vitro* dissolution test of delayed release tablets of Compritol HD5 ATO and Fenofibrate mixture. A) Dissolution behaviour of delayed tablets with constant 10% (w/w) drug loading and various shell thickness 1 mm, 1.5 mm and 2 mm, B) blowout of the initial 80 min of the dissolution profile showing the lag time caused by the presence of the drug-free shell layer. C) Dissolution profile of delayed tablets with constant geometry (shell thickness 1 mm) at different drug loading concentration namely 5%, 10%, 20% and 30%. D) blowout of the initial 50 min

## 5.2.3 Pulsatile release tablets

### 5.2.3.1 Optical spectroscopy and printed tablets geometrical evaluation

One of the main advantages of Additive Manufacturing is its capability to mass-produce personalised components without substantially increasing production time or costs [245, 84, 59]. Thus, once a system is capable of creating multi-material samples like the ones shown in the previous section, it is possible to scale it to extremely complex geometries provided the correct 3D digital design is available. This, however, is often non-trivial, and might require a few rounds of trial and errors since most tools for complex design are still in their infancy and struggle to identify potentially troublesome features.

Pulsatile release tablets are an example of this more complex multi-material design, and demonstrate the capabilities of the dual unit hot-melt inkjet printer discussed in Chapter 2.

With this geometry the goal was to push the systems capabilities and build upon what was learned from the delayed release tablets to get a better understanding of the effect of geometry on drug release. The tablet in Figure 5.3 was designed with two separate reservoirs satisfying the requirement for a potential complex dual burst release. This choice offered a challenge both in terms of the strain put on the new system via the request for complex geometrical material deposition and on the capacity to produce a suitable 3D geometry.

The 2D bitmaps for this section were produced following the slicing process described in Section 5.1.2.2. The original design was divided into its constituents and sliced according to layer height, this left us with five sets of repeated bitmaps, which not only contain the 2D design but also information about the paired material in the form of file name.

Our modified software was then capable of pairing the different files to the correct print head in order to deploy the desired material at the correct time to produce the sought after high precision multi-material designs.

As visible from the photo in Fig. 5.16 the solid dosage form was printed successfully and it appears homogeneous and well defined with only minor defects.

As was the case for the delayed release tablet the top surface was smooth with the exception of a small indentation in correspondence of the outside edge of the drug-loaded ring, from a visual inspection no defects are visible in correspondence to the central core. Nevertheless, the resultant tablet was solid and could be handled without issue. It is clear that the printing technique was successful and that the printed product does not differ greatly from the computer design. The process was a clear success and the end result was in good agreement with the parameters of the digital version as highlighted in Table 5.9



FIGURE 5.16: Photo of pulsatile release tablets.

### Optical microscopy

Optical microscopy was used to investigate the material transition between the core/shell and ring/shell interface.

In the attempt to expose the tablet middle cross section a print was stopped at the middle point and subsequently analysed using a Nikon Eclipse Lv100 ND microscope with NIS Elements software equipped with a 50x objective. From Fig. 5.17 all three tablet's regions are visible and well defined, namely the ring, shell and core regions. Similarly to what is visible in the delayed release tablets the interface is not perfectly smooth but instead presents a small valley. Such observations are in good agreement with what was observed from the visual analysis of the full tablet. Moreover the surfaces show the familiar printing lines common to all our tablets. Results are summarised in Table 5.9 alongside the tablets geometrical properties.

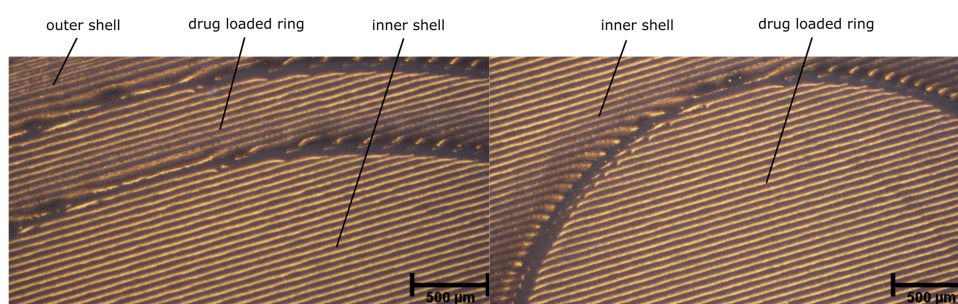


FIGURE 5.17: Optical microscope images of pulsatile release tablets. Detail of the interface between the ring/shell regions (A) and the core/shell regions(B)

### Scanning Electron Microscopy

Scanning Electron Microscopy was utilised as a complementary higher-resolution visualisation method, specifically to study the connection lines

between the drug loaded regions and the drug free ones. As for the previous cases a tablet was prepared by interrupting a print half way through to expose the middle cross section. In order to include all the features of interest in one frame a 30x magnification was employed. The print result was overall a success, every region was well formed, smooth with faint printing lines and only small defects in the top section of the junction line. The EDX analysis provides a first insight on drug distribution inside of the pulsatile tablet, the yellow dots in Fig. 5.18 represent signals from a Chlorine atoms suggesting that the API is localised inside the core and ring regions in good agreement with our theoretical design.

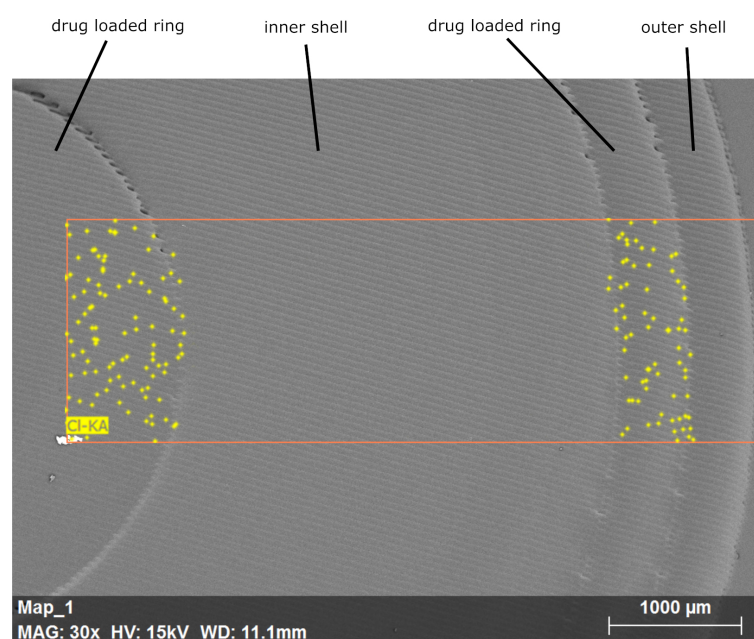


FIGURE 5.18: SEM images with EDX data overlay of pulsatile release tablets showcasing the bespoke geometry. The red perimeter delimits the EDX region of analysis, the yellow signals are associated with the presence of Chlorine atoms, suggesting that Fenofibrate localisation.

### 5.2.3.2 Content uniformity and weight variation

Building on the information gathered from the previous analysis, FTIR and weight variation were introduced as a further confirmation of the validity of our 3D design and its manufacturing. Firstly, five tablets were weighed and the outcomes averaged. To correctly interpret the results the theoretical tablets weight were calculated from the designed geometry and the estimated density studied in Section 4.1.1, and to do so the same procedure utilised in the analysis of the immediate and delayed release tablets was employed. The product of the calculations alongside the measured values are

reported in Table 5.9. The measured values are in good agreement with the digital version.

TABLE 5.9: Summary of the pulsatile release tablets geometrical and weight properties

	Printed tablet	Expected value
Diameter [mm]	$12.00 \pm 0.01$	12
Height [mm]	$9.14 \pm 0.08$	9
Weight [g]	$0.98 \pm 0.02$	$1.00 \pm 0.02$

### Fourier Transform Infrared Spectroscopy

Once again Fourier Transform Infrared Spectroscopy was utilised to further confirm the presence of Fenofibrate inside the printed tablets by recognising the C-Cl bond, characteristic of the Fenofibrate molecule. In Figure 5.19 are reported the spectra for core and ring regions alongside with the shell one. The blue box highlights the  $1598\text{ cm}^{-1}$ - $1650\text{ cm}^{-1}$  C=C peaks, while the red box highlights the  $765\text{ cm}^{-1}$  the major characteristic peaks of Fenofibrate.

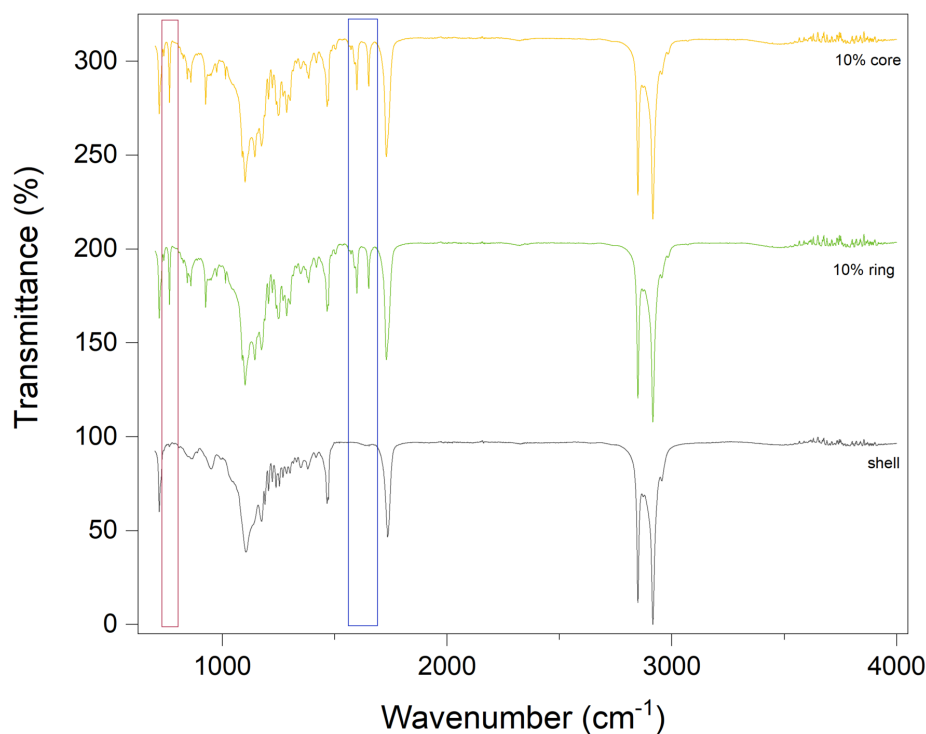


FIGURE 5.19: Fourier Transform Infrared Spectroscopy analysis of pulsatile release tablets. Highlighted in red the  $765\text{ cm}^{-1}$  C-Cl peak, in blue the  $1600\text{--}1650\text{ cm}^{-1}$  C=C peaks linked to Fenofibrate presence.

From the graph it is apparent how only the spectra relative to the core and ring regions present the peaks of interest strengthening the conviction that the API is located in only such regions. Furthermore by comparison with the values observed in the previous analysis it is clear that the drug concentration is compatible with the 10% loading estimated (Table 5.10).

TABLE 5.10: FTIR characterisation of pulsatile release tablets via the intensity of the Fenofibrate characteristic  $765\text{ cm}^{-1}$  peak.

	Fenofibrate	Tablet [%]	Reference [%]
Core	10% (w/w)	$37.9 \pm 1.0$	$37.0 \pm 3.5$
Ring	10% (w/w)	$37.5 \pm 2.4$	$37.0 \pm 3.5$

<sup>a</sup> The notation here utilised to identify the different geometries is consistent with what previously established in Table 5.1.

### 5.2.3.3 Raman spectroscopy

As for the pulsatile release tablets, Raman was used to study the chemical signature at the interface between the inner shell layer and the drug loaded core, as well as between the ring structure and the external shell. In figure Fig. 5.20 the results of the two line maps corresponding to the intersections between core/inner shell and the ring/outside shell are presented. The same figure also reports the tablets 3D schematics and a representative spectra for each of the four different regions far from the contact line, alongside the reference spectra for pure Compritol HD5 ATO and Fenofibrate. For the sake of consistency, the same notation is used as in section 5.2.2 where the system's zero has been made to coincide with the demarcation line between regions such that the drug loaded region falls in the negative range of the x-axis while the drug-free one is in the positive values on the x-axis.

From the analysis of the individual spectra in Fig. 5.20 B it is clear that the characteristic Fenofibrate  $1598\text{ cm}^{-1}$ - $1650\text{ cm}^{-1}$  peaks can be found only in the core and ring regions suggesting drug localisation. Similarly, when analysing Fig. 5.20 C and 5.20 D a clear change in behaviour occurs when crossing the zero of the system. Meaning that the Fenofibrate is concentrated in the area corresponding to negative values of the x-axis which identifies the core and ring regions in the C and D graphs respectively. Nevertheless, minor traces of the API can be found also in the shell region suggesting the possibility of minor chemical diffusion of Fenofibrate from the main areas of interest to the adjacent shell.

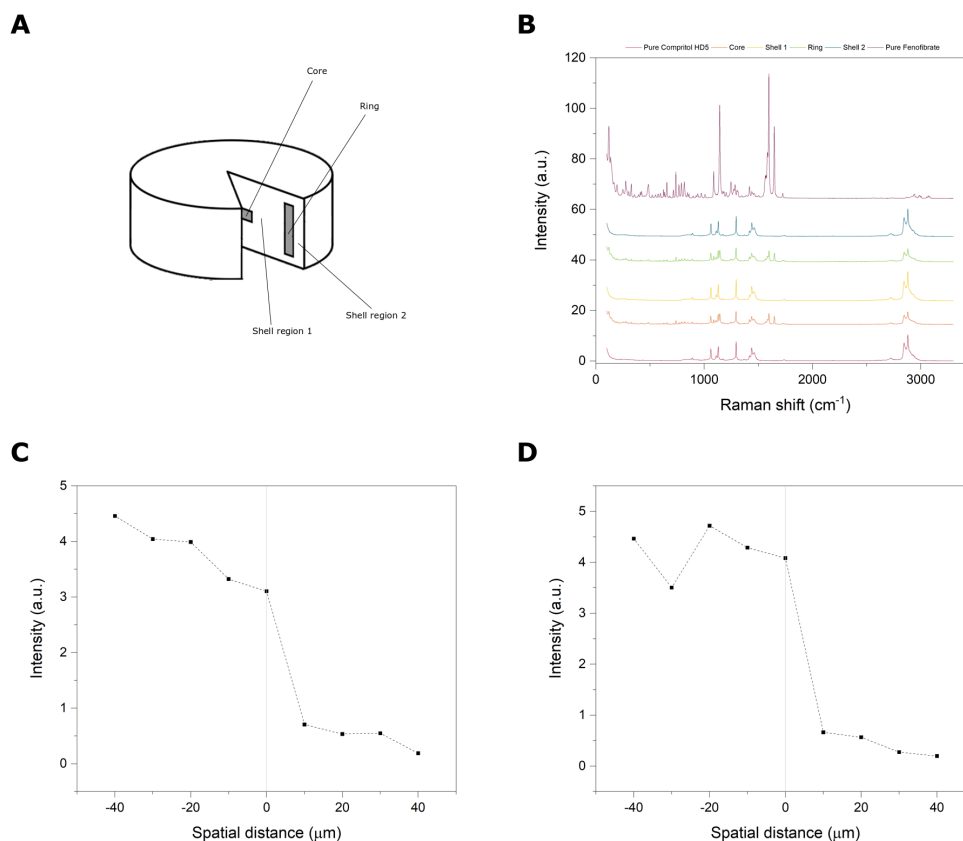


FIGURE 5.20: Raman spectra and linear mapping of the core-shell and ring-shell interfaces in pulsatile release tablet. A) Tablet schematics with labelling of the region of interest for the analysis. B) Spectra of: reference Compritol HD5 ATO (red), printed core far from the interface (orange), printed first shell far from the interface (yellow), printed ring far from the interfaces (green), printed external shell far from the interface (blue) and reference Fenofibrate (purple). C) Raman linear map of the chemical characterisation of the core-inner shell interface. Where on the x-axis "zero" corresponds to the interface, the negative numbers move into the core region and the positive into the shell section. D) Raman linear map of the chemical characterisation of the ring-external shell interface. Where on the x-axis "zero" corresponds to the interface, the negative numbers move into the core region and the positive into the shell section.

#### 5.2.3.4 *In vitro* drug release

As mentioned in the introduction, with this design the aim was to push the depositional capabilities of the designed printer system by producing a tablet displaying complex geometry containing multiple nested layer of drug-loaded and drug-free material to deliver a dual burst release. In the specific case the tablet visible in Fig. 5.3 were produced, with two drug reservoirs encased in a drug-free matrix. The study was carried out following the procedure described in Section 4.2.2.4, noticeably the buffer was completely substituted every 15 min. Due to the design restriction, after an initial 20 min

delay the drug was then released in an initial burst, during which 70% of the drug content was released within 330 min (5 h and 30 min) as visible in Fig. 5.21, 1<sup>ST</sup> release. This first pulse was then followed by a 45 min low-level release interval before a second burst lasting an additional 2 h, Fig. 5.21, 2<sup>ND</sup> release. This behaviour is compatible with the assumptions and restrictions imposed on the design.

Moreover, thanks to the nature of the experiment for which the buffer had to be periodically substituted to monitor the release in small intervals, it was possible to get an insight in the degradation and erosion process that the tablet went through during the experiment. Specifically, after approximately three hours, tablet flakes were visible at the bottom of the dissolution vessel suggesting that the exterior layer had peeled, potentially revealing the drug loaded ring underneath. From this first experiment the drug content of the residues is not known, since a removal of even the smallest sample could effect the end dissolution profile. The author thus limited the analysis to pure observation. However, the assumption of an exposed drug layer is supported by the spike in drug release rate recorded approximately at the same time. Such material behaviour can be explained by the weaker adhesion between regions made of different materials. A similar effect was recorded around the seventh hour when bigger fragments of the tablets could be seen at the bottom of the vessel, again a spike in release followed.

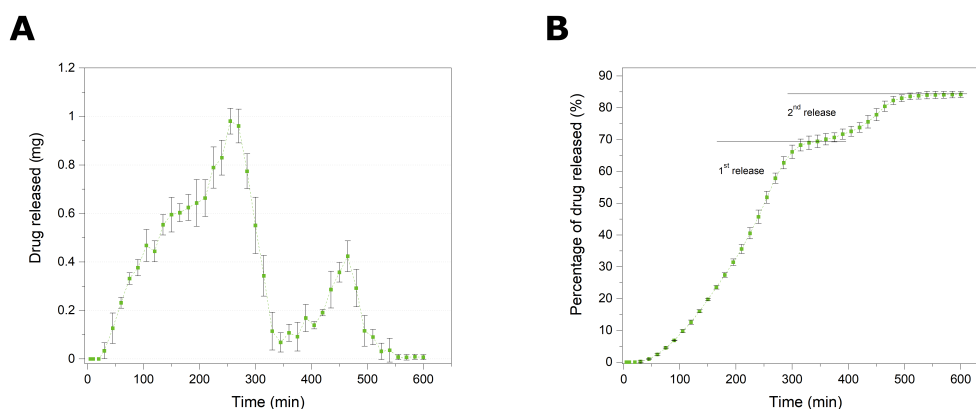


FIGURE 5.21: *In vitro* dissolution test of Pulsatile release tablets. (a) Shows the discrete release profile while (b) shows the cumulative release profiles obtained by addition of the data in graph (a).

### 5.3 Conclusions

To conclude, this chapter demonstrates the capability of the newly designed hot-melt 3D inkjet printer to deliver precise and accurate deposition of material droplets to produce multi-material solid dosage forms with complex geometries and drug distributions in a controlled manner.

Concurrently, it was also shown that a commonly used pharmaceutical lipid, Compritol HD5 ATO, can be printed as single ink material, or in combination with a model drug, Fenofibrate, without the need for additional solvents, removing the need for time consuming and expensive post processing steps. In addition, the process is likely usable with any other drug or drugs that have a higher degradation temperature and lower melting point than the operative printing process one (90 °C) and so could be potentially used in combination therapies.

It has also been shown how the drug is homogeneously distributed throughout the tablet (or desired area within the tablet), and that the tablet-to-tablet weight variation was within the recommended range of content variability. In conjunction, the well-defined interior structures was observed via both optical and spectroscopic techniques for the single material tablets with varied infill as well as the multi-material dosage forms suggesting a high level accuracy in material deposition. Furthermore, in this chapter it was demonstrated the capability of the system to fabricate tablets with tailored release profiles by smart designing the geometry with drug-free and drug-laden material localisation.

Similar to the previously published studies [70], it was established that the drug release from the tablet tended to be faster with the increase in surface area to volume ratio. Higher surface areas to volume ration indeed promote interaction between the material and the dissolution medium. Tablets with 45% infill (highest SA/V) produced the fastest release, while the 100% infill (full disc) showed the slowest. As a result, tablets with 100% infill were identified as a potential candidate for extended-release tablets, in contrast 45% infill tablets would be more applicable for immediate-release.

The dissolution profiles of the multi-material tablets best demonstrate the capabilities of the new system and the potential of three-dimensional design.

For tablets with an external drug-free (barrier) layer (1 mm, 1.5 mm and 2 mm), the drug release was prompt after an initial delay of 15 min, 20 min and 30 min respectively and continued for the remaining 12 h. This is consistent with what can be found in the literature [71, 102, 160], showing that the

use of drug-free shell gives a delay in the drug release. It was furthermore revealed that this is though not the only effect and that shell thickness has also a significant influence on dissolution profile. This type of solid dosage forms has thus the potential to be exploited for the production of delayed release tablets.

Lastly a dual reservoir tablet was prepared, where two concentric drug-loaded regions were encapsulated in a drug-free matrix. Due to the design restriction after an initial 20 min delay the tablet underwent a first drug released phase, during which 70% of the drug content was released within 330 min (5 h and 30 min). A second burst lasting an additional 2 h, was observed after a 45 min low release interval caused by the presence of the drug-free region that separates the two drug-loaded areas.

This behaviour is compatible with the assumptions and restrictions imposed by the design.

The behaviours observed clearly demonstrate that a multi-material hot melt inkjet printer provides a suitable system to produce complex three dimensional drug delivery unit and that 3D design has a major influence on drug delivery allowing to tailor the drug release profile so to obtain immediate, extended, delayed and pulsatile release.

## Chapter 6

# Conclusions and future work

The aim of this work was the design and development of a hot-melt inkjet 3D printing system for the production of functional multi-material solid dosage forms.

In the introductory chapter to this thesis I listed a series of objectives for this project. To conclude the same objectives are now revisited providing an overview of how they were fulfilled, any limitations and suggestions for future work. The original objectives included:

- Design and fabrication of a hot-melt inkjet manufacturing system capable of depositing multiple materials during a single additive process. Including:
  - Identification of critical features necessary to guarantee material ejection, deposition and solidification to form the desired 3D pattern.
  - Selection of a suitable dispensing unit and mechanical support system to allow for 3D movement and spatial control.
  - Creation of a digital model of the system and its practical implementation including calibration.
- Creation of a library of suitable excipient materials compatible with the hot-melt inkjet 3D printing process and suitable for pharmaceutical application. Selection of an appropriate test drug. Characterisation of the thermal, mechanical and chemical properties of the candidate materials, including the study of their density and shear viscosity, the analysis of their crystalline state and chemical composition through the use of FTIR and XRD and their response to thermal stress via DSC and TGA.
- Optimisation of the printing conditions for the pure materials selected in the previous section and the inks obtained combining each of the

excipients with the active ingredient at varying concentration, 5%, 10%, 20%, and 30 % w/w. Production of 3D disk shaped tablets to evaluate each carrier material drug release capabilities, described in terms of rate and drug content released over a 10h test run. Identification of the best performing excipient and drug loading.

- Design and production of a complex multi-material, multi-compartment proof-of-concept tablet showing complex time release, produced using the material selected in the previous ground work section.

## 6.1 Platform design and development

The creation of a working system relied on the adaptation of a pre-existing commercially available 3D printer (PiXDRO LP50), the fabrication of a new printing assembly and the development of a support system, including a temperature control unit, a power source and a drop deposition control system.

The decision to modify a pre-existing machine rather than designing a printer *ex novo* offered some advantages, but also imposed a series of limitations. Amongst the benefit of employing a commercially available machine the three dimensional control system is definitely the most advantageous feature. Conversely, the biggest disadvantages are the limitation in geometrical freedom and part weight due to the printer design and the maximum load supported by the commercially mounted motors.

The support system was designed with a modular approach in mind, which allowed for quick and secure assembly, while at the same time granting easy access to all parts for substitution and maintenance. Moreover, a modular approach allows for future developments such as non matching printing units.

Due to the initial desire to utilise the commercially available hot-melt reservoirs, the present printing assembly was designed capable of housing two printing units each comprising of an inkjet print-head capable of withstanding high temperatures (Spectra SE-128 printheads, Fujifilm, Japan), a heater and a standard high temperature reservoir. The presented design required multiple prototype cycles before meeting all the required criteria, in particular the weight limitation. The use of in-house Additive Manufacturing systems played a key role in this phase, allowing to produce each new iteration

in a fast and cost effective manner. The resulting complex geometrical design was manufactured using an in-house laser sinter 3D printer, specifically a P-100 Formiga (EOS GmbH Electro Optical Systems, Germany) loaded with Nylon PA12. The choice of material allowed to produce high temperature resistant light weight parts without sacrificing sturdiness. It is thus clear that 3D printing was not only the key focus of this work, but also an essential support system allowing the creation of complex parts that would have been either impossible or very costly to produce by other means. Furthermore, in the last iteration, in an attempt to further reduce the weight strain on the printer motors a lighter aluminium copy of the original reservoir was produced reducing the weight by 60%. The final assembly weighed 1.70 kg, safely inside the capabilities of the stepper motors and only 324 g more than the single unit.

With the addition of a complementary temperature control unit and power supply, the in-house fabricated reservoir performed as expected. Specifically, it was able to reach the desired temperature in the range of interest and maintaining it constant for the time required. This suggests that in the future it would be possible to produce reservoirs with bespoke geometry to enable the inclusion of more than two dispersing units, thus increasing the system capability to produce tablets with complex geometrical and compositional design. Furthermore, our choice to adopt a modular approach for the support structure implies that only minor modification will be necessary to implement these changes.

To complement the new setup an updated software package was developed built upon the pre-existing structures, these included script blocks focused on managing the individual printhead and their depositional interaction taking into consideration the differences in the layer height linked to variations in material thickness and pattern. Thus, it will find application regardless of the material of choice and supersede the use in this work.

As visible in Chapter 4, the jetting heads performed as expected and were capable of reliably delivering ink droplets. This suggests that our modification did not invalidate the printer functionality. Nevertheless, for the material tested the drop size was identified as larger than the desired 50  $\mu\text{m}$ . This results from the combination of the printhead delivered drop volume and the droplet spreadability. The latter is mainly dependant on the choice of material and specifically on the material viscosity and fluid-substrate interaction, leaving little room for improvement once the material has been selected. Concurrently, drop volume is mainly determined by the nozzle

main dimension. Indeed while it can be tailored by changing the printing impulse duration and intensity it shows a minimum volume of 30 pL as reported by the manufacturer. As a result, if smaller resolutions are needed different printheads should be taken into consideration.

## 6.2 Carrier selection and solid dosage forms evaluation

Several formulations were tested based on their potential printability as result of a literature study. Lipids were found to be the best contenders due to their favourable thermo-mechanical properties and for their use as enhancers in the delivery of poorly soluble drugs [209]. Interestingly, lipids cannot be easily processed using any other AM process, so thermal jetting would be a great alternative 3DP method to be developed. All the materials here tested were not originally formulated for additive manufacturing techniques, but instead for use as pharmaceutical excipients in traditional tableting methods. The fact that we were successful in printing these materials suggests that any other pharmaceutically graded material with viscosity and melting point in the range of interest is a potential candidate for this method without the need of further compositional modification or the addition of complementary excipients. Furthermore, while using traditionally available material the employment of our new system introduces new degrees of freedom allowing to produce complex multi-material structures which would either be impossible or very costly to produce by traditional means. For this work the materials characterised were divided as per their role in the tablet. Specifically were selected a test drug, Fenofibrate, and five carrier materials, Apifil CG, Candelilla, Compritol 888ATO, Compritol HD5 ATO and Precirol ATO. Carriers were selected as the best candidates on the base of their potential usefulness for multi-material AM, while Fenofibrate was selected as a test drug due to its low melting point, its high degradation temperature and the range of application.

Before being used as 3D printing inks all materials underwent rigorous testing, to ensure printability and to safeguard the extremely delicate and expensive printing unit, including determination of density, viscosity, chemical characterisation, melting and degradation temperature and drug loading capabilities. All ink mixtures, obtained by co-melting method, displayed a distinct chlorine peak when analysed using FTIR-ATR, which belonging

uniquely to the drug molecule confirmed its presence within the ink compounds. Concurrently, the study of the peak intensity combined with the weight investigation confirmed that indeed the ink preparation method was successful and the inks were composed of the correct ratio of drug to carrier. Furthermore, it was possible to determine that all the material taken into consideration, both carriers and drug, melt completely below the maximum working temperature of the machine  $\leq 90$  °C. In addition, the TGA results confirmed that all material can successfully survive the temperature required for printing and ink preparation without undergoing degradation. DSC also provided an initial overview of the crystalline state of the materials, more precisely it was noted that when in the mixtures Fenofibrate did not show its characteristic peak however it caused a shift towards lower temperatures of the excipient thermogram suggesting that while a part of it could be in a crystalline form this must be below the detection limit of the instrument indicating that the remaining content must be in a disorderly state. Lastly, the rheology study showed that if the correct temperature is selected all inks can flow with a Newtonian behaviour at high shear rates with viscosities within the printing range 8 mPa s to 20 mPa s. In addition, when Fenofibrate was added to the base excipients two distinct type of behaviour emerged. In the first case the viscosity of the ink increased with the Fenofibrate content and could be higher than the combined viscosity of the original materials, while in the second the opposite behaviour was observable. Notably, with the exception of Apifil all other pure lipids showed similar shear thinning behaviour, suggesting that the solution must be sought in the materials chemical composition and interaction with the drug molecule. In particular, characteristic of the material belonging to the first group is the presence of PEG esters. These results combined with reports in the literature [223], suggest that PEG and Fenofibrate are capable of forming localised agglomerates which in return would disrupt the original flow and cause the observed increment in viscosity. Further analysis would be recommended to investigate and better understand this phenomenon and to investigate its potential short and long term effect on drug stability. Despite the differences all materials and ink compounds were considered to be compatible with the hot-melt technology and suitable for printing.

For each of the five materials it was possible to determine a suitable set of printing condition to guarantee good drop formation, these included pressure and jetting wave function timings and intensity. It was discovered that a constant negative pressure of  $-20$  mbar was sufficient to prevent nozzle

plate flooding during idle times regardless of material. Furthermore, it was noted that the rise and fall time produce symmetric effect on droplet formation, where extremely short impulse times  $\leq 1 \mu\text{s}$  are not strong enough to generate a satisfying drop while increment of the inset/outset time past the optimum point cause slower droplets. Similar behaviour is also seen for the peak time. The optimised droplets displayed speed in the  $4 \text{ m s}^{-1}$  to  $6 \text{ m s}^{-1}$  range which is ideal for inkjet printing [80].

All materials achieved best 2D results when the overlap was set to approximately 60% of the droplet size, coherently with the upper limit of what previously reported [224, 95].

The results of 3D deposition were well-defined disk tablets sets prepared for each carrier and containing varying drug concentration from 5% to 30% (w/w) Fenofibrate. FTIR analysis of samples taken before and after the printing process show no change in the material, indicating that the printing process does not effect ink composition. Furthermore both FTIR and XRD analysis showed that there was no detectable interaction between the chosen excipients and the drug, with the latter being partially in a crystalline and partially in a disorderly state.

The *in vitro* drug release studies revealed that all tablets, independently from the main excipient or drug loading, were capable of producing sustained drug release for the duration of the study. In particular Candelilla produced the slowest sustained release making it a candidate for implants or prolonged release. In contrast Precirol ATO 5 and Compritol HD5 ATO were the best performing. This finding is of particular interest due to the diverse drug delivering mechanism at the base of the two. Precirol ATO 5, an insoluble matrix, relied mainly on dissolution as the main mechanism for drug release, while Compritol HD5 ATO tablet release was based on both diffusion and erosion mechanisms. As a result Compritol HD5 ATO was identified as the most suitable excipient for the further development of a multi-material design and the optimum drug loading was determined to be 10% w/w. These results demonstrate the validity of hot-melt inkjet 3D printing as a feasible method to produce simple tailored medicines with bespoke drug loading and release based on the choice of excipient.

### 6.3 Fabrication of 3D multi-material functional structures

Finally in Chapter 5 the information gathered was used to produce several proof-of-concept multi-material solid dosage forms with complex geometries and drug distributions (see section 5.1.2.1) to showcase the potential of the multi-material hot-melt approach proposed in this work. These included single and multi-material complex 3D patterns with defined localised drug loading where the drug-free ink is used as a release-retarding material to produce a series of tablet structures displaying immediate, extended, delayed and pulsatile drug release.

To address the immediate drug delivery design a disk tablet was developed containing a honeycomb infill as in Fig. 5.1 in chapter 5 to increase the surface area to volume ratio compared to the traditional disk tablet [95]. Delayed release tablets were modelled to include a drug loaded centre surrounded by a drug free shell acting as a rate-limiting barrier to active ingredient release. Lastly pulsatile release tablets were produced as proof-of-concept to show the possibilities offered by the multi-material printing. In this case the geometrical design is a tablet containing two nested drug-loaded regions encapsulated by inactive drug-free material.

Detailed characterisation of the tablets was performed to ensure that the multi-material hot melt inkjet printer is capable of providing precise deposition and produce complex three dimensional drug delivery unit in accordance with the digital design. For this purpose several different techniques were employed including FTIR, SEM-EDX, Raman, XRPD and *in vitro* drug release.

Optical and spectroscopic techniques confirmed the capability of the system to deliver precise and accurate deposition of material droplets by producing well-defined interior structures for both the single material tablets with varied infill and the multi-material dosage forms. In addition the study of Fenofibrate content in different drug-loaded regions within the tablets via FTIR suggests that the drug is homogeneously distributed. The analysis of the tablets weight confirmed tablet-to-tablet weight variation to be within the recommended range of content variability, overall suggesting that the new system is a suitable method for reliably producing tablets with complex multi-material 3D geometry.

From the study of the honeycomb shaped tablet it was possible to conclude that higher surface area to volume ratio geometries produce faster

drug release, due to the increased surface area in contact with the dissolution medium. As a result, tablets with 100% infill (solid disks) constitute a candidate as extended-release tablets, while 45% infill tablets can find application as immediate-release. Whilst similar approaches have been adopted by others in the past [137, 160, 70, 71] this is, to our knowledge, the first time that this approach has been tested on the ink materials presented in this work.

The honeycomb structured tablets offered an insight on the potential of smart design of tablet geometry as a method to produce tailored release profiles, building on this knowledge the multi-material tablets were designed to best encapsulate this geometrical freedom and to demonstrate the capabilities of the new system.

Tablets with an external drug free barrier layer showed an initial delay followed by a prompt drug release which continued for the remaining 12 h, where the extent of the delay in drug release was proportional to the thickness of the drug-free shell layer. This initial study suggests that for Compritol HD5 this delay correspond to approximately 15 min /mm of shell thickness. As a result this type of geometry is an example of delayed release tablet, it is important to notice that while the example here presented provided a maximum delay of 30 min this time can easily be tailored by altering the external shell layer thickness.

Lastly to best showcase the potential of the newly developed dual material system a dual reservoir tablet was prepared, where two concentric drug-loaded regions were encapsulated in a drug-free matrix. In agreement with what observed for the delayed tablets, the presence of the outer drug-free shell caused an initial 20 min delay quickly accompanied by a first drug released phase, during which 70% of the drug content was released within 330 min (5 h and 30 min). A second burst lasting an additional 2 h, was observed after a 45 min low release interval, during which less than 5% of drug was released.

The observed dual burst was in good agreement with the assumptions and restrictions imposed by the design, suggesting that a multi reservoirs tablet could act as a chrono-release tablet where the two bursts are separated by an inactive interval.

These results clearly demonstrate that a multi-material hot-melt inkjet printer provides a suitable system to produce complex three dimensional

drug delivery units and that 3D design has a major influence on drug delivery allowing to tailor the drug release profile so to obtain immediate, extended, delayed and pulsatile release.

While it was possible to reliably produce complex three dimensional multi-material dosage forms further tests and pattern re-designs would be required to study the extent of applicability of this new system. In particular this future work should focus on two main aspects: to understand to what extent geometry complexity can be exploited to be used in pharmaceutical applications, and move forward from single matrix material designs to multi carrier, multi active dosage forms. In Chapter 4 it was discovered that Candelilla is characterised by an extremely slow delivering rate, this makes it a poor choice as a carrier for the drug-loaded regions however this property makes it well suited as a retardant shell. Indeed, given the slow release rate of Candelilla it would be safe to assume that when compared to Compritol HD5 thinner shell walls would yield to similar results. This opens the door to a multitude of possibilities, focussing the attention on the well known pulsatile tablet geometry the inclusion of Candelilla as a drug free material while keeping Compritol HD5 as the Fenofibrate carrier would theoretically allow to extend the time elapsing between two drug release bursts while maintaining the same geometry. Furthermore, moving from the original design the use of thinner shell layers would allow for the inclusion of more than two drug loaded regions resulting in more than two bursts without changing the overall tablet size. The adoption of a release retardant material such as Candelilla would still allow for burst separation. In this work only one test drug was taken into consideration however it is possible to see how given the carrier materials this hot-melt approach can be extended to any drug that has a higher degradation temperature and lower melting point than the operative printing process (90 °C) and viscosity in the range of interest. The expansion of the library of active ingredients compatible with hot-melt inkjet printing technology would enable multi drug printing where the different drugs are loaded into different tablet regions to create complex delivery profiles, i.e. a concentric design with alternating drug loading should create an out of phase double pulsatile release of the two drugs[246]. These of course are speculations and rigorous analysis should be performed before any conclusion could be drawn. During the multi-material printing analysis a series of limitations were identified and should be taken into consideration when planning future developments. Particular attention should be reserved to the region of contact between the different materials, as mention in Chapter 2 this constitutes

a problematic area, specifically the focus should be in avoiding both physical and chemical interaction while ensuring good part stability. Another key aspect to be considered when mixing different inks materials is the variation in layer height, this problem was extensively discussed in Chapter 2 and a software solution was proposed, however it was never tested and should thus undergo rigorous evaluation before being utilised.

In conclusion the work in this thesis has demonstrated that multi-material hot-melt inkjet 3D printing provides a suitable technology to produce complex three dimensional oral solid dosage form. In addition, the use of a hot-melt approach, where heat is used as a way to maintain the material in a liquid state without the need of additional solvents, provides significant formulation benefits by eliminating the post processing solvent removal step and as a result making the solid dosage form readily available.

To our knowledge, it was here shown for the first time, a dual unit hot-melt 3D inkjet system inkjet printing capable of producing highly tailored multi-components tablets with precisely designed drug release profiles.

We believe that by exploiting the native properties of the system such as controlled geometrical freedom and tablets fast production and availability, in combination with the development of a library of materials and pre-made available tablets design we are paving the way towards a plug-and-play approach towards medicine, providing an opportunity for the production of advanced solid dosage forms with pre-determined release profiles on the base of geometry and material choice.

Still a lot of work is necessary before this could become an commercial reality and particular attention should be put in the study and improvement of both drug release prediction strategy as well as an expansion of the number of readily available excipients and active ingredients.

## Appendix A

# Appendix

### A.1 Code

Each of the printing unit is associated with a head profile recipe, namely "head0" and "head1", these contain all the information relative to the specific printing unit and its ink content. They include the printing parameter associated with the specific ink as well as the printhead orientation and system and printing temperature.

The main printing script "multi-recipe-anna" is then in charge of material deposition by calling and activating the correct profile on the base of the bitmap structure. Both the main script and the recipes include three main files, a logic instructional file (.CS file), a parameter definition and storage (.XML file) and an interface (.XML file). Since the last one is redundant for the sake of understanding the program functionality, in the following section we are going to present only the first two. All code as mentioned in section 2.3 the code here presented was built on pre-existing routines from the manufacturer (Mewyer Burger, Netherlands).

LISTING A.1: multi-recipe-anna.cs

```
1
2 /*
3 Anna 2019
4 this defines the minimum number of layer per each material
   to create a levelled surface.
5 it then calls the single head recipes and prints the
   respective bitmap accordingly.
6 the entire print is produced in block steps to avoid leening
   and smearing.
7 */
8
9
10 public void Initialize()
```

```
11 {
12 }
13 public void Execute()
14 {
15     string Recipelist = Parameters.GetValue("Recipe.Recipes");
16     string[] Recipes = Recipelist.Split(',');
17     string ParentRecipe = RecipeHandler.activeSetFile;
18     string name = Parameters.GetValue("Recipe.Name");
19     double LHO=Parameters.GetValue("Recipe.LH0[0] "); //layer
        height
20     double LH1=Parameters.GetValue("Recipe.LH1[0] ");
21     double NH0=Parameters.GetValue("Recipe.NH0[0] "); //number
        of layer
22     double NH1=Parameters.GetValue("Recipe.NH1[0] ");
23     Int BHO = 1;
24     double ratio = LHO/LH1;
25
26     while (true) {
27         var BH1 = BHO * ratio;
28         if ((BH1 % 1) == 0)
29         {
30             Console.WriteLine($"BHO: {BHO}, BH1: {BH1}"); //number
                of layer per material to be even
31             break;
32         }
33         BHO++;
34     }
35     double BL = LHO * BHO; //block size
36     double NBL = NH0 / BHO;
37
38     Simulator.Clear();
39     Parameters.SetValue("StandardPrint.AutoClearSimulator",false
        );
40
41
42     bool z_safe = true;
43     bool simOnly = (Parameters.GetIntValue("Simulator.
        SimulationType")==1);
44     Position sub = Positions.Get("SubstrateThickness");
45     double z = sub.GetAxisFloat(Position.Axes.Z);
46     double d = 0.03;
47     int i = 1;
48     int j = 1;
49     // Only check z_safe if not in simulation mode
50     if(!simOnly)
51     {
```

```
52 Helper.CheckPrintConditions();
53 PHD.StopHead(DataGen.Active.HeadInfo);
54 z_safe = Motion.CheckHomePos(Position.Axes.Z);
55 }
56
57 if(z_safe)
58 {
59     if ((!simOnly) & (Parameters.GetIntValue("Recipe.
60         DoMaintenance") >0))
61     {
62         Script.Run(Helper.GetScriptDir() + "maintenance.cs");
63     }
64
65     if(LH0>=LH1)
66     {
67         for(int b=1;b<=NBL;b++) //Different structural blocks
68         {
69             string active0 = string.Format("c:\\LP50\\Recipes\\12 Anna
70                 Recipe\\{0}.Recipe.xml", Head0);
71             string active1 = string.Format("c:\\LP50\\Recipes\\12 Anna
72                 Recipe\\{0}.Recipe.xml", Head1);
73             if(i<=b*BH0 && j<=b*BH1) //Repetitions of each
74                 structural block
75             {
76                 if(File.Exists(active0))
77                 {
78                     RecipeHandler.ActivateSet(active1,true);
79                     if(File.Exists("C:\\\\BMP files\\Anna\\Head1_"+name+i.
80                         ToString()+".bmp"))
81                     {
82                         Parameters.SetValue("Recipe.Bitmap","C:\\\\BMP files\\
83                             Anna\\Head1_"+name+i.ToString()+".bmp");
84                         Conversion.StartConversion(Parameters.GetValue("
85                             Recipe.Bitmap"));
86                         Script.Run(active0);
87                         Thread.Sleep(100);
88                     }
89                 }
90                 else
91                 {
92                     Helper.GenerateScriptWarning("Repeater",string.
93                         Format("Could not find bitmap: {0}!",Head1_"+name
94                             +i.ToString()+".bmp"));
95                 }
96                 z = z + LH1;
97                 SUB.Change(Position.Axes.Z, z);
98             }
99         }
100     }
```

```
89     else
90     {
91         Helper.GenerateScriptWarning("Repeater",string.Format(
92             "Could not find profile {0}!",Recipe));
93     }
94
95     if(File.Exists(active0))
96     {
97         RecipeHandler.ActivateSet(active0,true);
98         if(File.Exists("C:\\BMP files\\Anna\\Head0_"+name+i.
99             ToString()+".bmp"))
100         {
101             Parameters.SetValue("Recipe.Bitmap","C:\\BMP files\\
102                 Anna\\Head0_"+name+i.ToString()+".bmp");
103             Conversion.StartConversion(Parameters.GetValue("
104                 Recipe.Bitmap"));
105             Script.Run(active0);
106             Thread.Sleep(100);
107         }
108         else
109         {
110             Helper.GenerateScriptWarning("Repeater",string.
111                 Format("Could not find bitmap: {0}!",Head0_"+name
112                     +i.ToString()+".bmp"));
113         }
114         z = z + LH0;
115         SUB.Change(Position.Axes.Z, z);
116     }
117     else
118     {
119         Helper.GenerateScriptWarning("Repeater",string.Format(
120             "Could not find profile {0}!",Recipe));
121     }
122 }
123
124     else
125     { if(File.Exists(active0))
126     {
127         RecipeHandler.ActivateSet(active1,true);
128         if(File.Exists("C:\\BMP files\\Anna\\Head1_"+name+i.
129             ToString()+".bmp"))
130         {
131             Parameters.SetValue("Recipe.Bitmap","C:\\BMP files\\
132                 Anna\\Head1_"+name+i.ToString()+".bmp");
133             Conversion.StartConversion(Parameters.GetValue("
134                 Recipe.Bitmap"));
135             Script.Run(active0);
```

```

125     Thread.Sleep(100);
126 }
127 else
128 {
129     Helper.GenerateScriptWarning("Repeater", string.
        Format("Could not find bitmap: {0}!", Head1_ "+name
            +i.ToString()+".bmp"));
130 }
131 z = z + LH1;
132 SUB.Change(Position.Axes.Z, z);
133 }
134 else
135 {
136     Helper.GenerateScriptWarning("Repeater", string.Format(
        "Could not find profile {0}!", Recipe));
137 }
138 }
139 }
140 }
141 else
142 {
143 Helper.GenerateScriptWarning("Repeater", string.Format("Could
        not find profile {0}!", Recipe));
144 }
145
146 //
147 Parameters.SetValue("StandardPrint.AutoClearSimulator",
        true);
148 RecipeHandler.ActivateSet(ParentRecipe, true);
149 Motion.MoveTo("Service");
150 }
151 }
152 }

```

LISTING A.2: multi-recipe-anna.xml

```

1 <?xml version="1.0" encoding="utf-8"?>
2 <RecipeFlow xmlns:xsi="http://www.w3.org/2001/XMLSchema-
    instance" xmlns:xsd="http://www.w3.org/2001/XMLSchema">
3 <RecipeScript>repMix_file.cs</RecipeScript>
4 <Parameters>
5 <Parameter Name="Recipe.Name" Type="Text" Unit="" Default=
    "" Description="File name" Visible="Operator" Writable=
    "SystemEngineer" />
6 <Parameter Name="Recipe.Recipes" Type="Text" Unit=""
    Default="Head0,Head1" Description="Profiles to run in
    order" Visible="Operator" Writable="SystemEngineer" />

```

```
7 <Parameter Name="Recipe.LH0" Type="Number" Unit=""
  Default="1" Description="layer thickness H0" Visible="
  Operator" Writable="SystemEngineer" />
8 <Parameter Name="Recipe.LH1" Type="Number" Unit=""
  Default="1" Description="layer thickness H1" Visible="
  Operator" Writable="SystemEngineer" />
9 <Parameter Name="Recipe.NH0" Type="Number" Unit=""
  Default="1" Description="# layers material 0" Visible="
  "Operator" Writable="SystemEngineer" />
10 <Parameter Name="Recipe.NH1" Type="Number" Unit=""
  Default="1" Description="# layers material 1" Visible="
  "Operator" Writable="SystemEngineer" />
11 </Parameters>
12 </RecipeFlow>
```

## A.2 Materials review

The secondary goal of this research was to catalogue materials that fit into the operating range of the hot melt inkjet printer in order to widen the field of application of the technique.

In this section, a brief review of the excipients that have been taken into consideration for this purpose is presented. To start we decided to base our coarse grain selection on two main parameters: melting temperature and viscosity. In order to be printable a material needs to be completely melted at a temperature lower than 90 °C with a viscosity between 8 mPa s and 20 mPa s

Table [A.1](#) shows the list of materials evaluated, but that were not selected for testing. It is important to notice that the following list is far from complete and does not include material combinations.

TABLE A.1: Material review [247]

	Viscosity [mPa s]	Melting point [°C]	
<b>"Aristowax"</b>			
149/151·F ASTM	5.5 (99 °C)	140-142	✗
160/165·F ASTM	7.5(99 °C)	140-142	✗
<b>Beeswax</b>			
Yellow	12.1 (99 °C)-17.3 (80 °C)	62-66	✓
White	12.9 (99 °C)-19.6 (70 °C)	62-66	✓
Carnauba	33 (99 °C)	82	✗
Ceresin, lubricating	4.0 (99 °C)	59.5-71	✗
Ceresin, petroleum	10.0 (99 °C)	82.2	✓
<b>Paraffin</b>			
Scale wax, AMP	3.7(99°C)	35-40	✗
118/120 ° F AMP	3.9 (99 °C)	47.8-48.9	✗
124/126 ° F AMP	5.4 (70 °C)	51-52.2	✗
128/130 ° F AMP	5.9 (70 °C)	53.3-54.4	✗
	4.8 (80 °C)		
	4.0 (70 °C)		
132/134 ° F AMP	4.1 (99 °C)	55.5-56.6	✗
134/136 ° F AMP (hard)	5.8 (70 °C)	56.6-57.8	✗
	4.6 (80 °C)		
	3.6(99 °C)		
143/145 ° F AMP (hard)	7.2 (70 °C)	61.6-62.8	✗
	6.4 (80 °C)		
	4.2(99 °C)		
152/154 ° F AMP	7.9 (80 °C)	66.6-67.8	✗
	5.6 (99 °C)		
163/165 ° F AMP	7.4 (99 °C)	72.8-74	✗
<b>Polyethylene glycol (PEG)</b>			
600(570-630 mol. wt.)	10.5 (100 °C)	15-25	✓
1450(1305-1595 mol. wt.)	26.5 (100 °C)	42-46	✗
3350(3015-3685 mol. wt.)	90.8 (100 °C)	53-57	✗
Stearic acid,	11.3-11.9 (70 °C)	70	✓
Stearic acid USP	6.6 (70 °C)	57	✗
"Utahwax" (American ozocerite)	20 (95 °C)	70.7	✓

### A.3 Dimatix cartridge adaptation

The aim of this section is to present the work done to adapt a Dimatix inkjet cartridge to work as a hot-melt unit. This work was ultimately not successful, but helped us make a more reasoned choice.

The goal of this thesis was the development of a hot-melt inkjet 3D system capable of dispersing two different materials during the same additive manufacturing process based on a commercially sourced LP50 printer. The printer should thus be capable to host two printhead-reservoir units alongside with the necessary support and motion systems.

As seen in Chapter 2.2 one of the biggest limitations in the system development was the weight constriction, nominally 2.5 kg. The original Meyer Burger hot melt unit has an overall weight of 926 g making it hard to fit two of them plus the mount support within the limits. In contrast Dimatrix cartridges are much lighter, weighing less than 200 g, however do not have reservoir heating capabilities. During the design phase of the system it was considered to use the multi cartridge system developed by Dr. Sturges [248] and shown in Figure A.1. This consist of an in house designed and built dual set-up which includes a custom made supports structure allowing the mounting of two separate Dimatix dispersing units onto the printer holder, alongside with the software and hardware implementation to control such modifications [248].

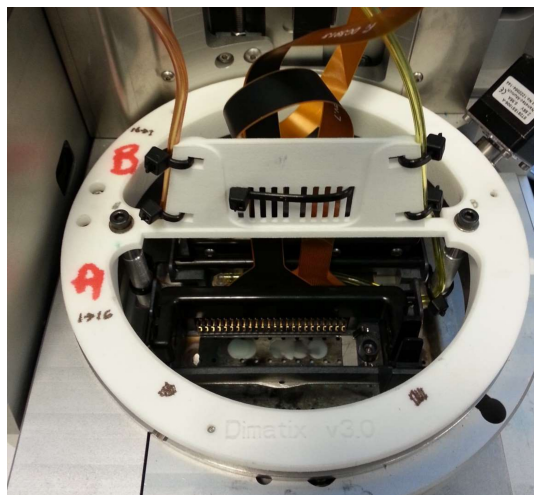


FIGURE A.1: Dual Dimatix assembly for the LP50 printer. Heads A and B are interfaced through the actual Dimatix interface device (sourced as spares). These are mounted on a metal plate, connected to a laser sintered hub. The whole assembly can rotate up to 90 deg counter clockwise.

To make the system suitable for hot-melt inkjet printing a heating element

had to be added to the cartridges' reservoirs. The Dimatix cartridge is a pressure controlled jetting system where the ink is stored within a flexible plastic bag inside a hard shell pressure chamber, see Figure A.2.

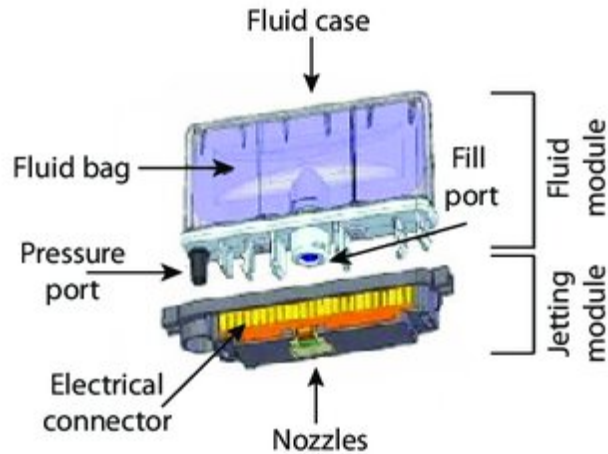


FIGURE A.2: Dimatix Material Cartridge. Constituted of a fluid module, fluid bag plus pressure chamber, and jetting module with the electrical connectors and nozzles.

This design makes it impossible to heat the ink directly without compromising the integrity of the outer shell, as a result, the heating element had to be positioned outside the casing as visible in Figure A.3.



FIGURE A.3: Dimatix Material Cartridge surrounded by a heating pad.

A TGA test was carried out on both the shell and bag material to ensure they could withstand the working temperature of the system, 90 °C. In Figure A.4 can be observed that both materials, show a single sharp thermo-oxidative decline with onset respectively at  $316.3 \pm 4.3$  °C for the external shell and  $318.9 \pm 3.5$  °C for the ink's bag. The results suggests that both material will not degrade at the temperature of interest.

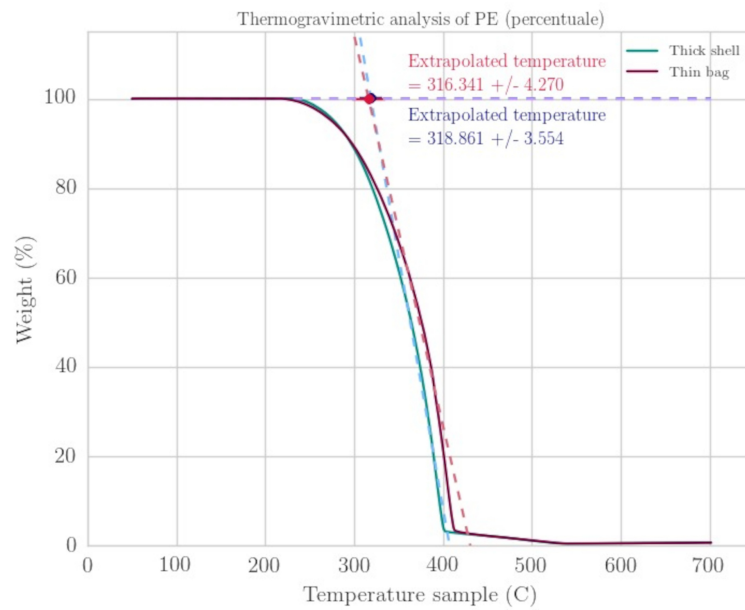


FIGURE A.4: Thermogravimetric curves of shell and bag materials samples from Dimatix cartridge

A small 5 mm hole was drilled in the outer shall and a thermocouple (PRO Type K Thermocouple, RS) was inserted to measure the chamber temperature. The remaining gape was sealed using high-temperature silicone sealants to restore the air seal. The external heating pad was connected to a power supply and the current set to 12V DC for one hour or until 90 °C were reached. During the experiment the signal from the thermocouple was read using a multimeter (Tenma 72-13440) while the temperature of the heating pad was measured using a IR thermometer (PRO 1327 Infrared Thermometer, RS). After 2 h the internal temperature was approximately 88 °C while the pad was reaching 180 °C, close to the starting degradation temperature of the material. Such a difference in temperature is caused by the presence of the air pocket separating the outer shell from the inner ink bag acting as an insulator preventing heat transfer. The experiment was interrupted and the cartridge set aside to cool. When inspected the cartridge showed sign of warping, melting and deformation. Due to the high temperature the material of the pressure chamber had softened during the experiment and bonded to the electric pad, such that wen the pad was removed it caused the shell to warp and tear as visible in Figure A.5.



FIGURE A.5: Damage to Dimatix cartridge after heating experiment

The idea of using a Dimatix cartridge was thus abandoned in favour of the original LP50 hot-melt inkjet unit as described in Chapter 2.2.



## Bibliography

- [1] R Gröning and G Heun. "Oral dosage forms with controlled gastrointestinal transit". In: *Drug Development and Industrial Pharmacy* 10.4 (1984), pp. 527–539.
- [2] Cyril P Bryan and G Elliot Smith. *Ancient Egyptian medicine: the papyrus ebers*. Vol. 6. Ares Chicago, 1974.
- [3] SAMIR YAHIA El-Gammal. "Pharmacy and medicine education in ancient Egypt". In: *Bull Inst Hist Med Hyderabad* 23.1 (1993), pp. 37–48.
- [4] IA Ramoutsaki et al. "Remedies used in Hellenic history." In: *Veterinary and human toxicology* 42.4 (2000), pp. 238–241.
- [5] Jerry Stannard. "Medicinal plants and folk remedies in pliny," *historia naturalis*". In: *History and Philosophy of the Life Sciences* 4.1 (1982), pp. 3–23.
- [6] Lise Wilkinson. "William Brockedon, FRS (1787-1854)". In: *Notes and records of the Royal Society of London* 26.1 (1971), pp. 65–72.
- [7] H Gjelstrup Kristensen and T Schaefer. "Granulation: a review on pharmaceutical wet-granulation". In: *Drug development and industrial pharmacy* 13.4-5 (1987), pp. 803–872.
- [8] Rajesh Agrawal and Yadav Naveen. "Pharmaceutical processing—A review on wet granulation technology". In: *International journal of pharmaceutical frontier research* 1.1 (2011), pp. 65–83.
- [9] Esratun Jannat et al. "Granulation techniques & its updated modules". In: *The Pharma Innovation* 5.10, Part B (2016), p. 134.
- [10] Srinivasan Shanmugam. "Granulation techniques and technologies: recent progresses". In: *BioImpacts: BI* 5.1 (2015), p. 55.
- [11] Peter Kleinebudde. "Roll compaction/dry granulation: pharmaceutical applications". In: *European Journal of Pharmaceutics and biopharmaceutics* 58.2 (2004), pp. 317–326.

- [12] Mohammad Kashif Iqbal et al. "Recent advances in direct compression technique for pharmaceutical tablet formulation". In: *International journal of pharmaceutical research and development* 6.1 (2014), pp. 49–57.
- [13] A G Mirani et al. "Direct compression high functionality excipient using coprocessing technique: A brief review". In: *Current drug delivery* 8.4 (2011), pp. 426–435.
- [14] Witold Jamróz et al. "3D printing in pharmaceutical and medical applications recent achievements and challenges". In: *Pharmaceutical research* 35.9 (2018), pp. 1–22.
- [15] Deng Guang Yu et al. "Three-dimensional printing in pharmaceuticals: promises and problems". In: *Journal of pharmaceutical sciences* 97.9 (2008), pp. 3666–3690.
- [16] Christopher John Tuck et al. "Rapid manufacturing facilitated customization". In: *International Journal of Computer Integrated Manufacturing* 21.3 (2008), pp. 245–258.
- [17] Nazila Yousefi and Ahmad Alibabaei. "Information flow in the pharmaceutical supply chain". In: *Iranian journal of pharmaceutical research: IJPR* 14.4 (2015), p. 1299.
- [18] Xufan Zhang et al. "Urban-rural differences in the association between access to healthcare and health outcomes among older adults in China". In: *BMC geriatrics* 17.1 (2017), pp. 1–11.
- [19] Aliasghar Ahmad Kiadaliri, Behzad Najafi, and Hassan Haghparast-Bidgoli. "Geographic distribution of need and access to health care in rural population: an ecological study in Iran". In: *International journal for equity in health* 10.1 (2011), pp. 1–7.
- [20] Alexandra J Greenberg et al. "Differences in access to and use of electronic personal health information between rural and urban residents in the United States". In: *The Journal of Rural Health* 34 (2018), s30–s38.
- [21] Claudia L Schur and Sheila J Franco. "Access to health care". In: *Rural health in the United States* (1999), pp. 25–37.
- [22] Jillian Clare Kohler et al. "An examination of pharmaceutical systems in severely disrupted countries". In: *BMC International Health and Human Rights* 12.1 (2012), pp. 1–11.

- [23] Samuel Roscoe et al. "Managing supply chain uncertainty arising from geopolitical disruptions: evidence from the pharmaceutical industry and brexit". In: *International Journal of Operations & Production Management* (2020).
- [24] Marsha Gold. "Beyond coverage and supply: measuring access to health-care in today's market." In: *Health Services Research* 33.3 Pt 2 (1998), p. 625.
- [25] Sudheer Gupta and Omkar D Palsule-Desai. "Sustainable supply chain management: Review and research opportunities". In: *IIMB Management review* 23.4 (2011), pp. 234–245.
- [26] Natalia Bellan et al. "Critical analysis of the regulations regarding the disposal of medication waste". In: *Brazilian Journal of Pharmaceutical Sciences* 48.3 (2012), pp. 507–518.
- [27] Hsiu-Yu Chien et al. "Study of medication waste in Taiwan". In: *Journal of Experimental & Clinical Medicine* 5.2 (2013), pp. 69–72.
- [28] Heba Shaaban et al. "Environmental contamination by pharmaceutical waste: assessing patterns of disposing unwanted medications and investigating the factors influencing personal disposal choices". In: *J Pharmacol Pharm Res* 1.1 (2018), p. 003.
- [29] Kathleen M Giacomini et al. "Pharmacogenomics and patient care: one size does not fit all". In: *Science translational medicine* 4.153 (2012), 153ps18–153ps18.
- [30] Brian B Spear, Margo Heath-Chiozzi, and Jeffrey Huff. "Clinical application of pharmacogenetics". In: *Trends in molecular medicine* 7.5 (2001), pp. 201–204.
- [31] Eric S Lander et al. "Initial sequencing and analysis of the human genome". In: (2001).
- [32] Liming Weng et al. "Pharmacogenetics and pharmacogenomics: a bridge to individualized cancer therapy". In: *Pharmacogenomics* 14.3 (2013), pp. 315–324.
- [33] Giuseppe Mercurio et al. "Cardiac function, physical exercise capacity, and quality of life during long-term thyrotropin-suppressive therapy with levothyroxine: effect of individual dose tailoring". In: *The Journal of Clinical Endocrinology & Metabolism* 85.1 (2000), pp. 159–164.

- [34] B Biondi et al. "Cardiac effects of long term thyrotropin-suppressive therapy with levothyroxine". In: *The Journal of Clinical Endocrinology & Metabolism* 77.2 (1993), pp. 334–338.
- [35] Charlotte Verrue et al. "Tablet-splitting: a common yet not so innocent practice". In: *Journal of advanced nursing* 67.1 (2011), pp. 26–32.
- [36] Susan Paparella. "Identified safety risks with splitting and crushing oral medications". In: *Journal of emergency nursing* 36.2 (2010), pp. 156–158.
- [37] Fang Zheng and Sheng-wu Huang. "Advances in study on three-dimensional printing in pharmaceuticals". In: *Chinese Herbal Medicines* 8.2 (2016), pp. 121–125.
- [38] Alvaro Goyanes et al. "Patient acceptability of 3D printed medicines". In: *International journal of pharmaceuticals* 530.1-2 (2017), pp. 71–78.
- [39] Debjit Bhowmik et al. "Controlled release drug delivery systems". In: *The Pharma Innovation* 1.10 (2012).
- [40] M Aqil and Asgar Ali. "Monolithic matrix type transdermal drug delivery systems of pinacidil monohydrate: in vitro characterisation". In: *European journal of pharmaceuticals and Biopharmaceutics* 54.2 (2002), pp. 161–164.
- [41] Sandip B Tiwari and Ali R Rajabi-Siahboomi. "Extended-release oral drug delivery technologies: monolithic matrix systems". In: *Drug delivery systems* (2008), pp. 217–243.
- [42] Kashmir Singh et al. "Osmotic pump drug delivery system: a novel approach". In: *Journal of Drug Delivery and Therapeutics* 3.5 (2013), pp. 156–162.
- [43] RS Thakor et al. "Osmotic drug delivery systems current scenario". In: *Journal of Pharmacy Research* 3.4 (2010), pp. 771–5.
- [44] Wan-Wan Yang and Erik Pierstorff. "Reservoir-based polymer drug delivery systems". In: *Journal of laboratory automation* 17.1 (2012), pp. 50–58.
- [45] Cynthia L Stevenson, John T Santini Jr, and Robert Langer. "Reservoir-based drug delivery systems utilizing microtechnology". In: *Advanced drug delivery reviews* 64.14 (2012), pp. 1590–1602.

- [46] Lida E Kalantzi et al. "Recent advances in oral pulsatile drug delivery". In: *Recent patents on drug delivery & formulation* 3.1 (2009), pp. 49–63.
- [47] Xiaoxing Lai et al. "Polypharmacy in the oldest old (over 80 years of age) patients in China: a cross-sectional study". In: *BMC geriatrics* 18.1 (2018), pp. 1–8.
- [48] Colleen A Colley and Linda M Lucas. "Polypharmacy". In: *Journal of general internal medicine* 8.5 (1993), pp. 278–283.
- [49] Emily R Hajjar, Angela C Cafiero, and Joseph T Hanlon. "Polypharmacy in elderly patients". In: *The American journal of geriatric pharmacotherapy* 5.4 (2007), pp. 345–351.
- [50] John Urquhart. "The indian polycap study (TIPS)". In: *The Lancet* 374.9692 (2009), pp. 781–782.
- [51] Peter Sleight, Hubert Pouleur, and Faiez Zannad. "Benefits, challenges, and registerability of the polypill". In: *European heart journal* 27.14 (2006), pp. 1651–1656.
- [52] José M Castellano et al. "A polypill strategy to improve adherence: results from the FOCUS project". In: *Journal of the American College of Cardiology* 64.20 (2014), pp. 2071–2082.
- [53] Jon Excell and S Nathan. *The rise of additive manufacturing. The Engineer*. 2010.
- [54] Johannes F Gottwald. *Liquid metal recorder*. US Patent 3,596,285. 1971.
- [55] P Ciraud. "Verfahren und Vorrichtung zur Herstellung beliebiger Gegenstände aus beliebigem schmelzbarem Material". In: *German patent application DE 2263777* (1973).
- [56] Hideo Kodama. "Automatic method for fabricating a three-dimensional plastic model with photo-hardening polymer". In: *Review of scientific instruments* 52.11 (1981), pp. 1770–1773.
- [57] William E Masters. *Computer automated manufacturing process and system*. US Patent 4,665,492. 1987.
- [58] 3D hub. 2021. URL: [https://www.3dhubs.com/?utm\\_campaign=gated\\_content&utm\\_medium=email&\\_hsmi=79739620&\\_hsenc=p2ANqtz-9gTE9Lvz70qthIxF8wwnFQzz0HfB2a05VxBN0-s1KJZYq\\_JMcy2sHvV6SwTCUv7NB9hcTSCwSFquAw9c0xAQEt\\_jb1BvNk&utm\\_source=gated\\_content](https://www.3dhubs.com/?utm_campaign=gated_content&utm_medium=email&_hsmi=79739620&_hsenc=p2ANqtz-9gTE9Lvz70qthIxF8wwnFQzz0HfB2a05VxBN0-s1KJZYq_JMcy2sHvV6SwTCUv7NB9hcTSCwSFquAw9c0xAQEt_jb1BvNk&utm_source=gated_content) (visited on 2021).

- [59] Helena N Chia and Benjamin M Wu. "Recent advances in 3D printing of biomaterials". In: *Journal of biological engineering* 9.1 (2015), p. 1.
- [60] Ilias El Aita, Jörg Breitzkreutz, and Julian Quodbach. "On-demand manufacturing of immediate release levetiracetam tablets using pressure-assisted microsyringe printing". In: *European Journal of Pharmaceutics and Biopharmaceutics* 134 (2019), pp. 29–36.
- [61] Ziyaur Rahman et al. "Additive manufacturing with 3D printing: Progress from bench to bedside". In: *The AAPS journal* 20.6 (2018), pp. 1–14.
- [62] Abdul Aleem Mohammed et al. "Optimization of semisolid extrusion (pressure-assisted microsyringe)-based 3D printing process for advanced drug delivery application". In: *Annals of 3D Printed Medicine* (2021), p. 100008.
- [63] Ilias El Aita et al. "3D-Printing with precise layer-wise dose adjustments for paediatric use via pressure-assisted microsyringe printing". In: *European Journal of Pharmaceutics and Biopharmaceutics* 157 (2020), pp. 59–65.
- [64] Shaban A Khaled et al. "3D extrusion printing of high drug loading immediate release paracetamol tablets". In: *International journal of pharmaceutics* 538.1-2 (2018), pp. 223–230.
- [65] Shaban A Khaled et al. "3D printing of tablets containing multiple drugs with defined release profiles". In: *International journal of pharmaceutics* 494.2 (2015), pp. 643–650.
- [66] Shaban A Khaled et al. "Desktop 3D printing of controlled release pharmaceutical bilayer tablets". In: *International journal of pharmaceutics* 461.1 (2014), pp. 105–111.
- [67] Shaban A Khaled et al. "3D printing of five-in-one dose combination polypill with defined immediate and sustained release profiles". In: *Journal of Controlled Release* 217 (2015), pp. 308–314.
- [68] James Comb, William Priedeman, and Patrick W Turley. "FDM® Technology process improvements". In: *1994 International Solid Freeform Fabrication Symposium*. 1994.
- [69] Deck Khong Tan, Mohammed Maniruzzaman, and Ali Nokhodchi. "Advanced pharmaceutical applications of hot-melt extrusion coupled with fused deposition modelling (FDM) 3D printing for personalised drug delivery". In: *Pharmaceutics* 10.4 (2018), p. 203.

- [70] Alvaro Goyanes et al. "Effect of geometry on drug release from 3D printed tablets". In: *International journal of pharmaceutics* 494.2 (2015), pp. 657–663.
- [71] Alvaro Goyanes et al. "3D printing of medicines: engineering novel oral devices with unique design and drug release characteristics". In: *Molecular pharmaceutics* 12.11 (2015), pp. 4077–4084.
- [72] Alvaro Goyanes et al. "Fused-filament 3D printing (3DP) for fabrication of tablets". In: *International journal of pharmaceutics* 476.1 (2014), pp. 88–92.
- [73] Fabrizio Fina et al. "Selective laser sintering (SLS) 3D printing of medicines". In: *International journal of pharmaceutics* 529.1-2 (2017), pp. 285–293.
- [74] Naseem A Charoo et al. "Selective laser sintering 3D printing—an overview of the technology and pharmaceutical applications". In: *Drug development and industrial pharmacy* 46.6 (2020), pp. 869–877.
- [75] Atheer Awad et al. "3D printing: Principles and pharmaceutical applications of selective laser sintering". In: *International Journal of Pharmaceutics* 586 (2020), p. 119594.
- [76] Fabrizio Fina et al. "Fabricating 3D printed orally disintegrating printlets using selective laser sintering". In: *International journal of pharmaceutics* 541.1-2 (2018), pp. 101–107.
- [77] CHRISTIAN Groth et al. "Three-dimensional printing technology". In: *J Clin Orthod* 48.8 (2014), pp. 475–85.
- [78] Xiaoyan Xu et al. "Stereolithography (SLA) 3D printing of an antihypertensive polyprintlet: Case study of an unexpected photopolymer-drug reaction". In: *Additive Manufacturing* 33 (2020), p. 101071.
- [79] Pamela Robles-Martinez et al. "3D printing of a multi-layered polypill containing six drugs using a novel stereolithographic method". In: *Pharmaceutics* 11.6 (2019), p. 274.
- [80] Brian Derby. "Inkjet printing of functional and structural materials: fluid property requirements, feature stability, and resolution". In: *Annual Review of Materials Research* 40.395–414 (2010), p. 8.
- [81] Ronan Daly et al. "Inkjet printing for pharmaceuticals—a review of research and manufacturing". In: *International journal of pharmaceutics* 494.2 (2015), pp. 554–567.

- [82] Emanuel M Sachs et al. *Three-dimensional printing techniques*. US Patent 5,204,055. 1993.
- [83] Leena Kumari Prasad and Hugh Smyth. "3D Printing technologies for drug delivery: a review". In: *Drug development and industrial pharmacy* 42.7 (2016), pp. 1019–1031.
- [84] Kyoung-Jin Lee et al. "Evaluation of critical formulation factors in the development of a rapidly dispersing captopril oral dosage form". In: *Drug development and industrial pharmacy* 29.9 (2003), pp. 967–979.
- [85] Deng Guang Yu et al. "Tablets with material gradients fabricated by three-dimensional printing". In: *Journal of pharmaceutical sciences* 96.9 (2007), pp. 2446–2456.
- [86] Chen-Chao Wang et al. "Development of near zero-order release dosage forms using three-dimensional printing (3-DP™) technology". In: *Drug development and industrial pharmacy* 32.3 (2006), pp. 367–376.
- [87] Monkhouse D.C. Rowe C.W. Wang C.C. "TheriForm technology. Modified release Drug Delivery Technology". In: *Drugs and Pharmaceutical Sciences* 126.1 (2000), pp. 376–394.
- [88] Jochen Mueller et al. "Mechanical properties of interfaces in inkjet 3D printed single-and multi-material parts". In: *3D Printing and Additive Manufacturing* 4.4 (2017), pp. 193–199.
- [89] Kathy Lu and William T Reynolds. "3DP process for fine mesh structure printing". In: *Powder technology* 187.1 (2008), pp. 11–18.
- [90] D Dimitrov, K Schreve, and N De Beer. "Advances in three dimensional printing-state of the art and future perspectives". In: *Rapid Prototyping Journal* 12.3 (2006), pp. 136–147.
- [91] Goole Jonathan and Amighi Karim. "3D printing in pharmaceuticals: A new tool for designing customized drug delivery systems". In: *International journal of pharmaceuticals* 499.1 (2016), pp. 376–394.
- [92] Elizabeth A Clark et al. "3D printing of tablets using inkjet with UV photoinitiation". In: *International journal of pharmaceuticals* 529.1-2 (2017), pp. 523–530.
- [93] Yinfeng He et al. "A Reactive Prodrug Ink Formulation Strategy for Inkjet 3D Printing of Controlled Release Dosage Forms and Implants". In: *Advanced Therapeutics* 3.6 (2020), p. 1900187.

- [94] Belen Begines et al. "Design of highly stabilized nanocomposite inks based on biodegradable polymer-matrix and gold nanoparticles for Inkjet Printing". In: *Scientific reports* 9.1 (2019), pp. 1–12.
- [95] Mary Kyobula et al. "3D inkjet printing of tablets exploiting bespoke complex geometries for controlled and tuneable drug release". In: *Journal of Controlled Release* 261 (2017), pp. 207–215.
- [96] David J Hauss. "Oral lipid-based formulations". In: *Advanced drug delivery reviews* 59.7 (2007), pp. 667–676.
- [97] J Vonderscher and A Meinzer. "Rationale for the development of Sandimmune Neoral". In: *Transplantation proceedings*. Vol. 26. 5. 1994, pp. 2925–2927.
- [98] R Neslihan Gursoy and Simon Benita. "Self-emulsifying drug delivery systems (SEDDS) for improved oral delivery of lipophilic drugs". In: *Biomedicine & pharmacotherapy* 58.3 (2004), pp. 173–182.
- [99] William N Charman. "Lipid vehicle and formulation effects on intestinal lymphatic drug transport". In: *Lymphatic transport of drugs*. Routledge, 2019, pp. 113–179.
- [100] David J Hauss et al. "Lipid-based delivery systems for improving the bioavailability and lymphatic transport of a poorly water-soluble LTB4 inhibitor". In: *Journal of pharmaceutical sciences* 87.2 (1998), pp. 164–169.
- [101] Bhagwant D Rege, Joseph PY Kao, and James E Polli. "Effects of non-ionic surfactants on membrane transporters in Caco-2 cell monolayers". In: *European journal of pharmaceutical sciences* 16.4-5 (2002), pp. 237–246.
- [102] Tochukwu C Okwuosa et al. "Fabricating a shell-core delayed release tablet using dual FDM 3D printing for patient-centred therapy". In: *Pharmaceutical research* 34.2 (2017), pp. 427–437.
- [103] Muqdad Alhijaj et al. "Impact of processing parameters on the quality of pharmaceutical solid dosage forms produced by fused deposition modeling (FDM)". In: *Pharmaceutics* 11.12 (2019), p. 633.
- [104] Muzna Sadia et al. "Adaptation of pharmaceutical excipients to FDM 3D printing for the fabrication of patient-tailored immediate release tablets". In: *International journal of pharmaceutics* 513.1-2 (2016), pp. 659–668.

- [105] *PiXDRO Inkjet Technology - Meyer Burger*.
- [106] *Spectra head Se 128 AA*.
- [107] Javier Ledesma Fernández. "Jetting of multiple functional materials by Additive Manufacturing". PhD thesis. University of Nottingham, 2018.
- [108] PM Meshram and Rohit G Kanojiya. "Tuning of PID controller using Ziegler-Nichols method for speed control of DC motor". In: *IEEE-international conference on advances in engineering, science and management (ICAESM-2012)*. IEEE. 2012, pp. 117–122.
- [109] Kwang Kon Koh et al. "Beneficial effects of fenofibrate to improve endothelial dysfunction and raise adiponectin levels in patients with primary hypertriglyceridemia". In: *Diabetes care* 28.6 (2005), pp. 1419–1424.
- [110] Julia A Balfour, Donna McTavish, and Rennie C Heel. "Fenofibrate. A review of its pharmacodynamic and pharmacokinetic properties and therapeutic use in dyslipidaemia." In: *Drugs* 40.2 (1990), pp. 260–290.
- [111] MJ Caslake et al. "Fenofibrate and LDL metabolic heterogeneity in hypercholesterolemia." In: *Arteriosclerosis, Thrombosis, and Vascular Biology* 13.5 (1993), pp. 702–711.
- [112] Yasmin Begum and Prathyusha Reddy. "Heightening the solubility of poorly soluble fenofibrate by Solid Dispersion Technique". In: *International Journal of Research in Pharmaceutical Sciences* 11.1 (2020), pp. 663–668.
- [113] Yaping Chen et al. "Enhanced bioavailability of the poorly water-soluble drug fenofibrate by using liposomes containing a bile salt". In: *International journal of pharmaceutics* 376.1-2 (2009), pp. 153–160.
- [114] V Jannin, E Pochard, and O Chambin. "Influence of poloxamers on the dissolution performance and stability of controlled-release formulations containing Precirol® ATO 5". In: *International journal of pharmaceutics* 309.1-2 (2006), pp. 6–15.
- [115] Filippou Kesisoglou, Santipharp Panmai, and Yunhui Wu. "Nanosizing—oral formulation development and biopharmaceutical evaluation". In: *Advanced drug delivery reviews* 59.7 (2007), pp. 631–644.
- [116] Jyh-Ding Wei et al. "Characterisation of fenofibrate dissolution delivered by a self-microemulsifying drug-delivery system". In: *Journal of Pharmacy and Pharmacology* 62.12 (2010), pp. 1685–1696.

- [117] Haibing He, Rui Yang, and Xing Tang. "In vitro and in vivo evaluation of fenofibrate solid dispersion prepared by hot-melt extrusion". In: *Drug development and industrial pharmacy* 36.6 (2010), pp. 681–687.
- [118] P Srinarong et al. "Strongly enhanced dissolution rate of fenofibrate solid dispersion tablets by incorporation of superdisintegrants". In: *European journal of pharmaceutics and biopharmaceutics* 73.1 (2009), pp. 154–161.
- [119] "CANDELILLA WAX, Evaluations of the Joint FAO/WHO Expert Committee on Food Additives (JECFA)". In: ().
- [120] D Brian Whitehouse. "CANDELILLA WAX". In: ().
- [121] Seigo Shinohara, Kiyoshi Okamura, and Tetsuo Kijima. *Glazing agent for an automobile*. US Patent 5,043,012. 1991.
- [122] Aboagyewa Asumadu-Mensah, Kevin W Smith, and Henelyta S Ribeiro. "Solid lipid dispersions: potential delivery system for functional ingredients in foods". In: *Journal of food science* 78.7 (2013), E1000–E1008.
- [123] Norsamsiah Muhamad Wahab et al. "Wax-Impregnated Cotton Fabrics as Cell Culture Platform". In: *Advanced Materials Research*. Vol. 1112. Trans Tech Publ. 2015, pp. 441–444.
- [124] ROBERT D HAGENMAIER and ROBERT A BAKER. "Edible coatings from candelilla wax microemulsions". In: *Journal of food science* 61.3 (1996), pp. 562–565.
- [125] Jorge A Aguirre-Joya et al. "The physicochemical, antifungal and antioxidant properties of a mixed polyphenol based bioactive film". In: *Heliyon* 4.12 (2018), e00942.
- [126] Jorge F Toro-Vazquez et al. "Candelilla wax as an organogelator for vegetable oils—an alternative to develop trans-free products for the food industry". In: *Edible Oleogels*. Elsevier, 2011, pp. 119–148.
- [127] Judith Ruiz-Martínez et al. "Candelilla Wax Edible Coating with *Flourensia cernua* Bioactives to Prolong the Quality of Tomato Fruits". In: *Foods* 9.9 (2020), p. 1303.
- [128] E Bosquez-Molina, I Guerrero-Legarreta, and EJ Vernon-Carter. "Moisture barrier properties and morphology of mesquite gum–candelilla wax based edible emulsion coatings". In: *Food Research International* 36.9-10 (2003), pp. 885–893.

- [129] Dariusz Kowalczyk. "Biopolymer/candelilla wax emulsion films as carriers of ascorbic acid—A comparative study". In: *Food Hydrocolloids* 52 (2016), pp. 543–553.
- [130] E Hernandez and RA Baker. "Candelilla wax emulsion, preparation and stability". In: *Journal of food science* 56.5 (1991), pp. 1382–1383.
- [131] An Huynh et al. "Evaluation of alkenones, a renewably sourced, plant-derived wax as a structuring agent for lipsticks". In: *International Journal of Cosmetic Science* 42.2 (2020), pp. 146–155.
- [132] Gattefosse, Apifil CG datasheet.
- [133] William L Coggshall, Roger A Morse, et al. "Beeswax: production, harvesting, processing and products." In: *Beeswax: production, harvesting, processing and products*. (1984).
- [134] Fritz Ullmann et al. *Ullmann's encyclopedia of industrial chemistry*. Vol. 5. Vch Weinheim, Germany, 1985.
- [135] Y Işcan, SA Wissing, RH Müller, et al. "Solid Lipid Nanoparticles (SLNTM) for topical drug delivery: incorporation of the lipophilic drugs N, N-diethyl-m-toluamide and vitamin K". In: *Die Pharmazie—An International Journal of Pharmaceutical Sciences* 60.12 (2005), pp. 905–909.
- [136] SM Pyo, CM Keck, and RH Müller. "Production of highly loaded Vitamin K1 nanostructures lipid carriers (NLC) against couperosis". In: ().
- [137] M. Kyobula. "Manufacturing of Oral Solid Dosage Forms Using 3D Inkjet Printing". In: (February 2017).
- [138] Gattefosse, Compritol 888 ATO datasheet.
- [139] A N'diaye et al. "Comparative study of the lubricant performance of Compritol® HD5 ATO and Compritol® 888 ATO: effect of polyethylene glycol behenate on lubricant capacity". In: *International journal of pharmaceuticals* 254.2 (2003), pp. 263–269.
- [140] V Jannin et al. "Comparative study of the lubricant performance of Compritol® 888 ATO either used by blending or by hot melt coating". In: *International journal of pharmaceuticals* 262.1-2 (2003), pp. 39–45.
- [141] MADY Omar. "Studying the release of diclofenac sodium from glycerides". In: *Int J Pharm Pharm Sci* 5.4 (2013), pp. 119–27.

- [142] Philippe Barthelemy et al. "Compritol® 888 ATO: an innovative hot-melt coating agent for prolonged-release drug formulations". In: *European journal of pharmaceutics and biopharmaceutics* 47.1 (1999), pp. 87–90.
- [143] SI Chemsá, A Maíza, and P Arnaud. "Sustained-Release Tablets of Hydrochlorothiazide, a Slightly Water-Soluble Molecule Using Glyceryl Behenate". In: *Pharmaceutical Chemistry Journal* 52.1 (2018), pp. 15–18.
- [144] Feng-Qian Li et al. "In vitro controlled release of sodium ferulate from Compritol 888 ATO-based matrix tablets". In: *International journal of pharmaceutics* 324.2 (2006), pp. 152–157.
- [145] Jamila Hamdani, André J Moës, and Karim Amighi. "Development and evaluation of prolonged release pellets obtained by the melt pelletization process". In: *International journal of pharmaceutics* 245.1-2 (2002), pp. 167–177.
- [146] Jamila Hamdani, André J Moës, and Karim Amighi. "Development and in vitro evaluation of a novel floating multiple unit dosage form obtained by melt pelletization". In: *International journal of pharmaceutics* 322.1-2 (2006), pp. 96–103.
- [147] Xiaochen Gu et al. "Evaluation and comparison of five matrix excipients for the controlled release of acrivastine and pseudoephedrine". In: *Drug development and industrial pharmacy* 30.10 (2004), pp. 1009–1017.
- [148] *Gattefosse, Compritol HD5 ATO datasheet.*
- [149] Chhanda Kapadia and Ketkee Deshmukh. "Comparative evaluation of Compritol® HD5 ATO with Sodium Stearyl Fumarate and PEG 6000 as amphiphilic, hydrodispersible pharmaceutical lubricants". In: *Journal of Excipients and Food Chemicals* 8.1 (2017), p. 1329.
- [150] Rania Hamed et al. "Influence of HPMC K100LV and Compritol® HD5 ATO on drug release and rheological behavior of HPMC K4M matrix tablets". In: *Journal of Pharmaceutical Innovation* 12.1 (2017), pp. 62–75.
- [151] *Gattefosse, Precirol ATO 5 datasheet.*
- [152] Marja Savolainen et al. "Evaluation of polar lipid–hydrophilic polymer microparticles". In: *International journal of pharmaceutics* 262.1-2 (2003), pp. 47–62.

- [153] Nuttanan Sinchaipanid, Varaporn Junyaprasert, and Ampol Mitrevej. "Application of hot-melt coating for controlled release of propranolol hydrochloride pellets". In: *Powder technology* 141.3 (2004), pp. 203–209.
- [154] Antonio María Rabasco Álvarez and María Luisa González Rodríguez. "Lipids in pharmaceutical and cosmetic preparations". In: *Grasas y Aceites*, 51 (1-2), 74–96. (2000).
- [155] Juergen Siepmann et al. "Lipids and polymers in pharmaceutical technology: Lifelong companions". In: *International journal of pharmaceuticals* 558 (2019), pp. 128–142.
- [156] Vanna Sanna et al. "Synthesis and evaluation of different fatty acid esters formulated into Precirol® ATO-based lipid nanoparticles as vehicles for topical delivery". In: *Chemical and Pharmaceutical Bulletin* 57.7 (2009), pp. 680–684.
- [157] Katsuaki Suganuma. *Introduction to printed electronics*. Vol. 74. Springer Science & Business Media, 2014.
- [158] Katsuaki Suganuma. "Printing Technology". In: *Introduction to Printed Electronics*. Springer, 2014, pp. 23–48.
- [159] Sung Hyun Park et al. "3D printed polymer photodetectors". In: *Advanced Materials* 30.40 (2018), p. 1803980.
- [160] Hossam Kadry et al. "Multi-purposable filaments of HPMC for 3D printing of medications with tailored drug release and timed-absorption". In: *International journal of pharmaceuticals* 544.1 (2018), pp. 285–296.
- [161] Michael H Chiu, Elmar J Prenner, et al. "Differential scanning calorimetry: an invaluable tool for a detailed thermodynamic characterization of macromolecules and their interactions". In: *Journal of Pharmacy and Bioallied Sciences* 3.1 (2011), p. 39.
- [162] Robert L Danley. "New heat flux DSC measurement technique". In: *Thermochimica acta* 395.1 (2002), pp. 201–208.
- [163] *Perkin Elmer, DSC 8000 datasheet*.
- [164] Joseph D Menczel et al. "Differential scanning calorimetry (DSC)". In: *Thermal analysis of polymers: Fundamentals and applications* (2009), pp. 7–239.

- [165] Günther Höhne, Wolfgang F Hemminger, and H-J Flammersheim. *Differential scanning calorimetry*. Springer Science & Business Media, 2013.
- [166] Paul Gabbott et al. "A practical introduction to differential scanning calorimetry". In: *Principles and applications of thermal analysis* (2008), pp. 1–50.
- [167] AW Coats and JP Redfern. "Thermogravimetric analysis. A review". In: *Analyst* 88.1053 (1963), pp. 906–924.
- [168] R Bruce Prime et al. "Thermogravimetric analysis (TGA)". In: *Thermal analysis of polymers: Fundamentals and applications* (2009), pp. 241–317.
- [169] Rod Bottom. "Thermogravimetric analysis". In: *Principles and applications of thermal analysis* 3 (2008), pp. 87–118.
- [170] Zhonghui Du, Xinhong Yu, and Yanchun Han. "Inkjet printing of viscoelastic polymer inks". In: *Chinese Chemical Letters* 29.3 (2018), pp. 399–404.
- [171] Claire McIlroy, OG Harlen, and NF Morrison. "Modelling the jetting of dilute polymer solutions in drop-on-demand inkjet printing". In: *Journal of Non-Newtonian Fluid Mechanics* 201 (2013), pp. 17–28.
- [172] Derek Albert Long. "Raman spectroscopy". In: *New York* (1977), pp. 1–12.
- [173] HA Barnes, Barnes Hutton JFK, and K Walters. *An Introduction to Rheology*, Elsevier Science Publishers. 1989.
- [174] Howard A Barnes. "A handbook of elementary rheology". In: (2000).
- [175] Leo H O Hellström et al. "Errors in parallel-plate and cone-plate rheometer measurements due to sample underfill". In: *Measurement Science and Technology* 26.1 (2014), p. 015301.
- [176] *Malvern, Kinexus datasheet*.
- [177] JM Deman and AM Beers. "Fat crystal networks: structure and rheological properties". In: *Journal of Texture Studies* 18.4 (1987), pp. 303–318.
- [178] Suresh S Narine and Alejandro G Marangoni. "Relating structure of fat crystal networks to mechanical properties: a review". In: *Food Research International* 32.4 (1999), pp. 227–248.
- [179] Alejandro G Marangoni. *Fat crystal networks*. Vol. 140. CRC Press, 2004.

- [180] Malcolm M Cross. "Rheology of non-Newtonian fluids: a new flow equation for pseudoplastic systems". In: *Journal of colloid science* 20.5 (1965), pp. 417–437.
- [181] Weilie Zhou et al. "Fundamentals of scanning electron microscopy (SEM)". In: *Scanning microscopy for nanotechnology*. Springer, 2006, pp. 1–40.
- [182] Ludwig Reimer. *Scanning electron microscopy: physics of image formation and microanalysis*. 2000.
- [183] *The Scanning Electron Microscope (SEM)*. 2021. URL: <https://www.eng-atoms.msm.cam.ac.uk/RoyalSocDemos/SEM> (visited on 2021).
- [184] *Sputter Coater Principles*. 2021. URL: [https://www.emsdiasum.com/microscopy/technical/datasheet/sputter\\_coating.aspx](https://www.emsdiasum.com/microscopy/technical/datasheet/sputter_coating.aspx) (visited on 2021).
- [185] Charles E Lyman et al. *Scanning electron microscopy, X-ray microanalysis, and analytical electron microscopy: a laboratory workbook*. Springer Science & Business Media, 2012.
- [186] Robert Parsons. "Sputter deposition processes". In: *Thin film processes II* 2 (1991), p. 177.
- [187] Theophanides Theophile. *Infrared spectroscopy: Materials science, engineering and technology*. BoD–Books on Demand, 2012.
- [188] C-P Sherman Hsu. "Infrared spectroscopy". In: *Handbook of instrumental techniques for analytical chemistry* 249 (1997).
- [189] J Fahrenfort. "Attenuated total reflection: A new principle for the production of useful infra-red reflection spectra of organic compounds". In: *Spectrochimica Acta* 17.7 (1961), pp. 698–709.
- [190] *How an FTIR Spectrometer Operates*. 2020. URL: [https://chem.libretexts.org/Bookshelves/Physical\\_and\\_Theoretical\\_Chemistry\\_Textbook\\_Maps/Supplemental\\_Modules\\_\(Physical\\_and\\_Theoretical\\_Chemistry\)/Spectroscopy/Vibrational\\_Spectroscopy/Infrared\\_Spectroscopy/How\\_an\\_FTIR\\_Spectrometer\\_Operates](https://chem.libretexts.org/Bookshelves/Physical_and_Theoretical_Chemistry_Textbook_Maps/Supplemental_Modules_(Physical_and_Theoretical_Chemistry)/Spectroscopy/Vibrational_Spectroscopy/Infrared_Spectroscopy/How_an_FTIR_Spectrometer_Operates) (visited on 2020).
- [191] O Llorente et al. "Study of the crosslinking process of waterborne UV curable polyurethane acrylates". In: *Progress in Organic Coatings* 99 (2016), pp. 437–442.

- [192] Matthew J Baker, Caryn S Hughes, and Katherine A Hollywood. *Biophotonics: Vibrational Spectroscopic Diagnostics*. Morgan & Claypool Publishers, 2016.
- [193] Ravi Kumar et al. "Formulation evaluation of mouth dissolving tablets of fenofibrate using sublimation technique". In: *Int J Chem Tech Res* 1.4 (2009), pp. 840–850.
- [194] PRGDJ Graves and D Gardiner. "Practical raman spectroscopy". In: *Springer* (1989).
- [195] Ewen Smith and Geoffrey Dent. "Modern Raman spectroscopy: a practical approach". In: (2005).
- [196] *Parts of a Raman Spectrometer*. 2019. URL: <https://courses.lumenlearning.com/labmethods/chapter/part-of-a-raman-spectrometer/> (visited on 2019).
- [197] Bertram Eugene Warren. *X-ray Diffraction*. Courier Corporation, 1990.
- [198] Leonid V Azároff et al. *X-ray Diffraction*. Vol. 3. 1. McGraw-Hill New York, 1974.
- [199] LD Whittig and WR Allardice. "X-ray diffraction techniques". In: *Methods of Soil Analysis: Part 1 Physical and Mineralogical Methods* 5 (1986), pp. 331–362.
- [200] Kye-Si Kwon. "Vision monitoring". In: *Inkjet-Based Micromanufacturing* (2012).
- [201] Gautam Singhvi and Mahaveer Singh. "In-vitro drug release characterization models". In: *Int J Pharm Stud Res* 2.1 (2011), pp. 77–84.
- [202] Vinod P Shah et al. "In vitro dissolution profile comparison—statistics and analysis of the similarity factor,  $f_2$ ". In: *Pharmaceutical research* 15.6 (1998), pp. 889–896.
- [203] Lyman Spalding. *The Pharmacopoeia of the United States of America*. 1820.
- [204] *Copley scientific, Dissolution Test Dis8000*.
- [205] Marja Savolainen et al. "Evaluation of controlled-release polar lipid microparticles". In: *International journal of pharmaceutics* 244.1-2 (2002), pp. 151–161.
- [206] Heinz-Helmut Perkampus. *UV-VIS Spectroscopy and its Applications*. Springer Science & Business Media, 2013.
- [207] H Förster. "UV/Vis spectroscopy". In: *Characterization I*. Springer, 2004, pp. 337–426.



- [218] Mónia AR Martins, Simão P Pinho, and João AP Coutinho. "Insights into the nature of eutectic and deep eutectic mixtures". In: *Journal of Solution Chemistry* 48.7 (2019), pp. 962–982.
- [219] Laziz Bouzidi et al. "Lubricating and waxy esters, I. Synthesis, crystallization, and melt behavior of linear monoesters". In: *Chemistry and physics of lipids* 165.1 (2012), pp. 38–50.
- [220] Xiangjun Shi, Yinghua Shao, and Xiaoxia Sheng. "A new polymorph of fenofibrate prepared by polymer-mediated crystallization". In: *Journal of Crystal Growth* 498 (2018), pp. 93–102.
- [221] Priscilla Chui Hong Wong, Paul Wan Sia Heng, and Lai Wah Chan. "Viscosity–temperature relationship of lipid-based excipients amenable for spray congealing: Derivation of a rheological parameter with good correlation to particle size". In: *European Journal of Lipid Science and Technology* 118.7 (2016), pp. 1062–1073.
- [222] Shankar Lalitha Sridhar and Franck J Vernerey. "The chain distribution tensor: linking nonlinear rheology and chain anisotropy in transient polymers". In: *Polymers* 10.8 (2018), p. 848.
- [223] Devalina Law et al. "Properties of rapidly dissolving eutectic mixtures of poly (ethylene glycol) and fenofibrate: the eutectic microstructure". In: *Journal of pharmaceutical sciences* 92.3 (2003), pp. 505–515.
- [224] Ri Li et al. "Drawback during deposition of overlapping molten wax droplets". In: *Journal of manufacturing science and engineering* 130.4 (2008).
- [225] Vassilios Karavelidis et al. "Evaluating the effects of crystallinity in new biocompatible polyester nanocarriers on drug release behavior". In: *International journal of nanomedicine* 6 (2011), p. 3021.
- [226] Jong-Cheol Jeong, Jaeyoung Lee, and Kilwon Cho. "Effects of crystalline microstructure on drug release behavior of poly ( $\epsilon$ -caprolactone) microspheres". In: *Journal of controlled release* 92.3 (2003), pp. 249–258.
- [227] Francesco Tres et al. "Real time Raman imaging to understand dissolution performance of amorphous solid dispersions". In: *Journal of controlled release* 188 (2014), pp. 53–60.
- [228] Francesco Tres et al. "Investigating the dissolution performance of amorphous solid dispersions using magnetic resonance imaging and proton NMR". In: *Molecules* 20.9 (2015), pp. 16404–16418.

- [229] Jennifer B Dressman et al. "Dissolution testing as a prognostic tool for oral drug absorption: immediate release dosage forms". In: *Pharmaceutical research* 15.1 (1998), pp. 11–22.
- [230] Suvakanta Dash et al. "Kinetic modeling on drug release from controlled drug delivery systems". In: *Acta Pol Pharm* 67.3 (2010), pp. 217–223.
- [231] KH Ramteke et al. "Mathematical models of drug dissolution: a review". In: *Sch. Acad. J. Pharm* 3.5 (2014), pp. 388–396.
- [232] Mario Grassi and Gabriele Grassi. "Mathematical modelling and controlled drug delivery: matrix systems". In: *Current drug delivery* 2.1 (2005), pp. 97–116.
- [233] Matthew Roberts et al. "Development and evaluation of sustained-release Compritol® 888 ATO matrix mini-tablets". In: *Drug development and industrial pharmacy* 38.9 (2012), pp. 1068–1076.
- [234] Rishabha Malviya. "Swelling and erosion based formulations for the treatment of chronic seizures using (3) 2 factorial design". In: *Middle-East Journal of Scientific Research* 11.1 (2012), pp. 77–84.
- [235] Kun Cheng et al. "Studies of hydroxypropyl methylcellulose donut-shaped tablets". In: *Drug development and industrial pharmacy* 25.9 (1999), pp. 1067–1071.
- [236] JOSE D. REYES. "Ethylene Vinyl Acetate (EVA) Copolymers and their Current and Future Use in Parenteral Applications". In: (2014).
- [237] Cherng-ju Kim. "Release kinetics of coated, donut-shaped tablets for water soluble drugs". In: *European journal of pharmaceutical sciences* 7.3 (1999), pp. 237–242.
- [238] JP Cleave. "Some geometrical considerations concerning the design of tablets". In: *Journal of Pharmacy and Pharmacology* 17.11 (1965), pp. 698–702.
- [239] Mohsen A Bayomi. "Geometric approach for zero-order release of drugs dispersed in an inert matrix". In: *Pharmaceutical research* 11.6 (1994), pp. 914–916.
- [240] H Yeşim Karasulu and Gökhan Ertan. "Different geometric shaped hydrogel theophylline tablets: Statistical approach for estimating drug release". In: *Il Farmaco* 57.11 (2002), pp. 939–945.

- [241] US Department of Health et al. *Size, shape, and other physical attributes of generic tablets and capsules guidance for industry*. 2015.
- [242] Peter Vandenabeele. *Practical Raman spectroscopy: an introduction*. John Wiley & Sons, 2013.
- [243] John R Ferraro. *Introductory raman spectroscopy*. Elsevier, 2003.
- [244] Hideo Nakae et al. "Effects of surface roughness on wettability". In: *Acta materialia* 46.7 (1998), pp. 2313–2318.
- [245] We Katstra et al. "Oral dosage forms fabricated by Three Dimensional Printing™". In: *Journal of controlled release* 66.1 (2000), pp. 1–9.
- [246] Weigang Wu et al. "A therapeutic delivery system for chronic osteomyelitis via a multi-drug implant based on three-dimensional printing technology". In: *Journal of biomaterials applications* 31.2 (2016), pp. 250–260.
- [247] George B Kauffman. "Ullmann's Encyclopedia of Industrial Chemistry Fifth Edition, First International Edition in English by Wolfgang Gehartz, Gail Schulz Thomas Kellersohn, Barbara Elvers, Stephen Hawkins, and Ulrike Winter (Eds.)" In: *The Chemical Educator* 5.1 (2000), pp. 49–53.
- [248] Craig Sturgess. "Fully reactive 3D inkjet printing of polydimethylsiloxane and polyurethane". PhD thesis. University of Nottingham, 2018.